KePASSA 2022

5th International Workshop on

Key Topics in Orbit Propagation applied to Space Situational Awareness

June 22-24, 2022

University of La Rioja
Logroño (Spain)

PROGRAM & ABSTRACT BOOK

KePASSA-22
5th International Workshop on Key Topics in Orbit Propagation applied to Space Situational Awareness

Program & Abstract Book
22-24 June 2022
University of La Rioja
Logroño (Spain)

Editors
Rosario López
Juan Félix San-Juan
Martín Lara

© The Authors, Logroño, 2022
© Universidad de La Rioja, 2022

ISBN: 978-84-09-42904-2
Edit: Universidad de La Rioja

Front page and back: University of La Rioja.

All rights reserved to authors. The total or partial reproduction of this work is strictly prohibited, without the strict authorization of the copyright owners, under the sanctions established in the laws.

PREFACE

For its fifth edition, KePASSA goes back to Logroño, where the series of workshops was kicked off in 2014.

The workshop aims to gather worldwide experts in the field of orbit propagation who deliver talks of top-notch scientific content in an informal, friendly and relaxed environment.

Orbit propagation, the main topic of the workshop, is one of the most challenging and complex aspects of astronautics and will play a key role in ensuring the sustainable use of space. The continuous development and upgrade of orbit propagation techniques is instrumental for tackling most of the SSA challenges, e.g. those posed by the imminent realization of mega-constellations, the creation of sensors capable of tracking hundreds of thousands of objects, and the implementation of a space traffic management and control system.

To allow researchers to present last-minute results KePASSA is a presentation-only workshop, although proceedings are edited when a sufficient number of authors requires it. Stimulating scientific discussions, creation of partnership and collaborations will be facilitated by the warm hospitality of La Rioja, its people, its food and, importantly, its wine. We are looking forward to meeting you soon and celebrating together another successful KePASSA meeting!

AIMS AND SCOPE

The workshop will be an opportunity to showcase the progress made since our last meeting in Logroño 2019 in the following topics:

- Analytical, semi-analytical, and numerical propagation methods
- Hybrid and statistical methods
- Uncertainty quantification and propagation
- State vector representation, orbital elements/coordinates
- Long-term and short-term propagation
- Resonances and chaos
- Series expansions
- Special functions
- Non-gravitational perturbations
- High fidelity models
- Symbolic computation
- Software packages for orbit propagation
- Third body and time dependence in the analytical method
- End-of-life disposal
- Collision probability computation
- Planetary protection
- High-Earth Orbits and Highly-Elliptical Orbits
- Relative dynamics

SPECIAL SESSIONS

- Analytical, semi-analytical, and numerical propagation methods
- Perturbation theory
- Resonances and chaos
- Hybrid and statistical methods
- Collision probability computation
- Uncertainty quantification and propagation
- Mission design
- Perturbation modeling and integration
- Relative dynamics

ORGANIZING COMMITTEE

Scientific Committee

- Alessi, Elisa María (Consiglio Nazionale delle Ricerche, Italy)
- Armellin, Roberto (University of Auckland, New Zealand)
- Cefola, Paul (State University of New York at Buffalo, USA)
- Deleflie, Florent (IMCCE/GRGS, Observatoire de Paris, France)
- Pini Gurfil (Technion- Israel Institute of Technology, Israel)
- Hautesserres, Denis (CNES, France)
- Lara, Martín (SCoTIC -UR, Spain)
- Francesca Letizia (European Space Agency, Germany)
- Jesús Peláez (Polytechnic University, Madrid)
- San-Juan, Juan Félix (SCoTIC-UR, Spain)
- Yáñez, Carlos (CNES, France)

Local Committee

- Carrillo, Hans (SCoTIC -UR, Spain)
- Deleflie, Florent (IMCCE/GRGS, Observatoire de Paris, France)
- Hautesserres, Denis (CNES, France)
- Higueras, Manuel (SCoTIC -UR, Spain)
- Lara, Martín (SCoTIC -UR, Spain)
- López, Rosario (SCoTIC -UR, Spain)
- Pérez, Iván (SCoTIC -UR, Spain)
- San-Juan, Juan Félix (SCoTIC -UR, Spain)
- Segura, Edna (SCoTIC -UR, Spain)

Friday, June 24, 2022

SESSION: PERTURBATION MODELING AND INTEGRATION

10:05–10:22 h Dynamical geometry associated with the collision manifold in the circular restricted three-body problem
J. FITZGERALD, S. ROSS

10:22–10:39 h Canonical Modeling of The Solar Radiation Pressure Perturbation – N. VEGH, V. MARTINUSI

10:39–10:56 h CUDA implementation of the first derivative of the gravity potential – C. RUBIO, J. GONZALO, J. SIMINSKI, A. ESCAPA

10:56–11:13 h CUDAjectory: a GPU-based software for massive parallel orbit propagation (VIDEO)
A.F. INNO, C. COLOMBO, A. MASAT, L. BUCCI, F. RENK

11:13–11:30 h Time integrator for second order in time problems
B. BUJANDA, A. DUQUE

11:30–11:50 h *Coffee break*

SESSION: RELATIVE DYNAMICS

11:50–12:07 h A Curvilinear Generalization of the Yamanaka-Ankersen State Transition Matrix
A. MARTÍNEZ-CACHO, C. BOMBARDELLI

12:07–12:24 h Influence of Apophis' spin axis variations on a spacecraft during the 2029 close approach with Earth
S. ALJBAAE, A.F.B.A. PRADO, J. SOUCHAY, V. CARRUBA

12:24–12:41 h Formation design selection based on time and cost of reset
D. MENZIO, A. MAHFOUZ, F. DALLA VEDOVA, H. VOOS

12:41–12:58 h A Closer Look at Two-Line Elements Data
A. CICCARELLI, C. BOMBARDELLI

13:00–13:15 h **KePASSA Closing**

13:15–14:45 h *Lunch time*

Activity: Solar de Samaniego Winery + Laguardia Tour

Extra cost: 70 € including Bus + activities
Bus: · 17:15 h – AC Hotel La Rioja
· 17:25 h – Fuente de Murrieta

18:00 h 1 hour-visit (museum and winery)
Ends with a taste of 2 wines and tapas.

19:30 h 1 hour-visit (Laguardia and calado -old underground winery)
Ends with a taste of wine

20:30 h Tapas in Laguardia in its festivity of St. Juan
Return: at 23:00/23:30 h

KePASSA 2022

5th International Workshop on Key Topics in Orbit Propagation Applied to Space Situational Awareness

June 22-24, 2022
University of La Rioja
Polytechnic building
Luis de Ulloa, 4
Logroño (Spain)

UNIVERSIDAD DE LA RIOJA 1992–2022
cnes CENTRE NATIONAL D'ÉTUDES SPATIALES
IMCCE l'Observatoire de Paris | PSL
SCOTIC Scientific Computation & Technological Innovation Center

EUROPEAN UNION European Structural and Investment Fund
La Rioja
SOLAR DE SAMANIEGO

More information:
https://kepassa2022.sciencesconf.org
rosario.lopez@unirioja.es

Imagen: ESA. The European Space Agency (www.esa.int)

PROGRAMME

Wednesday, June 22, 2022

9:00–9:15 h *Reception*

9:15–10:00 h **Opening ceremony**

10:15–10:50 h **Plenary. Long-term numerical propagation for earth orbiting satellites –** D. A. Vallado

10:50–11:15 h *Coffee break*

SESSION: ANALYTICAL, SEMI-ANALYTICAL, AND NUMERICAL PROPAGATION METHODS

11:15–11:32 h Bringing in break-up events within a space objects catalogue – A. Pastor, J. Siminski, G. Escribano, M. Sanjurjo-Rivo, D. Escobar

11:32–11:49 h Efficient Numerical Solution of the Low-Thrust Lambert's problem – L. Dell'Elce, A. J. Rosengren

11:49–12:06 h Flyby dynamical characterisation with Jacobian eigenvalues – A. Masat, C. Colombo, A. Boutonnet

12:06– 2:23 h Semi-analytical propagation of NEO binaries: the history of the Janus mission targets 1991 VH and 1996 FG3
O. Fuentes-Muñoz, A. Meyer, D. J. Scheeres

12:23–12:40 h Single-averaged analytical model for low-thrust collision avoidance manoeuvres
J. L. Gonzalo, C. Colombo

12:40–12:57 h Dynamics of a Close Earth Satellite by Picard Iterations
M. Lara

13:00–14:20 h *Lunch time*

SESSION: PERTURBATION THEORY

14:30–14:47 h Statistical analysis of the long-term dynamical behavior of uncontrolled geostationary satellites near an unstable equilibrium point (VIDEO)
R. Flores, M. Pontani, E. Fantino

14:47–15:04 h Improving long-term special perturbations efficiency for Low Earth Orbits – D. Amato, D. A. Vallado

15:04–15:21 h Simultaneously Quasi-Critical and Quasi-Heliosynchronous Orbits – R. Vilhena de Moraes, M. L. Galhego da Costa, A. F. B. A.Prado, J. P. S. Carvalho

15:21–15:38 h Semi-analytical computation of center-stable and center-unstable manifolds in the geostationary belt
M. Barcelona, À. Haro, J-M. Mondelo

15:38–15:55 h Validation of GTDS and DSST Standalone versions against precise orbit ephemerides
P. Cefola, J. Stratford, R. López, J. F. San-Juan

15:55–16:12 h Remarks on The Super-integrability of Dynamical Systems – V. Martinusi

16:15–16:30 h *Coffee break*

SESSION: RESONANCES AND CHAOS

16:30–16:47 h Iochroma asteroid family resonance perturbations (VIDEO)
A. Rosaev

16:47–17:04 h A detailed dynamical model for inclination-only dependent lunisolar resonances. Effects on the "eccentricity growth" mechanism – E. Legnaro, C. Efthymiopoulos

17:04–17:21 h An Arnold diffusion mechanism for the Galileo satellites
A. Pousse, M. Giralt, I. Baldomá, M. Guardia, E.M. Alessi

17:21–17:38 h Fourier Expansion of the J_2 Potential as a Prelude to Resonant Orbit Control Theory – N. Nailhot, P. Gurfil

17:38–17:55 h Lagrangian Descriptors for global dynamics (VIDEO)
J. Daquin, R. Pedenon-Orlanducci, M. Agaouglou, G. Garcia-Sanchez, A. M. Mancho

17:55–18:12 h Low energy interplanetary trajectories using multiple gravity assists – M. Werner, S. Ross

18:12–18:29 h Lunar mean-motion and secular resonances
A. J. Rosengren, Di Wu, L. Dell'Elce

Thursday, June 23, 2022

9:00–9:35 h **Plenary. A natural perturbation treatment of the Molniya orbital behavior, based on the TLE data set –** E. M. Alessi

SESSION: HYBRID AND STATISTICAL METHODS

9:35–9:52 h Improving the force model of SGP4 using Neural Network
H. Carrillo, E. Segura, R. López, J. F. San-Juan

9:52–10:09 h Apply the hybrid orbit propagator to the association problem in the GEO region
J. F. San-Juan, R. López, C. Yanez, M. Higueras

10:09–10:26 h Manoeuvre detection based on S3TSR data
R. Vazquez, J.M. Montilla, J. C. Sanchez, J. Galan-Vioque, J. Rey, J. Siminski

10:30–10:45 h *Coffee break*

SESSION: COLLISION PROBABILITY COMPUTATION

10:45–11:02 h Analysing transport phenomena in orbital conjunctions
R. Molina, G. Escribano, M. Sanjurjo-Rivo

11:02–11:19 h Astrodynamical methods for collision avoidance automation
J. Siminski, K. Merz, V. Schaus

11:19–11:36 h Automation of the collision risk management from conjunction data message reception up to the decision-making – A. Petit, R. Lucken, S. Redel, F. Deleflie, V. Morand, F. Laporte

11:36–11:53 h Covariance determination for uncertainty realism in collision probability estimates
A. Cano, A. Pastor, E. Arias, D. Sáez, J. Míguez, M. Sanjurjo-Rivo, D. Escobar

11:53–12:10 h Deep learning for all-vs-all conjunction detection
E. Stevenson, V. Rodriguez-Fernandez, H. Urrutxua, D. Camacho

12:10–12:27 h Fast Orbit Propagation for Conjunction Screening
A. Rivero, C. Bombardelli, R. Vázquez

12:30–14:00 h *Lunch time*

SESSION: UNCERTAINTY QUANTIFICATION AND PROPAGATION

14:17–14:34 h A convex optimisation-based approach to detect and estimate manoeuvres – L. Pirovano, R. Armellin

14:34–14:51 h Assessment of uncertainty propagation techniques to study the topology of the space resident population
M. Romano, T. Carletti, A. Lemaitre, J. Daquin

14:51–15:08 h Cislunar Space Domain Awareness: Improved characterization and uncertainty quantification
P. Machuca, A.J. Rosengren

15:08–15:25 h Combining Taylor polynomials and multifidelity dynamics for the efficient propagation of uncertainties in orbital mechanics – A. Fossà, R. Armellin, E. Delande, M. Losacco, F. Sanfedino

15:25–15:42 h Non-linear Set Propagation with Generalised Equinoctial Orbital Elements – M. Hallgarten La Casta, L. Sánchez Fernandez-Mellado, D. Amato, M. Vasile

15:45–16:05 h *Coffee break*

SESSION: MISSION DESIGN

16:05–16:22 h Disposal Options below the GEO protected region (VIDEO)
D.K. Skoulidou, S. Lemmens

16:22–16:39 h Preliminary analysis of an active debris removal mission for large constellations: A Constraint Programming methodology – A. Barea, J. L. Gonzalo, C. Colombo, H. Urrutxua

16:39–16:56 h GPU-assisted search for low-cost transfers between whiskered tori, with applications to resonance transfers in a restricted 4-body model – B. Kumar, R. Anderson, R. de la Llave

16:56–17:13 h Shape-based low-thrust trajectory optimization enhanced via orthogonal functions, collocation and regularization
S. Cuevas del Valle, H. Urrutxua, P. Solano-López

17:13–17:30 h Orbit Transfer using Theory of Functional Connections via change of variables (VIDEO)
A. Kardec de Almeida Junior, A. F. B. A. Prado, D. Mortari

17:30–17:47 h On optimal trajectories of solar sails (VIDEO)
A. Herasimenka

21:00–23:55 h *Cocktail and Gala Dinner at Delicatto Restaurant*
Bus: · 20:30 h – AC Hotel La Rioja
· 20:40 h – Fuente de Murrieta

Plenary:

DAVID A. VALLADO

LONG-TERM NUMERICAL PROPAGATION FOR EARTH ORBITING SATELLITES

David A. Vallado *

Numerical propagation techniques have been extensively studied and are routine for precise satellite operations. Most studies focus on time spans of a few days to several weeks, specific orbital classes, or interplanetary orbits. As long term numerical operations become more commonplace, it's useful to quantify accuracy performance for propagations of several months, to years. This talk performs long-term numerical propagation comparisons against reference orbits in a variety of orbital classes. Semianalytical techniques are also used in the comparisons including a general discussion of the initial osculating to mean element conversion. Simplified General Perturbations (SGP4) is discussed with some comments on the new SGP4-XP semianalytical routine. Finally, orbital size, shape, and orientation considerations are examined.

INTRODUCTION

Space Situational Awareness (SSA) implies the knowledge of how, what, where, when and why things are in orbit. I refine that definition so that SSA is the process by which an organization maintains orbital state and mission information on all objects in space with some level of accuracy, now, and at a future time. The general flow of events is to process observations with an Orbit Determination (OD) scheme (that uses a propagator with an integrator), and then to create an ephemeris with the same propagator and integrator. Propagators are either analytical and semianalytical (using mean elements), or numerical (using osculating elements). Mean elements are averaged based on separating secular, short and long periodic variations, and have many dependencies on the type of averaging. Osculating elements vary over time and should represent the best estimate of the satellite state at any given time. As such, precise SSA operations often use osculating elements, and mean element theories always have some way to extract osculating values at instants of time.

Researchers seek techniques to provide solutions to the various missions of SSA. One focus area is the rapid long-term propagation of satellite orbits. This is especially true for the analytical and semianalytical techniques. The SGP4 routine that has been used for many decades by the US Space Force is a prime example, and one that I'll focus on a little later. The initial development of a technique focuses less on the routine daily OD from observations to support SSA operations, but rather the speed and accuracy of the propagator. This often neglects the need to convert between elements, although it may be relevant in some cases, and is always considered as development matures. Accurately comparing semianalytical techniques to reference numerical ephemerides provides some interesting challenges as we'll see later.

There is interest in mega constellations today, mostly for Low Earth Orbit (LEO), and *if* all the projections come true, over 100,000 additional new payloads will reside in orbit – an increase of 3-4 times the current catalog! Additionally, as the new US Space Force S-band radar "fence" comes online, the space catalog may grow by many thousands of objects due to the improved observability of small debris objects.

Selecting which propagator is the most accurate approach always evokes a passionate discussion! Combined with trying to process a space catalog that's 5-10 times larger than it is today presents another challenge – not to mention how to transmit all the information to users! Numerical propagation is generally accepted as the most accurate for SSA mission operations (several weeks). But how does it perform 6 months out, a

* Senior Research Astrodynamicist, Commercial Space Operations Center, Center for Space Standards and Innovation, Colorado, 80920-6522. dvallado@comspoc.com.

year, or more? Are analytical and semianalytical techniques perhaps better for some situations? How do I get the initial state vectors so I can accurately compare each of these approaches?

If all the observations used to create the Two Line Element (TLE) catalog were publically available (they're not), one *could* process them all (OD) with each specific propagation technique to create initial mean or osculating element state vectors (lots of computer processing). The largest [only comprehensive*] collection of public data for space objects is the TLE database produced over time by the U.S. Air Force Space Command. This data derives from an analytical propagator (Simplified General Perturbations SGP4, Vallado et al. 2006) that produces an osculating ephemeris of modest accuracy given a mean element initial state. Unfortunately, the accuracy of the TLE catalog is not sufficient to perform highly accurate studies and the errors of the observations and the mathematical theory are intertwined. Thus, I do not consider OD from observations in this talk.

I also do not address covariance matrices in this talk even though they could be useful in understanding the accuracy. There are many formulations and their public availability is limited for most applications. For example, no covariance information exists for the TLE catalog. Finally, recognize that maneuvering satellites change the nature of the problem because the propagation must be accurate only for the length of time between maneuvers. This is often quite short and may be a few days to a few weeks.

Two solutions are readily available to find accurate reference ephemerides. Several non-maneuvering Satellite Laser Ranging (SLR) satellites have long, well defined, independent ephemerides. These ephemerides are produced in the Consolidated Predicted File (CPF) formats that are available for many SLR equipped satellites†. These are predicted orbits, so the accuracy is generally less than rigorous OD solutions of the SLR data, but they do afford a comparison at about the meter-level. Several centers produce the ephemerides‡. The CPF ephemerides can be considered Precision Orbit Ephemerides (POE's), or "truth" orbits.

The second source of reference ephemerides is to use a numerical technique to generate a reference orbit and then make the comparisons against this ephemeris. Rather than doing this without clarification, a section compares the numerical propagator and selected integrator to establish that the settings and approach are accurate compared to independent truth ephemerides.

The structure of the talk is as follows. First, I review some of the literature and error sources in integrators and generic propagation schemes. Next, the study methodology is setup including satellites, time spans, integrators, etc. The results lay out a sequenced approach to establishing accuracy. First, integrators are compared against each other to understand the specific implementations and any settings (ie step-size) that may need to be adjusted. After selecting a baseline integrator for the numerical propagation, comparisons are made to the CPF orbits to establish a baseline accuracy. To illustrate one analytical approach, comparisons are made to TLE vectors, both from a single state, to the regularly released TLE values. The comparisons to the CPF orbits reveal a need to obtain the proper initial state for all techniques (Vallado, 2007). Many comparisons are made for satellites in different orbital classes. Several semianalytical technique comparisons are shown against a GEO orbit. A discussion of SGP4 and the new SGP4-XP provides continuity on one of the most widely used analytical techniques available. Finally, there is a discussion of the accuracy from the orbital plane, size and shape characteristics. Essentially, the positional accuracy may degrade, but the orbital plane may be fairly accurate, and therefore sufficient for some applications.

PRIOR STUDIES

Many papers have examined aspects of this problem, or techniques used in this study. A few follow.

Montenbruck (1992) examines various numerical integrators for orbital propagation. He shows function calls vs digits accuracy for many Runge-Kutta methods, noting that many propagators exist that can fulfill modern mission analyses. He also remarks that traditional fixed size step workhorses like GEODYN, UTOPIA, and PEPSOC, etc still have a solid place in numerical propagation, and therefore SSA activities.

---

* ESA (2019) lists additional catalog sources as the JSC Vimpel Space Data, and the Keldysh Institute for Applied Mathematics (KIAM). Note that these sources do not exist for as long a historical interval as the TLE catalog.

† ftp://edc.dgfi.tum.de/pub/slr/cpf_predicts_v2 (accessed March 2022)

‡ https://ilrs.gsfc.nasa.gov/data_and_products/predictions/prediction_centers.html (Accessed June 2022).

Wilkins et al. (2000) examined creating a general perturbation (GP, analytical) catalog from the numerical catalog the Navy was producing at the time. This was the first large catalog conversion from osculating to mean elements, and it showed the benefits of increased density of observations (in the form of ephemerides instead of sparse observations). The paper also demonstrated the need to perform a PCE to properly find the best initial conditions for the mean element theory. I'll expand on this requirement later.

Bradley (2009) discusses symplectic propagators for long-period propagation (many years). He looks at several orbits. There is some focus on International Terrestrial Reference Frame (ITRF) propagation. Finally, he examines the number of function calls and EOP/ International Astronomical Union (IAU) transformations.

Hofsteenge (2013) examines long term debris propagations for hundreds of years including some symplectic integrators. He uses the TU Delft Astrodynamics Toolbox (Tudat) program. Hofsteenge concludes that symplectic methods are very efficient for Hamiltonian systems, but might be difficult to implement for other systems and applications. He noted the difficulty in determining the initial conditions, and the effect it had on the results.

Atallah (2019) examines several integrators, including the Adaptive Picard Chebyshev (Woollands and Junkins 2019). He describes several tests that can also be applied to integrator comparisons. Because my efforts were more general, I opted to use a simple positional comparison, but these additional tests could provide some rigor to future studies.

Vallado (2019) examined the long term propagation and this talk derives primarily from that paper.

METHODOLOGY

Several things were needed to accomplish this study. First, satellites were selected to represent various orbital classes that are relevant for SSA. Generic satellites were used for the initial integrator tests and for some semianalytical tests. Actual satellites were used in the comparison to independent orbits. Integrators and propagators were selected based on availability of code and programs. Reference orbits were generally selected from SLR satellites as they afford several orbital classes combined with very high accuracy.

Selected Satellites

The initial task was to select a number of satellites with existing POE information, or other high quality ephemerides that could be used for comparisons. The satellites selected for this study form a spectrum from LEO to Geosynchronous (GEO) satellites (Table 1). The epochs varied due to the presence of available information. A year or more of data was selected for as many satellites as possible, and periods of higher solar activity were preferred to highlight the effects of atmospheric drag on the lower altitude orbits. The additional satellites in the LEO category were designed to better determine the results in the drag regime, and at the lower end of the solar radiation pressure regime. The LEO satellites also account for repeat ground track, sun-synchronous and frozen orbit conditions which can exhibit interesting resonances. The study satellites in Table 1 permitted a quick look at various orbital classes, but the specific satellite parameters (coefficient of drag (c_D), coefficient of radiation pressure (c_{SR}), mass (m), area (A)) are often difficult to obtain.

The study interval was generally from 1 Jan 2018 00:00:00.000 to 1 Jul 2019 00:00:00.000, depending on the available data. The time frame for the analysis is important for LEO orbits. For atmospheric drag, solar maximum is desirable, but the last solar max was quite low.

Integrators and Propagators

All numerical propagations are performed with Ansys/AGI's Systems Tool Kit/High Precision Orbit Propagator (STK/HPOP). STK/HPOP lets you select the following types. I did not test other types of integrators (including symplectic, Picard Chebyshev, differential algebra, etc).

- RK4
- RK7/8
- RK8/9
- Burlisch-Stoer

- Gauss-Jackson*

Table 1: **Satellite Orbital Parameters:** This table lists the general orbital parameters for satellites used in the study. There are 2 overall categories. The simulated orbits were general orbits chosen for integrator performance evaluation. The SLR orbits contain orbital classes (Sun-synchronous, repeat ground-track, frozen orbit) that are useful in testing, and have accurate ephemerides for comparisons. The mass and area parameters were assumed, or derived from the Internet. The mass is often the initial mass – not intended to be definitive values! Acronyms: Highly Elliptical Orbit (HEO), Medium Earth Orbit (MEO), Global Positioning Satellite (GPS), Laser Relativity Satellite (LARES), Ajisai (the Japanese name for the Hydrangea plant, but also referred to as the Experimental Geodetic Satellite or Payload EGS/EGP), the Laser Geodynamics Satellite or Laser Geometric Environmental Observation Survey (LAGEOS 1 and 2), Etalon (1 and 2), the Chinese Beidou/Compass system and the Indian Regional Navigation Satellite System (IRNSS). The Japanese QZSS system provides maneuvers which may make some analysis possible (https://qzss.go.jp/en/technical/qzssinfo/).

Name	Category	Apogee Alt (km)	Perigee Alt (km)	*a*	*e*	*i* (°)	*n* (rev/day)	SSC #	Mass (kg)	Area (m2)
Simulated Propagation Orbits										
	LEO			7078.14	0.00100	28.50			100.00	20.000000
	HEO			26000.00	0.70000	63.40			200.00	20.000000
	GEO			42164.00	0.00100	0.02			3000.00	97.000000
SLR orbits										
Larets	LEO	691	674	7060.64	0.00120	98.10	14.633112	27944	23.82	0.0314159
Stella	LEO	806	795	7178.64	0.00077	98.90	14.273798	22824	48.00	0.0452389
LARES	LEO	1449	1439	7822.14	0.00064	69.50	12.549152	38077	386.80	0.1040621
Ajisai (EGS)	LEO	1497	1479	7866.14	0.00114	50.00	12.444007	16908	685.00	3.5968094
LAGEOS 1	MEO	5948	5838	12271.14	0.00448	109.90	6.386682	8820	406.97	0.2827433
COSMOS 1989 (Etalon 1)	MEO	19182	19069	25503.64	0.00222	64.20	2.131569	19751	1415.00	1.3150990
QZS-3 (MICHIBIKI-3)	GEO	35793	35780	42164.64	0.00015	0.10	1.002721	42917	2379.20	19.9200000
IRNSS-1B	GEO	35878	35691	42162.64	0.00222	29.30	1.002792	39635	1432.00	10.000
IRNSS-1D	GEO	35882	35690	42164.14	0.00228	29.20	1.002739	40547	1425.00	10.000
QZS-3	GEO	35793	35779	42164.14	0.00017	0.10	1.002739	42917		
COMPASS-I3	GEO	35957	35627	42170.14	0.00391	58.80	1.002525	37384		

I also chose a few analytical and semianalytical propagators to highlight important considerations for these techniques. Indeed, there are dozens and dozens of integrators and propagators (Vetter 2007, Table 5). The methods examined include:

- Chao and Hoots (Chao and Hoots, 2018). Note that this *method* is only equations for short period (SP) and long period (LP) variations and not a formal semianalytical approach per se.
- Draper Semianalytical Satellite Theory (DSST: McClain 1978, 1992 and Danielson 1994, 1995†)

* Note that the GJ in STK does not have an error control to adjust the step size to maintain accuracy. The GJ is coded in the summed form, which is accurate and stable but changing the step size is not easy. The normal step size control involves either halving or doubling the step when needed. Krogh (1974) discusses changing the steps size for multi-step methods. Without automatic error control, the user's step size selection is critical to accurate integration results. Choosing the step size consists of reducing it until it no longer seems to affect the end result.

† There are several versions of DSST. The original starting point is the F-77 standalone DSST baseline of 1984 (Early, 1986). The top-level architecture of the DSST Standalone was modified by Carter in the early 1990s to support the maneuver planning functions of the Radarsat-1 Flight Dynamics System (FDS). The new architectural approach is described in the Orbit Propagator Services section of the Radarsat FDS Software Design Document (SDD) (Cefola et al, 1994). Further significant additions were made to the F-77 DSST Standalone in 1997 (Neelon et al, 1997). These included the 50 × 50 geopotential, solid Earth tides models, and the J2000 coordinate system. The DSST Tesseral Linear Combination model (Proulx et al, 1981) and the Lunar-Solar short-periodic model (Slutsky, 1983) were included in the Standalone to improve the short-periodic model. The 1997 version of the Standalone included structured modules to ensure that physical quantities had the same names throughout the software. Cefola et al. (2009) discusses further testing of the DSST. In 2011 to 2013, the DSST algorithms were programmed in Java for the open source Orekit Flight Dynamics library, https://www.orekit.org/. Comparisons of long-term orbit propagations made with the Orekit java DSST and with the F77 DSST Standalone led to further improvements in the F77 DSST Standalone (Cefola et al, 2014). San-Juan et al. (2017, 2019, and 2020) document the development of a C/C++ DSST version of the F77 DSST Standalone. The C/C++ DSST started from the F77 version that existed at the start of 2014. Setty et al. (2016) has developed a further improved

- Semi analytical Tool for End of Life Analysis (STELA: Morand et al. 2013 and Deleflie 2011). https://logiciels.cnes.fr/en/content/stela
- Tool for High-Accuracy, Long-term Analyses for SSA (THALASSA: Amato, et al. 2019*)
- Simplified General Perturbations (SGP4, Vallado et al. 2006). SGP4 propagations are from STK and ODTK. This is an analytical technique.

Other semianalytical routines were envisioned for the study, but time didn't permit their inclusion.

- Long Term Orbit Propagator (LOP: Kwok, 1986, 1987)
- Highly Elliptic Orbit Semi-Analytical Theory (HEOSAT: Lara, San-Juan, and Hautesserres 2016 and Gondelach 2017)
- Planetary Orbital Dynamics (PLANODYN: Frey and Columbo 2018 and Wittig et al. 2014)

"Full" force models are generally used throughout the tests (defined as a 50 × 50 EGM-08 gravity field, Jacchia Roberts atmosphere, 3-body gravity, solar radiation pressure). For solar radiation pressure, the entry/exit conditions can occur at different times/steps with different interpolators. This requires some form of boundary mitigation, or smoothing to get all the approaches to treat the shadow discontinuity equally. Similarly, splining SPW indices produces more consistent results (Vallado and Finkleman 2014).

Reference orbit selection

Selecting the reference orbits consisted of satellites that had either independent high precision ephemerides, or observations from which precise orbits could be determined. In most cases, satellites without maneuvers were selected to permit long-term propagation effects to be understood. This proved challenging especially for GEO satellites. As mentioned earlier, the CPF orbits fulfilled this role. Files were combined to form 1-year ephemerides for each satellite.

Study Process

Several steps were necessary to conduct the study. First was to establish the accuracy for the baseline integrators in the numerical propagator.

- Compare integrators with the same force model, EOP and SPW data, and satellite configurations for generic LEO, HEO and GEO satellites.

Using the selected baseline integrator (RK78) and numerical propagator, compare differences (RSW) to the CPF orbits.

- Numerically propagate the first state vector in the ephemeris with complete force models and the actual observed EOP and SPW values.
- Perform a precise conversion of elements (PCE – use a differential correction to estimate the initial elements) on the ephemerides to better determine the initial state. Compare the PCE result and subsequent propagation to the CPF ephemerides.
- Examine the orbital plane characteristics of the PCE results to the CPF orbits.

Examine the performance of analytical and semianalytical techniques.

- Compare various analytical propagators (J2, J4, etc) to the LEO orbit.
- Compare a propagated single initial TLE to the CPF orbits.
- Compare the set of TLEs throughout the time interval to the CPF orbits. While this isn't really a long term propagation, it serves to show general performance over time.
- Compare the single point conversion from each technique from the osculating ephemeris to the CPF orbits.

---

version of the DSST Standalone at the German Space Operations Center (GSOC). This version has expanded functionality with respect to the short periodic model and in dynamic parameter estimation. Setty also developed an Orbit Determination Services program. Both the propagator and OD programs employ the same DSST source code library. Folcik (2019) maintains the GTDS baseline including GTDS/DSST at the MIT/Lincoln Laboratory.

* https://gitlab.com/souvlaki/thalassa Note that THALASSA has no averaged formulation, so it isn't a true semianalytical technique in the usual sense. Further improvements to the code may include these effects.

- Develop a differential correction process to perform a PCE process to determine a better initial state and compare to the CPF orbits.

CONCLUSIONS

Several aspects of long-term numerical propagation have been examined. The goal was to present information about how long a numerical propagator could produce reliable information, from an operational perspective, with which to feed a particular SSA mission area. While many results were surprisingly accurate, others were not. Attention to detail is important as many things must be set and default program values are often incorrect. At the macro level, it seems that about 1-10 km error after a year propagation is achievable from both numerical and semianalytical methods. The results showed that the time of processing is quite different, but the overall accuracy is about the same.

First, several integrators were compared to determine any differences. Step sizes became important for the RK4 integrator, and regularized time was critical to all orbits with eccentricity larger than about 0.3. For the RK4 integrator, the default value time step needs to be adjusted smaller to match the step-size controlled integrators. For a LEO orbit, about 5 secs (with a 50 × 50 gravity field, drag, solar radiation pressure, srp, and 3rd-body) seemed to work well for the RK4. Make sure splining for atmospheric and srp eclipse boundary mitigation is turned on. For the HEO orbits, "all" integrators needed time regularization to accurately propagate. The RK4 also needed time regularization with 840 steps per orbit. A RK7/8 was chosen as the common integrator for the remainder of the talk as representing a middle position of the perfomance of each integrator tested. After about 18 months, the results generally were about 1 km, and this seems reasonable.

Next, comparisions were made with the RK78 integrator and various real-world Consolidated Predicted Format (CPF) orbits. The single state vector propagtaion did ok in some cases, but very poorly in others. A short PCE was conducted using the reference ephemeris as observations, and this improved most of the tests to about 1 km uncertainty. However, the lower altitude orbits lacked sufficient observability in the PCE to refine the initial estimate. This step re-confirmed the necessity of using a PCE to refine the initial state.

A few analytical propagators were examined. The force models must match – huge differences were noted in just a couple weeks due to the presence of un-modeled forces. The TLE propagation was sometimes good, sometimes very poor. Unfortunately, there's no indicator as to whether or not the TLE is bad. The ensemble over time generally shows an average accuracy, but determining if a current change is the result of a maneuver, or an erroneous TLE is unknown in advance. Be especially cautious with any maneuvering satellite!

Semianalytical propagators were investigated. The usual comparison method assumes an initial mean element state is known, or that one is found through a PCE from observations (except for THALASSA). For this talk, neither were true so the focus was on the osculating to mean conversion, subsequent propagation, and formation of the propagated osculating ephemeris. The results showed that particular attention to detail is needed in the osculating to mean conversion. Single point conversions were expected to be approximate, and generally performed that way. A simple PCE was programmed using finite differencing for some of the semianalytical techniques. This improved the performance, but not in all cases. When developer (not open source) PCE tests were performed, the results improved dramatically. Additional tests were conducted for DSST and alternate versions of the method, and the WTD seemed to be a large contributor to the differences for 3-body perturbations. The source of the Sun and Moon state vectors seems to be a large influencer as well. Using analytical, interpolated, and full JPL DE models for the 3rd body positions over a period of a few months seem to produce very large variations in the resulting propagations.

Finally, the best positional accuracy isn't always needed. All the techniques showed remarkable ability to preserve the orbital plane even as the positional differences grew large. Depending on the mission requirements, it may be feasible to use techniques that introduce positional errors, but maintain the orbital plane orientation. Maneuver planning for a complete mission is one example.

SAMPLE REFERENCES

Amato, Davide, Aaron J. Rosengren, and Claudio Bombardelli. 2018. THALASSA: a fast orbit propagator for near-Earth and cislunar space. Paper AIAA 2018-1970 presented at the Space Flight Mechanics Meeting. Kissimmee, FL.

Amato, Davide, et al. 2019. Non-averaged regularized formulations as an alternative to semi-analytical orbit propagation methods. *Celestial Mechanics and Dynamical Astronomy*. v131: 21.

Cefola, P.J., Z. Folcik, R. Di-Costanzo, N. Bernard, S. J. Setty, and J. F. San Juan. 2014. Revisiting the DSST standalone orbit propagator. Paper AAS 14-411 presented at the AAS/AIAA Space Flight Mechanics Meeting. Santa Fe, NM.

Chao, (George) Chia-Chun, and Felix R. Hoots. 2018. *Applied Orbital Perturbations and Maintenance.* 2nd edition. AIAA Education Series. New York: AIAA Press.

Danielson, Donald A., C. P. Sagovac, B. Neta, L. W. Early. 1995. *Semianalytical Satellite Theory (SST): Mathematical Algorithms*. Technical Report NPS-MA-95-002. Monterey, CA: Naval Postgraduate School.

Deleflie, F. et al. 2011. Semi-analytical investigations of the long term evolution of the eccentricity of Galileo and GPS-like orbits. *Advances in Space Research*. v47(5): 811 – 821.

Fonte, D.J., and C. Sabol. 1995. Optimal DSST input desks for various orbit types. Tech Report, Phillips Laboratory, Space and Missiles Technology Directorate.

Frey, S., and C. Colombo. 2018. Extension of the King-Hele orbital contraction method and application to the Geostationary Transfer orbit re-entry prediction. Paper presented at the 4th International Space Debris Re-entry Workshop in Darmstadt, Germany.

Lamy, Alain, and Denis Hautesserres. 2019. Private communication.

Lara, M., J. F. San-Juan, and D. Hautesserres. 2016. A Semianalytical Orbit Propagator Program for Highly Elliptical Orbits. Proceedings of the 6th International Conference on Astrodynamics Tools and Techniques, Darmstadt, Germany.

McClain, Wayne D. 1978. A Recursively Formulated First-Order Semianalytic Artificial Satellite Theory Based on th*e Generalized Method of Averaging.* Vol. 2. CSC/TR-78/6001: Computer Sciences Corporation.

McClain, Wayne D. 1992. *Semianalytic Artificial Satellite Theory.* Vol. 1. Charles Stark Draper Laboratory. Corrected.

Milani, A. and A. Nobili. 1988. Integration error over very long time spans. *Celestial Mechanics*. v43: 1–34.

Montenbruck, Oliver. 1992. Numerical Integration Methods for Orbital Motion. *Celestial Mechanics and Dynamical Astronomy*. v53: 59-69.

Morand, Vincent., et al. 2013. Semi-Analytical Computation of Partial Derivatives and Transition Matrix Using Stela Software. Paper presented at the 6th European Conference on Space Debris. Darmstadt, Germany.

Proulx, Ron J., W. McClain, L. Early, and P. Cefola. 1981. A Theory for the Short-Periodic Motion Due to the Tesseral Harmonic Gravity Field. Paper AAS-81-180 presented at the AAS/AIAA Astrodynamics Specialist Conference. Lake Tahoe, NV.

Slutsky, M. 1983. The First-Order Short-Periodic Motion of an Artificial Satellite Due to Third-Body Perturbations: Numerical Evaluation. Paper AAS 83-393 presented at the AAS/AIAA Astrodynamics Specialist Conference, Lake Placid, NY.

San-Juan, Juan F., Rosario López, Ricardo Suanes, Iván Pérez, Srinivas J. Setty and Paul J. Cefola. 2017. Migration of the DSST Standalone to C/C++. Paper AAS 17-369 presented at the AAS/AIAA Space Flight Mechanics Meeting. San Antonio, TX.

Setty, Srinivas J., Paul J. Cefola, Oliver Montenbruck, and Hauke Fiedler. 2016. Application of Semi-analytical Satellite Theory orbit propagator to orbit determination for space object catalog maintenance. *Advances in Space Research*. v57: 2218–2233.

Vallado, David A., and Paul Cefola. 2012. Two-Line Element Sets – Practice and Use. Paper IAC-12.C1.6.12 presented at the 63rd International Astronautical Congress. October 1-5, 2012. Naples, Italy.

Vallado, David A., and David Finkleman. 2014. A Critical Assessment of Satellite Drag and Atmospheric Density Modeling. v95:141-165, *Acta Astronautica*.

Wagner, Elaine A. 1983. Application of the Extended Semianalytical Kalman Filter to Synchronous Orbits. MS. Thesis MIT. Cambridge, Massachusetts.

Wittig, Alexander, Roberto Armellin, Camilla Columbo, and Pierluigi Di Lizia. 2014. Long-term Orbital Propagation through Differential Algebra Transfer Maps and Averaging Semianalytical Approaches. Paper AAS 14-224 presented at the AAS/AIAA Spaceflight Mechanics Meeting. Santa Fe, NM.

Woollands, R., and J. Junkins. 2019. Nonlinear Differential Equation Solvers via Adaptive Picard-Chebyshev Iteration: Applications in Astrodynamics. *Journal of Guidance, Control and Dynamics*. v42:3.

Session 1:

ANALYTICAL, SEMIANALYTICAL, AND NUMERICAL PROPAGATION METHODS

Bringing in break-up events within a space objects catalogue

Alejandro Pastor*[1], Jan Siminski†[2], Guillermo Escribano‡[3], Manuel Sanjurjo-Rivo§[3], and Diego Escobar¶[1]

[1]GMV, 11 Isaac Newton, 28760 Tres Cantos, Madrid, Spain
[2]Space Debris Office, Robert-Bosch-Straße 5, 64293 Darmstadt, Germany
[3]University Carlos III of Madrid, Av. de la Universidad 30, 28911 Leganés, Madrid, Spain

1 Introduction

The 18th Space Defense Squadron (SDS) maintains one of the most complete and publicly available catalogue of space objects. It is published on Space-Track [1] and contains more than 25,000 objects of which more than half are classified as fragmentation debris. With the improvements in the Space Surveillance and Tracking (SST) sensor technologies, it is expected a significant increase in complexity of catalogue build-up and maintenance activities.

Break-up events represent the dominant source of objects in space catalogues. The number of such events includes explosions, collisions or anomalous events resulting in fragmentation and is estimated to be higher than 630 known events until now [2]. The contribution of each event towards the overall space objects population is complex and diverse. Two of the most massive events, involving a number of fragments in the order of the thousand are the Fengyun 1C anti-satellite weapon test in 2007 and the accidental collision of Cosmos 2251 and Iridium 33 in 2009, accounting for over 30% of all catalogued space objects until December 2021. In 2021, three main break-up events happened: the failure of NOAA 17 (10th March), an accidental collision of YunHai 1-02 with a small mission-related debris object (18th March) and the destruction of Cosmos 1408 in an anti-satellite weapon test (15th November). As of today, the number of detected and catalogued fragments by the 18th SDS associated to these events is 115 (1 decayed), 37 (4 decayed) and 1561 (243 decayed) objects respectively [1].

The early detection of the fragments generated during these irregular events, almost four per year on average over the last decade, poses a complex challenge for space objects catalogue build-up and maintenance processes. Fragments are a dense cloud of debris, making the identification of individual objects difficult. Then, a trade-off between detection time and reliability arises, where time favours the spreading of the objects along the orbit, thus reducing the probability of false associations and the uncertainty of the estimated trajectories. Latter step could be performed when sufficient data is available. However, the provision of Space Situational Awareness (SSA) products and services during the few first days after a break-up event can be crucial to avoid collisions between the fragments and other space objects, particularly in highly congested regimes, as in Low Earth Orbit (LEO). Reducing the time required to establish the trajectories of the fragments may enable the execution of collision avoidance manoeuvres of operational satellites with manoeuvre capabilities, and analyse potential collision cascade events which may endanger the space environment. The evolution of the cataloguing process of the fragments from Cosmos 1408 is a clear example of this complexity: 185 fragments detected and catalogued two weeks after the event (1st December), 718 the next month (903 total as of 1st January) and 494 the month following that (1397 total as of 1st February) [9]. Figure 1 [6] shows the number of tracked fragments for which orbit data was published on Space-Track [1].

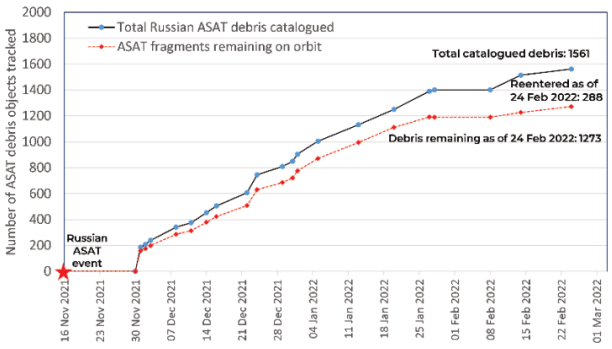

Figure 1: Cosmos 1408 debris fragments tracked to date [6].

This work tackles the whole cataloguing process after a break-up event, starting from a catalogue with no fragments from the fragmentation under-analysis, and until a well-established orbit is obtained for all the fragments. The procedure makes use of a ground-

*Email: apastor@gmv.com
†Email: jan.siminski@esa.int
‡Email: guescrib@ing.uc3m.es
§Email: msanjurj@ing.uc3m.es
¶Email: descobar@gmv.com

based radar sensor network, as well as the subsequent maintenance of the orbits. Association and catalogue maintenance performance is analysed on a time basis. This includes the confusion matrix evolution (true positives, false positives, and false negatives) during both the track-to-track and track-to-orbit as well as the accuracy of the estimated tr the fragments. The considered metrics a ating the robustness and efficiency of the conceived for real operational environme include the distributions of the figure of hypotheses during the association proces sociation process is formulated as a functi elements, association time and time sinc up, among other attributes identified spe mentation events. In addition, the tempo of the accuracy of the catalogued orbits and discussed, along with their correspo tainty.

2 Simulated dataset

Given the lack of publicly available sensing the Cosmos 1408 break-up event, the p fragments have been simulated. Since th yses on the resulting debris cloud sugges bution of fragments not matching the Na nautics and Space Administration (NAS Breakup Model (SBM) [5], we have us available Two Line Elements (TLEs) [1] to simulate the fragments trajectory. Firstly, Cosmos 1408 TLE data was fitted to obtain a state vector at the pinch point (15^{th} November 2021 at around 2:50 UTC [4, 3]). Secondly, the delta-v of each of the fragments (with respect to the parent object state at the pinch point) was obtained using TLE data as observations. Thirdly, trajectories of all the fragments were obtained by propagating the previously obtained states with a high-fidelity dynamical model. The resulting fragments' trajectories distributions and its consistencies are compared against NASA SBM and publicly available Gabbard plots. Finally, observations from a ground-based sensor network are simulated, including standard known sensor measurement noises.

3 Methodology

The simulated observations, packed as tracks, are provided to an operational multi-sensor multi-target track-to-track association framework [8] in charge of grouping tracks belonging to the same objects. In this context, a hypothesis, $\mathcal{H}$, represents an association of N tracks, $\{\mathcal{T}_i\}_{i=1,\dots,N}$, assumed to have been originated from a common object. To resolve the ambiguity, particularly shortly after the event, hypotheses are generated, scored, pruned, and promoted, as shown in Figure 2 [8], leading to the initialisation of new objects in the catalogue. These steps include several gating and complexity reduction techniques to filter out most of the false hypotheses and thus avoid a brute-force approach.

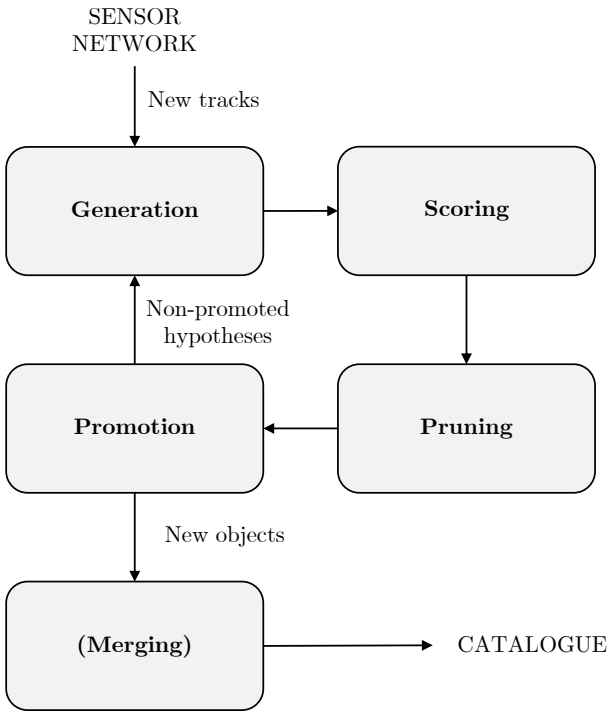

Figure 2: Steps of the track-to-track association methodology [8].

The generation step is in charge of creating new hypotheses by combining two already existing ones. Therefore, from two hypotheses of N tracks, $\mathcal{H}_A$ and $\mathcal{H}_B$, a new one, $\mathcal{H}_A \cup \mathcal{H}_B$, of $N+1$ tracks is generated, i.e.:

$$\mathcal{H}_A \cup \mathcal{H}_B = \left\{ \bigcup_{k=1}^{N-1} \mathcal{T}_k \right\} \cup \{\mathcal{T}_{A,N}\} \cup \{\mathcal{T}_{B,N}\} \qquad (1)$$
$$\mathcal{T}_k = \mathcal{T}_{A,k} = \mathcal{T}_{B,k} \qquad \forall k = 1, \dots, N-1$$

where $\mathcal{T}_{\alpha,k}$ is the k-th associated track of $\mathcal{H}_\alpha$. Note that according to the condition imposed before on the number of tracks of the new hypothesis, it is required that $\mathcal{H}_A$ and $\mathcal{H}_B$ have all but one track (N-th) in common.

Not all possible track combinations are considered during hypotheses generation since it would lead to a computationally unaffordable growth of the hypotheses tree. The following gating criteria are considered in this step:

1. Lower bound time span: the time span between the associated tracks must be higher than a certain fraction of the average orbital period, to

avoid associating tracks that are not sufficiently spaced in time (undesirable situation in terms of orbit observability).

2. Upper bound time span: the time span between the associated tracks must be lower than certain number of days to avoid dynamical model mismatching.

3. Estimated state difference: the difference between the estimated states is evaluated to avoid combining two associations that clearly belong to different orbital regions.

The figure of merit used for the scoring of a hypothesis consists in the difference between the actual observations, $\boldsymbol{z}$, and the a-posteriori computed observations, $\hat{\boldsymbol{z}}$, projected on the a-priori measurement covariance $\boldsymbol{P}_z^0$ [8], i.e.:

$$d^2\left(\mathcal{H}\right) = \frac{1}{|\mathcal{H}|}\sum_{\mathcal{T}\in\mathcal{H}}\frac{1}{|\mathcal{T}|}\sum_{\boldsymbol{z}\in\mathcal{T}}\left(\boldsymbol{z}-\hat{\boldsymbol{z}}\right)^T\left(\boldsymbol{P}_z^0\right)^{-1}\left(\boldsymbol{z}-\hat{\boldsymbol{z}}\right) \tag{2}$$

where $\boldsymbol{P}_z^0$ is the a-priori covariance of the measurements, a diagonal matrix containing the squared sigma of the expected noise of each measurement of the corresponding observation, assumed to be zero-mean Gaussian, and $|\cdot|$ denotes cardinality. Note that this figure of merit is a reduced chi-squared statistic (when the number of observations is much greater than the number of estimated parameters) and can also be seen as a Mahalanobis distance but evaluated in the measurement space rather than in the orbit space and projected in the a-priori covariance space. This figure of merit is used for hard decisions, such as hypothesis pruning (upper-bound threshold) and hypothesis promotion (lower-bound threshold).

This work follows [7] but considering radar instead of optical sensors and thus, a more challenging scenario from the cataloguing point of view given the greater number of fragments and dynamical model complexity: LEO instead of Geostationary Earth Orbit (GEO). Besides, not only the catalogue build-up process is tackled but also the maintenance counterpart. To do so, once the fragments are detected and catalogued, we correlate incoming tracks with the orbits via track-to-orbit association and update the estimated trajectory via orbit determination. This alleviates the track-to-track association and enables the update of the orbital estimates, required for maintaining the catalogue.

Finally, the use of dynamical models of varying fidelity, including analytical, semi-analytical and numerical propagators, during the track-to-track association, track-to-orbit correlation and orbit determination processes is investigated to enable a real-time capability while not jeopardising the accuracy of the final SSA products.

4 Acknowledgements

This project has received funding from the "Comunidad de Madrid" under "Ayudas destinadas a la realización de doctorados industriales" program (project IND2017/TIC7700). Besides, the authors would like to acknowledge the contributions from Srinivas Setty and Alfredo Antón for reviewing and providing the implementation of the NASA SBM, respectively.

References

[1] 18th Space Control Squadron. Space-Track, 2022. [Online; accessed 1-May-2022].

[2] ESA Space Debris Office. ESA's Annual Space Environment Report. Technical Report GEN-DB-LOG-00288-OPS-SD, ESA Space Debris Office, April 2022.

[3] EU SST. EU SST confirms the fragmentation of space object COSMOS 1408, 2022. [Online; accessed 1-May-2022].

[4] Jonathan McDowell. Jonathan's Space Report - The 2021 Nudol' test, 2022. [Online; accessed 1-May-2022].

[5] Darren McKnight, Matthew Stevenson, Matt Shouppe, James Rowland, Harry She, and Benedikt Reihs. Cosmos 1408 - Stress Test for LeoLabs. In *3rd International Conference on Space Situational Awareness (ICSSA)*, 2022.

[6] Daniel Oltrogge, Salvatore Alfano, David Vallado, Pete Zimmer, Robert Hall, Jim Wilson, Mike Siegers, and Joshua Aurich. Russian ASAT debris cloud evolution and risk. In *3rd International Conference on Space Situational Awareness (ICSSA)*, 2022.

[7] A. Pastor, G. Escribano, M. Sanjurjo-Rivo, and D. Escobar. Fragmentation detection via track-to-track association of optical observations. In *22nd Advanced Maui Optical and Space Surveillance Technologies (AMOS)*, 2021.

[8] A. Pastor, M. Sanjurjo-Rivo, and D. Escobar. Track-to-track association methodology for operational surveillance scenarios with radar observations. *CEAS Space Journal (accepted for publication, CEAS-D-21-00122R1)*, 2022.

[9] Jim Shell. Russian ASAT space debris update (LinkedIn), 2022. [Online; accessed Apr-2022].

Efficient Numerical Solution of the Low-Thrust Lambert's problem

Lamberto Dell'Elce*[1] and Aaron J. Rosengren†[2]

[1]Inria & Université Côte Azur, France
[2]University of California San Diego, US

Abstract

An algorithm for the numerical solution of low-thrust Lambert's problem is proposed. After averaging the extremal flow of the optimal control Hamiltonian, a one-parameter family of reduced-order two-point boundary value problems is solved. Sensitivities of the shooting function are then used in conjunction with an *ad hoc* near-identity transformation between averaged and osculating variables to achieve an accurate solution for all longitudes of the departure and arrival orbits. Hence, a single simplified shooting problem has to be solved to approximate the solution for any combination of departure and arrival dates (*i.e.*, to draw a pork chop chart). Both the averaged flow and the near identity transformation are efficiently evaluated via the fast Fourier transform algorithm, yielding a fully numerical procedure.

1 Introduction

Lambert's problem in its classical form consists in finding a Keplerian orbit joining two position vectors in a given transfer time. Solutions of this problem are extensively used for preliminary mission design since they offer the identification of launch opportunities and a rough evaluation of their cost by assuming impulsive maneuvers at the two boundary points. Specifically, pork-chop charts are maps of ΔV as a function of departure and arrival dates generated by recursively solving Lambert's problems. Recent interest was brought to the low-thrust counterpart of the problem. Because impulsive maneuvers are not allowed, the entire state vector is imposed at the two boundaries. Differently of the original problem, no exact closed form solution is available, so that assumptions on the shape and thrust direction are introduced to achieve efficient solutions [1] [2]. Equivalent of pork chop charts for low-thrust problems are referred to as bacon plots [3].

In our view, two problems need to be addressed when tackling low-thrust transfers on a fixed maneuvering time. First, minimum thrust magnitude necessary to carry out the maneuver has to be identified. Second, once a sufficiently-large thrust is chosen, minimum energy maneuvers can be found. This talk focuses on the first problem. A numerical methodology based on the averaging of the extremal flow of the optimal control system [4] is proposed. First, a reduced-order solution of the averaged Two-point boundary value problem (TPBVP) parametrized by the costate of the fast variable is solved. This step requires the solution of a single shooting problem followed by a numerical continuation procedure. This problem is independent of the thrust magnitude. The second step consists in identifying the costate of the fast variable (which is an integral of motion for the averaged system) for the desired boundary conditions. This is achieved by imposing a first-order conservation of the Hamiltonian at the two boundaries. Third, sensitivity of the shooting functions are computed. Finally, the thrust magnitude is identified by reconstructing a first-order approximation of the fast variables from the averaged solution.

2 Low-thrust Lambert's problem

Denote by $\boldsymbol{I}$ a set of integrals of motions of the two body problem (specifically, we use equinoctial elements) and by $\varphi \in \mathbb{S}^1$ the mean longitude. Hereafter, $\boldsymbol{I}$ and φ are referred to as slow and fast variables, respectively. Let t_0 and t_f be the desired departure and arrival dates. We are interested in finding the minimum thrust magnitude, ε, necessary to carry out the transfer between two Keplerian orbits with elements $(\boldsymbol{I}_0, \varphi(t_0))$ and $(\boldsymbol{I}_f, \varphi(t_f))$ in a time $t_f - t_0$. The optimal control problem that we tackle is

$$
\begin{aligned}
\min\ \varepsilon \qquad & \text{subject to:} \\
& \frac{\mathrm{d}\,\boldsymbol{I}}{\mathrm{d}\,t} = \varepsilon \sum_{i=1}^{m} \boldsymbol{f}_i(\boldsymbol{I}, \varphi)\, u_i \\
& \frac{\mathrm{d}\,\varphi}{\mathrm{d}\,t} = \omega(\boldsymbol{I}) + \varepsilon \sum_{i=1}^{m} g_i(\boldsymbol{I}, \varphi)\, u_i \qquad (1) \\
& \boldsymbol{I}(t_0) = \boldsymbol{I}_0, \qquad \varphi(t_0) = \varphi_0 \\
& \boldsymbol{I}(t_f) = \boldsymbol{I}_f, \qquad \varphi(t_f) = \varphi_f \\
& \|\boldsymbol{u}\| \leq 1 \qquad \forall\ t \in [t_0, t_f]
\end{aligned}
$$

*Email: lamberto.dell-elce@inria.fr.
†Email: ajrosengren@eng.ucsd.edu.

where $m = 3$, and $\boldsymbol{u}$ is the control variable taking values in the unit sphere of $\mathbb{R}^m$. Vector fields $\boldsymbol{f}_i$ and g_i are periodic with respect to the fast variable, and they are deduced by the Gauss variational equations (GVE) of the orbital elements set at hand.

The pre-Hamiltonian of Problem (1) is defined as

$$\mathcal{H}' = p_\varphi\, \omega(I) + \varepsilon \sum_{i=1}^{m} \left[\boldsymbol{p_I} \cdot \boldsymbol{f}_i(\boldsymbol{I}, \varphi) + p_\varphi g_i(\boldsymbol{I}, \varphi)\right] u_i \tag{2}$$

where $\boldsymbol{p_I}$ and p_φ denote adjoints of slow and fast variables, respectively. Application of Pontryagin maximum principle (PMP) yields the control action of the extremal flow $\boldsymbol{u}^*(\boldsymbol{I}, \varphi, \boldsymbol{p_I}, pF)$, namely

$$\boldsymbol{u}^* = \arg\max_{\|\boldsymbol{u}\|\leq 1} \mathcal{H}'\left(\boldsymbol{I}, \varphi, \boldsymbol{p_I}, p_\varphi, \varepsilon, \boldsymbol{u}\right) = \frac{\boldsymbol{H}}{\|\boldsymbol{H}\|}$$

where the i-th component of $\boldsymbol{H}$ is $H_i = \boldsymbol{p_I} \cdot \boldsymbol{f}_i(\boldsymbol{I}, \varphi) + p_\varphi g_i(\boldsymbol{I}, \varphi)$. Replacing $\boldsymbol{u}^*$ into Eq. (2) yields the Hamiltonian of the extremal flow:

$$\mathcal{H} = p_\varphi\, \omega(I) + \varepsilon K(\boldsymbol{I}, \boldsymbol{p_I}, \varphi, p_\varphi)$$

where $K := \|\boldsymbol{H}\|$. Transversality conditions are such that adjoints are free at both t_0 and t_f, so that necessary conditions for the optimality of Problem (1) are satisfied by finding a zero of the shooting function $S(\boldsymbol{p_I}(t_0),\, p_\varphi(t_0),\, \varepsilon)$ defined as

$$S(\boldsymbol{p_I}(t_0),\, p_\varphi(t_0),\, \varepsilon) = \begin{bmatrix} \boldsymbol{I}^*(t_f) - \boldsymbol{I}_f \\ \varphi^*(t_f) - \varphi(t_f) \\ \|\boldsymbol{p_I}(0)\| - 1 \end{bmatrix}$$

where $\boldsymbol{I}^*(t_f)$ and $\varphi^*(t_f)$ denote trajectories of $\boldsymbol{I}$ and φ emanated by $\mathcal{H}$ with initial conditions $\boldsymbol{I}_0$, $\varphi(t_0)$, $\boldsymbol{p_I}(t_0)$, $p_\varphi(t_0)$, and small parameter ε. The last equation of S is an arbitrary normalizing condition due to the homogeneity of $\mathcal{H}$ with respect to adjoints.

3 Averaged problem

States and adjoints are decomposed as

$$\begin{aligned} \boldsymbol{I} &= \boldsymbol{J} + \varepsilon \boldsymbol{\nu_I}(\boldsymbol{J}, \boldsymbol{p_J}, \varphi) \\ \boldsymbol{p_I} &= \boldsymbol{p_J} + \varepsilon \boldsymbol{\nu_{p_I}}(\boldsymbol{J}, \boldsymbol{p_J}, \varphi) \\ \varphi &= \frac{\psi}{\varepsilon} + \boldsymbol{\nu}_\varphi(\boldsymbol{J}, \boldsymbol{p_J}, \varphi) \\ p_\varphi &= \varepsilon\left(p_\psi + \boldsymbol{\nu}_{p_\varphi}(\boldsymbol{J}, \boldsymbol{p_J}, \varphi)\right) \end{aligned}$$

Hereafter, $\boldsymbol{J}$ and $\boldsymbol{p_J}$ are referred to as averaged state and adjoint, and $\boldsymbol{\nu}_\cdot$ denote short periodic variations. The adjoint p_ψ is well defined when ε approaches zero as discussed in [4].

3.1 Averaged shooting problem

The averaged Hamiltonian is defined as

$$\overline{\mathcal{H}} = \omega(\boldsymbol{J}) p_\psi + \frac{1}{2\pi}\int_0^{2\pi} K(\boldsymbol{J}, \boldsymbol{p_J}, \varphi, 0)\, \mathrm{d}\varphi$$

Rescaling time as $\mathrm{d}\tau = \varepsilon \mathrm{d}t$ yields the averaged shooting function

$$\overline{S}(\boldsymbol{p_J}(0), \tau_f | \boldsymbol{J}_0, \boldsymbol{J}_f, p_\psi) = \begin{bmatrix} \boldsymbol{J}^*(\tau_f) - \boldsymbol{J}_f \\ \|\boldsymbol{p_J}(0)\| - 1 \end{bmatrix} \tag{3}$$

We note that Problem (3) is independent of both ε and ψ. The notation $\overline{S}(\boldsymbol{J}(0), \tau_f | \boldsymbol{J}_0, \boldsymbol{J}_f, p_\psi)$ is introduced to emphasize that $\boldsymbol{J}(0)$ and τ_f are shooting variables, whereas $\boldsymbol{J}_0$, $\boldsymbol{J}_f$, and p_ψ are parameters.

3.2 Short-periodic variations

Short-periodic variations of slow variables, $\boldsymbol{\nu_I}$, and of adjoints, $\boldsymbol{\nu_{p_I}}$, $\boldsymbol{\nu}_{p_\varphi}$ are obtained by solving

$$\begin{aligned} \omega(\boldsymbol{J})\frac{\partial \boldsymbol{\nu_I}}{\partial \varphi} &= \frac{\partial K}{\partial \boldsymbol{p_I}} - \frac{\partial \overline{K}}{\partial \boldsymbol{p_I}} \\ \omega(\boldsymbol{J})\frac{\partial \boldsymbol{\nu_{p_I}}}{\partial \boldsymbol{I}} &= -\frac{\partial K}{\partial \boldsymbol{I}} + \frac{\partial \overline{K}}{\partial \boldsymbol{I}} - \left.\frac{\partial \omega}{\partial \boldsymbol{I}}\right|_{\boldsymbol{J}} \boldsymbol{\nu}_{p_\varphi} \\ \omega(\boldsymbol{J})\frac{\partial \boldsymbol{\nu}_{p_\varphi}}{\partial \varphi} &= -\frac{\partial K}{\partial \varphi} + \frac{\partial \overline{K}}{\partial \varphi} \\ \int_0^{2\pi} \boldsymbol{\nu_I}\, \mathrm{d}\varphi &= \int_0^{2\pi} \boldsymbol{\nu_{p_I}}\, \mathrm{d}\varphi = \int_0^{2\pi} \boldsymbol{\nu}_{p_\varphi}\, \mathrm{d}\varphi = 0 \end{aligned}$$

Denote by $[f]^k$ the k-th coefficient of the Fourier series of a function f, and by i the imaginary unit. The formal solution of Eq. 3.2 is

$$\begin{aligned} \boldsymbol{\nu_I} &= -\frac{i}{\omega(\boldsymbol{J})} \sum_{k\in\mathbb{Z}^0} \frac{1}{k} \left[\frac{\partial K}{\partial \boldsymbol{p_I}}\right]^{(\boldsymbol{k})} \frac{\partial \omega}{\partial \boldsymbol{I}} \mathrm{e}^{ik\varphi} \\ \boldsymbol{\nu_{p_I}} &= \frac{i}{\omega(\boldsymbol{J})} \sum_{k\in\mathbb{Z}^0} \frac{1}{k} \left\{ \left[\frac{\partial K}{\partial \boldsymbol{I}}\right]^{(\boldsymbol{k})} - [K]^{(\boldsymbol{k})} \frac{\partial \omega}{\partial \boldsymbol{I}} \right\} \mathrm{e}^{ik\varphi} \\ \nu_{p_\varphi} &= -\frac{K(\boldsymbol{J}, \boldsymbol{p_J}, \varphi, 0) - \overline{K}(\boldsymbol{J}, \boldsymbol{p_J})}{\omega(\boldsymbol{I})} \end{aligned}$$

We note that ν_{p_φ} establishes a first-order equivalence between the original and averaged Hamiltonians. Short-periodic variations can be efficiently evaluated by means of the fast Fourier transform (FFT).

4 Algorithm for the generation of bacon plots

We propose an algorithm for the generation of first-order solutions of Problem (1).

1. **Solve the average problem**

   $$\forall\, p_\psi \in \left[p_\psi^{min}, p_\psi^{max}\right] \text{ find } \boldsymbol{p_J}_0^{p_\psi}, \tau_f^{p_\psi} \text{ s.t.:}$$
   $$\overline{S}\left(\boldsymbol{p_J}_0^{p_\psi}, \tau_f^{p_\psi} | \boldsymbol{I}_0, \boldsymbol{I}_f, p_\psi\right) = 0$$

   We note that the same initial conditions of the osculating problem are used. After finding the solution for $p_\psi = 0$, a numerical continuation scheme can be used.

2. **Find compatible adjoint of fast variable**

$$\begin{aligned}&\text{find } p_\psi \text{ s.t.:}\\ &\nu_{p_\psi}\left(\boldsymbol{I}_0, \boldsymbol{p_J}_0^{p_\psi}, \varphi(t_0)\right) = -p_\psi,\\ &\nu_{p_\psi}\left(\boldsymbol{I}_0, \boldsymbol{p_J}\left(\tau_f^{p_\psi}\right), \varphi(t_f)\right) = -p_\psi,\end{aligned}$$

3. **Compute sensitivities**

$$\begin{aligned}&\text{find } \delta\tau_f,\ \delta\boldsymbol{p_J}_0,\ \delta\Delta\psi \text{ s.t.:}\\ &\frac{\partial\overline{S}}{\partial\tau_f}\delta\tau_f + \frac{\partial\overline{S}}{\partial\boldsymbol{p_J}}\delta\boldsymbol{p_J} = -\frac{\partial\overline{S}}{\partial\boldsymbol{p_J}_0}\delta\boldsymbol{p_J}_0 - \frac{\partial\overline{S}}{\partial J_f}\delta\boldsymbol{J}_f\\ &\delta\Delta\psi = \frac{\partial\Delta\psi}{\partial\tau_f}\delta\tau_f + \frac{\partial\Delta\psi}{\partial\boldsymbol{p_J}_0}\delta\boldsymbol{p_J}_0 + \frac{\partial\Delta\psi}{\partial\boldsymbol{J}_0}\delta\boldsymbol{J}_0\end{aligned}$$

where $\delta\boldsymbol{J}_0$ and $\delta\boldsymbol{J}_f$ are evaluated by means of the near-identity transformation as

$$\begin{aligned}\delta\boldsymbol{J}_0 &= -\boldsymbol{\nu}_I\left(\boldsymbol{I}_0, \boldsymbol{p_J}_0^{p_\psi}, \varphi(t_0)\right),\\ \delta\boldsymbol{J}_f &= -\boldsymbol{\nu}_I\left(\boldsymbol{I}_f, \boldsymbol{p_J}\left(\tau_f^{p_\psi}\right), \varphi(t_f)\right).\end{aligned}$$

4. **Identify minimum ε**

$$\begin{aligned}&\text{Find } \varepsilon \text{ s.t.:}\\ &\text{mod}\left(\frac{\Delta\psi^{p_\psi}}{\varepsilon}, 2\pi\right) = \varphi(t_f) - \varphi(t_0) - \delta\Delta\psi\end{aligned} \tag{4}$$

We stress that all steps only use the average system and the near-identity transformation. The small parameter, ε, only appears at the left-hand side of Eq. (4), whereas the right-hand side is independent of ε.

Recursively evaluating the algorithm for various departure and arrival dates allow to generate pork-chop charts of the minimum thrust force necessary to carry out the maneuver.

Concerning the complexity of the methodology: Step 1 implies first the solution of one average problem for $p_\psi = 0$ (this is the only shooting problem that has to be solved without *a priori* knowledge). Then, differential continuation can be used to obtain the solution in the range $\left[p_\psi^{min}, p_\psi^{max}\right]$. Step 2 involves the zero search of algebraic equations. Step 3 requires the solution of $(n+1)$-dimensional linear systems.

References

[1] D. Izzo. Lambert's Problem for Exponential Sinusoids. *Journal of Guidance, Control, and Dynamics*, 29(5):1242–1245, 2006.

[2] G. Avanzini, A. Palmas, and E. Vellutini. Solution of Low-Thrust Lambert Problem with Perturbative Expansions of Equinoctial Elements. *Journal of Guidance, Control, and Dynamics*, 38(9):1585–1601, 2015.

[3] R. C. Woolley, F. Laipert, A. K. Nicholas, and Z. Olikara. Low-thrust trajectory Bacon plots for Mars mission design. *Proceedings of the 29th AAS/AIAA Space Flight Mechanics Meeting*, 2019.

[4] L. Dell'Elce, J.-B. Caillau, and J.-B. Pomet. On the convergence of time-optimal maneuvers of fast-oscillating control systems. *Proceedings of the European Control Conference*, 2008–2013, 2021.

Flyby dynamical characterisation with Jacobian eigenvalues

Alessandro Masat*[1], Camilla Colombo†[1], and Arnaud Boutonnet‡[2]

[1]Politecnico di Milano, Milano, Italy, 20156
[2]European Space Agency (ESA-ESOC), Darmstadt, Germany, 64293

1 Introduction

The detection of flybys in the numerical propagation of interplanetary trajectories is a key aspect to enable planetary protection analyses. Their much faster dynamics, compared to the pure heliocentric motion, hinders the development of advanced orbital integrators: regularisation-based approaches and variation of parameters implementations are extremely sensitive on close approach events, and may fail in correctly predicting their effect on the propagated trajectory. Switching the integration/regularisation centre to the flyby body in case of close approaches is an effective workaround to retain all the benefits of advanced propagation techniques [1]. Nonetheless, this philosophy requires to properly define and, consequently, detect possible flyby events.

The commonly used concepts all rely on the definition of a spherical region that surrounds any solar system planet. In general, the stronger the gravitational field of the minor body, the larger its associated sphere. *Sphere of influence* (SOI) and *Hill's sphere* are the two usually adopted definitions. The former approximates the distance from the minor body where either the planet or the Sun can be considered as a perturbation of the other dynamics. The latter approximates the distance of the Lagrange points L_1 and L_2 from the planet [3]. Differently from these definitions, Debatin et al. [2] used the eigenvalues of the dynamics' Jacobian to measure the relative magnitudes of the contribution of the different bodies in an N-body system, and used it as robust step control mechanism. Similarly, Romano [5] used this criterion to detect flybys in planetary protection analyses.

This work analyses flybys from a different perspective. Rather than building on a concept based on equilibrium distances, the dynamical nature of the close approach is emphasised. The eigenvalues of the three-body problem dynamics' Jacobian leads to an analytical solution for a spheroidal locus of points that locally highlights which body is contributing the most to the dynamics variation. The results are also compared against the Circular Restricted Three-Body Problem (CR3BP) zero-velocity curves concept.

2 Jacobian eigenvalues for flyby detection

The dynamics' Jacobian is traditionally linked to the step size control for general numerical simulations. In particular, the maximum eigenvalue influences the stability of the numerical scheme [4]. Contrarily to predictor-corrector integrators (e.g. the Runge-Kutta family), the knowledge on the dynamics Jacobian is exploited to minimise the truncation error. In the orbital dynamics case, the work of Debatin et al. [2] used an analytical approximation of the maximum Jacobian eigenvalue of the N-body dynamics, building a fast integration algorithm with step size control. They approximate the square of the maximum Jacobian eigenvalue λ^2_{max} as the sum of the squares of all the separate two-body Jacobian eigenvalues:

$$\lambda^2_{max} \approx \sum_{i=1}^{N} \lambda_i^2 = \sum_{i=1}^{N} \frac{2\mu_i}{\left|\mathbf{r} - \mathbf{r}_i\right|^3} \tag{1}$$

with the subscript i denoting the i-th body, $\mathbf{r}$ the position and μ_i the gravitational parameter. This approximation becomes particularly reliable far from the boundaries of any sphere of influence/Hill's sphere, since in these regions either the Sun or the planet flown by heavily dominates the dynamics.

The later work of Romano [5] used a similar approximation approach to implement a flyby detection criterion. If the ratio between the eigenvalues of a given planet and the Sun grows above a user-specified tolerance, then a flyby event is detected. Romano also showed that this criterion encompasses the usually defined sphere of influence/Hill's sphere, in the case of threshold set equal to 1.

3 Dynamical meaning in the Three-body problem

The barycentric three-body Jacobian $\mathbf{J}$ is defined as:

$$\mathbf{J} = \begin{bmatrix} \mathbf{0} & \mathbf{I} \\ \mathbf{G} & \mathbf{0} \end{bmatrix} \tag{2}$$

*Email: alessandro.masat@polimi.it. PhD Candidate, Department of Aerospace Science and Technology.
†Email: camilla.colombo@polimi.it. Associate Professor, Department of Aerospace Science and Technology.
‡Email: arnaud.boutonnet@esa.int. Senior Mission Analyst, HSO-GFA, ESA-ESOC.

with $\mathbf{0}$ and $\mathbf{I}$ the 3×3 null and identity matrices, respectively, and $\mathbf{G}$ defined as:

$$\mathbf{G} = \sum_{i=1}^{2} \mathbf{G}_i = \sum_{i=1}^{2} \frac{\mu_i}{|\mathbf{d}_i|^5} \left(|\mathbf{d}_i|^2 \mathbf{I} - 3\mathbf{d}_i \mathbf{d}_i^T \right) \quad (3)$$

with $\mathbf{d}_i = \mathbf{r} - \mathbf{r}_i$. It can be proved that, in the two-body case, $\lambda_{j,\mathbf{J}} \equiv \lambda^2_{j,\mathbf{G}}$, with $j = 1, 2, 3$, and $\lambda^2_{max,\mathbf{G}}$ is defined as in Equation (1) [5]. λ^2 appears only on the right-hand side because the properties of the determinant of block-square matrices are introduced to compute the eigenvalues of $\mathbf{J}$.

Approximating the dynamics as if only the currently dominant body 1 was present reflects on the approximated Jacobian as $\mathbf{G} \approx \mathbf{G}_1$. The matrix Jacobian error becomes equal to $\mathbf{G}_2$. Since any $\mathbf{G}_i$ is symmetric (Equation (3)), its euclidean matrix norm equals its spectral radius, i.e. $|\mathbf{G}_i|_2 \equiv \rho(\mathbf{G}_i) \equiv \lambda_{max,\mathbf{G}_i}$. In other words, the maximum eigenvalue of $\mathbf{G}_2$ directly measures the error of $\mathbf{G} \approx \mathbf{G}_1$.

The color scale in Figure 1 shows the maximum Jacobian error values in the space near Jupiter, i.e. $\max\left[\lambda_{max,Sun}/\lambda_{max}, \lambda_{max,Jup}/\lambda_{max}\right]$, on the plane containing Jupiter's orbit about the Sun. Rather than crossing a fixed-shape spheroid, the proposed visualisation highlights the smooth transition nature of flybys. Even if fast, the whole continuous domain is crossed, starting from the interplanetary space, passing through a region where none of the two bodies dominates the gravitational acceleration change, and finally reaching a far greater planetary effect at low altitudes. Two higher error regions, called "Thickened regions" in Figure 1, appear nearly perpendicularly to the Sun-Jupiter direction. The possible reason of their appearence is explored in Section 5.

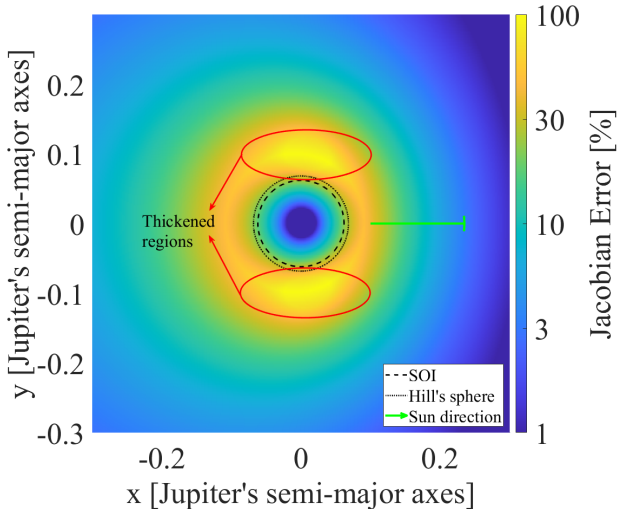

Figure 1: Jupiter's Jacobian percent error (color scale), compared against Hill's surfaces (dotted) and SOI (dashed).

Equivalently, this criterion highlights the highest curvature regions of the three-body gravitational potential $V = -\mu_1/|\mathbf{d}_1| - \mu_2/|\mathbf{d}_2|$, since it can be proved that $\mathbf{G} \equiv Hessian(V)$. In other words, the space regions determining a flyby may be identified by the local curvature of the gravitational potential.

4 Analytical loci of points

Replacing the $\mathbf{G}, \mathbf{J}$ subscript notation with the body names, a direct comparison can be made with the parametrisation $\lambda_{max,Jup}/\lambda_{max,Sun} = \gamma$. As done in Figure 1, centering the reference frame on Jupiter leads to an analytical expression for the spheroidal loci with common γ, whose radius $\tilde{r}$ is:

$$\tilde{r}(\theta) = r_{Sun-Jup} \frac{-\alpha \cos\theta + \sqrt{\alpha(1 - \alpha \sin^2\theta)}}{1 - \alpha} \quad (4)$$

with θ the angle between the direction of $\tilde{r}$ and the direction identified by the line connecting the Sun and Jupiter, and $\alpha = (\gamma \mu_{Jup}/\mu_{Sun})^{2/3}$. The $2/3$ exponent arises because of the third power of the eigenvalue expression (Equation (1)), and a squaring taken to remove the square root of the vector norm operator.

Figure 2 extends Figure 1, comparing the analytical loci of points obtained with Equation (4) against the computed values of the Jacobian error (on the color scale), for γ equal to 0.1, 1, and 10. The cases $\gamma = 0.1, 10$ (dashed red lines) well bound the regions where the Jacobian approximation error is higher than 10%. Thickened regions aside, the case $\gamma = 1$ (solid red line) perfectly predicts the "critical" distances where the error is maximised.

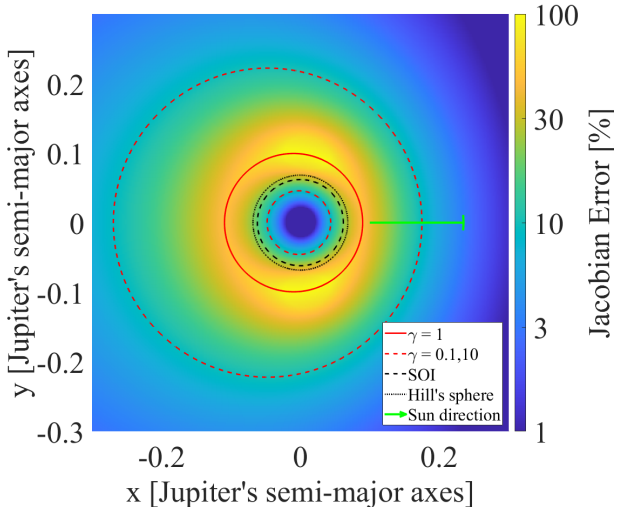

Figure 2: Jupiter's Jacobian percent error (color scale), compared against Hill's surfaces (dotted), SOI (dashed), and analytical loci of points (red).

The "critical" spheroid (parametrised by $\gamma = 1$) can be used as robust flyby detection criterion, assessing if and when a propagation crosses that boundary,

aiming to the minimisation of the truncation error introduced by the interrupted integration. In fact, for the Sun-Earth case this distance falls within the minimum error range identified by Amato et al. [1].

5 Visualisation in the CR3BP

The CR3BP provides further insight on the nature of the thickened regions observed in Figures 1 and 2. Figure 3 shows the perfect alignment of the zero-velocity surfaces, plotted as grey/shadowed areas, with the Jacobian error, on the plane containing Jupiter's orbit about the Sun. The red lines represent different values of γ, equal to 1 (solid), 0.1 or 10 (dotted) and 0.01 (dashed). The selected Jacobi constant to plot the zero-velocity surfaces was only chosen to highlight their alignment with the thickened regions, without particular meaning. On the zero-velocity curves the kinetic energy content of the test particle, the centrifugal reaction due to the non-inertial rotating frame, and the gravitational attraction of both bodies all balance out. Simplifying the dynamical model along this curves may become inaccurate, particularly if close to the Hill sphere boundaries, as highlighted by the thickened error regions. In other words, the mutual effect of the two bodies on how the dynamics changes is more prominent along the zero-velocity surface direction, on a wider region than the sole "critical spheroid".

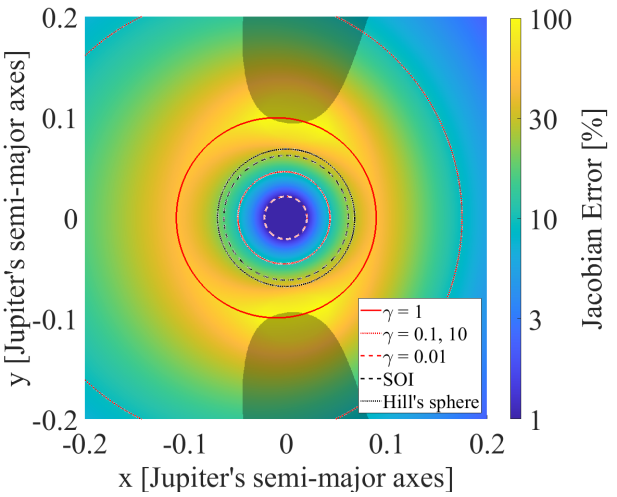

Figure 3: Jupiter's Jacobian percent error (color scale), compared against Hill's surfaces (dotted), SOI (dashed), analytical loci of points (red), and zero-velocity surfaces (grey/shadowed).

6 Conclusion

This work proposes a flyby characterisation approach that accounts for the dynamical nature of the encounter, focussing on the changes on the dynamics caused by the body flown by. The actual smooth transition of the motion from interplanetary to planetary is also modelled, highlighting regions of space where none of the two body is clearly dominating, and approximating the dominance that each body has in each point of the planet neighbourhood.

Apart from the regions nearby the critical distance and along the zero-velocity curves, the proposed parametric analytical model accurately predicts the loci of points of common Jacobian error. Setting the parameter equal to 1 allows the use of the "critical" spheroid as robust flyby detection criterion. Additionally, future works will analyse whether this criterion is also a suitable approach to improve the characterisation of shallow encounters.

Deeper details on the model will be given in the oral presentation, as well as further insight on the comparison with the CR3BP regime and the relation with zero-acceleration saddle points.

Acknowledgments

The research leading to these results has received funding from the European Research Council (ERC) under the European Union's Horizon2020 research and innovation programme as part of project COMPASS (Grant agreement No 679086), `www.compass.polimi.it`, and the European Space Agency (ESA) through the Open Space Innovation Platform (OSIP) co-funded research project "Robust trajectory design accounting for generic evolving uncertainties", Contract No. 4000135476/21/NL/GLC/my.

References

[1] Davide Amato, Giulio Baù, and Claudio Bombardelli. Accurate orbit propagation in the presence of planetary close encounters. *Monthly Notices of the Royal Astronomical Society*, 470(2):2079–2099, Sep 2017.

[2] Frank Debatin, A. Tilgner, and Friedhelm Hechler. Fast numerical integration of interplanetary orbits. In *ESA Special Publication*, volume 255 of *ESA Special Publication*, pages 329–333, Dec 1986.

[3] W.D. McClain and D.A. Vallado. *Fundamentals of Astrodynamics and Applications*. Space Technology Library. Springer Netherlands, 2001.

[4] A Quarteroni, R Sacco, and F Saleri. *Numerical Mathematics Texts in Applied Mathematics*. 2007.

[5] Matteo Romano. *Orbit propagation and uncertainty modelling for planetary protection compliance verification*. PhD thesis, Politecnico di Milano, Supervisors: Colombo, Camilla and Sánchez Pérez, José Manuel, Feb 2020.

Semi-analytical propagation of NEO binaries: the history of the Janus mission targets 1991 VH and 1996 FG3

Oscar Fuentes-Muñoz*[1], Alex J. Meyer[1], and Daniel J. Scheeres[1]

[1]University of Colorado Boulder, USA

Abstract

The orbits of small bodies in the Solar system experience fast changes during planetary encounters and slowly evolve under secular long-term perturbations. We present a semi-analytical propagation tool that combines the two effects into a single simulation framework for rapid, long-term propagation of small bodies in the inner solar system. The perturbed analytical propagation is interrupted to numerically solve the detected planetary close encounters. The orbits of binary asteroids are sensitive to the perturbation of planetary close encounters. Thus, we study the orbital history of binary asteroids (35107) 1991 VH and (175706) 1996 FG3, that will be visited by the NASA SIMPLEx mission Janus in 2026. As a result we obtain statistics of the close encounters that could disrupt the relative orbit of the binaries along their history.

1 Introduction

The study of primitive bodies in the solar system can provide an understanding of the formation and evolution of the solar system. The Near-Earth Object (NEO) population provides a unique opportunity to investigate and understand these processes, as they have been transported close to Earth from their previous lives in the main asteroid belt. This interest has led agencies around the world to promote a number of past [1, 2], present [3] and future NEO exploration missions[4] like mission Janus, that will visit NEO binaries (35107) 1991 VH and (175706) 1996 FG3[5].

The long term evolution of NEOs is driven by their secular interaction with the planets of the solar system and close planetary encounters[6]. We develop a semi-analytical propagation tool that combines secular perturbation solutions and the detection and solution of planetary encounters. Once a close encounter is detected, the variation in the heliocentric elements of the asteroid is computed numerically. The variation is computed by a quadrature of the Lagrange Planetary Equations in which we assume the unperturbed trajectory of the flyby in the dynamics. Then, the perturbed propagation is continued until the next encounter. As the orbit drifts in the inner solar system close encounters are possible with different planets and in different conditions. Using an analytical method for a large fraction of the simulation time speeds up the propagation. In [7] we provide a thorough comparison of the different elements of the simulation framework with numerical integration to validate the overall statistics of long-term simulations.

At least 15% of the population of near-Earth asteroids are binaries, and many of them are found in a stable state. However, close encounters can perturb the orbit and spin state of binary systems. In this presentation we study the evolution of two binary asteroids: (35107) 1991 VH and (175706) 1996 FG3. Using radar and photometry data, it was determined that (175706) 1996 FG3 is in a stable state whereas (35107) 1991 VH is in a chaotic state [8, 9]. This chaotic state could be explained by a planetary close encounter that could have happened recently[10]. For this reason, we study the long-term dynamics of the orbits of the two targets and characterize the frequency of these disruptive encounters.

2 Semi-analytical propagation methodology

2.1 Analytical long-term dynamics

The gravitational interaction between N-bodies can be modelled by studying the relevant terms in the perturbing gravitational potential and solving the Lagrange Planetary Equations. The first-order solution for the secular perturbation is known as Laplace-Lagrange theory[11]. The Laplace-Lagrange theory is an accurate representation of the long-term motion of the planets in the Solar System. For this reason, this is the model chosen to track the planets over the long-term simulations. In addition, it can be used including only Jupiter as a solution for the secular dynamics of NEOs.

*Corresponding Author: oscar.fuentesmunoz@colorado.edu

2.2 Planetary Close Encounters

The effect of a planetary encounter on the heliocentric orbit can be computed with analytical, semi-analytical or numerical methods. The analytical solution of close encounters is obtained by mapping the asteroid to the planetocentric frame[12, 13]. However, this approach is limited in applicability to very close encounters and asteroids not co-moving with the planet. Semi-analytical tools are convenient for the resolution of distant encounters[14]. In this work we use an integration of Lagrange Planetary Equations[15, 7] assuming the unperturbed trajectory of the flyby in the perturbing potential.

3 Simulation Results

3.1 Semi-analytical long-term dynamics

The chaotic nature of the orbital dynamics in the inner Solar System implies that the study of the orbital evolution over long timescales should be done statistically. Given the uncertainty in the orbit solution of an asteroid, we can sample a large number of particles and study the dynamical paths that the different particles take. Because of the sensitivity to initial conditions in planetary encounters, very well determined distributions diverge in a few centuries to widely different paths. We demonstrate these effects by propagation of 1000 particles that sample uncertainty distributions around (35107) 1991 VH for 1Myrs, as shown in Figure 1.

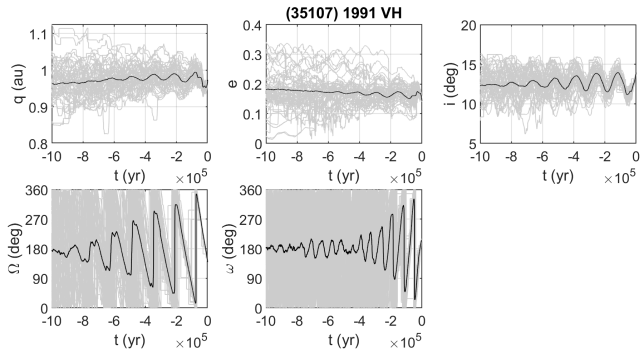

Figure 1: 1Myr Monte Carlo semi-analytical propagation of asteroid (35107) 1991 VH. Grey: individual runs. Black: median of 1000 runs. Elements shown are perihelion distance, eccentricity, inclination, argument of the ascending node, argument of perihelion. Extracted from [7].

Figure 1 shows how the initially close distribution becomes a wide statistical distribution when propagated far into the past. The orbit evolution of (35107) 1991 VH is mostly a spread around the initial conditions.

After a few hundred thousand years the longitude of the perihelion becomes uniformly distributed, whereas the evolutions of q,e,i are better described by a random walk. In [7] we parametrize this models to effectively compare the stochastics of the long-term dynamics of the examples studied.

3.2 Binary asteroid disruption

The statistics of close encounters that are recorded during the semi-analytical propagation can be used to estimate the frequency in which encounters excite the relative orbits of binary systems. The effect of an encounter on the binary orbit can be computed analytically [16, 17]. Meyer & Scheeres, 2021[9] provided a thorough study of the perturbation and disruption of binary systems during planetary close encounters.

For singly synchronous binary asteroids the perturbation can be studied analytically as the variation in the Keplerian elements of the binary. The analytical expressions in [16] are used here as an estimate of the variation as a function of the relative velocity and distance of closest approach.

Using the results of [9] we can define thresholds on how close and slow must encounters be to cause a certain level of excitation of the binaries. Figure 2 shows these results as the contours in the background. We defined low excitation as an average variation in binary eccentricity of 0.1, and high excitation the variation in eccentricity of 1, which would mean the complete disruption of the binary.

Here we study two binary asteroid systems to estimate the probability that they have been excited recently and along their long-term histories: the targets of the Janus mission, (35107) 1991 VH and (175706) 1996 FG. We overlap all the planetary close encounters found below 0.003au (1 LD = 0.0025au). The Earth (blue) and Mars (red) encounters are shown in Figure 2.

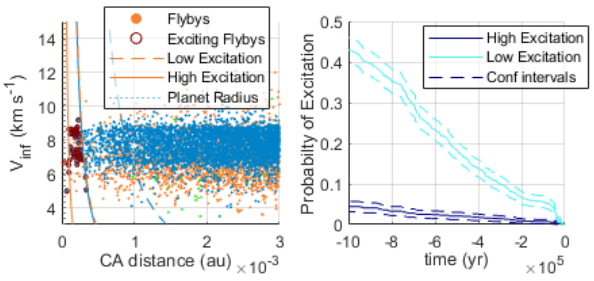

Figure 2: Potentially disruptive encounters of (35107) 1991 VH in the last 1Myr. Left: Contours of the excitation thresholds and recorded encounters with Mars (orange), Earth (blue). Right: probability of excitation over the simulation time.

If we count the encounters found below the previous thresholds over time, we can estimate the probabilities that these exciting encounters occurred. These results indicate that at least a low excitation is frequent along the orbital histories of these binaries.

4 Conclusions

Using the semi-analytical propagation tool we replicate the main dynamical effects in long-term numerical integration of asteroids in the inner solar system. We estimate which close encounters can cause significant perturbations in the binary systems (35107) 1991 VH and (175706) 1996 FG. By sampling a large number of particles from the orbit uncertainties in both binary systems we estimate that some disruption is expected in a million year timescale. The damping of these perturbations from energy dissipation will have to be considered to better understand the current states of the two systems.

References

[1] A. F. Cheng, "Near Earth Asteroid Rendezvous: Mission Summary," in *Asteroids III*, 2002.

[2] M. Yoshikawa, J. Kawaguchi, A. Fujiwara, and A. Tsuchiyama, "Hayabusa sample return mission," in *Asteroids IV*, 2015.

[3] Y. Tsuda, M. Yoshikawa, M. Abe, H. Minamino, and S. Nakazawa, "System design of the hayabusa 2-asteroid sample return mission to 1999 JU3," *Acta Astronautica*, 2013.

[4] A. F. Cheng, A. S. Rivkin, P. Michel, J. Atchison, O. Barnouin, L. Benner, N. L. Chabot, C. Ernst, E. G. Fahnestock, M. Kueppers, P. Pravec, E. Rainey, D. C. Richardson, A. M. Stickle, and C. Thomas, "AIDA DART asteroid deflection test: Planetary defense and science objectives," *Planetary and Space Science*, 2018.

[5] D. Scheeres, J. McMahon, E. Bierhaus, J. Wood, L. Benner, C. Hartzell, P. Hayne, J. Hopkins, R. Jedicke, L. L. Corre, A. Meyer, S. Naidu, P. Pravec, M. Ravine, and K. Sorli, "Janus: A NASA SIMPLEx mission to explore two NEO Binary Asteroids," *Bulletin of the AAS*, vol. 52, no. 6, 2020. [Online]. Available: https://baas.aas.org/pub/2020n6i217p06

[6] P. Michel, C. Froeschlé, and P. Farinella, "Secular dynamics of asteroids in the inner solar system," *Celestial Mechanics and Dynamical Astronomy*, vol. 69, pp. 133–147, 1997.

[7] O. Fuentes-Muñoz, A. J. Meyer, and D. J. Scheeres, "Semi-analytical near-Earth objects propagation: the orbit history of (35107) 1991 VH and (175706) 1996 FG3," *The Planetary Science Journal (submitted)*, 2021.

[8] P. Pravec, P. Scheirich, P. Kušnirák, K. Hornoch, A. Galád, S. Naidu, D. Pray, J. Világi, Š. Gajdoš, L. Kornoš *et al.*, "Binary asteroid population. 3. secondary rotations and elongations," *Icarus*, vol. 267, pp. 267–295, 2016.

[9] A. J. Meyer and D. J. Scheeres, "The effect of planetary flybys on singly synchronous binary asteroids," *Icarus*, vol. 367, p. 114554, 2021. [Online]. Available: https://www.sciencedirect.com/science/article/pii/S001910352100227X

[10] D. C. Heggie and F. A. Rasio, "The effect of encounters on the eccentricity of binaries in clusters," *Monthly Notices of the Royal Astronomical Society*, vol. 282, no. 3, pp. 1064–1084, 1996.

[11] C. D. Murray and S. F. Dermott, *Solar System Dynamics*. Cambridge University Press, 2000.

[12] E. J. Öpik, *Interplanetary encounters: close-range gravitational interactions*, ser. Developments in solar system- and space science. Elsevier Scientific Pub. Co., 1976. [Online]. Available: https://books.google.com/books?id=-HXvAAAAMAAJ

[13] G. B. Valsecchi, E. M. Alessi, and A. Rossi, "An analytical solution for the swing-by problem," *Celestial Mechanics and Dynamical Astronomy*, vol. 123, no. 2, pp. 151–166, Oct. 2015.

[14] E. M. Alessi and J. P. Sánchez, "Semi-Analytical Approach for Distant Encounters in the Spatial Circular Restricted Three-Body Problem," *Journal of Guidance, Control, and Dynamics*, vol. 39, p. Number 2, 2015.

[15] O. Fuentes Munoz and D. J. Scheeres, "Extremely long-term asteroid propagation," in *AIAA Scitech 2020 Forum*, 2020, p. 464.

[16] J. Fang and J. L. Margot, "Binary asteroid encounters with terrestrial planets: Timescales and effects," *Astronomical Journal*, 2012.

[17] B. F. Collins and R. Sari, "Lévy flights of binary orbits due to impulsive encounters," *Astronomical Journal*, 2008.

Single-averaged analytical model for low-thrust collision avoidance manoeuvres

Juan Luis Gonzalo*[1] and Camilla Colombo†[1]

[1]Politecnico di Milano, Dept. of Aerospace Science and Technology, Via la Masa 34, 20158 Milan, Italy

Abstract

Analytical models for low thrust collision avoidance manoeuvres in Earth orbit are proposed, based on a single-averaging of Gauss's planetary equations over one revolution of the eccentric anomaly. The equations are linearised in the small thrust acceleration to separate dynamics over the tangential and normal directions. A piecewise quasi-optimal thrust orientation profile is then defined from an impulsive manoeuvre model.

1 Introduction

The increasing market penetration of low thrust propulsion solutions, together with the growth in satellite traffic and debris accumulation, fosters the need for improved tools for collision avoidance (COLA) activities. Low thrust propulsion provides a higher propellant efficiency at the cost of a lower maximum thrust. This reduction in control authority increases the complexity of manoeuvre design and requires longer execution times. These aspects are particularly challenging for COLA, because the occurrence of a close approach (CA) potentially requiring to implement a collision avoidance manoeuvre (CAM) can only be predicted with a limited warning time (typically up to a week [1]). Furthermore, the operator will normally prefer to delay the CAM decision as much as possible, to avoid unnecessary service disruptions and propellant use in case updated conjunction data confirms that the risk is below decision thresholds. Regarding traffic increase, there is a trend towards reducing operator workload through AI-based tools to assist decision making procedures [2, 3] and increasing the level of COLA autonomy of spacecraft [4]. One example is SpaceX's Starlink, that incorporates an automatic COLA system (although little information is publicly available).

Analytical and semi-analytical CAM models can be a powerful tool to address some of these challenges. They provide low-computational-cost, medium-accuracy solutions useful for preliminary risk assessment, parametric and sensitivity analyses, initial guess generation for high-accuracy numerical methods, and support for the training of AI and machine learning models. In recent works, the authors have proposed a series of analytical and semi-analytical models for constant low thrust CAMs [5, 6, 7, 8, 9]. They are based on single-averaged solutions of Gauss's planetary equations over the eccentric anomaly, with different approaches for the recovery of fast periodic oscillations and time law characterisation. The results obtained so far demonstrate the good performance of the tangential model when adequate choices are made for the short periodic and time law characterisation.

This work overviews the main outcomes from the tangential model, and presents new developments for CAMs with a generic in-plane orientation. The equations of motion are linearised for small thrust magnitude, allowing to separate the tangential and normal contributions. A model for normal CAM is derived, following the same structure of the tangential one. Although for most orbital elements the solution is simple, the argument of pericentre and time law involve several elliptic integrals that must be adequately separated into their secular and short-period evolutions to reach accurate and computationally efficient expressions. Then, the quasi-optimal orientation of thrust is approximated in a piecewise fashion leveraging previous impulsive CAM models. This allows to construct a model for a low thrust CAM by separating it into a sequence of thrust and coast arcs

2 Dynamical model

The displacement in the plane of the nominal CA due to a low-thrust CAM is modelled as proposed in [6, 7, 8, 9]. Particularly, the change in orbital elements at the time of closest approach (TCA) is obtained from Gauss's planetary equations, and then mapped to changes in position and velocity through linearised relative motion equations around the nominal trajectory. This work focuses on the modelling of the change of orbital elements $\boldsymbol{\alpha} = [a, e, i, \Omega, \omega, M]^{\mathrm{T}}$ due to a generic in-plane CAM.

The evolution of $\boldsymbol{\alpha}$ in time is given by Gauss's plan-

*Email: juanluis.gonzalo@polimi.it
†Email: camilla.colombo@polimi.it

etary equations:

$$\frac{\mathrm{d}\boldsymbol{\alpha}}{\mathrm{d}t} = \mathbf{G}(\boldsymbol{\alpha}, t; \mathbf{a}_t) \tag{1}$$

where t is time, and $\mathbf{a}_t$ is the perturbing acceleration. From now on, it is assumed that the only acceleration present corresponds to an in-plane CAM. Furthermore, for small acceleration magnitude $a_t = |\mathbf{a}_t|$, Eq. (1) can be linearised in a_t and the contributions from the tangential and normal components can be treated separately, similar to the approach by Gao [10].

2.1 Variable change and time law

For each thrust orientation, Eq. (1) is averaged over one revolution in eccentric anomaly E. To do this, a change of independent variable from t to E is required. An approximate differential time law for $E(t)$ is obtained by taking the derivative of Kepler's equation assuming constant a and e over one revolution. While this hypothesis on a and e is consistent with the averaging procedure, numerical tests showed an important error contribution from the time law. This is because the angular reference for the osculating E changes due to thrust; while this effect is not included in the differential time law derived from Kepler's equation, it can be incorporating through an apse-line correction from the osculating change in ω.

An alternative approach is to consider Gauss's differential equation for E. The Kepler's-based time law is then identified as the solution neglecting the direct effect of thrust on E; from now on, it will be referred to as zeroth-order time law. Using the full differential equation for E to perform the change of independent variable and expanding up to first order in a_t, the differential equations for $\boldsymbol{\alpha}$ remain the same as for the zeroth-order time law, while a differential time law of first order in a_t is obtained, no longer requiring the apse-line correction.

2.2 Secular and short-periodic terms

The Gauss's planetary equations in E for both tangential and normal constant thrust can be integrated to obtain solutions in terms of incomplete elliptic integrals. However, having to evaluate special functions at each time step has an impact on computational cost. Instead, the single-averaged solution for $\boldsymbol{\alpha}$ is expressed as a secular term plus short-period oscillations. The secular terms are linear, with slopes function of complete elliptic integrals that only need to be evaluated once for the nominal orbital elements of the orbit. The short-period corrections are expressed as a series expansion on the reference eccentricity, and contain sinusoidal harmonics multiple of one revolution in E. The number of harmonics retained is a function of the order of the expansion in eccentricity.

The decomposition into secular and short-period terms for ω under constant normal thrust is particularly challenging, and has been performed as part of this work. The process revealed that the expansion of the oscillatory term scales well with eccentricity, while the accuracy of the secular evolution degrades rapidly if a full series expansion is considered rather than treating it as a combination of complete elliptic integrals. This supports previous findings that the expansion in small e behaves well even for nominal orbits in the geostationary transfer orbit (GTO) region [9].

2.3 Piecewise thrust orientation

The previous model characterises the displacement at TCA due to a constant CAM applied for a time Δt before CA. By patching a sequence of thrust and coast arcs, it is possible to model more complex, multi-revolution CAM profiles. The orientation of $\mathbf{a}_t$ on each thrust arc can be approximated as the impulsive one at a point of the arc (e.g., the middle point). Following the impulsive model in [5], this orientation is obtained as the eigenvector associated to the largest eigenvalue of the state transition matrix relating velocity changes at CAM time to position changes at TCA. Alternatively, for given covariance matrices of spacecraft and debris at TCA, the eigenproblem for minimum collision probability can be used instead. Furthermore, it can be proven that the eigenvalue magnitude is a proxy for how efficient it is to perform the CAM at that point. This can be used to automatically set the relative weights between thrust magnitude at the different arcs, as well as to set thrust/coast conditions, reducing the free parameters of the design problem.

3 Numerical results

A test case corresponding to a single constant tangential thrust arc followed by a coast arc is presented. A spacecraft on a GTO is selected, as a worst-case scenario for the errors due to the series expansion in e for the short-period terms. The spacecraft chosen is SDO T2, a 12U CubeSat, whose Keplerian elements at epoch t_0 =2022-05-05T10:28:43 according to Space-Track[1] are $\boldsymbol{\alpha} = [\ 24208.529\,\mathrm{km},\ 0.72823,\ 26.4980\,\mathrm{deg},\ 318.9837\,\mathrm{deg},\ 179.9623\,\mathrm{deg},\ 357.3555\,\mathrm{deg}]$. Its nominal period is $T = 10.42\,\mathrm{h}$. At t_0, a zero-miss distance CA with a debris is assumed, with relative velocity $\mathbf{v}_{s/c} - \mathbf{v}_{deb} = [0.34, 0.58, 0.22]\,\mathrm{km/s}$ in Earth-centred inertial (ECI) frame. Figure 1 shows the deflection achievable in the encounter plane δb (where b is the miss distance) and the numerical error of the analytical model compared to a high-accuracy numerical solution δb_{num}, for a thrust acceleration of $10^{-7}\,\mathrm{m/s^2}$

[1] https://www.space-track.org

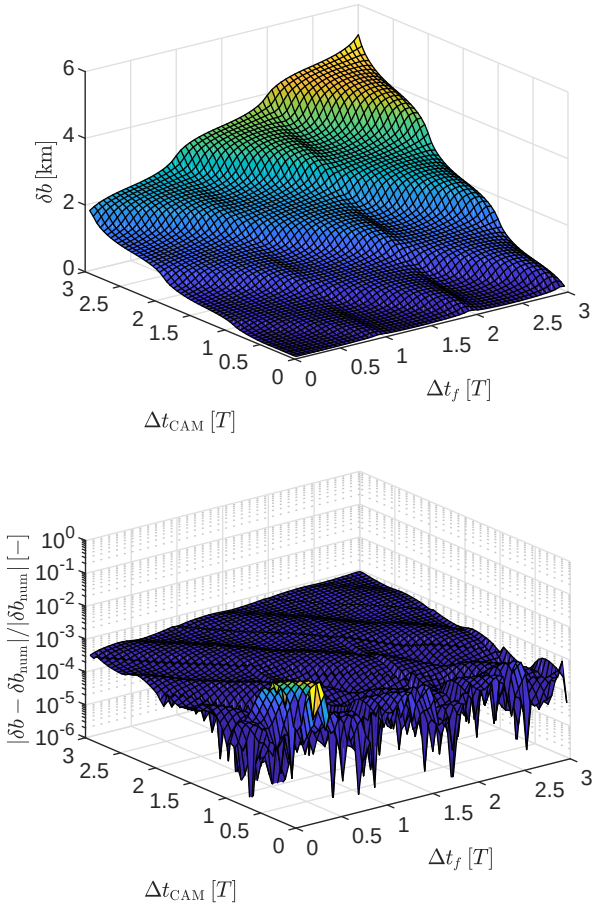

Figure 1: Deviation in the plane of the CA (top) and error of the analytical model (bottom) for a GTO test case.

and different lengths of the thrust arc, Δt_{CAM}, and coast arc, Δt_{f}. Errors remain small except for very short Δt_{CAM} and Δt_{f}, which are not interesting from a practical point of view because they correspond to very small deviations. In this region, the separation in secular and short-period terms is not yet adequately developed from a dynamical perspective, and the later are dominating (with higher associated errors).

4 Conclusions

An analytical CAM model based on the single-averaging of Gauss's planetary equations has been presented. New contributions with respect to previous works focus on the introduction of the solution for normal thrust, the separation of a generic in-plane thrust orientation into tangential and normal contributions, and the approximation of a CAM profile through coast and thrust arcs with thrust orientation and relative magnitude derived from the impulsive CAM model.

5 Acknowledgements

This work has received funding from the European Research Council under the European Union's Horizon 2020 research and innovation programme within the project COMPASS (grant agreement No 679086). Part of this work has also received funding from the European Space Agency project "ELECTRO-CAM: Assessment of collision avoidance manoeuvre planning for low-thrust missions" (call AO/1-10666/21/D/SR).

References

[1] V. Braun, T. Flohrer, H. Krag, K. Merz, S. Lemmens, B. Bastida Virgili, and Q. Funke, Operational support to collision avoidance activities by ESA's Space Debris Office, *CEAS Space Journal*, **8:3** (2016), 177–189.

[2] M. Vasile, V. Rodriguez-Fernandez, R. Serra, D. Camacho, and A. Riccardi, Artificial intelligence in support to space traffic management, in: *68th International Astronautical Congress*, International Astronautical Federation, Adelaide, Australia, 25–29 Sep. 2017, 3822–3831. Paper no. IAC–17.A6.7.1.

[3] T. Uriot, D. Izzo, L.F. Simões, R. Abay, N. Einecke, S. Rebhan, J. Martinez-Heras, F. Letizia, J. Siminski and K. Merz, Spacecraft collision avoidance challenge: Design and results of a machine learning competition, *Astrodynamics* (2021).

[4] B. Bastida Virgili, T. Flohrer, H. Krag, K. Merz, and S. Lemmens, CREAM - ESA's proposal for collision risk estimation and automated mitigation, in: *First International Orbital Debris Conference (IOC)*, Sugarland (TX), US, 9–12 December 2019. Paper 6031.

[5] J.L. Gonzalo, C. Colombo, and P. Di Lizia, Analytical framework for space debris collision avoidance maneuver design, *Journal of Guidance, Control and Dynamics*, **44:3** (2021), 469–487.

[6] J.L. Gonzalo, C. Colombo, and P. Di Lizia, Introducing MISS, a new tool for collision avoidance analysis and design, *Journal of Space Safety Engineering*, **7:3** (2020), 282–289.

[7] J.L. Gonzalo, C. Colombo, and P. Di Lizia, A semi-analytical approach to low-thrust collision avoidance manoeuvre design, in: *70th International Astronautical Congress*, Washington, D.C., USA, 21–25 Oct. 2019. Paper no. IAC-19.A6.2.3.

[8] J.L. Gonzalo and C. Colombo, Lightweight algorithms for collision avoidance applications, in: *11th ESA GNC*, Virtual conference, 22–25 June 2021.

[9] J.L. Gonzalo, C. Colombo, and P. Di Lizia, Computationally efficient approaches for low-thrust collision avoidance activities, in: *72nd International Astronautical Congress*, Dubai, UAE, 25–29 October 2021. Paper no. IAC-21-A6.10-B6.5.5.

[10] Y. Gao, Near-optimal very low-thrust earth-orbit transfers and guidance schemes, *Journal of Guidance Control and Dynamics*, **30:2** (2017), 529–539.

Dynamics of Close Earth Satellites by Picard Iterations

Martin Lara*[1]

[1]SCoTIC, University of La Rioja, Madre de Dios 53, 26006 Logroño, La Rioja, Spain

The proliferation of crowded constellations of small satellites in low Earth orbit (LEO), ranging from the current 150 units of Planet Labs[1] to the eventual 42000 programmed for SpaceX's Starlink satellite megaconstellation,[2] is producing a revival in the use of simple analytical solutions of the artificial satellite problem, which fit quite well for their design and operation [1]. This fact motivates me to revisit the main effects on the LEO dynamics of the gravitational disturbances of Keplerian motion. As is well known, they are due to the dominant effect of the Earth's zonal harmonic of the second degree, whose nondimensional coefficient is customarily denoted J_2 [2].

Beyond the integrable equatorial case [3] the J_2 problem lacks of the needed integrals that would guarantee the existence of a closed form solution [4]. Nevertheless, the non-integrability can be ignored in practice for the small value of the Earth's $J_2 = \mathcal{O}(10^{-3}) > 0$, which makes the size of the regions in which chaos may emerge negligible [5]. Indeed, machine-precision accuracy can be preserved for long times with high order perturbation solutions of the J_2 problem [6]. However, the length of the series involved in this kind of solution, together with the inadequacy of the J_2 model for simulating the real dynamics of circumterrestrial orbits, makes that highly accurate solutions of the J_2 problem are of limited interest in practice.

Conversely, the bulk of the J_2 dynamics is captured by much simpler *intermediary orbits*, which share the mean dynamics of the satellite problem at least up to $\mathcal{O}(J_2)$ effects. To wit, on average, the intermediary orbit must undergo a small linear variation of the right ascension of the ascending node, and a small but steady motion of the argument of the perigee in the orbital plane. These general properties of the oblateness perturbation are usually derived from an average representation of the disturbing function $\mathcal{D}$ of the J_2 problem [7]. That is,

$$\langle\mathcal{D}\rangle_M = \frac{1}{2\pi}\int_0^{2\pi}\mathcal{D}\,\mathrm{d}M = \frac{1}{4}J_2\frac{\mu}{p}\frac{R_\oplus^2}{p^2}\eta^3\left(1-3c^2\right), \quad (1)$$

where μ is the gravitational parameter, $R_\oplus$ is the Earth's equatorial radius, $p = a\eta^2$, a is the orbit semimajor axis, $\eta = (1-e^2)^{1/2}$, e is orbital eccentricity, c is the cosine of the orbit inclination I, and M is the mean anomaly [8].

*Email: mlara0@gmail.com. Research supported by Project PID 2020-112576GB-C22, AEI/ERDF, EU. Illustrative conversations with J. Roa, Sr. GNC Engineer at Starlink, SpaceX, are happily acknowledged.

[1]www.planet.com/our-constellations/ (as May 3, 2022).

[2]www.space.com/spacex-starlink-satellites.html (as May 3, 2022).

Replacing (1) in the variation of parameters equations, we readily obtain the well-known mean variations of the right ascension of the ascending node Ω and the argument of the perigee ω. Namely,

$$\overline{\frac{\mathrm{d}\Omega}{\mathrm{d}t}} = -nJ_2\frac{R_\oplus^2}{p^2}\frac{3}{2}c, \quad \overline{\frac{\mathrm{d}\omega}{\mathrm{d}t}} = nJ_2\frac{R_\oplus^2}{p^2}\frac{3}{4}(5c^2-1), \quad (2)$$

where $n = (\mu/a^3)^{1/2}$ is the mean motion. While (2) reasonably agrees with the average dynamics, the average rate of variation of the mean anomaly obtained with this procedure [9, 10, 11]

$$\overline{\frac{\mathrm{d}M}{\mathrm{d}t}} = n + nJ_2\frac{R_\oplus^2}{p^2}\frac{3}{4}\eta(3c^2-1), \quad (3)$$

soon yields large in-track errors with respect to which would be expected from a $\mathcal{O}(J_2)$ average solution. Rather than starting from an average disturbing function, I will show that the mean rate in (3) is amended when the average dynamics is computed by neglecting the periodic terms from the true solution. The latter is obtained using Picard's constructive proof for the existence and unicity of solutions to ordinary differential equations [12].

Thus, let

$$\frac{\mathrm{d}\xi_i}{\mathrm{d}\tau} = \chi_i(\xi_j,\tau), \quad \xi_i(\tau_0) = \xi_{i,0}, \quad i,j = 1,\ldots m, \quad (4)$$

be a first order differential system in which τ is the independent variable, and ξ_i are m dependent variables. Assuming that the functions χ_i are analytic, they are replaced by corresponding Taylor series expansions in powers of $\Delta\tau = \tau - \tau_0$. When constraining to such interval $\Delta\tau$ that the differences $\xi_j - \xi_{j,0}$ remain small enough, these differences can be neglected, and hence an analytical approximation to the solution of (4) is computed from the convergent sequence

$$\xi_{i,k} = \xi_{i,0} + \int_{\tau_0}^{\tau}\chi_i[\xi_{j,k-1}(\tau,\xi_{j,0}),\tau]\,\mathrm{d}\tau, \quad (5)$$

which starts from $\xi_{i,1} = \xi_{i,0} + \int_{\tau_0}^{\tau}\chi_i(\xi_{j,0},\tau)\,\mathrm{d}\tau$.

I apply this procedure to the variations of the traditional Keplerian variables a, e, I, Ω, ω, and M, whose detailed expressions can be consulted elsewhere [13]. However, to deal with strict elements the variation of M is replaced by [7]

$$\frac{\mathrm{d}\beta}{\mathrm{d}t} = \frac{\mathrm{d}M}{\mathrm{d}t} - \sqrt{\frac{\mu}{a^3}}. \quad (6)$$

Still, M is present in the variation equations through its implicit dependence on the true anomaly f. Then, in order for the variation equations to take a form amenable to solution by Picard iterations, the integration is carried out in a fictitious time τ, given by the differential relation

$$\mathrm{d}t = (r^2/G)\,\mathrm{d}\tau, \tag{7}$$

where $G = \sqrt{\mu p}$ is the specific angular momentum.

Comparison of (7) with Kepler's law of areas shows that τ evolves at the same rate as the argument of the latitude. Alternatively, for an $\mathcal{O}(J_2)$ solution the fictitious time can be replaced by f as the independent variable [14, 15]. Then, the variations in the physical time are replaced by

$$\frac{\mathrm{d}\xi_j}{\mathrm{d}f} = \frac{r^2}{G}\frac{\mathrm{d}\xi_j}{\mathrm{d}t}, \qquad j = 1, \ldots 6, \tag{8}$$

which are integrated in closed form of the eccentricity by Picard iterations starting from the initial values a_0, e_0, I_0, Ω_0, ω_0, and $\beta_0 = 0$, for f_0. The first iteration results in

$$\begin{aligned}
a_1 &= a_0 + a_0\varepsilon[a_{1,\mathrm{P}}(f) - a_{1,\mathrm{P}}(f_0)]\\
e_1 &= e_0 + \varepsilon[e_{1,\mathrm{P}}(f) - e_{1,\mathrm{P}}(f_0)]\\
I_1 &= I_0 + \varepsilon c[I_{1,\mathrm{P}}(f) - I_{1,\mathrm{P}}(f_0)]\\
\Omega_1 &= \Omega_0 - 6\varepsilon c\Delta M + \varepsilon c[\Omega_{1,\mathrm{P}}(f) - \Omega_{1,\mathrm{P}}(f_0)]\\
\omega_1 &= \omega_0 + 3\varepsilon(5c^2-1)\Delta M + \varepsilon[\omega_{1,\mathrm{P}}(f) - \omega_{1,\mathrm{P}}(f_0)]\\
\beta_1 &= 3\varepsilon\eta(3c^2-1)\Delta M + \varepsilon[\beta_{1,\mathrm{P}}(f) - \beta_{1,\mathrm{P}}(f_0)]
\end{aligned} \tag{9}$$

where $\varepsilon = \frac{1}{4}J_2R_\oplus^2/p^2$, $\Delta M = M - M_0$, and $\xi_{1,\mathrm{P}}$ are such trigonometric polynomials that $\langle\xi_{1,\mathrm{P}}(f)\rangle_M = 0$. Refer to [13] for detailed expressions.

Next, $M_1 = M_0 + \beta_1(f) + \sqrt{\mu}\int_{t_0}^{t} a_1(t)^{-3/2}\,\mathrm{d}t$, from (6), where the integrand $a_1(t)^{-3/2}$ is replaced by an $\mathcal{O}(J_2)$ approximation to obtain a solution in closed form of e. Thus,

$$M_1 = M_0 + n^*(t - t_0) + \varepsilon\left[M_{\mathrm{P}}(f) - M_{\mathrm{P}}(f_0)\right], \tag{10}$$

in which

$$n^* = n\left[1 + 3\varepsilon\eta(3c^2-1) + \tfrac{3}{2}\varepsilon a_{1,\mathrm{P}}(f_0)\right], \tag{11}$$

and the detailed form of M_{P} can be consulted in [13].

Finally, from (7),

$$t = t_0 + \int_{f_0}^{f} \frac{\left[\left(1-e_1^2\right)a_1\right]^{3/2}}{(1+e_1\cos f)^2\mu^{1/2}}\,\mathrm{d}f. \tag{12}$$

Note that, in a typical ephemeris evaluation, the errors introduced in the physical time determination may be as important as those of the elements [16].

Removing the purely periodic terms $\xi_{1,\mathrm{P}}(f)$ from (9) it is readily obtained that, in the approximation provided by the first Picard iteration, the semi-major axis, eccentricity, and inclination, remain constant on average. On the other hand, (2) is recovered by differentiation of the secular terms of Ω_1 and ω_1 with respect to the physical time. Analogously, the removal of purely short-period terms from (10) shows that, at the precision of the first Picard iteration, M advances, on average, at the rate n^* given in (11), thus amending (3) with the additional term $\frac{3}{8}nJ_2(R_\oplus/p)^2a_{1,\mathrm{P}}(f_0)$.

The accuracy of the first Picard iteration with respect to the true, numerically integrated solution is illustrated in the left column of Fig. 1 for an example eccentric orbit with $a_0 = 9500$ km, $e_0 = 0.2$, $I_0 = 20^\circ$, $\Omega_0 = 6^\circ$, $\omega_0 = 274^\circ$, and $M_0 = 0$ ($\mu = 398600.4415\,\mathrm{km}^3/\mathrm{s}^2$, $R_\oplus = 6378.1363$ km, $J_2 = 0.001082634$). The mild behavior of the errors of M is due to the new secular term in (11). It can be checked that when n^* is replaced in (10) by (3), the error of M grows by about two orders of magnitude at the end of the one-day interval shown in the current example, reaching an amplitude close to 1° — or about 200 km along-track as opposed to the km level reached when using (11).

The first iteration of Picard's method misses the long-period effects of the true solution, which are clearly apparent in Fig. 1 coupled with the short-period errors. A refinement of the analytical solution that captures non-resonant long-period effects of the dynamics is obtained by an additional iteration of (5). To $\mathcal{O}(J_2)$, the whole procedure is equivalent to substituting M by n^*t in (9), and replacing the appearances of the constant ω_0 throughout $\xi_{1,\mathrm{P}}$ by the low frequency $\omega(f) \equiv \omega_0 + 3(5c^2-1)(\varepsilon f)$ [13].

The improvements produced by the second Picard iteration are illustrated in the right column of Fig. 1. While the errors start with the same amplitudes as before, the influence of the long-period terms becomes now evident, and the amplitude of the errors remains mostly constant along the propagation, improving the errors with respect to the first Picard iteration by about one order of magnitude at the end of the one-day propagation interval. Remaining secular and long-period components are a consequence of the $\mathcal{O}(J_2)$ truncation of the Picard iterations solution.

References

[1] Starlink GNC Team, *Starlink Conjunction Avoidance with Crewed Space Stations*, Memo No. SAT-51385, SpaceX, Hawthorne, CA, April 23, 2022.

[2] R.H. Merson and D.G. King-Hele, Use of artificial satellites to explore the Earth's gravitational field: Results from Sputnik 2 (1957β), *Nature* **182** (1958), 640–641.

[3] D.J. Jezewski. An analytic solution for the J_2 perturbed equatorial orbit. *Celestial Mech* **30** (1983), 363–371.

[4] M. Irigoyen & C. Simó. Non integrability of the J_2 problem. *Celest Mech Dyn Astr*, **55** (1993), 281287.

[5] C. Simó. Measuring the lack of integrability of the J_2 problem for Earth's satellites, in: *Predictability, Stability, and Chaos in N-Body Dynamical Systems*, NATO ASI Series, 272, Springer, Boston, MA, 1991, 305–309.

[6] M. Lara. Solution to the main problem of the artificial satellite by reverse normalization. *Nonlinear Dynam* **101** (2020), 1501–1524.

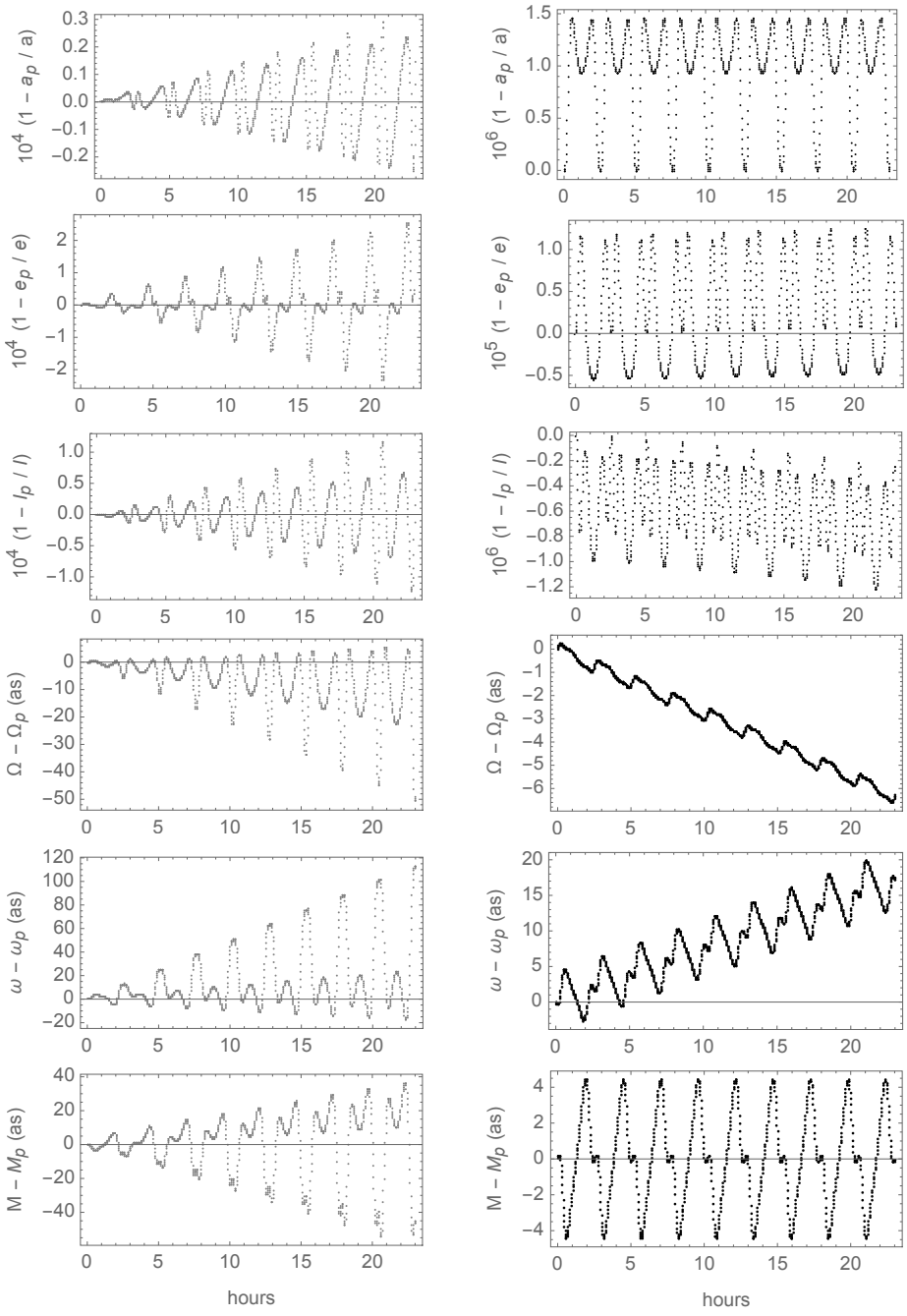

Figure 1: Errors of the first (left column) and second Picard iteration (right colum) of the test orbit [13].

[7] R.H. Battin. An Introduction to the Mathematics and Methods of Astrodynamics, Revised Edition. AIAA Education Series. AIAA, Reston, VA, 1999.

[8] M. Lara, Hamiltonian Perturbation Solutions for Spacecraft Orbit Prediction, De Gruyter Studies in Mathematical Physics, 54, De Gruyter, Berlin/Boston, 2021.

[9] Y. Kozai. The motion of a close earth satellite. *Astron J* **64** (1959), 367–377.

[10] W.M. Kaula. Theory of Satellite Geodesy. Blaisdell, Waltham, MA, 1966. Reprint: Dover, Mineola, NY, 2000.

[11] F.L. Markley & J.F. Jeletic. Fast orbit propagator for graphical display. *J Guid Control Dynam* **14** (1991), 473–475.

[12] W. Hurewicz. Lectures on Ordinary Differential Equations, 2nd Edition. The M.I.T. Press, Cambridge, MA, 1970.

[13] M. Lara. Earth satellite dynamics by Picard iterations, preprint, 2022, `arXiv:2205.04310`

[14] A.E. Roy. Orbital Motion, 4th edition. Institute of Physics Publishing, Bristol, UK, 2005.

[15] J. Herrera-Montojo, H. Urrutxua, & J. Peláez. An asymptotic solution for the main problem, paper AIAA 2014-4155 (2014), 19 pp.

[16] M. Lara. Note on the analytical integration of circumterrestrial orbits, *Adv Space Res*, **69** (2022), 4169–4178.

Session 2:

PERTURBATION THEORY

Statistical analysis of the long-term dynamical behavior of uncontrolled geostationary satellites near an unstable equilibrium point

Roberto Flores*[1], Mauro Pontani†[2], and Elena Fantino‡[3]

[1]Centre Internacional de Métodes Numèrics en Enginyeria (CIMNE), Gran Capità s/n, 08034 Barcelona, Spain
[2]Department of Astronautical, Electrical, and Energy Engineering, Sapienza University of Rome, via Salaria 851, 00138 Rome, Italy
[3]Space and Planetary Science Center, and Department of Aerospace Engineering, Khalifa University of Science and Technology, P.O. Box 127788, Abu Dhabi, United Arab Emirates

1 Introduction

The long-term dynamics of decommissioned spacecraft in geostationary orbit is an area of active research due to its implications for the continued safe operation of communication satellites (see, for example, [1, 2]). In [3] we determined that moderate changes on the initial conditions can lead to vastly different longitudinal motion patterns. For some combinations of initial longitude and epoch (which influences the solution through the positions of Sun and Moon) the sensitivity is so extreme that it was not possible to obtain a converged trajectory beyond a horizon of 60 years. To improve the understanding of the phenomenon and better characterize the sensitivity to initial conditions, we present a Monte Carlo simulation of bundles of uncontrolled spacecraft released near one of the unstable equilibrium points. Contrary to initial expectations, it is found that the bundles can maintain high spatial coherence over time scales of decades. These intervals of ordered behavior are interspersed with sudden increases in scatter. The time interval between these abrupt changes is very close to the precession period of the orbital plane due to the combined effects of lunisolar perturbations and Earth's polar flattening. This is strongly suggestive of a connection between the two phenomena.

2 Numerical model

In a previous study [3] it was determined that the most relevant perturbations for our problem are the harmonics of Earth's gravity field up to degree and order 8, solar radiation pressure and lunisolar third-body perturbations.

*Email: rflores@cimne.upc.edu
†Email: mauro.pontani@uniroma1.it
‡Email: elena.fantino@ku.ac.ae. Corresponding author

2.1 Earth orientation modeling

The state vector of the spacecraft is integrated in an ECI (Earth Centered Inertial) reference aligned with ICRF (International Celestial Reference Frame). The non-uniform terrestrial gravitational field is computed in the ITRF (International Terrestrial Reference Frame), requiring a coordinate transform to take into account precession and nutation of Earth's rotational axis. We used the IAU 2000/2006 combined precession-nutation model [4] based on the non-rotating CIO (Celestial Intermediate Origin). This paradigm supersedes classical models based on the ascending node, offering important efficiency advantages. For the scope of our calculations, an accuracy of 1 arcsec is sufficient. Further improvements would require including polar motion, which is not predictable with current technology [5] (i.e., it can only be measured *a posteriori*). To improve the computational efficiency, we used a reduced version of the precession-nutation model based on [6], but modified to maintain an accuracy of 1" over 500 years instead of a century.

2.2 Terrestrial gravity field modeling

To model Earth's gravitational field, we followed the guidelines from the IRS Conventions 2010 standard [7]. It establishes EGM2008 [8] as the recommended geopotential model with some adjustments: (i) the progressive drift of the zonal harmonics up to degree 4 is included with a linear correlation; (ii) the original value of J_2 is replaced with an improved estimation based on 17 years of SLR (Satellite Laser Ranging) which is expected to improve on the 4 years of GRACE (Gravity Recovery and Climate Experiment) data used in EGM2008. The harmonic synthesis is based on the modified forward row recursion scheme from [9]. It is suitable for ultra-high-degree expansions ($N > 2000$) and has been vectorized to improve performance in current CPU architectures.

2.3 Third-body graviatational perturbations

To compute the position of the Earth and the Moon, we used tabulated orbital elements obtained from JPL's Solar System Dynamics website [10]. To recover the elements at an arbitrary date, the table is interpolated using cubic splines. To improve the accuracy of the calculation, third-body perturbations are computed using the modified Battin form [11] which mitigates the ill-conditioning due to the large difference between the orbital radius of the satellite and the Earth-Sun distance.

2.4 Solar radiation pressure perturbation

The acceleration due to solar radiation pressure has been estimated assuming a spherical satellite with perfect reflectivity and a mass-to-area ratio of 300 kg/m^2. The eclipses are modeled assuming a cylindrical Earth shadow.

2.5 Numerical integration

Our orbit propagation suite [12] integrates the equations of motion in Cartesian coordinates. For this work, we used an adaptive embedded Runge-Kutta (RK) scheme of orders 7(8) derived by Fehlberg [13]. We used linear extrapolation, retaining the 8th order solution.

3 Trajectory propagation

We assumed that a satellite inside its standard operational window loses control suddenly. We generated a collection of trajectories using slightly different initial positions to asses the evolution of the scatter with time. It is common practice among satellite operators to maintain an operational window of +/- 0.05º around the nominal position. This is slightly more stringent than ITU requirements [14]. We assumed that leaving the operational window is a rare occurrence, corresponding to a 3σ event. Thus, the standard deviation of the initial angular position would be 0.016º. We generated a binormal distribution of longitudes and latitudes centered on the point of maximum instability (165.3ºE), that serves as initial condition for the trajectory propagation. In reality, the longitude and latitude of the satellite are not randomly distributed, but depend on the station keeping strategy. However, given that our goal is to study the dynamical properties of the system instead of the peculiarities of each operator, we deem this approach acceptable. Furthermore, we can analyze if the evolution in time affects the normality of the distribution.

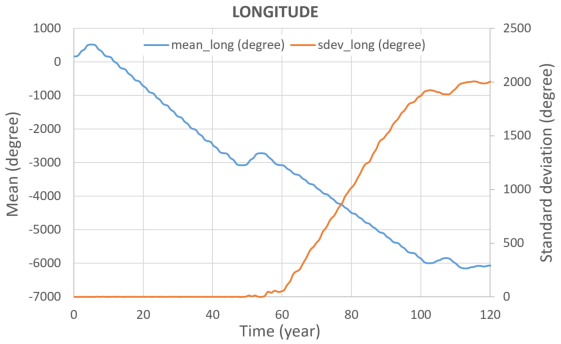

Figure 1: Longitude mean and std. dev.

3.1 Initial results

For the first batch of simulations, we used as initial epoch January 1, 2020 at 0:00 UTC (JDN 2458849.5), because it is one of the dates investigated in [3]. For each trajectory in the bundle, the initial altitude is determined with an iterative solver, in order to obtain a period of one stellar day. This is required because, due to the irregularities in the gravitational field, the height is different from the ideal value for a spherical Earth (the satellites must be placed approximately 600 m higher). While the change in orbital radius seems small (1 part in 70 000), the effect on the orbital period is important. If left uncompensated, it would cause the cloud of satellites to drift rapidly in longitude.

The trajectories have been propagated for 120 years to include two full cycles of precession of the orbital plane (which changes its inclination by 15º over a span of 52 years, see [3]). Figure 1 shows the evolution of the mean and standard deviation of longitude for a bundle of 600 trajectories. The most striking feature is the small scatter during the first 50 years, with a sudden increase afterwards.

To highlight the change in behavior, the first 50 years are shown in Figure 2, where we see that the scatter remains below 1.5º most of the time. The short period (2 years) drops in dispersion correspond to passages through the unstable equilibrium points, where the longitudinal drift slows down and causes the trajectories to regroup.

In Figure 3, we see that the sudden increase in longitude scatter coincides with the end of an inclination cycle. Note that the scatter of the inclination remains below 0.035º for the 120 years of the simulation. This agrees very well with the prediction of the simplified analytical model [3].

To test changes in normality of the trajectory bundle, we computed the excess kurtosis and skewness (which are null for normally distributed variables) of the longitude distribution (Figure 4). There is a drastic change after 50 years, with both parameters increasing by several orders of magnitude in the times-

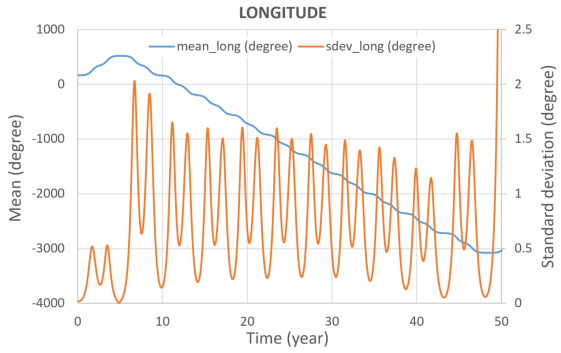

Figure 2: Longitude mean and std. dev.

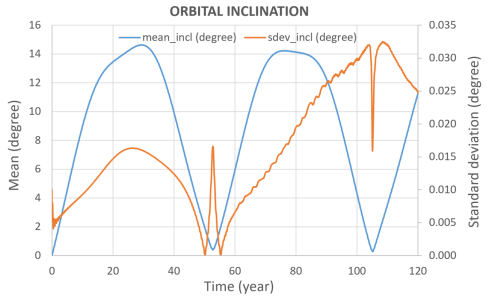

Figure 3: Inclination mean and std. dev.

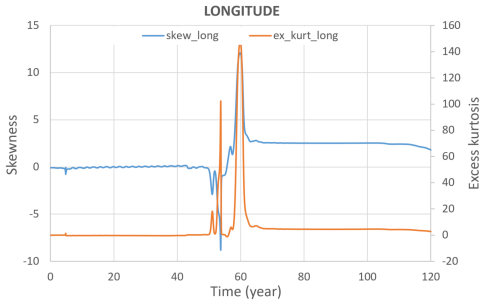

Figure 4: Longitude exc. kurtosis and skewness.

pan of a decade, and then leveling off at a new value indicating a large departure from normality.

4 Conclusions

We found that the scatter of a bundle of trajectories departing from the point of maximum instability shows an irregular behavior. There are periods of limited changes separated by short episodes of increase in dispersion. Simulations with different initial epoch have shown that these episodes do not always coincide with the minimum of the inclination cycle, but their separation in time remains close to 50 years. Numerical experiments also demonstrated that the phenomenon remains after removing solar radiation pressure and gravity harmonics of degree 4 and higher. This hints to connection with the mechanism responsible for the complex longitudinal behavior (see [3]).

Funding acknowledgements: Khalifa University's internal grants CIRA-2021-65 (8474000413) and KU-SPSC (8474000336); Severo Ochoa Programme for Centres of Excellence in R&D (CEX2018-000797-S).

References

[1] A. Celletti and C. Galeş, On the dynamics of space debris: 1:1 and 2:1 resonances, *J. Nonlinear Sci.* **24** (2014), 1231–1262

[2] C. Colombo and I. Gkolias, Analysis of orbit stability in the geosynchronous region for end-of-life disposal, *7th European Conference on Space Debris*, Darmstadt, Germany (2017)

[3] S. Proietti, R. Flores, E. Fantino and M. Pontani, Long-term orbit dynamics of decommissioned geostationary satellites, *Acta astronautica* **182** (2021), 559–573.

[4] J.L. Hilton, N. Capitaine, J. Chapront et al. "Report of the International Astronomical Union Division I Working Group on Precession and the Ecliptic, *Celestial Mechanics and Dynamical Astronomy* **94** (2006)

[5] S.E. Urban and P.K. Seidelman, *Explanatory Supplement to the Astronomical Almanac (3rd Ed.)*, University Science Books, Melville-NY, 2012.

[6] N. Capitaine amd P.T. Wallace, Concise CIO based precession-nutation formulations, *Astronomy and Astrophysics* **478** (2008), 277–284

[7] G. Petit and B. Luzum (eds.), *IERS Conventions (2010) - IERS Technical Note 36*, Verlag des Bundesamts für Kartographie und Geodäsie, Frankfurt am Main, 2010.

[8] N.K. Pavlis, S.A. Holmes, S.C. Kenyon et al., The development and evaluation of the Earth gravitational model (EGM2008), *J. Geophys. Res.* **117** (2008), B04406

[9] S. A. Holmes and W.E. Featherstone, A unified approach to the Clenshaw summation and the recursive computation of very high degree and order normalised associated Legendre functions, *Journal of Geodesy* **76** (2002), 279–299

[10] *NASA JPL HORIZONS Web-Interface*, https://ssd.jpl.nasa.gov/horizons.cgi, Last accessed: May 2022.

[11] R. H. Battin, *An Introduction to the Mathematics and Methods of Astodynamics, Revised Ed.*, AIAA Education Series, Reston-VA, 1999.

[12] R. Flores, B. M. Burhani and E. Fantino, A method for accurate and efficient propagation of satellite orbits: A case study for a Molniya orbit, *Alexandria engineering journal* **60** (2021), 2661–2676.

[13] E. Fehlberg, *Classical Fifth-, Sixth-, Seventh-, and Eight-Order Runge-Kutta Formulas with Stepsize Control*, Technical report, TR R-287, NASA Johnson Space Center, Houston-TX, 1968.

[14] *RECOMMENDATION ITU-R S.484-3 Station-keeping in longitude of geostationary satellites in the fixed-satellite service*, International Telecommunication Union, Geneva, 1974-1978-1982-1992.

Improving long-term special perturbations efficiency for Low Earth Orbits

Davide Amato*[1] and David A. Vallado†[2]

[1]Department of Aeronautics, Imperial College London, United Kingdom
[2]Commercial Space Operations Center (Comspoc), Center for Space Standards and Innovation, United States of America

1 Introduction

Currently, the defining challenge for Space Surveillance and Tracking (SST) is the exponential increase in tracked objects in LEO. The primary reasons for this rapid increase are the introduction of the SpaceX Starlink constellation (along with others that are under development, such as OneWeb and Amazon Kuiper), and the introduction of new sensor systems that are expected to successfully decrease the minimum size detection threshold down to one centimetre. It is reasonable to assume that future SST activities will need to track and perform routine conjunction analysis on a number of objects in excess of 100 000 in the near future, most of these orbiting in LEO. This translates into a need for accurate and efficient orbit propagation algorithms, which underpin orbit determination methods at the core of SST.

The long-term propagation of low Earth satellite orbits has classically relied on semi-analytical techniques based on the method of averaging, which provide significant computational savings compared to special perturbations when the characteristic time scales of the perturbations are well separated from the orbital period. However, the accuracy of semi-analytical approaches is intrinsically limited by the approximations that make the averaging process feasible [1]. For instance, the process commonly starts from truncated series expansions in small parameters, in which orders higher than the second and coupling terms among different perturbations are often (although not always) neglected. Most importantly, the accuracy in osculating position and velocity is intrinsically limited by the fidelity of the mean-to-osculating transformation for the theory under consideration. The fact that semi-analytical propagators work in mean element space also results in a consequence of particular importance to obtain accurate propagations, which can be crucial for the reproduction of trajectories in sensitive dynamical regimes [2]. Initial conditions for a semi-analytical method must be assigned in mean element space to avoid initial errors that will, in general, experience secular growth. However, operational measurements and ephemerides are commonly available in osculating space, and the osculating-to-mean transformations depend on the details of the particular averaging theory under consideration. The highest accuracy for the osculating-to-mean transformation can be obtained through Precise Conversion of Elements (PCE), that is by using differential corrections to find the mean initial conditions corresponding to a given osculating state. Being an iterative process, PCE is computationally expensive and may partially offset the computational efficiency advantage of semi-analytical methods [3].

In this talk, we will focus on several practical aspects aimed at improving orbit propagation efficiency in the Low Earth Orbit regime with special perturbations methods as an extension of the THALASSA orbit propagation code [1], which offer a potential alternative to semi-analytical methods for long-term propagation. Because special perturbations work in osculating space, there is no need for any osculating-to-mean transformations or PCE. THALASSA has been shown to be particularly efficient for highly elliptical orbits, MEOs, and GEOs. However, there has been limited focus on improving its efficiency and accuracy for LEO orbits, which are the focus of this talk. In particular, we focus on the selection and efficient implementation of perturbations within the physical model, a study of numerical integrator performance along with different formulations (extending those in References [4, 5]), and on the implementation programming language.

2 Physical model

The perturbations to be included in the physical model must be selected and modelled carefully to improve the overall computational efficiency of the code. The primary additional orbital perturbations to include are expanded gravitational fields and atmospheric models. The gravitational field is of importance because newer models rely on increasingly large numbers of coefficients; for instance, the state-of-the-art EGM-08 is a 2160×2160 model. The efficient calculation of the Legendre polynomials and associated functions for such large models is a critical step.

*Email: d.amato@imperial.ac.uk.
†Email: dvallado@comspoc.com.

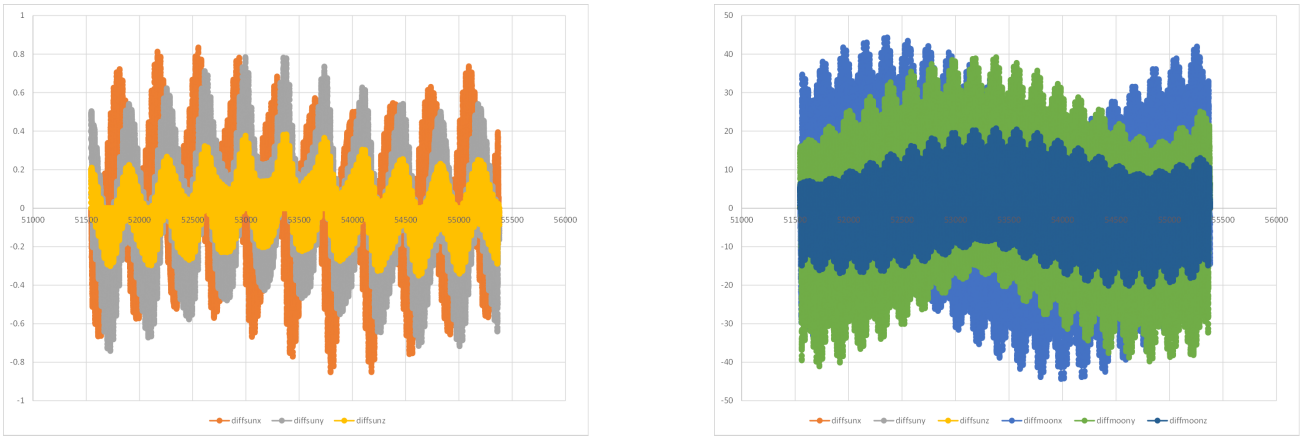

Figure 1: Position error components (in km) of interpolated ephemerides with respect to JPL DE ephemerides over about 11 years. Solar differences (left) and lunar differences (right). Note the difference in scales.

Currently, THALASSA relies on the Pines method [6], which has been shown to achieve an improvement of about 30% in computational cost over the classical Legendre recursion formulas, besides avoiding the singularities at the poles for the perturbing accelerations. We evaluate the improvement in computational efficiency obtained by adopting improved geopotential computational techniques [7]. The specification of the transformations between the celestial (Earth-centered Inertial) and terrestrial (Earth-centered, Earth-fixed) reference frame is also important for the calculation of the geopotential. Here, we choose to implement the IAU 2006/2000 CIO series transformations to move between inertial and Earth-fixed coordinates. Because the series summations include several thousand terms, it's possible to pre-calculate the XYs series coefficients and perform a simple interpolation.

Regarding the modelling of atmospheric density, there are numerous atmospheric models to choose from. MSIS-00 is a convenient, well used model for our implementation [8]. While it suffers from some known biases in temperature and species composition [9], it offers a modestly good method of incorporating geomagnetic and solar flux indices into the propagation effort.

Third body perturbations also can assume various forms to achieve different accuracies. The JPL DE series are generally regarded as the most accurate values but calculating the Sun and Moon position vectors throughout a propagation scheme can be computationally intensive. As shown in fig. 1, a simple interpolation scheme can recover the Sun and Moon positions over 11 years to under 2 km and 50 km, respectively, while being cheap to evaluate.

Due to the aleatoric uncertainty in modelling perturbations (in particular atmospheric drag for LEO) it is not useful to propagate LEO orbits with models of extremely high fidelity without having accurate information on the object characteristics. For instance, if the attitude or the drag coefficient of the object are unknown, the advantage in accuracy resulting from using very high degrees and orders for the geopotential might be overshadowed by the mismodelling of the atmospheric drag. Given these considerations, we characterise the accuracy gains deriving from including high-fidelity perturbations and from the integrator tolerance in terms of a trade-off with respect to the required computational cost.

To test the accuracy of the approach, we use the Consolidated Predicted Format (CPF) ephemerides that are independently generated. In general, these ephemerides are accurate to the few meter range, which is sufficient for our application. Using the CPF ephemerides, we quantify the increase in accuracy (and CPU time) gained when gradually increasing the complexity of the model (including the reference frame implementation here).

3 Numerical integrator and formulation

Besides the overall computational performance, several practical criteria must be considered when choosing a numerical integration scheme, especially if it is to be applied to the integration of regularised equations of motion. A differentiable solution is often required between the integration nodes of time-marching numerical schemes (this is often called *dense output*). This is the case when the solution is required at fixed time steps when using a variable-timestep integrator. This is also a crucial capability when using regularised formulations, whose independent variable is fictitious time. Ideally, the solution would be of the same order of accuracy everywhere in the propagation interval, however this is not always achievable without incurring in increased function calls and thus computational cost. In conjunction with dense output, another desirable aspect for a numerical integration scheme is the availability of reliable root-finding

methods. These are required for returning the solution values at given epochs when the physical time is a dependent variable, or for conjunction analysis.

Through the collection of numerical integration schemes in the `DifferentialEquations.jl` Julia package, we study the numerical performance of integrator-formulation pairs, extending the work in Reference [4]. We use the criteria described above to refine the integrator choice depending on the particular application.

4 Julia for astrodynamics applications

The THALASSA orbit propagation code had been originally implemented in Fortran 95. Although Fortran remains one of the most common languages for astrodynamics applications, research user experience in the past three years has evidenced several issues arising when using the code across different architectures, especially when external libraries are needed. Although the latest Fortran standards provide an excellent set of extensions to the programming language, their implementation into compilers working across all platforms is often slow. Using the latest Fortran features often results in compiler errors when the code must be run on architectures that are different from that on which the code has been developed.

Therefore, we choose Julia as the implementation language for a new version of THALASSA, which is under development as a self-contained Julia package. Benchmarks show that the numerical performance of Julia is close to that of C++ and Fortran for several astrodynamics problems [10, 11], whereas its syntax is relatively close to that of MATLAB and Python. Julia is under active development and runs on all main platforms, which is expected to reduce portability issues. We compare the performance of the new THALASSA version in Julia to the original Fortran version in the solution of orbit propagation toy problems.

References

[1] D. Amato et al. "Non-averaged regularized formulations as an alternative to semi-analytical orbit propagation methods". In: *Celestial Mechanics and Dynamical Astronomy* 131.5 (2019), p. 21. ISSN: 1572-9478. DOI: 10.1007/s10569-019-9897-1.

[2] D. Amato et al. "Recovering the chaotic orbit of Cosmos 862". In: KePASSA 2019. Toulouse, France, 2019.

[3] D. A. Vallado. "Long-term numerical propagation for Earth orbiting satellites". In: 2019 AAS/AIAA Astrodynamics Specialist Conference. Paper AAS 19-601. Portland, ME, USA, 2019.

[4] J. Roa. *Regularization in Orbital Mechanics: Theory and Practice*. De Gruyter, 2017. ISBN: 978-3-11-055912-5.

[5] A. M. Atallah et al. "Accuracy and Efficiency Comparison of Six Numerical Integrators for Propagating Perturbed Orbits". In: *The Journal of the Astronautical Sciences* 67.2 (2020), pp. 511–538. ISSN: 2195-0571. DOI: 10.1007/s40295-019-00167-2.

[6] S. Pines. "Uniform Representation of the Gravitational Potential and its Derivatives". In: *AIAA Journal* 11.11 (1973), pp. 1508–1511. ISSN: 0001-1452, 1533-385X. DOI: 10.2514/3.50619.

[7] E. Fantino and S. Casotto. "Methods of harmonic synthesis for global geopotential models and their first-, second- and third-order gradients". In: *Journal of Geodesy* 83.7 (2009), pp. 595–619. ISSN: 0949-7714, 1432-1394. DOI: 10.1007/s00190-008-0275-0.

[8] J. M. Picone et al. "NRLMSISE-00 empirical model of the atmosphere: Statistical comparisons and scientific issues". In: *Journal of Geophysical Research: Space Physics* 107 (A12 2002), SIA 15–1–SIA 15–16. ISSN: 01480227. DOI: 10.1029/2002JA009430.

[9] J. T. Emmert et al. "NRLMSIS 2.0: A Whole-Atmosphere Empirical Model of Temperature and Neutral Species Densities". In: *Earth and Space Science* 8.3 (2021). ISSN: 2333-5084, 2333-5084. DOI: 10.1029/2020EA001321.

[10] D. Padilha et al. "Modern Numerical Programming with Julia for Astrodynamic Trajectory Design". In: AAS/AIAA Space Flight Mechanics Meeting. Virtual, 2021.

[11] H. Eichhorn et al. "A comparative study of programming languages for next-generation astrodynamics systems". In: *CEAS Space Journal* 10.1 (2018), pp. 115–123. ISSN: 1868-2502, 1868-2510. DOI: 10.1007/s12567-017-0170-8.

Simultaneously Quasi-Critical and Quasi-Heliosynchronous Orbits

R. Vilhena de Moraes*[1], M. Lívia Galhego da Costa†[1], A. F. B. A. Prado‡[2], and J. P. S. Carvalho§[3]

[1]GDOP, São Paulo State University, Guaratinguetá, Brazil.
[2]DIDMC, National Institute for Space Research, São José dos Campos, Brazil.
[3]CETENS, Federal University of Recôncavo da Bahia, Feira de Santana, Brazil.

The classic values of critical inclination are 63.43° and 116.57° for the direct and retrograde orbits respectively when only secular terms due to central body oblateness are considered in the gravitational potential.(GARFINKEL, 1960; MERSMAN, 1962; LUBOWE, 1969; ALLAN, 1970; HUGHES, 1981). These values are found by equating the temporal variation of the argument of pericenter to zero. The inclination values for sun-synchronous orbits are by their turn constant and retrograde for each fixed pair of semimajor axis and eccentricity, and they are found by equating the temporal variation of the longitude of the ascending node to angular velocity of the central body around the Sun.(HANSON, 1961; PARK; JUNKINS, 1995)

If sectoral terms are also included into disturbing function the equations of motion become coupled, turning the search for critical and heliosynchronous inclinations much more complex than the classic case. Thus it is necessary to treat the problem with a different approach from the classic one in order to find them.

Following [Tzirti et al. (2009)], the quasi-critical inclination concept was refined and based on it the quasi-heliosynchronous inclination concept was introduced on previously works(COSTA et al., 2019; COSTA, 2020; COSTA et al., 2020) with the aim to propose a different method from what are found in the literature(DE SAEDELEER; HENRARD, 2005; CARVALHO et al., 2009) to search for those special inclinations when the dynamic model adopted takes into consideration other disturbing terms in addition to the zonal ones.

It was defined as quasi-critical the inclination that given as initial condition makes the argument of pericenter remain on average constant and as quasi-heliosynchronous the one that makes the orbital plane precess on average with the same central body angular velocity around the Sun. In this way, both are the generalizations of the critical and heliosynchronous inclinations respectively when the equatorial ellipticity effects are also considered into the gravitational potential in addition to the oblateness of the center body.(TZIRTI et al., 2009; COSTA et al., 2019; COSTA, 2020; COSTA et al., 2020)

The hamiltonian formalism together with the Delaunay action-angle variables were used. A synodic reference frame was defined to eliminate the explicit temporal dependence of the hamiltonian function corresponding to the sectoral perturbation.(DE SAEDELEER; HENRARD, 2005; DE SAEDELEER; HENRARD, 2004; CARVALHO et al., 2009; GIACAGLIA et al., 1970; NIE; GURFIL, 2018; PALACIÁN, 2002) The first order average equations of motion were obtained through the elimination of the short-period terms (HORI, 1966; CARVALHO et al., 2009; NIE; GURFIL, 2018; TZIRTI et al., 2009). And the decoupling of the average equations of motion was treated by the hamiltonian function of the system.(COSTA, 2020; COSTA et al., 2020)

An optimization approach was applied to find them.(COSTA et al., 2019; COSTA, 2020; COSTA et al., 2020; FRIEDLANDER, 1994; WALTZ et al., 2006; LUENBERGER; YE, 2008) The technique employed verifies whether an arbitrary initial inclination given as initial guess minimizes the absolute value of the area between the curves that describe the temporal variation of the argument of pericenter according to the averaged model considered and its frozen value (time derivative equals zero).(COSTA et al., 2019; COSTA, 2020; COSTA et al., 2020) In a similar manner, the technique verifies whether an arbitrary initial inclination minimizes the absolute value of the area between the curves that describe the temporal variation of the longitude of the ascending node according to the averaged model and its desired value for the sun-synchronous case (orbital plane precessing at the same rate as the central around the Sun).(COSTA et al., 2019; COSTA, 2020; COSTA et al., 2020) The orbits which are solutions of the initial value prob-

*Email: rodolpho.vilhena@gmail.com. Research supported by grant #303102/2019-5 from the National Council for Scientific and Technological Development (CNPq); grant #2016/24561-0 from São Paulo Research Foundation (FAPESP) and the financial support from the Coordination for the Improvement of Higher Education Personnel (CAPES).
†Email: livia.thibes@unesp.br.
‡Email: antonio.prado@inpe.br.
§Email: jeanfeg@gmail.com.

lems formed by the equations of motion and the optimal initial conditions were named quasi-critical and quasi-heliosynchronous, respectively.

During the studies described above it was verified the existence of inclinations of artificial satellites which are both quasi-critical and quasi-heliosynchronous at same time around some natural bodies of the Solar System whose ratios between oblateness and equatorial ellipcity were small. It was decided to analyze such phenomenon.

Therefore, the main goal of the current work is to present the results obtained from those analyses. The problem is modeled as a nonlinear optimization problem whose objective function is the quasi-heliosynchronous condition with an equality constraint being the quasi-critical condition and other inequality constraints inherent to the sphere of influence of the central body. The solutions are found using a barrier method that alternates between linear search and trust regions.(FRIEDLANDER, 1994; WALTZ et al., 2006; LUENBERGER; YE, 2008)

Optimal initial conditions which are simultaneously quasi-critical and quasi-heliosynchrounous are found. And, therefore, optimal trajectories which are simultaneously quasi-critical and quasi-heliosynchronous around natural bodies with small ratio J_2/C_{22} are found and presented.

Keywords. Canonical perturbation theory, quasi-critical orbits, quasi-heliosynchronous orbits, nonlinear programming, space vehicle around planetary satellites.

References

ALLAN, R. R. The Critical Inclination Problem: a Simple Treatment. *Celestial Mechanics and Dynamical Astronomy*, v. 2, p. 121–122, 1970.

CARVALHO, J. P. S.; VILHENA DE MORAES, R.; PRADO, A. F. B. A. Nonsphericity of the Moon and Near Sun-Synchronous Polar Lunar Orbits. *Mathematical Problems in Engineering*, Hindawi Publishing Corporation, v. 2009, 2009.

COSTA, M. L. G. T. X. *Órbitas Quase-Críticas e Quase-Heliossíncronas em Torno de Satélites Naturais*. Dissertação (Mestrado) — Instituto Nacional de Pesquisas Espaciais, 2020.

COSTA, M. L. G. T. X. et al. Quasi-Heliosynchronous Orbits. In: *Proceedings of the 2019 AAS/AIAA Astrodynamics Specialist Conference - AAS 19-780*. Portland, ME: American Astronautical Society, 2019.

COSTA, M. L. G. T. X. et al. An Optimization Approach to Search for Quasi-Critical Inclinations for Direct and Retrograde Orbits: Applications for Artificial Satellites Around Io. *The European Physical Journal Special Topics*, v. 229, p. 1429–1440, 2020.

DE SAEDELEER, B.; HENRARD, J. Analytical Theory of an Artificial Satellite of the Moon. *Annals of the New York Academy of Sciences*, Blackwell Publishing Ltd Oxford, UK, v. 1017, n. 1, p. 434–449, 2004.

DE SAEDELEER, B.; HENRARD, J. The Combined Effect of J_2 and C_{22} on the Critical Inclination of a Lunar Orbiter. *Advances in Space Research*, v. 37, n. 1, p. 80–87, 2005.

FRIEDLANDER, A. *Elementos de Programação Não-Linear*. 1994. ⟨https://www.ime.unicamp.br/~friedlan/livro.htm⟩.

GARFINKEL, B. On the Motion of a Satellite in the Vicinity of the Critical Inclination. *The Astronomical Journal*, v. 65, p. 624, 1960.

GIACAGLIA, G. E. O.; MURPHY, J. P.; FELSENTREGER, T. L. A Semi-Analytic Theory for the Motion of a Lunar Satellite. *Celestial Mechanics and Dynamical Astronomy*, v. 3, n. 1, p. 3–66, 1970.

HANSON, J. N. Nodal Rotation for Continuous Exposure of an Earth satellite to the Sun. *American Rocket Society Journal*, v. 31, n. 5, p. 640–645, 1961.

HORI, G. I. Theory of General Perturbations with Unspecified Canonical Variables. *Publications of the Astronomical Society of Japan*, v. 18, n. 4, p. 287, 1966.

HUGHES, S. The Critical Inclination: Another Look. *Celestial Mechanics and Dynamical Astronomy*, v. 25, p. 235–266, 1981.

LUBOWE, A. G. How Critical is the Critical Inclination? *Celestial Mechanics*, Springer, v. 1, n. 1, p. 6–10, 1969.

LUENBERGER, D. G.; YE, Y. *Linear and Nonlinear Programming*. New York: Springer US, 2008. v. 116. (International Series in Operations Research and Management Science, v. 116).

MERSMAN, W. A. Critical Inclination Problem in Satellite Orbit Theory. *Celestial Mechanics*, 1962.

NIE, T.; GURFIL, P. Lunar Frozen Orbits Revisited. *Celestial Mechanics and Dynamical Astronomy*, v. 130, n. 10, p. 61, 2018.

PALACIÁN, J. Normal Forms for Perturbed Keplerian Systems. *Journal of Differential Equations*, Elsevier, v. 180, n. 2, p. 471–519, 2002.

PARK, S.-Y.; JUNKINS, J. L. Orbital Mission Analysis For a Lunar Mapping Satellite. *Journal of the Astronautical Sciences*, v. 43, n. 2, p. 207–217, 1995.

TZIRTI, S.; TSIGANIS, K.; VARVOGLIS, H. Quasi-Critical Orbits for Artificial Lunar Satellites. *Celestial Mechanics and Dynamical Astronomy*, v. 104, n. 3, p. 227–239, 2009.

WALTZ, R. A. et al. An interior algorithm for nonlinear optimization that combines line search and trust region steps. *Mathematical Programming*, v. 107, n. 3, p. 391–408, 2006.

Semi-analytical computation of center-stable and center-unstable manifolds in the geostationary belt.

Miquel Barcelona*[1], Àlex Haro†[2], and Josep-Maria Mondelo‡[1]

[1]CERES-IEEC & Departament de Matemàtiques, Universitat Autònoma de Barcelona
[2]Departament de Matemàtiques i Informàtica, Universitat de Barcelona & Centre de Recerca Matemàtica, Barcelona, Spain

1 Introduction

This talk is devoted to present a methodology for the computation of center-stable and center-unstable manifolds of fixed points in Hamiltonian systems using the parameterization method. We introduce a new parameterization style that uncouples the hyperbolic part from the central one in the system of reduced equations, providing parameter space with fiber structure. The method is applied to the computation of center-stable and center-unstable manifolds of the center×center×saddle fixed points of the geostationary belt. Results are presented on the accuracy of the planar and vertical families of Lyapunov periodic orbits.

2 The model

The equations of motion at the Earth gravitational field expressed in a body-fixed coordinate frame are denoted as

$$\dot{Z} = F(Z), \tag{1}$$

for $Z = (x_1, \ldots, x_6)$ being x_1, x_2, x_3 the position of the body and x_4, x_5, x_6 its momenta. This autonomous system of differential equations is Hamiltonian with

$$H = \frac{1}{2}(x_4^2 + x_5^2 + x_6^2) + \omega(x_2 x_4 - x_1 x_5) - U(x_1, x_2, x_3),$$

where ω is the angular velocity of the Earth and U is its gravitational potential considered as an expansion of truncated spherical harmonics series of degree and order 8 [5].

*Email: mbarcelona@mat.uab.cat. Research supported by spanish grant PID2020-118281GB-C31 and the UAB PIF grant B21P0040.

†Email: alex@maia.ub.es. Research supported by spanish grants PGC2018-10 0699-B-I0 0 (MCIU-AEI-FEDER, UE), 2017 SGR 1374 (AGAUR), MSCA 734557 (EU Horizon 2020), and MDM-2014-0445 (MINECO).

‡Email: jmm@mat.uab.cat. Research supported by spanish grants MCINN-AEI PID2020-118281GB-C31 and PID2019-104851GB-I00.

P_j	x_1 (km)	x_2 (km)	x_3 (km)
P_1	10913	40696	$-0.135 \cdot 10^{-2}$
P_2	-40041	13112	$8.345 \cdot 10^{-5}$
P_3	-11083	-40650	$-0.137 \cdot 10^{-2}$
P_4	41286	-8408	$0.421 \cdot 10^{-2}$

Table 1: Positions of the fixed points of system (1).

As it is well known, system (1) presents 4 equilibrium points for which $F(P_j) = 0$, $j = 1, \ldots, 4$ [3]. Their corresponding positions are given in Table 1.

The eigenvalues of these fixed points are

$$\begin{aligned} \mathrm{Spec}DF(P_j) &= \{\pm i\alpha_1^{(j)}, \pm i\alpha_2^{(j)}, \pm i\alpha_3^{(j)}\}, \quad j = 1, 3 \\ \mathrm{Spec}DF(P_j) &= \{\pm i\omega_p^{(j)}, \pm i\omega_v^{(j)}, \pm\lambda^{(j)}\}, \quad j = 2, 4, \end{aligned} \tag{2}$$

with specific values presented in Table 2. Then, they exhibit two different linear behaviors: P_1 and P_3 are center×center×center while P_2 and P_4 are center×center×saddle. For the case of the unstable equilibrium points, the Lyapunov's Center Theorem applies for both pair of complex eigenvalues giving rise to two parametric families of periodic orbits born at the equilibrium point. Each one of these families spans a 2-dimensional manifold which is tangent to the real and imaginary part of the eigenvectors associated to each $\pm i\omega_{p,v}$ at the equilibrium point [4, 6]. For P_2 and P_4, these two families are known as the planar and vertical Lyapunov families of periodic orbits, since the eigenvectors of the two pair of complex eigenvalues have small vertical component and small planar component, respectively.

P_j	α_1	α_2	α_3
P_1	$7.30027 \cdot 10^{-5}$	$7.29972 \cdot 10^{-5}$	$9.87534 \cdot 10^{-8}$
P_3	$7.30027 \cdot 10^{-5}$	$7.29972 \cdot 10^{-5}$	$8.03249 \cdot 10^{-8}$
P_j	λ	ω_p	ω_v
P_2	$9.32958 \cdot 10^{-8}$	$7.29974 \cdot 10^{-5}$	$7.30027 \cdot 10^{-5}$
P_4	$8.66383 \cdot 10^{-8}$	$7.29973 \cdot 10^{-5}$	$7.30027 \cdot 10^{-5}$

Table 2: Eigenvalues of the differential of the vector field in (1) evaluated at its fixed points.

3 Parameterization method for center-unstable and center-stable manifolds

By means of the parameterization method we find invariant manifolds of these unstable fixed points. We start by diagonalizing system (1) via the change $Z = P_j + Qz$, in such a way that the new system of ODE $\dot{z} = G(z)$ has the origin as a fixed point and the differential of the vector field evaluated at the new fixed point is diagonal made by the eigenvalues of Table 2. Let us denote by $W : \mathbb{C}^d \to \mathbb{C}^6$ the parameterization of the manifold and $f : \mathbb{C}^d \to \mathbb{C}^d$, the reduced vector field for this new system, so that the differential equations for of the reduced vector field are $\dot{s} = f(s)$. So, by taking $d = 5$ and a correct ordering of the eigenvectors with the central part at the beginning, we will obtain the center-stable or the center-unstable manifolds. This is done, by solving the invariance equation

$$G(W(s)) = DW(s)f(s), \tag{3}$$

order by order for W and f expressed as power series expansions. In this way, at the coefficient level, we obtain the cohomological equations for each order k,

$$\begin{aligned}(\langle\bar{\lambda}, m\rangle - \lambda_i)W^i_m + f^i_m = R^i_m, \quad i \in \{1, \dots, d\}\\ (\langle\bar{\lambda}, m\rangle - \lambda_i)W^i_m = R^i_m, \quad i \in \{d+1, \dots, n\},\end{aligned} \tag{4}$$

where i denotes the component of the vector, $m = (m_1, \dots, m_d)$ are the exponents of each s_i satisfying that $|m| = k$, λ_i are the eigenvalues of the fixed point conveniently ordered, R is computed from all the known terms up to order $k-1$.

At each order k, in order to solve the first part of equation 4 we can either (a) take $W^i_m = 0$ and $f^i_m = R^i_m$ or (b) take $f^i_m = 0$ and $W^i_m = R^i_m/(\langle\bar{\lambda}, m\rangle - \lambda_i)$. In case (b), it is necessary to not have *inner resonances*, while to solve the second part of the cohomological equation one needs not to have *cross resonances*. A *style of parameterization* is a rule that determines the choice between (a) and (b) as a function of (i, m).

In [1] there is a rule to define parameterization styles (called *mixed* there) that allow us to compute $W(s)$ in a way that sub-manifolds of the form $\{s_{i_1} = s_{i_2} = \cdots = s_{i_J} = 0\}$ are invariant by the flow. In this work, we introduce an additional rule that allows us to uncouple the last equation of the reduced system ODE from the remaining ones, this is: if $f(s) = (f^1(s), \dots, f^d(s))$, $f^i(s)$ does not depend on s_d for $i = 1, \dots, d-1$. This is achieved by taking $f^i_m = 0$, $W^i_m = R^i_m/(\langle\bar{\lambda}, m\rangle - \lambda_i)$ if $m_d \neq 0$ for $1 \leq i \leq d-1$. In this way, parameter space can be considered a fibered space in which the base of the fibers is described by the first $d-1$ coordinates and the last one is the coordinate in each fiber.

4 Computation of Lyapunov families and error estimation

In order to give an idea of the size of the neighborhood in which the computed expansions are accurate we compute a planar and vertical families of Lyapunov orbits and perform an error estimation [2]. The computed parameterizations are obtained by means of a mixed uncoupling style in which we set $d = 4$ to obtain the center manifold and $d = 5$ to obtain the center-stable or center-unstable manifold together with the uncoupling of the last component. In the first case, we ask the submanifolds $\{s_3 = s_4 = 0\}$ and $\{s_1 = s_2 = 0\}$ to be invariant, while in the second case we need to add the condition $\{s_5 = 0\}$ to be invariant as well. In this way, thanks to the choice of the order of the eigenvectors, the planar Lyapunov family is described by orbits of the form $(s_1, s_2, 0, 0, 0)$, while the vertical one is given by $(0, 0, s_3, s_4, 0)$ in parameter space.

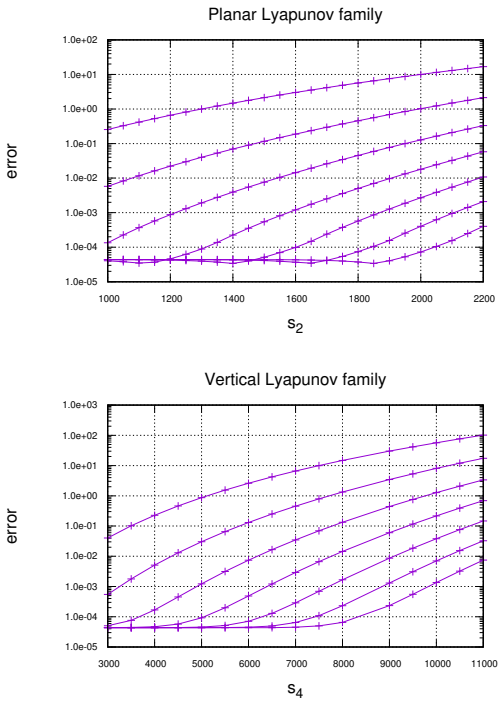

Figure 1: Errors in the orbit for different orders of the expansions and in terms of the amplitude of the planar and vertical orbits (km).

In order to quantify the accuracy of the expansions, we take the error in the orbit as a metric. This is, given an initial condition s in parameter space for any of both family of orbits, the error in the orbit is given by

$$e_O(T, s) = \sup_{t\in[0,T]} ||W(\phi_t(s)) - \Phi_t(W(s))||, \tag{5}$$

for T the period of the orbit, Φ_t the flow of the original

vector field in (1) and ϕ_t the flow of the reduced vector field.

Then, for different values of initial conditions of the form $(0, s_2, 0, 0, 0)$ and $(0, 0, 0, s_4, 0)$ that constitute initial conditions for planar and vertical Lyapunov orbits respectively, the error in the orbit is computed. This is done for different orders of the expansions and it is also compared with respect to the amplitude of the orbit for the fixed point P_2 . In Figure 1 we display the evolution of this error for different orders of the expansions $k = 4, 6, 8, 10, 12, 14, 16$ from top to bottom. It can be seen that the error increases at the same time the amplitude does, which means it is larger when the orbit reaches higher levels of energy. This behavior is more noticeable in the case of the planar family.

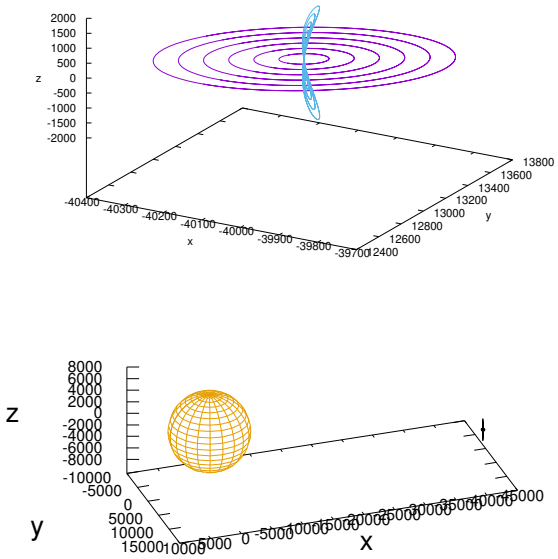

Figure 2: Representation in 3D of the family of planar and vertical orbits in original coordinates and with respect to the Earth with expansions of order 12.

Taking a fixed order $k = 12$ for the expansions, which provides an accurate approximation in a moderately large neighborhood, we display some of these orbits for both families in terms of the original coordinate frame and taking kilometers as units for the axes. This is done in Figure 2 top. Figure 2 bottom shows the position and size of these orbits with respect to the Earth.

5 Conclusions

The performed error estimation give us an idea of the degree of the accuracy of the computed expansions via parameterization method. These results are useful in order to determine for which levels of energy the parameterizations are still valid. The talk will present results not only for Lyapunov orbits but for whole isoenergetic slices of the center manifold. Computations related to the hyperbolic part will also be included.

References

[1] A. Haro, M. Canadell, J.-L. Figueras, A. Luque, and J. M. Mondelo. *The parameterization method for invariant manifolds: from rigorous results to effective computations*, volume 195 of *Applied Mathematical Sciences*. Springer, 2016.

[2] A. Haro, J.-M. Mondelo, and B. F. Villac. Dynamical characterization of 1:1 resonance crossing trajectories at Vesta. Paper AAS 12-131, 22nd AAS/AIAA Space Flight Mechanics Meeting, January 29 - February 2, Charleston, South Carolina, USA, 2012.

[3] W. M. Kaula. *Theory of satellite geodesy*. Blaisdell Pub. Co, 1966.

[4] K. R. Meyer, G. R. Hall, and D. Offin. *Introduction to Hamiltonian Dynamical Systems and the N–Body Problem*. Springer–Verlag, 2nd edition, 2009.

[5] O. Montenbruck and E. Gill. *Satellite Orbits: Models, Methods and Applications*. Springer, corr. 3rd printing edition, 2005.

[6] C. L. Siegel and J. K. Moser. *Lectures on celestial mechanics*. Classics in Mathematics. Springer-Verlag, Berlin, 1995. Translated from the German by C. I. Kalme, Reprint of the 1971 translation.

Validation of GTDS and DSST Standalone versions against precise orbit ephemerides

Paul J. Cefola*[1,3], Jacob Stratford†[2], Rosario López‡[3], and Juan Félix San-Juan§[3]

[1]Research Scientist, Department of Mechanical & Aerospace Engineering, University at Buffalo (SUNY), Amherst, NY. Also Consultant in Aerospace Systems, Spaceflight Mechanics, and Astrodynamics, Vineyard Haven, MA.

[2]Graduate student in Electrical Engineering at Brigham Young University, Provo, Utah.

[3]Scientific Computing & Technological Innovation, University of La Rioja, Logroño, La Rioja, Spain.

Abstract

GTDS [1, 2, 3, 4] has played a significant role in Space Research: as an orbit propagation (OP) and determination (OD) suite, as a prototype for subsequent operational systems, and as a platform for Astrodynamics education and research. This research includes enhancement of the physical models, development of the Draper Semi-analytical Satellite Theory (DSST) OP method [5, 6], development of DSST Weighted Least Squares and Kalman Filter OD methods [7, 9, 10], test of other analytical and semi-analytical propagators, and port to several operating systems. This effort has led to new operational orbit determination systems and standalone tools and libraries in classical programming languages such as Fortran, C/C++, and Java and interfaces with Python and Julia. Given these applications, it is essential to understand the accuracy of the GTDS physical models and the DSST algorithm in their different versions. The recent availability of independent, very precise orbit ephemerides offers new opportunities to evaluate the accuracy and the computational efficiency of the current version of GTDS and the Fortran, C/C++, and Java DSST Standalone implementations [11, 12, 13, 14]. We started the investigation by considering the Jason-2 and Lageos-2 orbits. The Jason-2 satellite is in a near circular orbit at 1330 km, and is perturbed by the geopotential, lunar-solar, and solar radiation pressure. The Lageos-2 is in a less circular orbit at 5780 km. Very precise ephemeris for both orbits is available from the NASA Crustal Dynamics Data Information System (CDDIS). Our general approach is to least-squares fit the GTDS Cowell and the GTDS DSST orbit propagators to the CDDIS orbits. For Jason-2, with a one minute spacing between the ECEF vectors and a one-day fit span, the GTDS Cowell orbit propagator fits the CDDIS data with a converged iteration position residual RMS of 1.5 meters (Figure 1). The ECEF x and y residuals (both the positions and velocities) exhibit a 12-hour signature envelop with multiple higher frequencies. The ECEF z residuals exhibit only the multiple higher frequencies. For the GTDS DSST fit, the converged iteration position residual RMS increases to 2.1 meters (Figure 2). Similar Cowell and DSST least-squares fits were conducted for the Lageos-2 case. The GTDS Cowell orbit propagator fits the CDDIS data for Lageos-2 with a converged iteration position residual RMS of 1.37 meters (Figure 3). Again, the ECEF x and y residuals exhibit a 12-hour envelop with multiple higher frequencies. The ECEF z residuals exhibit only the multiple higher frequencies. For the GTDS DSST fit, the converged iteration position residual RMS increases to 3.9 meters (Figure 4).

For the Jason-2 case, the envelops of the DSST residual plots follow the envelops for the respective Cowell residual plots. However, there are additional periodic terms in the DSST residual plots. These additional frequencies are intermediate between the high frequencies and the 12-hour terms in Figure 1.

The differences between the DSST and Cowell residuals are larger for the Lageos-2 case than for the Jason-2 case. Also, the 12-hour signature seems less obvious in some of the Lageos-2 DSST plots. This suggests that the increase in the Lageos-2 DSST residuals is connected to the treatment of the lunar-solar perturbations.

In the full paper, we plan a more detailed analysis of the differences between the DSST and Cowell residuals for each of the orbital cases.

*Email: paulcefo@buffalo.edu.
†Email: jacob.stratford00@gmail.com.
‡Email: rosario.lopez@unirioja.es.
§Email: juanfelix.sanjuan@unirioja.es.

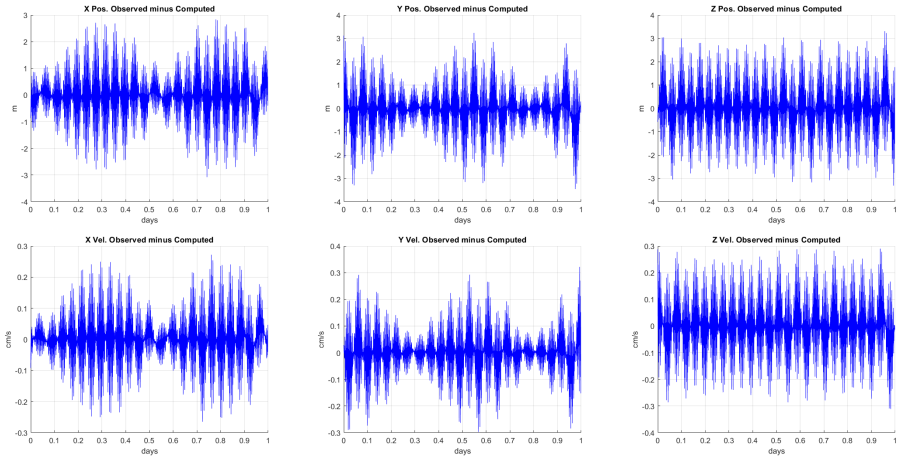

Figure 1: Jason-2 GTDS Cowell DC Converged Iteration ECEF Measurement Residuals (EGM96 50x50, Jacchia-Roberts, Lunar Solar Point Masses, SRP, SET, J2000 Integration Coordinate System) (position differences are in meters and velocity differences are in cm/sec).

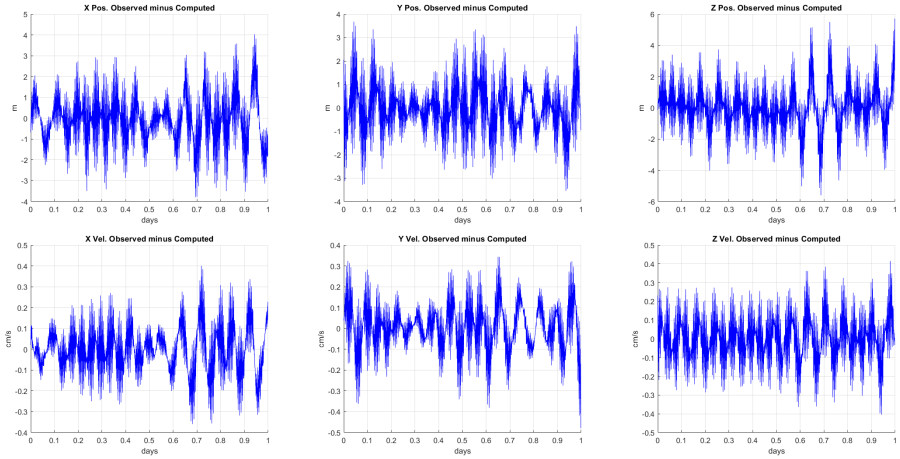

Figure 2: Jason-2 GTDS DSST DC Converged Iteration ECEF Measurement Residuals (GGM01S 50x50, Lunar Solar Point Masses, SRP, SET, J2000 Integration Coordinate System) (position differences are in meters and velocity differences are in cm/sec).

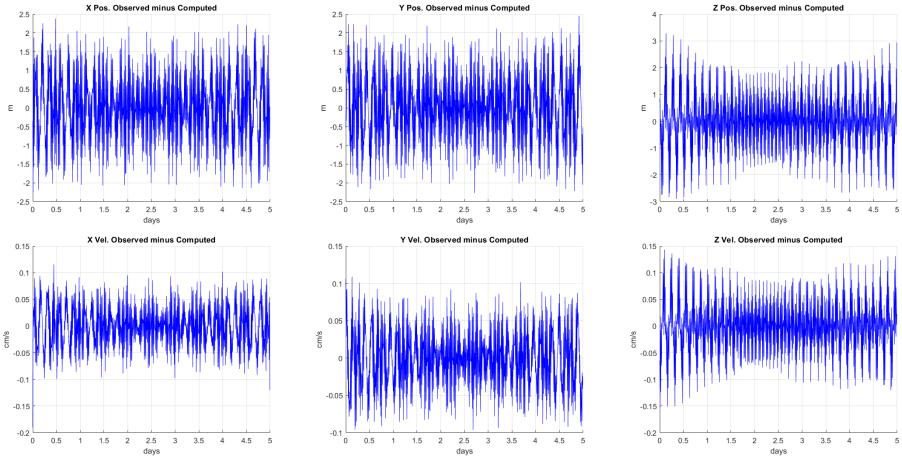

Figure 3: Lageos-2 Cowell DC Converged Iteration ECEF Measurement Residuals (EGM96 50x50, Jacchia-Roberts, Lunar Solar Point Masses, SRP, SET, J2000 Integration Coordinate System) (position differences are in meters and velocity differences are in cm/sec).

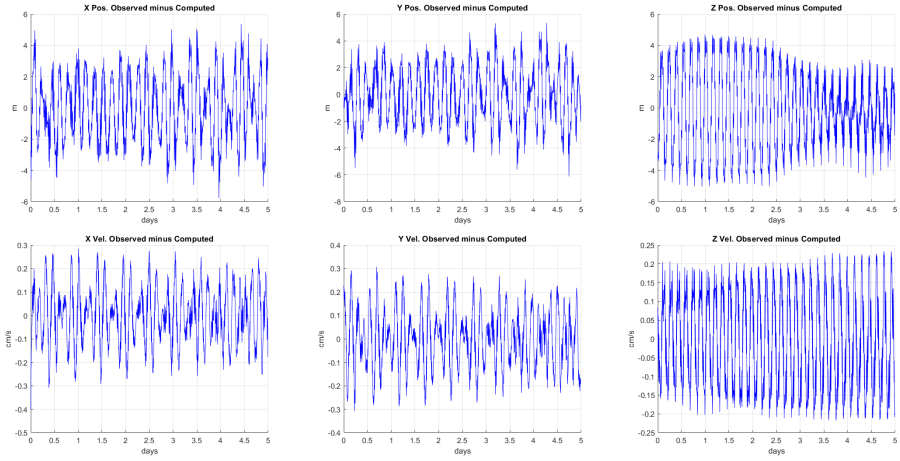

Figure 4: Lageos-2 GTDS DSST DC ECEF Measurement Residuals (GGM01S 50x50, Lunar Solar Point Masses, SRP, SET, J2000 Integration Coordinate System, DSST Short-period model: SPGRVFRC set to complete model, SRP short period motion, Short-Period J2 partials) (position differences are in meters and velocity differences are in cm/sec).

References

[1] J. O. Cappellari, A. C. Long, C. E. Velez, and A. J. Fuchs, "Goddard Trajectory Determination System (GTDS)," Goddard Space Flight Center, Tech. Rep. CSC/TR-89/6021, 1989.

[2] P. J. Cefola, "R&D GTDS semianalytical satellite theory input processor," Charles Stark Draper Laboratory, Cambridge, MA, USA, Intralab Memorandum ESD-92-582 (SGI GTDS-92-001), December 1992, (rev. 1, February 1993).

[3] J. R. Vetter, "Fifty years of orbit determination: Development of modern astrodynamics methods," *Johns Hopkins APL Technical Digest*, vol. 27, no. 3, pp. 239–252, 2007.

[4] T. Stengle and S. Hoge, "Evolution and reengineering of nasa's flight dynamics facility (fdf)," in *SpaceOps 2008 Conference*, 2008, p. 3276.

[5] J. G. Neelon, Jr., P. J. Cefola, and R. J. Proulx, "Current development of the Draper Semianalytical Satellite Theory standalone orbit propagator package," *Advances in the Astronautical Sciences*, vol. 97, pp. 2037–2052, 1998, paper AAS 97-731.

[6] Z. Folcik and P. Cefola, "Very long arc timing coefficient and solar lunar planetary ephemeris files and application," in *Proceedings 29th AAS/AIAA Space Flight Mechanics Meeting*, Ka'anapali, HI, USA, January 13-17 2019, paper AAS 19-401.

[7] Z. J. Folcik, "Orbit determination using modern filters/smoothers and continuous thrust modeling," Master's thesis, Department of Aeronautics and Astronautics, Massachusetts Institute of Technology, Cambridge, MA, USA, June 2008.

[8] P. Cefola, C. Sabol, K. Hill, and D. Nishimoto, "Demonstration of the dsst state transition matrix time-update properties using the linux gtds program," in *Advanced Maui Optical and Space Surveillance Technologies Conference*. Maui, HI, USA: Maui Economic Development Board, September 2011.

[9] S. Setty, P. J. Cefola, and J. F. San-Juan, "Space Situational Awareness capabilities of the Draper Semi-analytical Satellite Theory," in *Proceedings 6th International Conference on Astrodynamics Tools and Techniques, ICATT 2016*. Darmstadt, Germany: European Space Agency (ESA), March 2016.

[10] S. J. Setty, P. J. Cefola, O. Montenbruck, and H. Fiedler, "Application of Semi-analytical Satellite Theory orbit propagator to orbit determination for space object catalog maintenance," *Advances in Space Research*, vol. 57, no. 10, pp. 2218–2233, May 2016.

[11] P. J. Cefola, J. F. San-Juan, L. Maisonobe, P. Parraud, and R. Di Constanzo, "Semi-analytical satellite theory for the OREKIT open-source space flight dynamics library," in *Proceedings 5th International Conference on Astrodynamics Tools and Techniques, ICATT 2012*. Noordwijk, The Netherlands: European Space Agency (ESA), May-June 2012.

[12] P. J. Cefola, B. Bentley, L. Maisonobe, P. Parraud, R. Di-Constanzo, and Z. Folcik, "Verification of the Orekit Java implementation of the Draper Semi-Analytical Satellite Theory," *Advances in the Astronautical Sciences*, vol. 148, pp. 3079–3110, 2013, paper AAS 13-398.

[13] P. J. Cefola, Z. Folcik, R. Di-Costanzo, N. Bernard, S. Setty, and J. F. San-Juan, "Revisiting the DSST standalone orbit propagator," *Advances in the Astronautical Sciences*, vol. 152, pp. 2891–2914, 2014, paper AAS 14-411.

[14] J. F. San-Juan, R. López, R. Suanes, I. Pérez, S. J. Setty, and P. J. Cefola, "Migration of the DSST Standalone to C/C++," *Advances in the Astronautical Sciences*, vol. 160, pp. 2419–2437, 2017, paper AAS 17-369.

Remarks on The Super-integrability of Dynamical Systems

Vladimir Martinusi*[1]

[1]Department of Aerospace Engineering & Asher Space Research Institute,
Technion – Israel Institute of Technology

Abstract

The super-integrability plays a fundamental role in Astrodynamics, since its properties are indirectly used in canonical perturbation theory involving Lie transforms. The present work emphasizes that any integrable dynamical system (in the sense of the Liouville-Arnold theorem) is in fact maximally super-integrable. As a practical application, the complete reduction of some relevant classical dynamical systems is presented in an algebraically explicit closed-form.

1 Introduction

A Hamiltonian system with its phase space of dimension $2N$, $N \geq 1$, is said to be super-integrable [1] if it possesses n independent (in the sense of the Poisson brackets) first integrals, $n > N$, and the energy-level sets are compact. Complete integrability (in the sense of the Liouville-Arnold Theorem [2, 3]) requires only a number of integrals equal to half the dimension of the phase space (including the Hamiltonian itself). The maximal super-integrability of a dynamical system implies that it has exactly $2N-1$ independent first integrals, and therefore the Hamiltonian can be written as a function of only one momentum. Such example is the classical Kepler problem where the Hamiltonian, expressed with respect to the Delaunay variables (l, g, h, L, G, H), has the expression:

$$\mathcal{H}_K = -\frac{\mu^2}{2L^2} \tag{1}$$

The dependence of the Hamiltonian of only one momentum is of vital importance in the Lie-Deprit canonical perturbation theory [4], since it makes the homological equation

$$\{\mathcal{W}_n, \mathcal{H}_K\} = \mathcal{H}_{0,n} - \mathcal{H}_{n,0} \tag{2}$$

reducible to a simple quadrature:

$$\mathcal{W}_n = -\frac{1}{n}\int (\mathcal{H}_{0,n} - \mathcal{H}_{n,0})\,\mathrm{d}l \tag{3}$$

Because of the explicit outcome of Eq. (3), it is possible to explicitly determine each term of the Lie transform asymptotical expansion that converts the new (or primed variables) into the osculating ones, thus building an approximate solution to the non-integrable, perturbed original dynamical system.

The present work proves that any integrable dynamical system (in the sense of Liouville) is locally reducible to a maximally super-integrable dynamical system. Moreover, when the system is super-integrable (i.e. the Hamiltonian can be expressed as a function of exactly N independent first integrals), this reduction is always made by an explicit contact transformation.

2 Completely Integrable Dynamical Systems

Definition 1 *A Hamiltonian system with its phase space $\mathcal{P}$ of dimension $2N$, $N \geq 1$, is said to be completely integrable if there exist the functions $I_k : \mathcal{P} \to \mathbb{R}$, $k = 1...N-1$ such that*

$$\{I_k, I_m\} = 0,\ \{I_k, \mathcal{H}\} = 0,\ m = 1..N-1 \tag{4}$$

where $\mathcal{H}$ is the Hamiltonian.

Corollary 2 *If a Hamiltonian system is completely integrable, then there exist $N-1$ independent functionals I_k, $k = 2..N$, and two functions $r, R : \mathbb{R} \to \mathbb{R}$ such that the Hamiltonian can be expressed as:*

$$\mathcal{H} = \mathcal{H}(r, R, I_2, .., I_N) \tag{5}$$

and:

$$\begin{aligned} &\{I_k, I_m\} = 0 \quad \{I_k, \mathcal{H}\} = 0 \\ &\{r, R\} = 1 \quad\ \ \{r, I_m\} = 0 \\ &\{R, I_m\} = 0 \\ &\{r, \mathcal{H}\} = \frac{\partial \mathcal{H}}{\partial R} \quad \{R, \mathcal{H}\} = -\frac{\partial \mathcal{H}}{\partial r} \end{aligned} \tag{6}$$

where $2 \leq m \leq N$.

Corrolary 2 implies that the phase space can be reparametrized, after a canonical transformation, by the generalized coordinates r, q_k and by their conjugates R, I_k, $k = 2...N$. Assume that there exists a

*Email: vmartinusi@technion.ac.il

region of the phase space where the equation:

$$\mathcal{H}\left(r,R,I_2,..,I_N\right)=L_1 \tag{7}$$

can be solved for R_1, yielding:

$$R=F\left(r,L_1,I_2,..,I_N\right) \tag{8}$$

Denote

$$\begin{aligned}\mathbf{q} &= \left[\begin{array}{cccc} r & q_2 & ... & q_N \end{array}\right]^T\\ \mathbf{I} &= \left[\begin{array}{cccc} R & I_2 & ... & I_N \end{array}\right]^T\\ \mathbf{Q} &= \left[\begin{array}{ccc} Q_1 & ... & Q_N \end{array}\right]^T\\ \mathbf{L} &= \left[\begin{array}{ccc} L_1 & ... & L_N \end{array}\right]^T\end{aligned}$$

Consider the canonical transformation

$$(\mathbf{q},\mathbf{I})\rightarrow(\mathbf{Q},\mathbf{L})$$

generated by the function $\mathcal{W}=\mathcal{W}\left(\mathbf{q},\mathbf{L}\right)$:

$$\mathcal{W}=\int_{\rho(\mathbf{L})}^{r}F\left(s,L_1,L_2,..,L_N\right)\mathrm{d}s+\sum_{k=2}^{N}q_kL_k \tag{9}$$

such that:

$$\mathbf{Q}=\left[\frac{\partial\mathcal{W}}{\partial\mathbf{L}}\right]^T,\ \mathbf{I}=\left[\frac{\partial\mathcal{W}}{\partial\mathbf{q}}\right]^T \tag{10}$$

Here $\rho\left(\mathbf{L}\right)$ denotes one root of the equations in x :

$$F\left(x,L_1,I_2,..,I_N\right)=0$$

and we impose that this root is simple.

It follows that:

$$\begin{aligned}Q_k &= q_k+\int_{u(\mathbf{L})}^{q_1}\frac{\partial F}{\partial L_k}\left(s,L_1,L_2,..,L_N\right)\mathrm{d}s &(11)\\ I_1 &= R_1 &(12)\\ I_m &= L_m,\ 2\leq m\leq N &(13)\end{aligned}$$

Consequently, the Hamiltonian system has been reduced to its Darboux form [5], namely:

$$\mathcal{H}=L_1 \tag{14}$$

so it is maximally superintegrable, its $2N-1$ constants being $Q_2,...,Q_N$ and $L_1,...L_N$.

Theorem 3 *A completely integrable Hamiltonian system is locally maximally super-integrable.*

3 Super-Integrable Dynamical Systems

If a dynamical system with phase space of dimension N has more than N independent first integrals, then of course the Hamiltonian is one of them and the rest can be organized (after a canonical change of variables) into a subset of a set of canonical variables. The most general case is when the Hamiltonian is expressed such hat exactly N first integrals other than the Hamiltonian are emphasized, so let us assume that:

$$\mathcal{H}=\mathcal{H}\left(I_1,...I_N\right) \tag{15}$$

The constants I_k can be organized as being the conjugate momenta in a set of canonical variables $(\mathbf{q},\mathbf{I})$. Consider the canonical transformation $(\mathbf{q},\mathbf{I})\rightarrow(\mathbf{Q},\mathbf{L})$ by the function $\mathcal{W}=\mathcal{W}\left(\mathbf{Q},\mathbf{I}\right)$:

$$\mathcal{W}=Q_1\mathcal{H}\left(I_1,...I_N\right)+\sum_{k=2}^{N}Q_kI_k \tag{16}$$

It follows that:

$$\mathbf{q}=\left[\frac{\partial\mathcal{W}}{\partial\mathbf{I}}\right]^T,\ \mathbf{L}=\left[\frac{\partial\mathcal{W}}{\partial\mathbf{Q}}\right]^T \tag{17}$$

yielding:

$$\begin{aligned}\mathbf{Q} &= \mathbf{M}\mathbf{q} &(18)\\ L_m &= I_m, 2\leq m\leq N &(19)\\ L_1 &= \mathcal{H}\left(I_1,...I_N\right) &(20)\end{aligned}$$

where $\mathbf{M}$ is the inverse of the Jacobian matrix

$$\mathbf{M}=\frac{\partial\left(\mathcal{H},I_2,...I_N\right)}{\partial\left(I_1,I_2,...I_N\right)} \tag{21}$$

It follows that if a Hamiltonian system is displayed in its minimal super-integrable form (for example, the case where it has been reduced to action-angle variables), there exists an explicit canonical transformation that reduces it to its Darboux form, namely the Hamiltonian itself is one of the canonical variables. The statement that any Hamiltonian system that has been reduced to action-angle variables is maximally-super-integrable is a weaker form of **Theorem 3**.

4 Applications

4.1 Complete reduction of Brouwer's solution to the Main Problem in Artificial Satellite Theory

At second order, Brouwer's integrable approximation [6] is expressed in Delaunay elements as:

$$\mathcal{H}_2=-\frac{\mu^2}{2L^2}+J_2F_1\left(L,G,H\right)+\frac{J_2^2}{2}F_2\left(L,G,H\right) \tag{22}$$

making it suitable for the approach in presented in Section 3. In order to emphasize the Keplerian nature of the fully-reduced system, let us impose that the canonical change of variables that completely reduces the problem is generated by:

$$\mathcal{W}=Q_1\frac{\mu}{\sqrt{-2\mathcal{H}_2\left(L,G,H\right)}}+Q_2G+Q_3H \tag{23}$$

yielding:

$$\begin{aligned} G_1 &= G;\ H_1 = H && (24)\\ l_1 &= \left(-2\mathcal{H}_2\right)^{3/2}\left[\mu\partial_L\mathcal{H}_2\right]^{-1} l && (25)\\ g_1 &= g - \partial_G\mathcal{H}_2\left[\partial_L\mathcal{H}_2\right]^{-1} l && (26)\\ h_1 &= h - \partial_H\mathcal{H}_2\left[\partial_L\mathcal{H}_2\right]^{-1} l && (27)\end{aligned}$$

and the fully reduced Hamiltonian:

$$\mathcal{H}_2 = -\frac{\mu^2}{2L_1^2} \tag{28}$$

4.2 Complete Reduction of Deprit's Radial Intermediary

Consider $(r, \theta, \nu, R, \Theta, N)$ the set of canonical polar-nodal variables [7] and the second order Deprit radial intermediary [8, 9]:

$$\mathcal{H}_2 = \mathcal{H}_0 + \mathcal{H}_1 + \frac{1}{2}\mathcal{H}_2 \tag{29}$$

$$\begin{aligned} \mathcal{H}_0 &= \frac{1}{2}\left(R^2 + \frac{\Theta^2}{r^2}\right) - \frac{\mu}{r}\\ \mathcal{H}_1 &= \frac{\mu k}{2pr^2}\left(1 - 3c^2\right)\\ \mathcal{H}_2 &= \frac{3k^2}{4}\frac{\Theta^2}{p^4r^2}\left(7c^2 - \frac{1}{3}\right)\end{aligned}$$

with

$$k = \frac{J_2 r_{eq}^2}{2};\ p = \frac{\Theta^2}{\mu};\ c = \frac{N}{\Theta} \tag{30}$$

Before proceeding with the full reduction, introduce the new set of canonical variables $(r, \varphi, \upsilon, R, p, c)$, where p, c are defined in Eq. (30) and:

$$\varphi = \frac{\mu}{2\sqrt{\Theta}}\left(c\theta + \nu\right);\ \upsilon = \Theta\nu \tag{31}$$

The Hamiltonian $\mathcal{H}_2$ from Eq. (30) becomes:

$$\begin{aligned} \mathcal{H}_2 &= \frac{1}{2}\left(R^2 + \frac{\mu p}{r^2}\right) - \frac{\mu}{r} && (32)\\ &\quad + \frac{\mu k}{2pr^2}\left(1 - 3c^2\right)\\ &\quad + \frac{3k^2}{4}\frac{\mu}{p^3r^2}\left(7c^2 - \frac{1}{3}\right)\end{aligned}$$

Denote $\Delta = 1 + \partial_p F\left(p, c\right)$. The transformation:

$$\begin{aligned} \varphi_1 &= \frac{\varphi}{\Delta} && (33)\\ \upsilon_1 &= \upsilon - \frac{\varphi}{\Delta}\partial_c F\left(p, c\right) && (34)\\ p_1 &= F\left(p, c\right) && (35)\end{aligned}$$

to $(r, \varphi_1, \upsilon_1, R, p_1, c)$ is canonical, with $F\left(p, c\right)$ defined as:

$$F\left(p, c\right) = p + \frac{k}{2p}\left(1 - 3c^2\right) + \frac{3k^2}{4p^3}\left(7c^2 - \frac{1}{3}\right) \tag{36}$$

The Hamiltonian $\mathcal{H}_2$ from Eq. (32) is reduced to the Hamiltonian of a Keplerian motion:

$$\mathcal{H}_2 = \frac{1}{2}\left(R^2 + \frac{\mu p_1}{r^2}\right) - \frac{\mu}{r} \tag{37}$$

that can be, if prefered, fully reduced to the Darboux form by applying the considerations from Section 2.

5 Conclusions

It has been proved that any integrable system is maximally super-integrable, and thus reducible to the Darboux coordinates, where the Hamiltonian itself is one of the canonical variables (making time its conjugate coordinate). Two methods of reduction were presented, one when the Hamiltonian is displayed in its Liouville form (N first integrals that are in involution) or in its action-angle form (the latter producing an explicit canonical transformation to the reduced form). The result has been applied to show that, in fact, any integrable approximation in Astrodynamics is locally reducible to a classical Kepler problem.

References

[1] A. S. Mishchenko and A. T. Fomenko, "Generalized Liouville method of integration of Hamiltonian systems," *Functional Analysis and Its Applications*, vol. 12, pp. 113–121, Apr 1978.

[2] J. Liouville, "Note sur l'intégration des équations différentielles de la Dynamique, présentée au Bureau des Longitudes le 29 juin 1853.," *Journal de Mathématiques Pures et Appliquées*, pp. 137–138, 1855.

[3] V. I. Arnold, *Mathematical Methods of Classical Mechanics*. New York : Springer-Verlag, 1989.

[4] A. Deprit, "Canonical transformations depending on a small parameter," *Celestial Mechanics*, vol. 1, pp. 12–30, Mar. 1969.

[5] J. Marsden, U. Marsden, L. M. Society, J. Cassels, and N. Hitchin, *Lectures on Mechanics*. Lecture note series / London mathematical society, Cambridge University Press, 1992.

[6] D. Brouwer, "Solution of the problem of artificial satellite theory without drag," *Astronomical Journal*, vol. 64, p. 378, Nov. 1959.

[7] E. Whittaker and W. McCrae, *A Treatise on the Analytical Dynamics of Particles and Rigid Bodies*. Cambridge Mathematical Library, Cambridge University Press, 1988.

[8] A. Deprit, "The Elimination of the Parallax in Satellite Theory," *Celestial Mechanics*, vol. 24, pp. 111–153, June 1981.

[9] M. Lara, "LEO intermediary propagation as a feasible alternative to Brouwer's gravity solution," *Advances in Space Research*, vol. 56, 06 2014.

Session 3:

RESONANCES AND CHAOS

Iochroma asteroid family resonance perturbations

Alexey Rosaev*[1]

[1]Regional Scientific and Educational Mathematical Center Centre of Integrable System(150000, Sovetskaya Str. 14, Yaroslavl, Russia).

Abstract

The dynamics of very young compact asteroid cluster associated with asteroid 39991 Iochroma is studied. It is shown that Iochroma family lie between two three body resonances 3A-3J-1M and 2A-5J-3S and perturbed by both of them. It is remarkable, that one part of the family is perturbed mostly 3A-3J-1M resonance when other part by 2A-5J-3S resonance. In this paper we approximated the orbital elements of all members of Iochroma family by harmonic oscillations with different frequencies.

Based on these approximations, we have determined the position of these resonances and boundary between them.

Additionally, we report about one new member of Iochroma family: (2016 UT3).

1 Introduction

The cluster associated with asteroid 39991 Iochroma (1998 HR37) was discovered by Pravec & Vokrouhlicky (2009) [1]. The cluster consists of 5 members with relative velocity smaller than 20 m/s. The four secondaries were discovered in 20052008. We have repeated search for new orbits in vicinity Iochroma cluster by the Lowell observatory catalogue on date 15 June 2021 and have found only one new member: 2016 UT3. The values of proper elements calculated by Knezevic & Milani [2] were given from AsDys site in Table 1. The values of Lyapunov Characteristic Exponents are significantly different between 1.87 and 32.03 Myrs. It notes that orbits of clusters have different stability by some reasons, maybe due to resonances.

However, there is no detailed study of this group of minor planets up to present. Even the age of 39991 (1998 HR37) association long time had not be estimated. Only recently, Pravec et al in paper [3] give two estimations for the age of family 190^{+200}_{-100} kyrs and 140^{+130}_{-70} kyrs.

Here we report about our studying this cluster, including age estimation, important resonances search for and recent dynamical evolution.

2 Numeric integration and approximation

To study the dynamic evolution of asteroid families in this paper, the equations of the motion of the systems were numerically integrated orbits over 800 kyr using the N-body integrator Mercury and the Everhart integration method.

To the nominal resonance position calculation, we use values of semimajor axis of planets, averaged over time of integration: 1.52368 AU for Mars, 5.20259 AU for Jupiter, 9.5549 AU for Saturn always in this paper.

To study interaction considered pair with resonance and to determine position of resonance center (chaotic zone center) we apply integration of orbits of asteroid with significant values of Yarkovsky effect ($A_2 = 1 \times 10^{-13}$ and different gravitation perturbations.

In the present paper we suppose the following approximation expressions for the orbital elements by method [4]:

$$\begin{aligned} \Omega &= \Omega_0 + st + a_1 \cos s_1 t + b_1 \sin s_1 t + ... \\ \widehat{\omega} &= \widehat{\omega}_0 + gt + a_1 \cos g_1 t + b_1 \sin g_1 t + ... \end{aligned} \quad (1)$$

3 Results

In result we have obtained that Iochroma family is unique: it lies between two three-body mean motion resonances and perturbed both of them. The nearest 3-body resonance to the Iochroma family is: 3-3J-1M ($\delta = +0.00041$ AU from core of family) at 2.445415 AU (2.4454751 AU by Smirnov & Schevchenko [5]). When we use integration with only Jupiter and Mars perturbations and Yarkovsky effect we immediately

*Email: hegem@mail.ru.

Table 1: Proper elements of Iochroma family (26.20.2020)

Asteroid	g,"/yr	s,"/yr	e	a, AU	LCE
39991 Iochroma	41.9146	-46.3827	0.159164	2.44472	3.52
340225 (2006 BR54)	41.9146	-46.3823	0.159154	2.44472	3.24
349730 (2008 YV80)	41.9174	-46.3845	0.159162	2.44476	1.87
428243 (2006 YE19)	41.9192	-46.3851	0.159156	2.44479	11.26
513212 (2005 UU94)	41.9462	-46.384	0.158685	2.44528	8.07

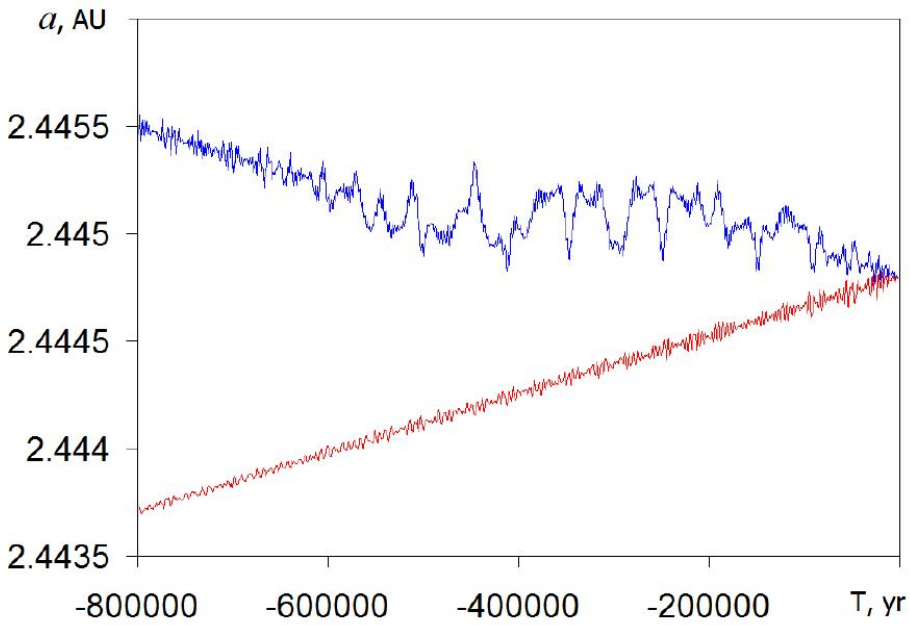

Figure 1: The semimajor axis evolution of 428243 (2006 YE19) with large Yarkovsky effect ($A_2 = 10^{13}$) Mars and Jupiter perturbations.

detect it. The chaotic zone center by numeric integration data is about 2.44502 AU (δ =+0.00039 AU from nominal position) for the 3-3J-1M resonance (Figure 1). The nearest (and most perturbed) to the resonance asteroids are (428243) 2006 YE19 and (513212) 2005 UU94. But when we use only Jupiter and Saturn perturbations and Yarkovsky effect, we detect perturbations with center about 2.44450 AU. Most probably, it is 2-5J-3S resonance with nominal position at 2.445661 AU (2.445333 AU by Smirnov & Schevchenko [5]) (δ=-0.00116 AU from nominal position).

However we note some shift of Jupiter-Saturn-asteroid resonance relative the nominal resonance position. Therefore we have the problem of the exact identification of this resonance and its interaction with 3J 1M -3A resonance and effect on Iochroma family dynamics.

Using our approximation (1) for eccentricity, we detect the resonance related perturbations and calculate the positions of the 3-3J-1M and 2-5J-3S resonances. The results are in the fine agreement with numerically detected position of resonances.

4 Conclusions

The dynamics of very young compact asteroid cluster associated with asteroid 39991 Iochroma is studied. It is shown that Iochroma family lie between two three body resonances 3A-3J-1M and 2A-5J-3S and perturbed by both of them. The interaction between close resonances can leads to their overlapping and as consequence, to arise of chaos.

References

[1] Pravec, P., Vokrouhlicky, D., Significance analysis of asteroid pairs., *Icarus* **204** (2009), 580–588.

[2] Knezevic, Z., Milani, A., Proper element catalogs and asteroid families., *Astronomy and Astrophysics* **403** (2003), 1165–1173.

[3] Pravec, P.P. et al., Asteroid clusters similar to asteroid pairs., *Icarus* **304** (2018), 110–126.

[4] Rosaev A., Plavalova E., The Fourier approximation for orbital elements for the members of very young asteroid families., *PSS* **202** (2021), 105233.

[5] Smirnov E.A., Shevchenko I.I., Massive identification of asteroids in three-body resonances., *Icarus* **222(1)** (2013), 220–228.

A detailed dynamical model for inclination-only dependent lunisolar resonances. Effects on the "eccentricity growth" mechanism.

Edoardo Legnaro*[1] and Christos Efthymiopoulos†[2]

[1]Department of Physics, Aristotle University of Thessaloniki, Thessaloniki, 54124, Greece, , Research Center for Astronomy and Applied Mathematics, Academy of Athens, Athens, 11527, Greece.
[2]Department of Mathematics, University of Padova, Via Trieste 63, Padova, 35121, Italy

Abstract

We focus on inclination-only dependent lunisolar resonances, which shape the dynamics of a MEO object over secular time scales (i.e. several decades). Following the formalism of [4], we discuss an analytic model yielding the correct form of the separatrices of each one of the major lunisolar resonances in the "action" space (i, e) (inclination, eccentricity) for any given semi-major axis a. We then highlight how our method is able to predict and explain the main structures found numerically in Fast Lyapunov Indicator (FLI) cartography. We focus on explaining the dependence of the FLI maps from the initial phase of the argument of perigee ω and of the longitude of the ascending node Ω of the object and of the moon Ω_L. In addition, on the basis of our model we discuss the role played by the $\Omega - \Omega_L$ and the $2\Omega - \Omega_L$ resonances, which overlap with the inclination-only dependant ones as they sweep the region for increasing values of a, generating large domains of chaotic motion. Our results provide a framework useful in designing low-cost satellite deployment or space debris mitigation strategies, exploiting the natural dynamics of lunisolar resonances that increase an object's eccentricity up until it reaches a domain where friction leads to atmospheric re-entry.

1 Introduction

The work we are going to discuss is an extension on [4].

For a long time the problem of lunisolar resonances has remained quite underrated, but it gained more and more interest with the increased awareness of the threat imposed by space debris. Indeed, the possibility has been demonstrated to design low cost end-of-life (EoL) disposal strategies exploiting resonant effects that increase an object's eccentricity up until it reaches a domain where friction leads to atmospheric re-entry (see [2], [6], [3], [1] and references therein).

Our main contributions in the present work can be summarized as follows.

- We provide an analytic framework useful to understand the structure of all inclination-only dependent lunisolar resonances and to compute the correct form of their separatrices in the "action" space (i. e. the space of the elements (e, i)) (see Figure 2). Our analysis extends the one done in [4] by providing a more detailed treatment of the crossing domain of each lunisolar resonance with the $\Omega - \Omega_L$ and $2\Omega - \Omega_L$ resonances. As an example, we will provide all the details for the particular case of the $2g$ resonance. Results for all the major lunisolar resonances (the $g + h$, $2g + h$, $2g$, $2g - h$, $g - h$) are summarized in the form of tables with numerical coefficients in the appendix.

- We show the correspondence between the theoretical phase portraits at each resonance and the numerical stability maps computed by the "Fast Lyapunov Indicator" (FLI, see [5]).

- We provide quantitative estimates for the maximum eccentricity, as a function of the initial inclination, which can be reached via the "eccentricity growth" mechanism, separately for each resonance, providing also the limits in inclination within which the mechanism is active, as well as the dependence of these limits on the initial phases Ω, Ω_L. In fact, analogously to [4], we identify these limits by the values of the inclination that marks the transition of circular orbits $(e = 0)$ from stable to unstable via an analogue of the Konzai mechanism.

2 The Hamiltonian Model

Consider a MEO object under the influence of the Earth, the Moon and the Sun in an Earth-centered inertial frame. We assume circular orbits for the Moon

*Email: legnaro@academyofathes.gr
†Email: christos.efthymiopoulos@math.unipd.it
We acknowledge the support of the Marie Curie Initial Training Network Stardust-R, grant agreement Number 813644 under the H2020 research and innovation program.

and the Sun, where the longitude of the solar ascending node is constant: $\Omega_S = 0$. Since we are interested in the secular dynamics, we perform an average on the short-periodic terms.

3 Analytic Theory

The steps we follow in order to study a particular resonance are the following. Consider an inclination-only dependent lunisolar resonance $\sigma = k_1\omega + k_2\Omega$ (with $k_1 \neq 0$) located at $i_\star$. First, we look for a suitable set of coordinates to study the resonance. We do so by looking for a canonical trasformation to resonant variables J_R, J_F, u_R, u_F) where u_R is related to the resonant angle $k_1\omega + k_2\Omega$ and u_F is a fast angle. Finally, by introducing *Poincaré variables* $X = \sqrt{2J_R}\sin u_R$, $Y = \sqrt{2J_R}\cos u_R$, we arrive at a resonant form of the Hamiltonian $H(X, Y, J_F, u_F, A, \Omega_L)$. The canonical change of variables f is chosen so that H is a polynomial in the variables X and Y.

Next, in order to better understand the dynamics, we look for an integrable approximation of the Hamiltonian H. We first derive an analytic approximation for $J_F(t)$, and then to plug it inside the full Hamiltonian. By averaging over the angles we will end up with an *integrable model* of the dynamics in the variables X and Y.

4 Conclusions

This derived integrable model allows gives phase portraits (show at the bottom of Figure 2) that allow to predict the shape of FLI maps, since these show the intersection with a scanning direction given by the angle u_R with the figure-8 separatrix.

Also, the model can be used to compute the limiting values i_1 and i_2 within which circular orbits are unstable. This can be used to estimate the width in inclination of a given resonance for any semi-major axis a.

We built our integrable model assuming a single resonance. Because of this, the prediction of the separatrices is accurate far from the intersections with the $\Omega - \Omega_L$ and $2\Omega - \Omega_L$ resonances, but in any case the prediction of the width of the resonance is always quite accurate. Moreover, we have seen how our model is able to explain the dependence of the FLI maps from the phases of the angles ω, Ω and Ω_L (see Figrue 3): given a particular resonance, the combination of the angles ω and Ω gives the value of the angle u_R which defines the direction in which the integrable phase portrait is seen. Then, the initial phase of Ω_L affects the shape of the central manifold (the whole phase portrait is moved up or down) and the angle Ω defines where we are on a particular torus of the central manifold. So in this way the instability region where the central manifold becomes normally hyperbolic is shifted along the two limiting tori. Such prediction is shown on the left of Figure 1.

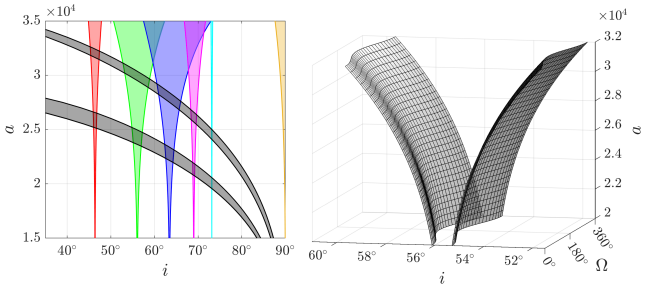

Figure 1: (Left) Theoretical amplitude of the resonances considered in this paper as a function of the altitude. The resonances are: $g + h$ (red), $2g + h$ (green), $2g$ (blue), $2g - h$ (magenta), $g - h$ (cyan), and in gray the $\Omega - \Omega_L$ (lower) and $2\Omega - \Omega_L$ (higher). (Right) Analytical 3D representation of the $2g + h$ resonance.

Acknowledgments

We acknowledge the support of the Marie Curie Initial Training Network Stardust-R, grant agreement Number 813644 under the H2020 research and innovation program: https://doi.org/10.3030/813644.

References

[1] Elisa Maria Alessi, Alessandro Rossi, GB Valsecchi, Luciano Anselmo, Carmen Pardini, Camilla Colombo, HG Lewis, Jerome Daquin, Florent Deleflie, Massimiliano Vasile, et al. Effectiveness of gnss disposal strategies. *Acta Astronautica*, 99:292–302, 2014.

[2] EM Alessi, F Deleflie, AJ Rosengren, A Rossi, GB Valsecchi, J Daquin, and K Merz. A numerical investigation on the eccentricity growth of gnss disposal orbits. *Celestial Mechanics and Dynamical Astronomy*, 125(1):71–90, 2016.

[3] Roberto Armellin and Juan F San-Juan. Optimal earth's reentry disposal of the galileo constellation. *Advances in Space Research*, 61(4):1097–1120, 2018.

[4] Jérôme Daquin, Edoardo Legnaro, Ioannis Gkolias, and Christos Efthymiopoulos. A deep dive into the $2g + h$ resonance: separatrices, manifolds and phase space structure of navigation satellites. *Celestial Mechanics and Dynamical Astronomy*, 134(1):1–31, 2022.

[5] Claude Froeschlé, Elena Lega, and Robert Gonczi. Fast lyapunov indicators. application to asteroidal motion. *Celestial Mechanics and Dynamical Astronomy*, 67(1):41–62, 1997.

[6] Despoina K Skoulidou, Aaron J Rosengren, Kleomenis Tsiganis, and George Voyatzis. Medium earth orbit dynamical survey and its use in passive debris removal. *Advances in Space Research*, 63(11):3646–3674, 2019.

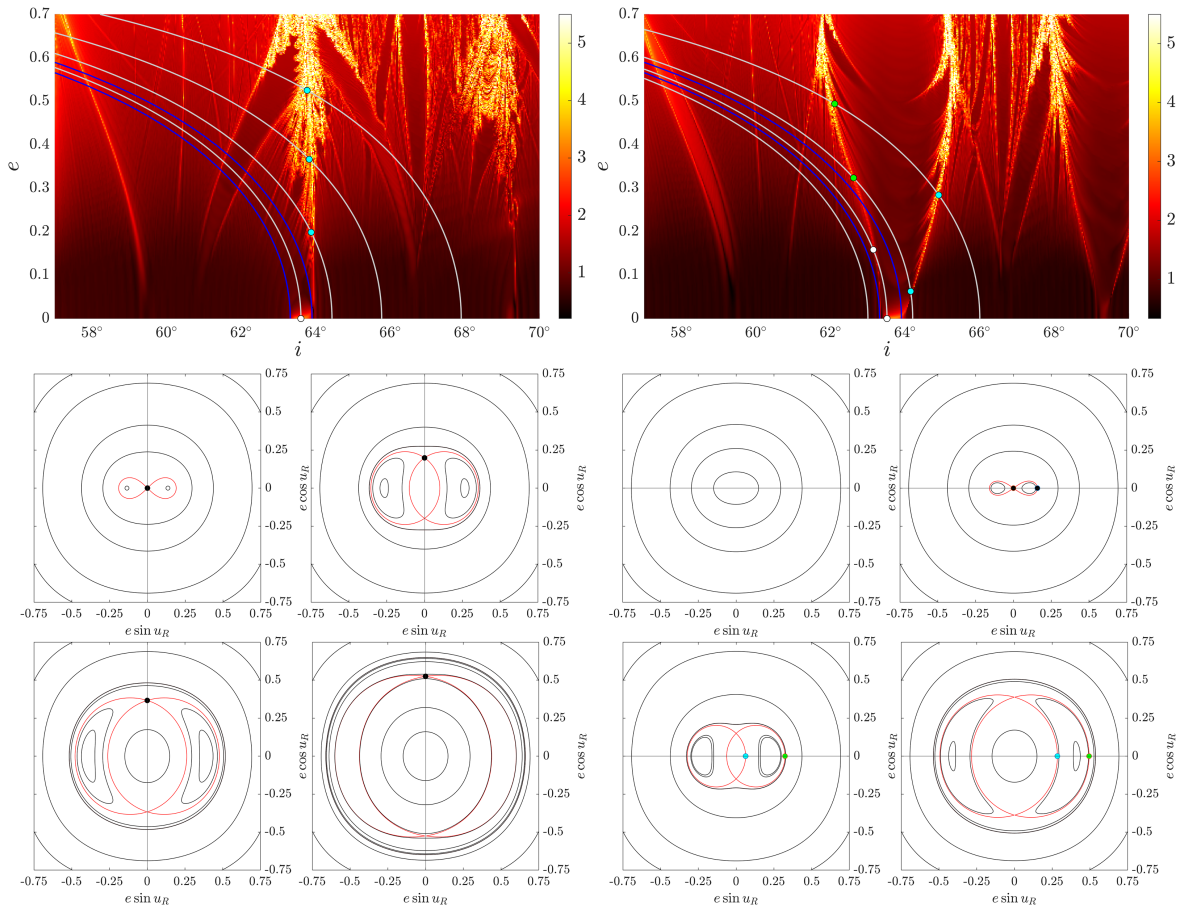

Figure 2: Analytic predictions for the vertical (left) and horizontal (right) scanning direction. Blue lines in the FLI maps correspond to the fast drift planes for i_1 and i_2.

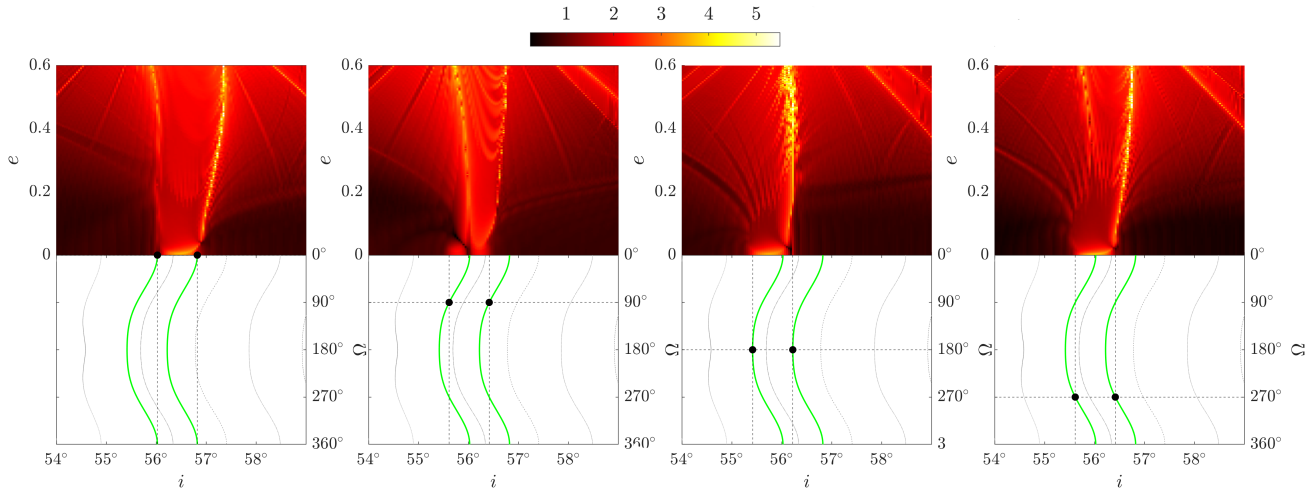

Figure 3: Analytic bounds of the hyperbolic region against an FLI map for the resonance $2g + h$ at 20000 km. The bounds are shifted along the tours for different values of Ω_0.

An Arnold diffusion mechanism for the Galileo satellites

Alexandre Pousse*[1], Mar Giralt†[2], Inmaculada Baldomá‡[2,3], Marcel Guardia§[2,3], and Elisa Maria Alessi¶[1]

[1]Istituto di Matematica Applicata e Tecnologie Informatiche, Consiglio Nazionale delle Ricerche, Milano, Italy
[2]Departament de Matemàtiques & IMTECH, Universitat Politècnica de Catalunya, Barcelona, Spain
[3]Centre de Recerca Matemàtiques, Barcelona, Spain

1 Introduction

The proliferation of space debris orbiting Earth has stimulated the investigations on their dynamical environments and, especially, on the effect of the small disturbing forces that act on their long-term dynamics (see, e.g., [1], [2]). Among them, the third-body perturbation of the Sun and the Moon generate complex resonant structures that provide non trivial behaviors and chaotic motion (see, e.g.,[3]). As a matter of fact, these resonances, together with the ones associated with the solar radiation pressure, organize the distribution of space debris for high-altitude orbits in the long term in the same way as mean-motion resonances create instabilities in the Solar system. It is enough to mention the so-called Kirkwood gaps of the Asteroid Belt, located exactly at mean-motion resonances of low order with Jupiter (see, e.g, [4]). In-depth investigations of resonances represent an effective mean to mitigate the space debris problem (see, e.g., [5]). Their understanding may provide natural mechanisms that allow to control the long-term dynamics of satellites and, therefore, manage the space traffic. In this framework, we will discuss about the dynamics of a test-particle in the $2g + h$ resonance, where g is the argument of perigee and h the longitude of the ascending node of its orbit.

The first part of the talk, sketched in Sect. 2, will be dedicated to formulate the problem and present a perturbative scheme that leads to an integrable Hamiltonian which gives a complete understanding of the resonant dynamics. Then, recalling that the Galileo constellation orbits the Earth in a small neighborhood of the $2g + h$ resonance, we will discuss about the topology of the phase space in the case of a Galileo navigation satellite (see Sect. 3). Finally, going back to the full problem, we will outline our strategy step by step in order to obtain a rigorous proof of Arnold diffusion in the considered problem (see Sect. 4). As proposed by Daquin et al.[6], this mechanism of diffusion may provide a practical application in order to manage the end-of-life of the Galileo constellation by pumping-up the eccentricity of the orbit and slowly guiding the satellites to a reentry in the Earth's atmosphere.

*Email: alexandre@mi.imati.cnr.it
†Email: mar.giralt@upc.edu
‡Email: immaculada.baldoma@upc.edu
§Email: marcel.guardia@upc.edu
¶Email: elisamaria.alessi@cnr.it

2 Modeling the problem

We consider the dynamics of a test particle whose Kepler motion around Earth is disturbed by the secular and quadrupolar approximations of the geopotential (usually known as the J_2 effect) and of the third-body perturbation due to the Moon. The Delaunay action-angle variables are introduced in order to preserve the symplectic geometry of the problem:

$$\begin{array}{lll} L = \sqrt{\mu a}, & G = L\sqrt{1-e^2}, & H = G\cos I, \\ l = M, & g = \omega, & h = \Omega, \end{array}$$

where μ is the mass parameter of the Earth and $(a, e, I, \Omega, \omega, M)$ denote respectively the semi-major axis, the eccentricity, the inclination with respect to the equatorial plane, the longitude of the node, the argument of the perigee, and the mean anomaly of the particle.

The problem is approached through the perturbation theory. For that purpose, we define the small parameter $\alpha = a/a_{\mathrm{M}}$ which characterizes the distance of the Moon (a_{M} denotes the semi-major axis of the Moon) with respect to the orbit of the satellite. In that framework, the Hamiltonian of the problem can be written

$$\mathrm{H_K}(L) + \mathrm{H_0}(L, G, H) + \alpha^3 \mathrm{H}_1^{I_{\mathrm{M}}}(L, G, H, g, h, t).$$

where $\mathrm{H_K}$ is the unperturbed Kepler motion of the particle, while $\mathrm{H_0}$ and $\mathrm{H}_1^{I_{\mathrm{M}}}$ model respectively the variations generated by the Earth's J_2 effect and by the Moon. For the sake of conciseness, the readers are referred to the paper [7] for the detailed expressions of each term. We only point out that the Moon's disturbing effect depends on time since its orbit is inclined with respect to the ecliptic ($I_{\mathrm{M}} \simeq 5^\circ$), and experiences a linear drift in the longitude of the node, with a period of about 18.6 years.

2.1 The "$2g + h$" resonance

Our work focuses on a peculiar region of the phase space for which the solutions are characterized by a resonant angle $x = 2g + h$ that oscillates around a given value. At first order, the unperturbed Hamiltonian ($\alpha = 0$), which is integrable, reveals the location of the resonance in the phase space, that is for all $G \neq 0$ and $H = G\cos I_\star$ with a critical inclination $I_\star \simeq 56.06^\circ$ in the prograde case[1]. Besides, in a small enough neighborhood of $I_\star$, the angular variables evolve at different rates, g and h being "fast" angles with respect to x which undergoes a "slow" drift in $\mathcal{O}(|I - I_\star|)$. In the full problem ($\alpha > 0$), the phase space is no more integrable, however the timescales separation still remains as long as $|I - I_\star|$ and α are small enough. A classical way to take advantage of this feature consists in introducing a suitable set of action-angle variables. We propose the symplectic transformation

$$\Upsilon : (l, L, x, y, h, \Gamma, t) \mapsto (l, L, g, G, h, H, t)$$

such as

$$y = \frac{\sqrt{\mu a}}{2}\sqrt{1-e^2}, \quad \Gamma = \frac{\sqrt{\mu a}}{2}\sqrt{1-e^2}\,(2\cos I - 1)\,,$$

in order to deal with a resonant action y that only depends on the variations of the eccentricity. Hence, the variations of the inclination are deduced from Γ.

2.2 A suitable perturbative treatment

The Hamiltonian of the full problem is time-dependent due to motion of the Moon's node with respect to the ecliptic. In order to overcome this difficulty, a first reduction is performed by considering the orbit of the Moon in the ecliptic plane, that is, for $I_\mathrm{M} = 0$, which makes the longitude of the ascending node not defined. In that framework, the full problem becomes the perturbation of an autonomous Hamiltonian by a remainder in $\mathcal{O}(\alpha^3 I_\mathrm{M})$.

The autonomous Hamiltonian has 3 degrees of freedom, with a conserved quantity L. Another reduction is possible by exploiting the timescales separation and replacing the original Hamiltonian by another one in which the fast oscillations have been removed. In other words, we perform an averaging of the autonomous Hamiltonian over the the fast angle h. According to the perturbation theory, the autonomous Hamiltonian is mapped to the averaged one added to a remainder in $\mathcal{O}(\alpha^6)$.

As a consequence, the two steps of reduction provide an averaged Hamiltonian

$$\mathrm{H_K} + \mathrm{H}_0 \circ \Upsilon + \alpha^3 \int_0^{2\pi} \mathrm{H}_1^0 \circ \Upsilon \mathrm{d}h,$$

[1]The retrograde case located in $I_\star \simeq 110.99^\circ$ will not be considered during the talk.

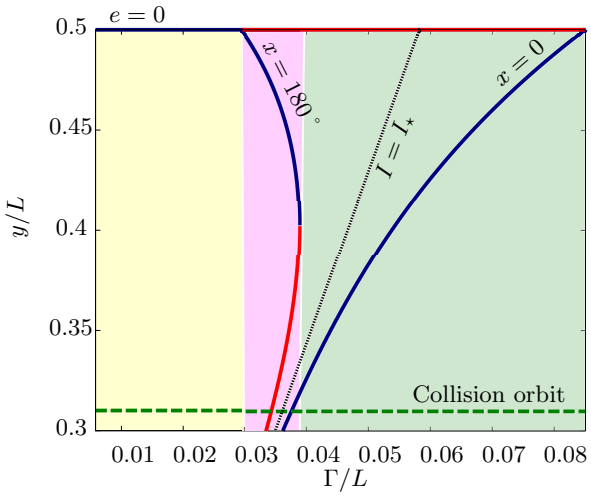

Figure 1: Location of the three families of fixed points, denoted "$e = 0$", "$x = 0$" and "$x = 180^\circ$" in the dimensionless action space $(\Gamma/L, y/L)$. Blue and red curves correspond respectively to segment of centers and saddles. Green, purple and yellow areas are associated with 3 different topologies of phase portraits.

that only depends on (L, x, y, Γ) and for which L and Γ are first integrals. Considering L and Γ as parameters, the description of the phase portrait obtained for various values of Γ allows to understand the global dynamics of the $2g + h$ resonance.

3 The resonant dynamics of a Galileo satellite

From now on, we consider a Galileo satellite that orbits Earth at $a = 29600$ km, that is, for a small parameter $\alpha = 0.077$. The explicit expressions of H_0 and H_1^0 given in [7] combined with our perturbative scheme provide a family of integrable Hamiltonian, parametrized by Γ, that can be written as follow:

$$\mathcal{H}^\Gamma(x, y) = y^{-5}(A + \alpha^3\sqrt{B}C\cos x)$$

where A, B and C are polynomial functions in (Γ, y).

For each value of Γ, the derived equations of motion allow to compute fixed points that necessarily satisfy one of the following conditions:

$$e = 0, \;\; e > 0 \text{ with } x = 0, \; e > 0 \text{ with } x = 180^\circ.$$

For each condition, a one-parameter family of fixed points is highlighted while the Hessian matrix of the Hamiltonian provides the evolution of its stability. We point out that the resonant variables (x, y), derived from the Delaunay coordinates, have an important failing, that prevents from computing the stability of the fixed points associated with the circular orbit. This difficulty is overcome with the introduction of canonical polar coordinates

$$(\xi, \eta) = \sqrt{2L - 4y}\,(\cos(x/2), \sin(x/2))$$

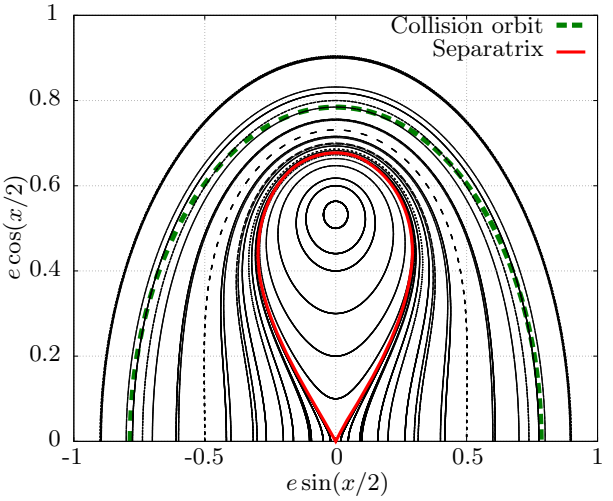

Figure 2: Phase portrait of the averaged Hamiltonian for a Galileo satellite ($\alpha = 0.077$) with $\Gamma/L = \cos I - 1/2$ and $I = 56^\circ$.

that are equivalent to $(e\cos(x/2), e\sin(x/2))$ for quasi-circular orbits.

Figure 1 depicts the location and stability of the three families of fixed points in the dimensionless action space $(\Gamma/L, y/L)$. The families "$x = 0$" and "$x = 180^\circ$" extend from either side of the critical inclination. By varying Γ, "$x = 0$" remains a center, while "$x = 180^\circ$" and "$e = 0$" bifurcate. Hence, by varying Γ, three topologies of phase portraits can be identified: a saddle and a center, respectively in $e = 0$ and $x = 0$ in the green region, two saddles and two centers, respectively in $e = 0$, $x = 180^\circ$ and $x = 0$, $x = 180^\circ$ in the purple region, and a saddle and two centers, respectively in $x = 180^\circ$, $e = 0$ and $x = 0$ in the yellow region. As a consequence, as depicted in the phase portrait of Fig. 2, for a Galileo satellite in circular orbit with $I = 56^\circ$ (green region), a small departure in eccentricity will necessarily lead to a slow increasing of the eccentricity that can reach high values, comparable to the one associated with the collision orbit with the Earth's surface ($e \simeq 0.78$). Two dynamics are possible: a resonant motion inside the separatrix with x and e that oscillate respectively around 0° and $e \simeq 0.55$ with large amplitudes, and a non-resonant motion with x that circulates.

4 A strategy to prove Arnold diffusion

Our aim is to obtain a rigorous proof of existence of a drift in actions, that may increase the eccentricity of a Galileo satellite in the full problem. A normally hyperbolic invariant manifold (NHIM), that has stable and unstable invariant manifolds will be a key tool to construct the drifting orbits.

The ideal case given by our integrable approximation of the problem provides a global understanding of the "$2g + h$" resonance. More precisely, for a fixed value of energy, the dynamics is foliated by two dimensional invariant tori with constant Γ (either resonant or non-resonant depending on the value of Γ). For each value of Γ belonging to a given non empty range $[\Gamma_-, \Gamma_+]$, the averaged Hamiltonian has a saddle in $\xi = \eta = 0$, and the union of these saddles forms a NHIM.

Going back to the non-averaged problem defined by the Hamiltonian with $I_{\rm M} = 0$, Γ is not integrable any more but the energy is still preserved. In physical terms, the eccentricity cannot increase significantly. In that framework, we will show that each saddle becomes now a hyperbolic periodic orbit implying that the considered NHIM is foliated by invariant two dimensional tori.

In the full problem given by $I_{\rm M} > 0$, the time dependence due to the motion of the Moon's node is added and the energy is not a first integral anymore. The dynamics in the NHIM will be more complicated, but expected to be $I_{\rm M}$-close to integrable (we recall that $I_{\rm M} \simeq 5^\circ$). In such a case, the homoclinic structures constructed in the previous steps will be used in order to obtain Arnold diffusion orbits. Through this strategy, we will build orbits that travel along the invariant manifolds and undergo an increase of energy corresponding to a drift in eccentricity.

References

[1] E. M. Alessi, G. Schettino, A. Rossi, G. B. Valsecchi A. Natural highways for end-of-life solutions in the LEO region. *Celest. Mech. Dyn. Astr.* **130** (2018) 34.

[2] A. J. Rosengren, D. K. Skoulidou, K. Tsiganis, G. Voyatzis, Dynamical cartography of Earth satellite orbits, *Advances in Space Research*, **63(1)** (2019) 443-460.

[3] A. J. Rosengren, E. M. Alessi, A. Rossi, and G. B. Valsecchi. Chaos in navigation satellite orbits caused by the perturbed motion of the Moon. *Monthly Notices of the Royal Astronomical Society*, **449(4)** (2015) 3522–3526.

[4] Wisdom, J. The origin of the Kirkwood gaps: a mapping for asteroidal motion near the 3/1 commensurability. *Astronom. J.*, **87** (1982) 577–593.

[5] A. Rossi, E. M. Alessi, G. Schettino, V. Schaus, G. B. Valsecchi, How an aware usage of the long-term dynamics can improve the long-term situation in the LEO region. *Acta Astronautica, 174* (2020) 159-165.

[6] J. Daquin, E. Legnaro, I. Gkolias, I., C. Efthymiopoulos. A deep dive into the $2g + h$ resonance: separatrices, manifolds and phase space structure of navigation satellites. *Celest. Mech. Dyn. Astr.*, **134** (2022) 6.

[7] A. Celletti, C. Gales, G. Pucacco, A. J. Rosengren. Analytical development of the lunisolar disturbing function and the critical inclination secular resonance. *Celest. Mech. Dyn. Astr.*, **127** (2017) 259–283.

Acknowledgements

A. P. and E. M. A. acknowledge the support of the project entitled "*Co-orbital motion and three-body regimes in the solar system*" funded by Fondazione Cariplo through the program: "*Promozione dell'attrattività e competitività dei ricercatori su strumenti dell'European Research Council—- Sottomisura rafforzamento*". I. B. has been partly supported by the Spanish MINECO–FEDER Grant PGC2018–098676–B–100 (AEI/FEDER/UE) and the Catalan grant 2017SGR1049. M. Giralt and M. Guardia have received funding from the European Research Council (ERC) under the European Union's Horizon 2020 research and innovation programme (grant agreement No. 757802). M. Guardia is also supported by the Catalan Institution for Research and Advanced Studies via an ICREA Academia Prize 2019. This work is supported by the Spanish State Research Agency, through the Severo Ochoa and María de Maeztu Program for Centers and Units of Excellence in R&D (CEX2020-001084-M).

Fourier Expansion of the J_2 Potential as a Prelude to Resonant Orbit Control Theory

Nadav Mailhot*[1] and Pini Gurfil†[1]

[1]Department of Aerospace Engineering, Technion – Israel Institute of Technology, Haifa 3200003, Israel

1 Introduction

Recently, the use of a Fourier series approximation has been successfully used to design low-thrust trajectories [1, 2]. A Fourier series representation of the thrust vector components, and their secular effect on the averaged orbital elements, has also been developed [3], finding that the averaged dynamics depend only on 14 thrust Fourier coefficients. This method has been further used in the solution of orbital targeting problems [4]. The set of 14 thrust Fourier coefficients was later reduced to a set of 6 essential coefficients, which allow for efficient control of the orbital elements [5]. Fourier decomposition of thrust has also been applied to create an artificial resonance with the orbital dynamics, yielding fuel-efficient cross-track maneuvering [6].

Further work has developed the Fourier series representation of the thrust and the resulting change in orbital elements in terms of the mean anomaly [7]. This provides some significant advantages relative to the use of the eccentric anomaly, because the mean anomaly is proportional to time, such that the Fourier series truly constitutes a spectral decomposition. Nie and Gurfil [7] introduced the concept of resonant control, which involves an artificial resonance between the control and the corresponding coefficients of the Gauss variational equations. By examining the secular change of the orbital elements through averaging, it was shown that this technique can improve fuel consumption and/or transfer time relative to previous methods.

This research aims to extend the concept of resonant control to a perturbed space environment. In the current work, we present the first step towards building a resonant control formalism under perturbations. In particular, we present a complete Fourier series expansion of the J_2 potential and the corresponding variational equations. We compare the Fourier-based expansion to exact integration and to Brouwer's solution, so as to assess the order of the Fourier series required to capture the dominant effects of the perturbation. The expansion of the J_2 perturbation into a Fourier series and the incorporation thereof into the Lagrange planetary equations constitutes an important result on its own right. In fact, this result can potentially be a generating mechanism for a new artificial satellite theory, competing with well-established theories such as Brouwer's and Kozai's theories. It is planned to use the obtained spectral decomposition in order to compare propagation of orbits to semianalytical theories. It will be examined whether the newly-developed formalism can be used for short-period and/or long-period elimination without using Hamiltonian-mechanics-based generating functions.

To incorporate the J_2 perturbation into the resonant control formalism, it must be represented as a Fourier series. This can be achieved by first developing the Fourier series in mean anomaly of the perturbing potential.

2 Approach

The perturbing potential due to the J_2 zonal harmonic is given by [8]

$$R = -\frac{\mu J_2 r_{eq}^2}{2a^3\left(1-e^2\right)^3}\left(1+e\cos f\right)^3\left(3\sin^2\left(\omega+f\right)\sin^2 i-1\right) \tag{1}$$

where r_{eq} is the mean equatorial radius. This can be expanded as

$$\begin{aligned} R &= R_0\left(C_5\cos^5 f + C_4\cos^4 f\right. && (2)\\ &+ C_3\cos^3 f + C_2\cos^2 f + C_1\cos f + C_0 && (3)\\ &+ S_4\cos^4 f\sin f + S_3\cos^3 f\sin f + S_2\cos^2 f\sin f && (4)\\ &+ \left. S_1\cos f\sin f\right) && (5)\end{aligned}$$

where

$$R_0 = -\frac{\mu J_2 r_{eq}^2}{2a^3\left(1-e^2\right)^3} \tag{6}$$

and

$$\boldsymbol{C} = \begin{bmatrix} C_0 \\ \vdots \\ C_5 \end{bmatrix} = \begin{bmatrix} 3\sin^2 i\cos^2\omega - 1 \\ 9e\sin^2 i\cos^2\omega - 3e \\ 9e^2\sin^2 i\cos^2\omega + 3\sin^2 i\left(\sin^2\omega - \cos^2\omega\right) - 3e^2 \\ 3e^3\sin^2 i\cos^2\omega + 9e\sin^2 i\left(\sin^2\omega - \cos^2\omega\right) - e^3 \\ 9e^2\sin^2 i\left(\sin^2\omega - \cos^2\omega\right) \\ 3e^3\sin^2 i\left(\sin^2\omega - \cos^2\omega\right) \end{bmatrix} \tag{7a}$$

$$\boldsymbol{S} = \begin{bmatrix} S_1 \\ \vdots \\ S_4 \end{bmatrix} = \begin{bmatrix} 6\sin^2 i\sin\omega\cos\omega \\ 18e\sin^2 i\sin\omega\cos\omega \\ 18e^2\sin^2 i\sin\omega\cos\omega \\ 6e^3\sin^2 i\sin\omega\cos\omega \end{bmatrix} \tag{7b}$$

*Email: mailhotn@campus.technion.ac.il
†Email: pgurfil@technion.ac.il

The trigonometric functions of f can all be expanded into a Fourier series in M.

To illustrate the subtlety of such expansions, we will detail herein, as an illustrative example, the expansion of $\cos^2 f$. Since $\cos^2 f$ is an even periodic function of M,

$$\cos^2 f = A_0 + \sum_{k=1}^{\infty} A_k \cos kM \tag{8}$$

The constant term is given by

$$A_0 = \frac{1}{2\pi}\int_{-\pi}^{\pi} \cos^2 f dM = \frac{1}{2\pi}\int_{-\pi}^{\pi} \frac{(\cos E - e)^2}{1 - e\cos E} dE \tag{9}$$

define the complex variable $z \triangleq e^{iE}$ so

$$dE = \frac{-i}{z} dz \tag{10a}$$

$$\cos E = \frac{1}{2}\left(z + \frac{1}{z}\right) \tag{10b}$$

$$\frac{1}{1 - e\cos E} = -\frac{2}{e}\frac{z}{(z-\alpha)(z-\beta)} \tag{10c}$$

where

$$\alpha = \frac{1+\sqrt{1-e^2}}{e}, \qquad \beta = \frac{1-\sqrt{1-e^2}}{e} \tag{11}$$

Note that $\alpha\beta = 1$ and $0 < \beta < 1 < \alpha$. Then Eq. (9) becomes

$$A_0 = \frac{1}{2\pi}\oint_C \underbrace{\frac{i}{2e}\frac{\left(z^2 - 2ez + 1\right)^2}{z^2(z-\alpha)(z-\beta)}}_{f(z)} dz \tag{12}$$

where C is the unit circle in the complex plane. The integral is evaluated using the residue theorem. The integrand has two singular points in C, $z_1 = 0$ and $z_2 = \beta$. The residues of the integrand at these points are

$$\operatorname*{Res}_{z=z_1} f(z) = \lim_{z\to 0}\left[\frac{d}{dz}\frac{i}{2e}\frac{\left(z^2 - 2ez + 1\right)^2}{(z-\alpha)(z-\beta)}\right] = -\frac{i}{2e}(4e - \beta - \alpha) \tag{13a}$$

$$\operatorname*{Res}_{z=z_2} f(z) = \lim_{z\to \beta}\left[\frac{i}{2e}\frac{\left(z^2 - 2ez + 1\right)^2}{z^2(z-\alpha)}\right] = \frac{i}{2e}\frac{\left(\beta^2 - 2e\beta + 1\right)^2}{\beta\left(\beta^2 - 1\right)} \tag{13b}$$

The constant term, Eq. (12), is then

$$\begin{aligned} &\frac{1}{2\pi} 2\pi i\left[-\frac{i}{2e}(4e - \beta - \alpha) + \frac{i}{2e}\frac{\left(\beta^2 - 2e\beta + 1\right)^2}{\beta\left(\beta^2 - 1\right)}\right] \\ = \; & -\frac{\beta\left(2e^2 - 4e\beta + \beta^2 + 1\right)}{e\left(\beta^2 - 1\right)} = 2 - \frac{1}{e^2} + \frac{\sqrt{1-e^2}\left(1 - e^2\right)}{e^2} \end{aligned} \tag{14}$$

The other terms are given by

$$A_k = \frac{1}{\pi}\int_{-\pi}^{\pi} \cos^2 f \cos kM dM = \frac{1}{\pi}\int_{-\pi}^{\pi} \frac{(\cos E - e)^2}{1 - e\cos E}\cos kM dE \tag{15}$$

Using the identity

$$\begin{aligned} &\exp(ikM) = \sum_{n=-\infty}^{\infty} J_n(-ke)\exp\left[i(n+k)E\right] \\ = \; & \sum_{n=-\infty}^{\infty} J_n(-ke) z^{n+k} \end{aligned} \tag{16}$$

and the aforementioned complex change of variables the coefficient becomes

$$\begin{aligned} A_k = \; & \frac{1}{\pi}\sum_{n=-\infty}^{\infty} J_n(-ke) \\ & \oint_C \frac{i}{2e}\frac{\left(z^4 - 4ez^3 + \left(4e^2 + 2\right)z^2 - 4ez + 1\right) z^{n+k-2}}{(z-\alpha)(z-\beta)} dz \\ = \; & \frac{1}{\pi}\sum_{n=-\infty}^{\infty} J_n(-ke)\frac{i}{2e(\alpha - \beta)} \\ & \oint_C \underbrace{\left(z^4 - 4ez^3 + \left(4e^2 + 2\right)z^2 - 4ez + 1\right) z^{n+k-2}\left(\frac{1}{z-\alpha} - \frac{1}{z-\beta}\right)}_{f(z)} dz \end{aligned} \tag{17}$$

Due to the presence of the term z^{n+k-2}, the residue cannot be evaluated as before and it must instead be obtained from the Laurent expansion. The integral part of this can be split into integrals of the form

$$\oint_C f(z) dz = \sum_{m=0}^{4} a_m \oint_C z^m z^{n+k-2}\left(\frac{1}{z-\alpha} - \frac{1}{z-\beta}\right) dz \tag{18}$$

substituting the expansions

$$\frac{1}{z-\alpha} = -\sum_{l=0}^{\infty}\left(\frac{1}{\alpha}\right)^{l+1} z^l = -\sum_{l=0}^{\infty}\beta^{l+1} z^l \tag{19a}$$

$$\frac{1}{z-\beta} = \sum_{l=0}^{\infty}\beta^l z^{-l-1} \tag{19b}$$

we arrive at the Laurent expansion

$$\begin{aligned} & z^m z^{n+k-2}\left(\frac{1}{z-\alpha} - \frac{1}{z-\beta}\right) \\ = \; & -\sum_{l=0}^{\infty}\beta^{l+1} z^{m+n+k+l-2} + \beta^l z^{m+n+k-2-l-1} \end{aligned} \tag{20}$$

The residue of this series is the coefficient for which the power of z is equal to -1.

$$\operatorname*{Res}_{z=0} = \begin{cases} -\beta^{l+1} & m+n+k+l-2 = -1 \\ -\beta^l & m+n+k-3-l = -1 \end{cases} \tag{21}$$

Solving for l and substituting results in

$$\operatorname*{Res}_{z=0} = \begin{cases} -\beta^{-m-n-k+2} & m+n+k-2 \le 0 \\ -\beta^{m+n+k-2} & m+n+k-2 \ge 0 \end{cases} = -\beta^{|m+n+k-2|} \tag{22}$$

Thus the integral part of the coefficient becomes

$$\begin{aligned}&\oint_C f(z)\,dz\\ =\;& 2\pi i\left[-\beta^{|n+k+2|}+4e\beta^{|n+k+1|}\right.\\ -\;& \left.\left(4e^2+2\right)\beta^{|n+k|}+4e\beta^{|n+k-1|}-\beta^{|n+k-2|}\right]\end{aligned} \tag{23}$$

And overall the coefficients are

$$\begin{aligned}A_k =\;& \frac{1}{2\sqrt{1-e^2}}\sum_{n=-\infty}^{\infty} J_n(-ke)\\ &\left[\beta^{|n+k+2|}-4e\beta^{|n+k+1|}+\left(4e^2+2\right)\beta^{|n+k|}\right.\\ -\;& \left.4e\beta^{|n+k-1|}+\beta^{|n+k-2|}\right]\end{aligned} \tag{24}$$

Alternatively,

$$A_k = \frac{1}{2\sqrt{1-e^2}}\sum_{n=-\infty}^{\infty} J_n(-ke)\,\boldsymbol{a}^T\boldsymbol{g} \tag{25}$$

where

$$\boldsymbol{a} = \begin{bmatrix} 1 & -4e & 4e^2+2 & -4e & 1 \end{bmatrix}^T \tag{26}$$

and

$$\begin{aligned}\boldsymbol{g} &= \begin{bmatrix} g_0 & g_1 & \cdots & g_4 \end{bmatrix}^T\\ g_j &= \beta^{|j+n+k-2|},\; j=0,1,\ldots 4\end{aligned} \tag{27}$$

The other functions of f in Eq. (5) can be obtained in a similar fashion.

References

[1] E. Taheri and O. Abdelkhalik, "Shape-based approximation of constrained low-thrust space trajectories using Fourier series," *Journal of Spacecraft and Rockets*, vol. 49, no. 3, pp. 535–545, 2012.

[2] E. Taheri and O. Abdelkhalik, "Initial three-dimensional low-thrust trajectory design," *Advances in Space Research*, vol. 57, no. 3, pp. 889–903, 2016.

[3] J. S. Hudson and D. J. Scheeres, "Reduction of low-thrust continuous controls for trajectory dynamics," *Journal of Guidance, Control, and Dynamics*, vol. 32, no. 3, pp. 780–787, 2009.

[4] J. S. Hudson and D. J. Scheeres, "Orbital targeting using reduced eccentric anomaly low-thrust coefficients," *Journal of Guidance, Control, and Dynamics*, vol. 34, no. 3, pp. 820–831, 2011.

[5] H. Chul Ko and D. J. Scheeres, "Essential thrust-Fourier-Coefficient set of averaged gauss equations for orbital mechanics," *Journal of Guidance, Control, and Dynamics*, vol. 37, no. 4, pp. 1236–1249, 2014.

[6] C. Gazzino and P. Gurfil, "Optimization of satellite orbits with resonant cross-track control," *Journal of Guidance, Control, and Dynamics*, vol. 42, no. 9, pp. 1946–1961, 2019.

[7] T. Nie and P. Gurfil, "Resonant control of satellite orbits," *Journal of Guidance, Control, and Dynamics*, vol. 44, pp. 2126–2142, aug 2021.

[8] R. H. Battin, *An introduction to the mathematics and methods of astrodynamics*. American Institute of Aeronautics and Astronautics, 1987.

Lagrangian Descriptors for global dynamics

Jérôme Daquin*[1], Rémi Pédenon-Orlanducci†[2], Makrina Agaoglou‡[3], Guillermo García-Sánchez §[3], and Ana M. Mancho ¶[3]

[1]naXys, Namur Institute of Complex Systems, Department of Mathematics, University of Namur
[2]ENSTA Paris, Institut Polytechnique de Paris
[3]Instituto de Ciencias Matemáticas, CSIC, C/Nicolás Cabrera 15, Campus Cantoblanco, 28049 Madrid, Spain

Abstract

We report on a new global dynamics indicator based on the theory of Lagrangian Descriptors. The diagnostic, valid for discrete and continuous multidimensional systems, is used for discriminating between ordered and deterministic chaotic motions. Its implementation does not require the computation of the tangent vector dynamics (no variational equations needed) and is based solely on the knowledge of orbits on finite time window. We have benchmarked the tool against several discrete and continuous models by reproducing phase portraits obtained either through iterations of the mapping or portrayed by stability maps (computed with variational indicators). The method succeeds in revealing the topology of the phase spaces, and in particular the geography and interactions among resonances in nearly-integrable settings. The indicator thus appears to be relevant for the fields of celestial mechanics, astrodynamics and dynamical astronomy.

1 Introduction

This contribution reports on the new global dynamics indicator we introduced in [1]. The indicator is apt to demarcate chaotic and ordered motions for autonomous multidimensional velocity fields and their discrete time analogue. The method is based on the theory of Lagrangian Descriptors (LDs) rooted in the study of oceanographic and geophysical flows [4].

For the sake of brevity, let us focus predominantly on the formalism related to the continuous case. We consider the differential system,

$$\dot{x} = f(x),\ x \in D \subset \mathbb{R}^n, \tag{1}$$

where the vector field $f \in C^k$, $k \geq 1$. From a general perspective, and to paraphrase [5], a Lagrangian Descriptor is a functional that considers a bounded, positive quantity that is an intrinsic geometrical or physical property of the dynamical system along a trajectory. For an initial condition $x_0 \in D$ and a final time $t > 0$, the LD associated to x_0 and t takes the form

$$\mathrm{LD}(x_0, t) = \int_{-t}^{t} (g \circ h)\big(\phi^s(x_0)\big)\, \mathrm{d}s, \tag{2}$$

where ϕ^s denotes the flow at time s supposedly defined on $\mathcal{I} = [-t, t]$. The choice of the observables g and h determines what is averaged along the trajectory. A popular choice in the literature is $h = f$ (*i.e.,* the velocity field itself) and $g(\bullet) = \|\bullet\|_2$ the Euclidean L_2-norm. Under this choice, Eq. (2) becomes

$$\mathrm{LD}(x_0, t) = \int_{-t}^{t} \|\dot{x}(s)\|_2\, \mathrm{d}s, \tag{3}$$

and represents the length of the trajectory computed over the time window[1] $[-t, t]$ and passing through x_0 at time $t = 0$. The analogue of Eq. (3) for the discrete mapping $x_{n+1} = F(x_n)$ reads

$$\mathrm{LD}(x_0, n) = \sum_{j=0}^{n-1} \sqrt{\sum_i (x_{j+1}^i - x_j^i)^2}, \tag{4}$$

where x_j^i denotes the i-th component of x at time j. In what follows, we consider time windows of the form $[0, t]$ or $[\![0, n]\!]$.

2 Regularity of the LD metric and the $\|\Delta\mathrm{LD}\|$ chaos indicator

In order to highlight the driving principles of the LD, it is instructive to consider the integrable pendulum

$$\mathcal{H}(I, \phi) = \frac{I^2}{2} - \cos\phi, \tag{5}$$

*Email: jerome.daquin@unamur.be. F.R.S.-FNRS fellow
†Email: remi.pedenon-orlanducci@ensta-paris.fr
‡Email: makrina.agaoglou@icmat.es. Juan de la Cierva Incorporación Researcher
§Email: guillermo.garcia@icmat.es
¶Email: a.m.mancho@icmat.es

[1]We refer to [7] for a geometrical and intrinsic counterpart of the temporal LD proposed in Eq. (3) developed for integrable models.

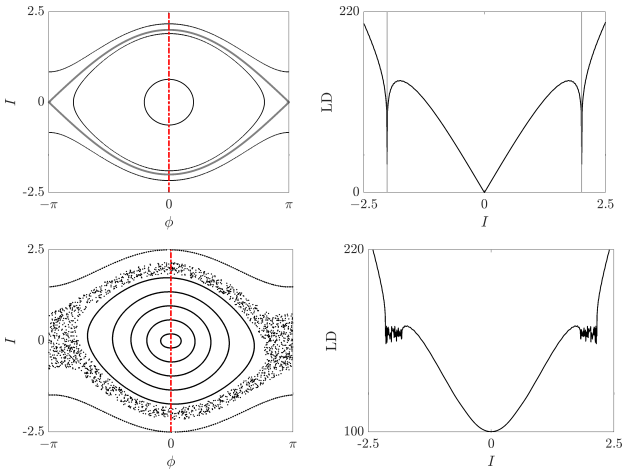

Figure 1: Phase space of $\mathcal{H}$ and $\mathcal{H}_\mu$, $\mu = 0.1$, and LD landscapes computed along the red dashed lines at $t = 100$. The LD metric becomes singular when the action crosses the separatrix (vertical gray lines) and is irregular within the hyperbolic domain.

and the periodically perturbed Hamiltonian

$$\mathcal{H}_\mu(I, \phi, t) = \frac{I^2}{2} - (1 + \mu \cos t) \cos \phi, \tag{6}$$

where $(I, \phi) \in \mathbb{R} \times \mathbb{T}$, $\mu \in \mathbb{R}$ is a parameter. When $\mu = 0$, $\mathcal{H}_\mu$ reduces to $\mathcal{H}$. The parameter μ measures the "distance" with respect to the integrable pendulum. The Fig. 1 presents the phase spaces of $\mathcal{H}$ and $\mathcal{H}_\mu$, $\mu = 0.1$, obtained respectively using the level-set method and by iterating the stroboscopic map associated to $\mathcal{H}_\mu$ (snapshots of the dynamics at every $T = 2\pi$ period). The computations of the LD landscapes encapsulate the key-point in detecting hyperbolic structures with the LD method, to know, the loss of regularity of the LD application when crossing hyperbolic structures. Besides a few simple examples where rigorous proofs have been termed (linear saddle, and rotated version of it, see [5, 3]), no general results have been established. The idea that the LD metric should be regular on regular motions, and non-differentiable on hyperbolic domains appears as an ansatz.

Nevertheless, building further on this assumption, we find convenient to introduce the norm of the Laplacian of the LD (as we work in finite dimension, norms are equilvalent. In the following, we use the L_1-norm). This scalar measures the regularity of the LD metric. Let us denote by $x = (x_1, \ldots, x_n)$ the initial condition, and let t be the final time. One introduces the quantity

$$\|\Delta\mathrm{LD}(x,t)\| = \left\| \sum_{i=1}^{n} \frac{\partial^2 \mathrm{LD}(x,t)}{\partial x_i^2} \right\| = \sum_{i=1}^{n} \left| \frac{\partial^2 \mathrm{LD}(x,t)}{\partial x_i^2} \right|.$$

We claim that $\|\Delta\mathrm{LD}\|$ is a relevant global chaos indicator.

3 Validation

The $\|\Delta\mathrm{LD}\|$ indicator has been validated against several discrete and continuous models for which stability maps, computed with a corpus of variational indicators, might be found in the literature. The models we considered in [1] include the two-dimensional standard map (SM), a 4-dimensional nearly-integrable mapping supporting a dense web of resonances, the 2 degree-of-freedom (DoF) Hénon-Heiles systems and the 3-DoF Froeschlé-Guzzo-Lega (FGL) system. For the sake of concision, we exemplify our results for the SM and the FGL Hamiltonian.

3.1 The standard map

The SM is a paradigmatic area-preserving map with a rich dynamical template [6]. The smooth map

$$(x, y) \mapsto (x', y') = f_k(x, y), \tag{7}$$

is defined on $\mathbb{T} \times \mathbb{R}$ as

$$f_k : \begin{cases} x' = x + y + F_k(x) \mod 1, \\ y' = y + F_k(x), \end{cases} \tag{8}$$

where $F_k(x) = -k \sin(2\pi x)/(2\pi)$. The map is integrable for $k = 0$, and contains resonant domains, organised in chains, as soon as $k \neq 0$. The resonant domains are related to the existence of periodic orbits, possibly unstable, and thus coming with stable and unstable manifolds. When increasing the strength of the perturbation k, the width of the various resonant domains increase and have the possibility to overlap. This produces connected chaotic paths in the phase space. We refer to [6] for omitted details.

Fig. 2 shows the phase space analysis obtained either by iterating the mapping or by computing the $\|\Delta\mathrm{LD}\|$ indicator for $k = 0.6$ and $k = 1$ over a fine mesh of initial conditions. Note that Eq. (4) is computed without the mod 1 in Eq. (8). The $\|\Delta\mathrm{LD}\|$ indicator recovers indisputably the geometry of the various "separatrices," and the fine distribution of ordered and chaotic motions.

3.2 The Froeschlé-Guzzo-Lega Hamiltonian

The FGL Hamiltonian refers to the 3-DoF Hamiltonian

$$\mathcal{H}_\epsilon = \frac{I_1^2}{2} + \frac{I_2^2}{2} + I_3 + \epsilon f(\phi_1, \phi_2, \phi_3), \tag{9}$$

where $(I, \phi) \in \mathbb{R}^3 \times \mathbb{T}^3$ and

$$f(\phi_1, \phi_2, \phi_3) = \frac{1}{(\cos\phi_1 + \cos\phi_2 + \cos\phi_3 + 4)}. \tag{10}$$

For $k = (k_1, k_2, k_3) \in \mathbb{Z}^3_\star$, the dense set of unperturbed resonances

$$k \cdot \partial_I \mathcal{H}_0 = k_1 I_2 + k_2 I_2 + k_3 = 0, \tag{11}$$

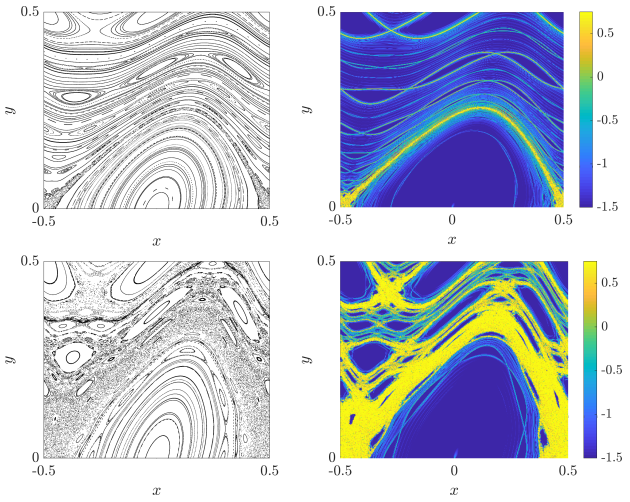

Figure 2: (Top line) Phase space of the SM for $k = 0.6$ obtained by iterating trajectories up to the final time $n = 750$ (left panel) and using the $\|\Delta LD\|$ indicator computed at $n = 150$ (right panel). (Bottom line) Same computations performed with $k = 1$.

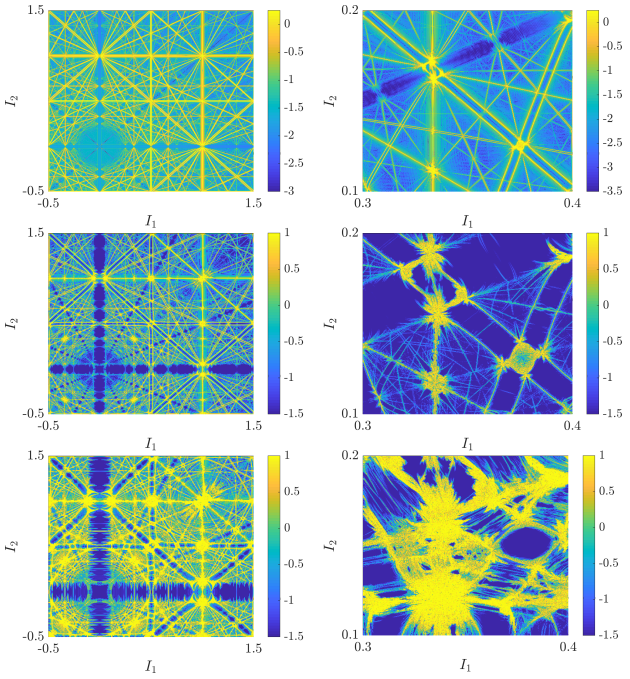

Figure 3: $\|\Delta LD\|$ stability maps at several scales associated to the FGL Hamiltonian of Eq. (9) for $\epsilon = 0.001$ (top line), $\epsilon = 0.01$ (middle line) and $\epsilon = 0.04$ (bottom line). The $\|\Delta LD\|$ indicator recovers resonant and chaotic templates.

translates as straight lines into the (I_1, I_2) action plane. Fig. 3 presents the evolution of the resonant web for increasing values of the perturbing parameters at various scales of the (I_1, I_2) plane. The computational setup (final time, choice of the sections, resolution of the mesh of initial conditions) follows strictly the seminal work of [2] for which Fast Lyapunov Indicator (FLI) maps have been computed. The agreement between the $\|\Delta LD\|$ and FLI analysis advocates for the use of $\|\Delta LD\|$ as global chaos indicator.

4 Conclusion

This contribution has introduced a new global dynamics indicator based on the Lagrangian Descriptor theory. The $\|\Delta LD\|$ indicator, derived from the Laplacian of the LDs, encapsulates the regularity of the LD metric. It is able to discriminate between ordered and chaotic motions. The tool has been benchmarked against several multidimensional discrete and continuous models. In particular, resonant and chaotic templates can be recovered through $\|\Delta LD\|$ cartography. The $\|\Delta LD\|$ indicator does not rely on the tangent vector dynamics and has thus the benefit to be free of variational equations. This property, already handy by itself, also implies a computational advantage over variational methods.

References

[1] Daquin J and Pédenon-Orlanducci, R and Agaouglou, M and García-Sánchez, G and Mancho, A M, Global dynamics based on Lagrangian Descriptors. Applications to discrete and continuous systems (2022), `in preparation`.

[2] Froeschlé, C and Guzzo, M and Lega, E, Graphical evolution of the Arnold web: from order to chaos, *Science*, **289** (2000), 2108–2110

[3] Lopesino, C and Balibrea-Iniesta, F and García-Garrido, V J and Wiggins, S and Mancho, A M, A theoretical framework for Lagrangian descriptors, *International Journal of Bifurcation and Chaos*, **27** (2017)

[4] Mendoza, C and Mancho, A M, Hidden geometry of ocean flows, *Physical review letters*, **105** (2010)

[5] Mancho, A M and Wiggins, S and Curbelo, J and Mendoza, C, Lagrangian descriptors: A method for revealing phase space structures of general time dependent dynamical systems, *Communications in Nonlinear Science and Numerical Simulation* **18** (2013), 3530–3557

[6] Meiss, JD, Symplectic maps, variational principles, and transport, *Reviews of Modern Physics*, **64** (1992), 795-848

[7] Pedenon-Orlanducci R and Carletti T and Lemaitre A and Daquin J, Geometric parametrisation of Lagrangian Descriptors for 1 degree-of-freedom systems, preprint, 2022, `arXiv:2112.05857v2`

Low energy interplanetary trajectories using multiple gravity assists

Matthew A. Werner*[1] and Shane D. Ross†[1]

[1]Aerospace and Ocean Engineering, Virginia Polytechnic Institute and State University, USA

Abstract

Much effort in recent times has been devoted to the study of low energy transport in multibody gravitational systems; despite continuing advancements in computational abilities, such studies can often be demanding or time consuming in the 3-body and 4-body settings. In this work, the Hamiltonian describing the planar circular restricted 3-body problem is rewritten for systems having small mass parameters ($\mu \ll 1$), resulting in a 2D symplectic twist map describing successive Keplerian orbits altered by close approaches with the secondary. This map, like the true dynamics, admits resonances and other invariant structures in its phase space – particularly, the map contains rotational invariant circles reminiscent of McGehee's invariant tori, adding a new quantitative description to existing chaotic zone estimates about the secondary. In absence of invariant circles barring motion, the map primarily serves as a tool for rapidly investigating naturally occurring transfers between loose orbits about each secondary in the patched 4-body problem. Any identified transfers could then be refined in the continuous system. In this work, the projection of the McGehee torus within the interior realm is identified and quantified, and a transfer from Earth to Venus is exemplified.

1 Introduction

Transfer between gravitational bodies can be well approximated by patching the corresponding 4-body problem into separate 3-body problems. In its simplest form, the system is planar and the secondaries orbit the primary in circular fashion. This provides the ability to use more widely understood and developed toolkits of the PCR3BP to analyze transfers within the 4-body problem. Particularly, some questions of interest include:

- Is a transfer possible?
- Can a transfer be found?
- Over what timescale does the transfer occur?

*Email: m.werner@vt.edu.
†Email: sdross@vt.edu.

2 A return map at apoapse and periapse

A reduced order model of the PCR3BP for mass parameters $\mu \ll 1$, where the motion of the particle is largely Keplerian about the primary, developed by Ross and Scheeres [3] is expressed

$$\underbrace{\begin{pmatrix}\omega_{n+1}\\ K_{n+1}\end{pmatrix}}_{\mathbf{x}_{n+1}} = \underbrace{\begin{pmatrix}\omega_n - 2\pi(-2K_{n+1})^{-3/2}\\ K_n + \mu f(\omega_n;\bar{a},\bar{e})\end{pmatrix}}_{\mathbf{F}(\mathbf{x}_n)}, \qquad (1)$$

where $\mathbf{x} = (\omega, K) \in S^1 \times \mathbb{R}$ are the phase space variables on the cylinder and $f : S^1 \to \mathbb{R}$ is the kick function parameterized by the elements $(\bar{a}, \bar{e}) \in \mathbb{R} \times (0, 1)$. The (approximated) Poincaré map of the restricted problem, $\mathbf{F}$, is referred to as the Keplerian map.

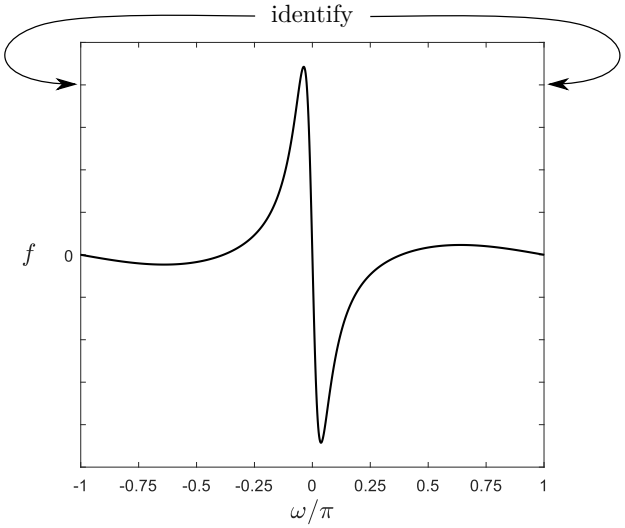

Figure 1: Generic shape of the kick function.

The map (1) captures the particle's 2-body orbital elements ω and K, respectively denoting the rotating frame's argument of periapse and Keplerian energy, using a Poincaré section at apoapse (periapse) within the interior (exterior) realm. In either case, the motion loosely shadows the manifold emanating from its corresponding libration point (i.e. L_1 (L_2) for interior (exterior) motion) and is governed by the Tisserand parameter.

$$C = \frac{1}{a} + 2\sqrt{a(1-e^2)} \qquad (2)$$

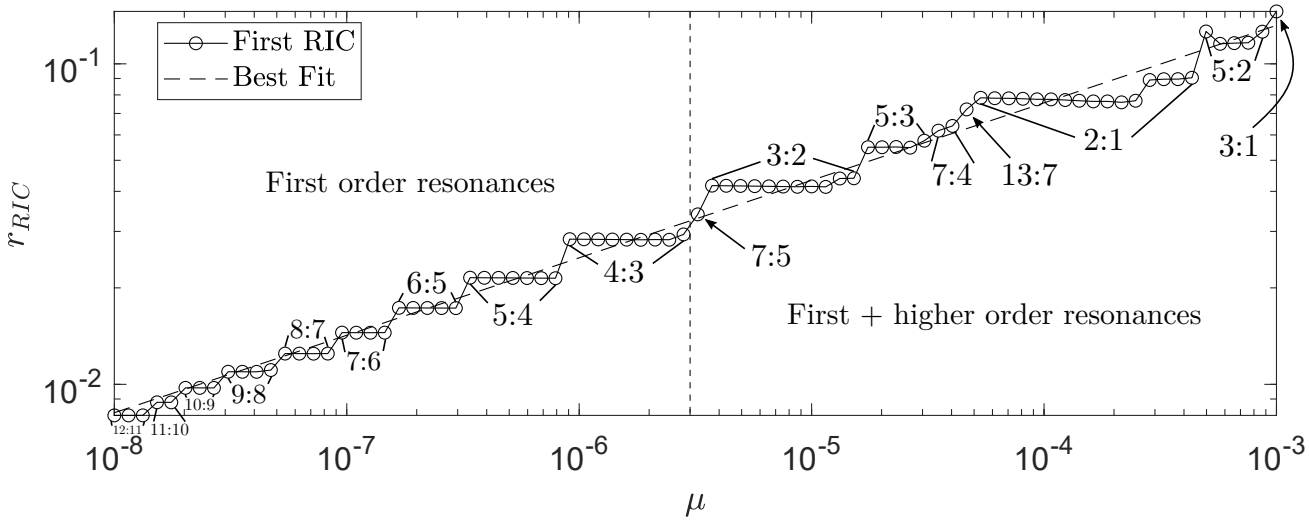

Figure 2: Growth of the chaotic zone near the secondary for a fixed Jacobi constant.

3 Boundary of chaos – rotational invariant circles

One notable property of the map is that transport becomes impossible when reduced to the 2-body problem, where $\mu = 0$ [3]. In the language of symplectic twist maps, each of these orbits $\{\mathbf{x}_n \mid n \in \mathbb{Z}\}$ for any initial angle $\omega_0 \in S^1$ and every initial energy $K_0 < 0$ forms a *rotational invariant circle* (RIC) [2]. Most of these invariant objects are destroyed when μ is increased from 0, yet some persist near the secondary.

The significance of these circles is that they are complete barriers to transport in the (ω, K) phase space, thus limiting the range that gravitational assists can transport a particle in a given 3-body system; the *nearest* circles are the invariant tori harking back to McGehee [1]. The region between the secondary and its nearest RIC defines a chaotic zone

$$r_{RIC} = 1 \pm a_{RIC}(1 \mp e_{RIC}), \tag{3}$$

where $a = -1/2K$, $e = e(a; C)$ follows from (2), and the top (bottom) sign indicates exterior (interior) motion. Likewise, the distance from the primary defining the extent of the transport from the secondary is $a_{RIC}(1 \pm e_{RIC})$.

For a fixed energy, the circles are typically found to surround first order resonances, with higher order resonances filling the gaps as the mass parameter μ varies as shown in Fig. 2. This boundary of the chaotic zone lies far beyond the sphere of influence and Hill sphere [3]; it extends the estimate of Wisdom [5] by considering the chaotic zone along the energy surface provided by the Tisserand parameter (instead of along $e = 0$).

3.1 Identifying RICs

A useful property of rotational invariant circles on the cylinder is that they form graphs [2]; that is, $a = a(\omega)$ is a smooth function of the angle ω on an RIC. To find the first circle, the phase space is searched for each μ by (pseudo)randomly picking initial conditions $\mathbf{x}_0$ increasingly distant from the secondary and testing if the resulting orbit after a sufficient number of iterates *could* be smooth. That is, the resulting orbit is neither chaotic, a librational circle, nor a cantorus.

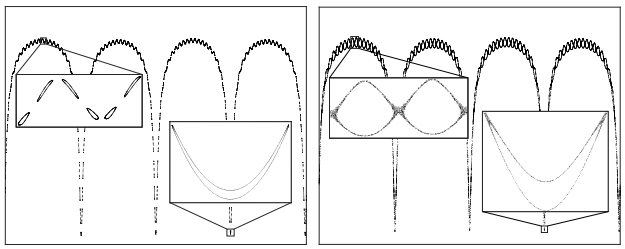

Figure 3: **Left**: A cantorus. **Right:** A chaotic orbit. Both orbits are shown in (ω, a) space and closely resemble (indeed, are near) an RIC, but cannot be RICs themselves due to multivaluedness.

Rather quickly, non-RIC orbits can be identified and eliminated by checking their arc length, amplitude, and gradient; difficulty arises when attempting to discern unresolved cantori from an RIC, though this is typically not an issue since the RIC is nearby anyways.

3.2 Possibility of a transfer

Given a fixed energy and a pair of 3-body systems, where one is normalized in the other's units such that the semimajor axes of the secondaries are 1 and A, a transfer will be possible if the corresponding RICs exist beyond the *switching orbit*; see Fig. 4. Such an orbit is given by the intersection of energy surfaces provided by the Tisserand parameter (2).

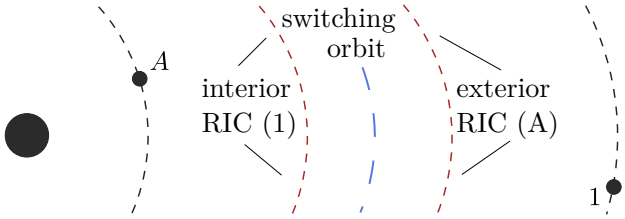

Figure 4: Configuration of RICs for possible transfer.

4 Interplanetary transfer

Transit in the phase space can be understood via lobe dynamics (or turnstiles) [3, 4]. Each lobe is a region of phase space bounded by segments of the stable and unstable manifolds of the Keplerian map's hyperbolic fixed points. For computational purposes here, such lobes have finite area and, hence, nonzero measure. Given the possibility (realized by a sufficiently large, transitable portion of phase space unimpeded by RICs), initial conditions effecting a transfer can be found by randomly sampling the phase space.

Orbits of the Keplerian map (1) are iterated starting from the initial condition $\mathbf{x}_0$ until within an ε-neighborhood of the corresponding 3-body system's libration point and switching orbit (provided that $\mathbf{x}_0$ is suitable for transport). By continuity, there exists an initial condition nearby that exactly reaches these destinations, though $\mathbf{x}_0$ typically suffices since the exact initial condition can be difficult to find.

4.1 Earth to Venus

Using an energy corresponding to the Jacobi constant (and associated Tisserand parameter) $C = 3$, which is a proxy for the energies of L_1 and L_2, a transfer between Earth and Venus is found using the method described above. In units of the Sun-Earth system (so that all distances are AU), the parameters used to define the kick functions, point of switching, etc. are found in Table 1. Note that only the semimajor axis is needed since the eccentricity is induced by (2); the reference trajectory $\bar{r}$ parameterizes the kick function with the elements $\bar{a}$ and $\bar{e}$ in accordance with (1). To renormalize in terms of the Sun-Venus system, one simply takes $a \mapsto a/A$, where $A = 0.723$ AU is the semimajor axis of Venus.

The particle's trajectory is shown in Fig. 5. In forward time, the particle departs from a loose capture around Earth represented as $W_E^u(L_1)$, the unstable manifold of L_1 into the interior realm of the Sun-Earth system. The particle repeatedly interacts with Earth until reaching the switching orbit, where it then enters (leaves) the Sun-Venus (Sun-Earth) system. Through the same means, the particle makes its approach near $W_V^s(L_2)$, the stable manifold of L_2 from the exterior realm of the Sun-Venus system.

Table 1: Earth-Venus transfer parameters

	$W_E^u(L_1)$	$\bar{r}_E$	Switch	$\bar{r}_V$	$W_V^s(L_2)$
a	0.953	0.905	0.858	0.808	0.758

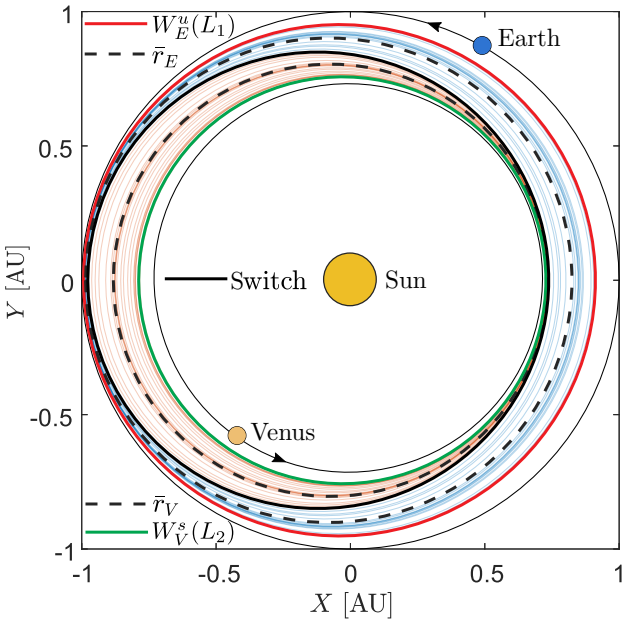

Figure 5: Earth-Venus transfer using multiple gravity assists (shown is every 50th iterate).

The time required for this transfer is 1391 years. While faster transfers may exist, such a result indicates that naturally occurring interplanetary transfer typically takes thousands of years. However, interselenial systems (i.e. between moons of a planet) often must overcome *much* less distance while retaining sizeable mass parameters; in this regard, transfer can be expected to occur on the scale of several years [3].

References

[1] R. McGehee. *Some homoclinic orbits for the restricted three-body problem.* PhD thesis, University of Wisconsin, Madison, 1969.

[2] J. Meiss. Symplectic maps, variational principles, and transport. *Reviews of Modern Physics*, 64(3):795, 1992.

[3] S. D. Ross and D. J. Scheeres. Multiple gravity assists, capture, and escape in the restricted three-body problem. *SIAM Journal on Applied Dynamical Systems*, 6 (3):576–596, 2007.

[4] S. Wiggins. *Chaotic transport in dynamical systems*, volume 2. Springer, 1992.

[5] J. Wisdom. The resonance overlap criterion and the onset of stochastic behavior in the restricted three-body problem. *The Astronomical Journal*, 85:1122–1133, 1980.

Lunar mean-motion and secular resonances

Aaron J. Rosengren*[1], Di Wu†[1], and Lamberto Dell'Elce‡[2]

[1]University of California San Diego
[2]Inria & Université Côté Azur, France

Abstract

The nonlinear astrodynamics in the cislunar space beyond the geosynchronous belt (xGEO), encompassing secular, resonant, chaotic, close-encounter, and manifold dynamics, is dramatically different than the weakly perturbed Keplerian approach used for over a half century for the detection and tracking of objects near Earth. Yet, to date, only the relatively short timescale dynamics of libration-point orbits (LPOs) and and their associated invariant manifolds have been partially coupled with the cardinal questions and problems posed by cislunar space situational awareness (SSA). Here, we uncover the foundational dynamics in the entire cislunar regime, including lunar mean-motion resonances (MMRs) and secular resonances, which have hitherto not been rigorously investigated, to holistically improve SSA capabilities beyond the traditional geocentric domains.

1 Introduction

For the investigation of the Earth's magnetosphere and the interplanetary space outside of it, satellites with orbits of high eccentricity, large semi-major axis, and multi-day period are often used . Under the influence of the Moon and the Sun, a highly eccentric orbit of a deep space probe can become nearly circular or a nearly circular orbit might become eccentric, while orbital inclination may also exhibit large shifts. For orbits where the semi-major axis is a substantial fraction of the Moon's, several orbital revolutions may be sufficient to lower the perigee height below the Earth if an unfavorable orbital configuration is chosen [1]. Among the first and perhaps the most interesting of this class of very distant, highly eccentric satellites was the Soviet space probe, Luna 3 (1959 Theta 1), which circumnavigated the Moon (passing through its sphere of influence) and returning to the Earth on a new elliptical trajectory. Luna 3 twice suffered close approaches with the Moon, and despite having an initial perigee height outside of the GEO belt, after only 11 revolutions it plummeted to Earth [2].

The Interstellar Boundary Explorer (IBEX) and the Transiting Exoplanet Survey Satellite (TESS), two modern Luna-3 like orbits, are distinguished by their high apogee distances and lunar mean-motion resonance (MMR) phasing [**?**, **?**]. IBEX (2008-051A), with its nominal mission lasting only 2 years, had to change its operational orbit for its extended mission to avoid violating altitude and eclipse mission constraints. Its nominal orbit turned out to be chaotic and unpredictable beyond 2.5 years, as a result of significant lunar perturbations, and IBEX was subsequently placed in a novel 3:1 MMR with the Moon ($P_M/3$). Following suit, TESS (2018-038A) orbits in a 2:1 lunar MMR ($P_M/2$), which was established using a lunar swing-by maneuver.

While mean-motion resonances (MMRs) (commensurabilities of orbital periods) constitute one of the most important and far-reaching aspects of dynamical astronomy, they have remained seriously underrated in Earth-satellite dynamics in part because the orbits of most traditional satellites are too low to be affected by mean-motion commensurabilities. *What are the Kirkwood gaps of cislunar space?* This question is of great current interest for mission planners now that we are locating our space-based assets, such as the IBEX and TESS, in predominant lunar MMRs that have hitherto only been treated in piecemeal. Here, we uncover the lunar mean-motion and secular resonances that significantly affect the structure of cislunar space beyond GEO and provide global maps of the principal heteroclinic connections between the various resonance regions that form the basic skeleton of dynamical transfers.

2 Numerical Investigations

The dynamical classification of trajectories can be investigated numerically using the broad family of *Lyapunov* and affiliated indicators. Many first-order stability indicators, including the fast-Lyapunov indicator (FLI) and Mean Exponential Growth factor of Nearby Orbits (MEGNO) method, are based on the propagation of the variational system and on the mon-

*Email: ajrosengren@eng.ucsd.edu. Research supported by the Air Force Office of Scientific Research, under grant agreement FA9550-21-1-0191.
†Email: d8wu@ucsd.edu.
‡Email: lamberto.dell-elce@inria.fr.

itoring of the stretching of the tangent vector with time [3]. These robust stability indicators can be used to locate the orbital resonances that significantly affect the global structure of phase space, as well as to capture and reveal space manifolds. Furthermore, these state-of-the-art tools can be used to treat both geocentric and selenocentric orbits (governed by the perturbed two-body problem) and libration-point orbits (governed by the restricted three-body problem) in a more holistic framework.

Writing the n-dimensional dynamical system in first-order autonomous form, $\dot{x} = f(x)$, where $x \in \mathbb{R}^n$ and $f : \mathbb{R}^n \to \mathbb{R}^n$ represents the vector field, the variational system in $\mathbb{R}^{2n}$ can be stated as

$$\dot{x} = f(x), \quad \dot{w} = \Big(\frac{\partial f(x)}{\partial x}\Big) w,$$

where $w \in \mathbb{R}^n$ stands for the deviation (or tangent) vector. The FLI follows from the variational system and enables the discrimination between ordered and chaotic motions.

The indicator at time t is defined by:

$$\mathrm{FLI}(x(0), t) \equiv \sup_{\tau \leq t} \log ||w(\tau)||.$$

FLI increases almost linearly with time for chaotic orbits, and approximately logarithmically for the regular motions. The MEGNO is two times the difference between the FLI and its time-average and has been adopted in the `REBOUND` software package [4], which forms the basis for these investigations. The computation of the FLI or MEGNO on two-dimensional grids of initial conditions provides a clear qualitative representation of the underlying phase-space structures.

3 Preliminary Results

As an example of how the proposed global-stability approaches can aid in mission design and analysis and cislunar SSA, consider the NASA IBEX satellite. As described earlier, IBEX's nominal orbit turned out to be chaotic and unpredictable as a result of significant lunar perturbations, and IBEX was subsequently placed in a novel resonant orbit with the Moon that is stable to this day. Figure 1 shows that an a priori analysis of the global phase space, as permitted by the FLI or MEGNO, would not only ensure that missions have predictable behaviors over the nominal (and possibly extended) scenario, thus avoiding an IBEX-like situation, but that such spacecraft can safely meet their demise through Earth reentry (without the need to make future significant orbital adjustments á la ESA's INTEGRAL mission [5]).

The precarious state of IBEX's nominal operational orbit, perched on the threshold of chaos, is clearly revealed by Figure 1 (*top panel*). A full understanding of the nature and consequences of the chaos in

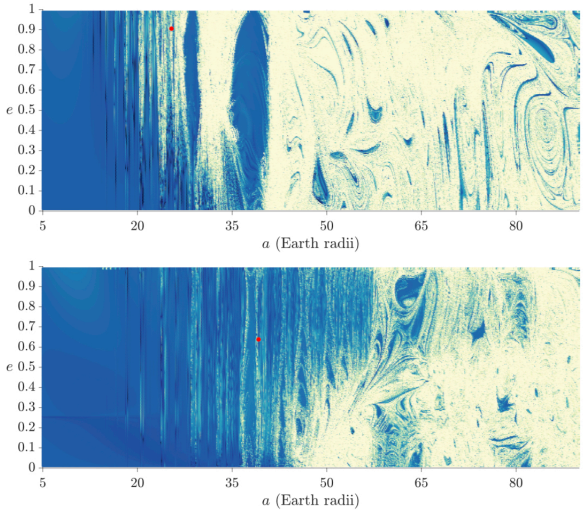

Figure 1: MEGNO maps of the entire cislunar region beyond MEO, adopting a dynamical model in `REBOUND` that contains the Sun and Moon as perturbers. The map samples over a dense grid of initial values of (a, e), where the initial inclination i, argument of perihelion ω, longitude of ascending node Ω, and mean anomaly M are set equal to that of the orbits of IBEX (*top*) and TESS (*bottom*). Stable orbits appear with a *darker* color, while *lighter* regions correspond to chaotic orbits. The locations of IBEX and TESS are given by the *red dot*. The phase space region near the Moon is highly chaotic.

these environments would have certainly helped in the early design phases of the mission. Such knowledge was partially used in the design of TESS's orbit [6], located in Figure 1 (*bottom panel*) in a narrow strip of stability; however, there remain many unresolved issues with our understanding of lunar MMRs, for which the numerical and theoretical underpinnings of this work will help needed shed light on.

4 Concluding Remarks

A many-sided and detailed investigation of the resonant structure of xGEO space, aside from its own particular significance, is of prime importance for SSA beyond GEO as such resonances significantly affect the global structure of orbital phase space. Furthermore, the manifolds emanating from unstable first-order MMRs, which can enable rapid dynamical transfers, have been largely underappreciated and unexplored in the planetary-science context [7] and only recently investigated in the astrodynamics of icy-world missions [8]. These voids in fundamental knowledge is a central motivation of this work.

References

[1] A.J. Rosengren, H. Namazyfard, G.E.O. Giacaglia, Effects of higher-order multipoles of the lunar dis-

turbing potential on elongated orbits in cislunar space, *European Physics Journal Special Topics* **229** (2020), 1545–1555.

[2] D. Amato, R. Malhotra, V. Sidorenko, A.J. Rosengren, Lunar close encounters compete with the circumterrestrial Lidov–Kozai effect: The dynamical demise of Luna 3, *Celestial Mechanics and Dynamical Astronomy* **132** (2020), 35 (18 pp).

[3] Ch. Skokos, The Lyapunov Characteristic Exponents and Their Computation, *Lecture Notes in Physics* **790** (2010), 63–135.

[4] H. Rein, D.M. Hernandez, D. Tamayo, Hybrid symplectic integrators for planetary dynamics, *Monthly Notices of the Royal Astronomical Society* **485** (2019), 5490–5497.

[5] R. Armellin, J.F. San-Juan, M. Lara, End-of-Life Disposal of High Elliptical Orbit Missions: The Case of INTEGRAL, *Advances in Space Research* **56** (2015), 479–493.

[6] G.R. Ricker, J. N. Winn, R. Vanderspek, et. al., Transiting Exoplanet Survey Satellite, *Journal of Astronomical Telescopes, Instruments, and Systems* **1** (2015), 014003 (10 pp.).

[7] N. Todorović, D. Wu, A.R. Rosengren, Transiting Exoplanet Survey Satellite, *Science Advances* **6** (2020), eabd1313 (7 pp.).

[8] R. L. Anderson, Tour design using resonant-orbit invariant manifolds in patched circular restricted three-body problems, *Journal of Guidance, Control, and Dynamics* **44** (2021), 106–119.

Plenary:

E.M. ALESSI

A natural perturbation treatment of the Molniya orbital behavior, based on the TLE data set

Elisa Maria Alessi*[1]

[1]Istituto di Matematica Applicata e Tecnologie Informatiche "E. Magenes", Consiglio Nazionale delle Ricerche, Via Alfonso Corti 12, 20133 Milan, Italy

Abstract

In this talk, I will summarize the main results obtained, with other collaborators, by analyzing 42 TLEs historical time series of the Molniya satellite constellation. The constellation is put in a dynamical environment so rich that it represents a perfect testbed for different numerical and analytical approaches to explain the main features of the long-term behavior (of about 40 years) in eccentricity and semi-major axis.

1 Introduction

The Molniya constellation was one of the first space constellations, if not the first one, to be put in orbit in the mid '60s. To cover the Russian territory, the orbit of the satellites was designed to satisfy these very peculiar features:

- it is a highly elliptical orbit ($a \approx 26650$ km, $e \approx 0.73$), so it is subject to the perturbation of both the atmospheric drag and the third body (Moon and Sun) gravitational attraction;
- it is semi-synchronous with a period of about 12 hours, so it is in 2:1 resonance with the period of rotation of the Earth;
- the argument of pericenter is frozen with respect to the perturbation due to the oblateness effect. This is achieved because the inclination is set at $i \approx 63.4°$, value that also corresponds to a lunisolar resonance.

In the past works [1, 2, 3, 4], we analyzed the long-term behavior in eccentricity and semi-major axis exhibited by the Two-Line Elements (TLE) datasets corresponding to 42 Molniya satellites. Here, I will describe the main dynamical features identified and the main tools used. The final aim is to look for a synergy between the pseudo-observational data and a natural perturbation approach.

In Fig. 1, we show some illustrative examples of the long-term evolution analyzed. The time series cover a timespan of about 40 years. The evolution in eccentricity (in the middle) shows a periodic behavior with different components, while the evolution in semi-major axis (on the left) can be of 4 types: if the pericenter altitude (on the right) gets lower than 250 km, then the semi-major axis experiences significant jumps; otherwise we have a periodic behavior that can change amplitude over time.

In the first part of the talk, I will explain how we characterize and rank the periodic components of the eccentricity evolution, while in the second part I will show how we can explain the intermittency phenomenon in semi-major axis (Fig. 1, bottom row).

2 Eccentricity evolution

Following [2], a numerical propagator has been set up to find out the simplest dynamical model that is able to follow the eccentricity evolution corresponding to the TLEs. The equations of motion considered account only for the oblateness effect and the lunisolar perturbations, the former averaged on the orbital period of the spacecraft, the latter also with respect to the orbital period of the third body. A hierarchy of models has been tested up to order 4. In addition, a Lomb-Scargle analysis has been performed to single out the main frequencies of the eccentricity time series. It turns out that, in the cases where the semi-major axis does not experience large variations, the eccentricity can be modeled by accounting for the periodic components corresponding to the following arguments:

1. 2ω (Moon and Sun),
2. $2\omega + \Omega$ (Moon and Sun),
3. $2\omega - \Omega$ (Moon and Sun),
4. Ω (Moon and Sun),
5. $2\omega + \Omega - \Omega_{Moon}$,

*Email: elisamaria.alessi@cnr.it. Research partially supported by Fondazione Cariplo through the program Promozione dell'attrattività e competitività dei ricercatori su strumenti dell'European Research Council - Sottomisura rafforzamento.

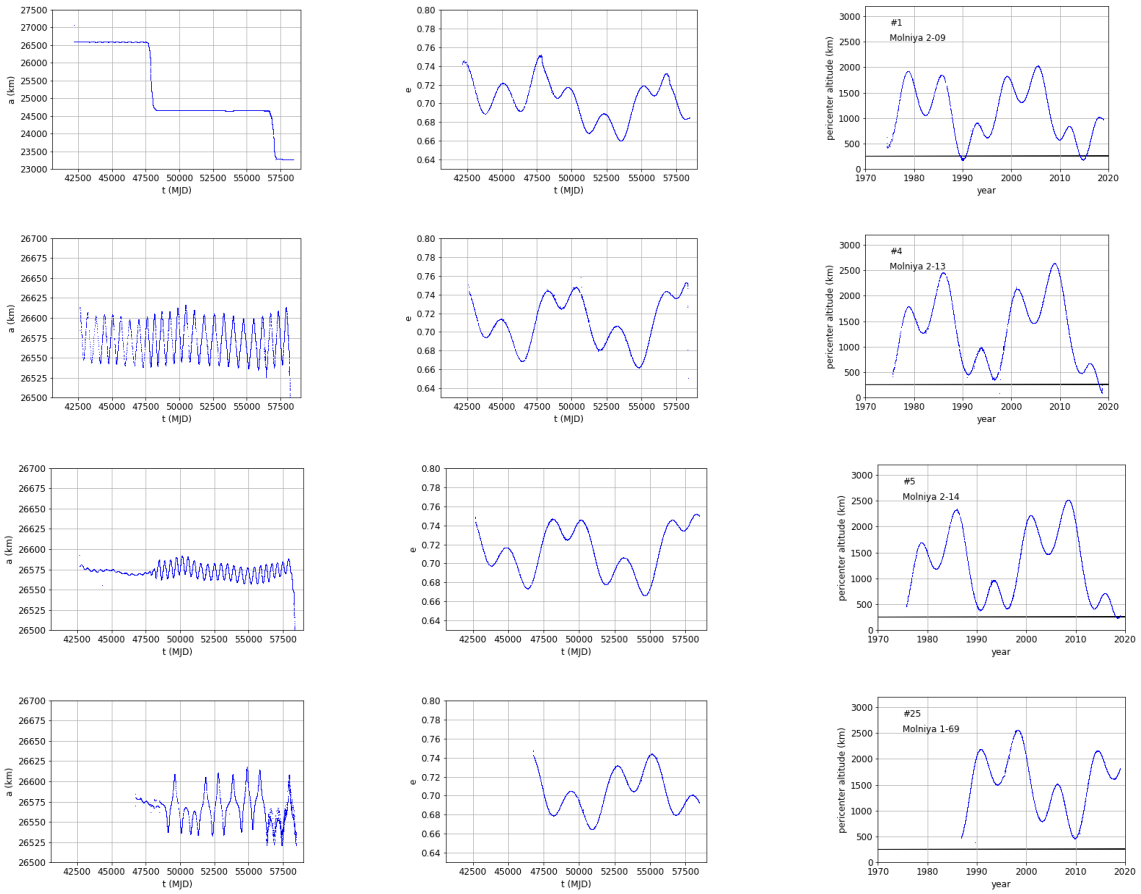

Figure 1: Behavior in semi-major axis (left), eccentricity (middle) and pericenter altitude corresponding to the TLEs analyzed. Figures from [2].

6. $\Omega - \Omega_{Moon}$,
7. $2\omega + \Omega_{Moon}$,
8. $2\omega - \Omega_{Moon}$,
9. $2\omega - \Omega + \Omega_{Moon}$.

where ω and Ω are the argument of pericenter and the longitude of the ascending node, respectively, of the orbit of the satellite taking as reference the equatorial plane, while Ω_{Moon} is the longitude of the ascending node of the Moon, taking as reference the ecliptic plane. In the timespan analyzed, the main periods detected are the ones associated with the following frequencies

- $2\dot{\omega} + \dot{\Omega}$ (about 7 years),
- $2\dot{\omega} + \dot{\Omega}_{Moon}$ (about 25 years),
- $2\dot{\omega} + \dot{\Omega} - \dot{\Omega}_{Moon}$ (about 11 years).

In [3], we have demonstrated that the above terms can be justified only by ranking the terms of the lunisolar expansion not with respect to their amplitude (i.e., the coefficient in front of the cosine term), but with respect to this amplitude and the frequency of the argument of the cosine term. In particular, if we write the Hamiltonian due to the lunisolar perturbation in a general form as

$$\mathcal{H}(G,H,g,h;L) = C_0\mathcal{A}_0(G,H;L) + \sum_{\alpha} C_\alpha \mathcal{A}_\alpha(G,H;L)\cos(\varphi_\alpha),$$

where $(G,H,g,h;L)$ are Delaunay elements, then the long-term behavior in G can be written [5], under generic assumptions of linearity for the evolution of φ_α, as

$$\Delta G = \sum_{\alpha} \frac{C_\alpha \mathcal{A}_\alpha}{\dot{\varphi}_\alpha} \frac{\partial \varphi_\alpha}{\partial g} \Big[\cos(\varphi_{\alpha,0}) - \cos(\varphi_{\alpha,T})\Big].$$

If we consider a ranking based only on $C_\alpha\mathcal{A}_\alpha$ instead on $\frac{C_\alpha\mathcal{A}_\alpha}{\dot{\varphi}_\alpha}$, we can justify only the first 5 positions in the enumeration above.

3 Semi-major axis evolution

For the semi-major axis evolution, we have focused our efforts to explain the so-called *intermittency phe-*

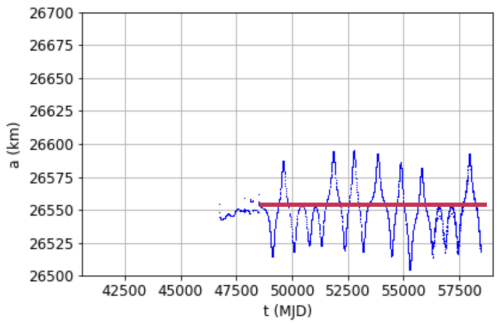

Figure 2: Intermittency phenomenon detected for some satellites for the semi-major axis evolution. Adapted from [2].

nomenon. As shown in Fig. 2, with this we mean that the upper bound of the semi-major oscillation changes. All the details of what follows are given in [4].

We have adopted a hierarchy of models accounting for the tesseral contribution, averaged over the corresponding fast variable, and the doubly-averaged lunisolar perturbation. More specifically, by considering only the oblateness effect and the first term in the tesseral expansion at order 2, we deal with an integrable model that has one elliptic and one hyperbolic equilibrium points corresponding to the Molniya semi-major axis. At the same time, other two terms in the same tesseral expansion are resonant, but the location of the equilibrium points and the width of the corresponding libration regions is such that they are contained in the main resonant domain. This means that the dynamics is not expected to exhibit large chaotic seas, but only a mild chaotic behavior in the neighborhood of the separatrices of the integrable model. This is confirmed by moving from the 1 degree-of-freedom model to a 2 degree-of-model and computing a suitable Poincaré section. The mild chaotic behavior is the responsible for the intermittency phenomenon. A satellite that moves in the vicinity of the separatrix can alternate from the libration region to the circulation region and viceversa, every time it gets close enough to the hyperbolic periodic orbit, thanks to the chaotic nature of the corresponding neighborhood.

The coupling between the tesseral perturbation and the lunisolar one is obtained by computing FLI maps for two additional dynamical models, that consider the third-body effect on the argument of pericenter and on the eccentricity (and inclination). In the former case, the perturbation is weak, while in the latter the region filled by the hyperbolic manifold turns out to be larger and more structured.

As a final confirmation, satellites Molniya 1-69 and Molniya 1-87 have been located in the FLI maps. They actually orbit in the hyperbolic tangle, as shown in Fig. 3.

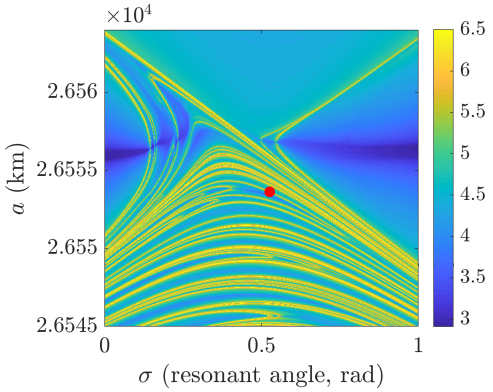

Figure 3: Location of satellite Molniya 1-69 projected into the FLI map. Courtesy of Jerome Daquin, adapted from [4].

4 Open points

The TLEs data sets offer a unique opportunity to analyze the long-term behavior of the Molniya orbits and to test different numerical and dynamical systems theory tools. What is left is to use the same data to model effectively the tesseral-lunisolar-atmospheric drag coupling and to understand the change in the oscillation that can occur in the semi-major evolution for some satellites (Fig. 1 third row on the left). Also, according to our analysis the eccentricity evolution does not show, in the timespan considered, a chaotic behavior. This seems somehow not in agreement with the KePASSA 2019 competition, but it might be explained either in relation to the semi-major axis evolution or to the initial value of the pericenter argument.

References

[1] A. Buzzoni, J. Guichard, E.M. Alessi, G. Altavilla, A. Figer, A. Carbognani, G. Tommei. Spectrophotometric and dynamical properties of the Soviet/Russian constellation of Molniya satellites, *Journal of Space Safety Engineering* 7 (2020), 255-261.

[2] E.M. Alessi, A. Buzzoni, J. Daquin, A. Carbognani, G. Tommei. Dynamical properties of the Molniya satellite constellation: long-term evolution of orbital eccentricity, *Acta Astronautica* 179 (2021), 659-669.

[3] T. Talu, E.M. Alessi, G. Tommei. On the Dominant Lunisolar Perturbations for Long-Term Eccentricity Variation: The Case of Molniya Satellite Orbits, *Universe* 7 (2021), 482.

[4] J. Daquin, E.M. Alessi, J. O' Leary, A. Lemaitre, A. Buzzoni. Dynamical properties of the Molniya satellite constellation: long-term evolution of the semi-major axis, *Nonlinear Dynamics* 105 (2021), 2081-2103.

[5] C.D. Murray, S.F. Dermott, *Solar System Dynamics*, Cambridge University Press, 2012.

Session 4:

HYBRID AND STATISTICAL METHODS

Improving the Force Model of SGP4 using Neural Network

Hans Carrillo*[1], Edna Segura†[1], Rosario López‡[1], and Juan Félix San-Juan§[1]

[1]Scientific Computing & Technological Innovation (SCoTIC), University of La Rioja, Logroño, La Rioja, Spain.

Abstract

The trajectory of any resident space object (RSO) can be determined using three different orbit propagation methods. Special Perturbation (SP) propagators use numerical techniques to integrate the equations of motion, including a complete and accurate force model. SP propagators provide very accurate orbit predictions, but the high computational cost limits the performance of this approach. General Perturbation (GP) propagators apply perturbation theories to develop an approximate analytical solution to the equations of motion. GP propagators consider simplified force models, which limit their accuracy. However, these propagators perform much faster than numerical methods. Finally, the third type is the semianalytical propagators, which combine the strengths of SP and GP propagators. In either case, an orbit propagation program depends uniquely on the initial states and some physical parameters to make its predictions.

The hybrid methodology was introduced in 2008. It is a non-invasive technique that improves the accuracy of any orbit propagator without increasing the computational cost. This methodology has been applied to different SP, GP and semianalitical propagators. In [1, 2] different families of hybrid orbit propagators based on statistical time series techniques were developed, whereas in [3, 4, 5] the proposed propagators were based on machine learning techniques.

In this work, we apply the hybrid methodology to improve the force model and the integration method of the well-known SGP4 orbit propagator [6, 7] using neural network (NN). The new propagator is named HSGP4. The NN is trained using the difference in the argument of latitude between accuracy ephemeris and SGP4 for Galileo-type orbits.

For this experiment, we consider 180 of the 312 time series used in [5]. This reduced set only includes time series with positive trends in the first revolutions, of which approximately 60%, 110 series, are used during the training and validation processes of the forecasting model. In contrast, approximately 40%, 70 series, are reserved for evaluating the generalization capability of the model. On the other hand, each of the 110 series is divided into two subseries: 14 revolutions, which represent approximately 200 hours, constitute the training interval used for fitting the model's parameters and the following 6 revolusions are used for validation. It is worth noting that the first two revolutions are necessary to start the network predictions.

The NN architecture [8, 5] consists of an input layer of 169 neurons, two hidden layers with 256 and 128 neurons, and an output layer with one neuron. The first hidden layer applies a linear function as activation function, whereas the exponential linear unit (elu) for the second. The batch size parameter is 64, and the optimizer to determine weights and bias of the connection among the nodes was given by *adam* (adaptive moment estimation). The cost function to use in this work will be the popular error score RMSE (root mean square error).

Fig. 1 shows the box-and-whisker plots of the distance errors between AIDA and SGP4 for the 110 TLEs of the predictive model. The time span considered is up to 12 days from the epoch of the TLE. The relatively small values of the median in this Figure is a consequence that more of the 50% of the time series ε^{θ} have small values of the trend components.

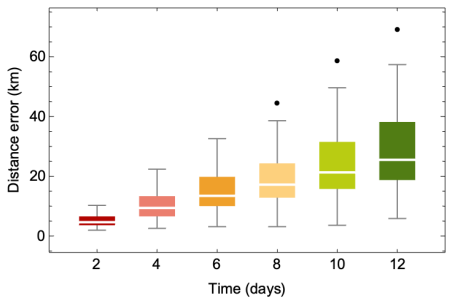

Figure 1: Box-and-whisker plots showing the distance error (km) between AIDA and SGP4 for the sample of 110 TLEs and a time span of 12 days.

Fig. 2 shows the box-and-whisker plots of the distance errors between AIDA and BestHSGP4 for the dataset of 110 TLEs. The BestHSGP4 propagator is obtained when the time series of the error is zero, $\varepsilon^{\theta} = 0$, that is, $\theta^{\text{AIDA}} = \theta^{\text{SGP4}}$. Compared with the

*Email: hans-mauricio.carrillo@unirioja.es.
†Email: edna-viviana.segura@alum.unirioja.es.
‡Email: rosario.lopez@unirioja.es.
§Email: juanfelix.sanjuan@unirioja.es.

previous box plot, whereas the maximum distance of SGP4 is approximately 68.94 km after twelve days, the maximum error of BestHSGP4 is reduced to only 1.96 km.

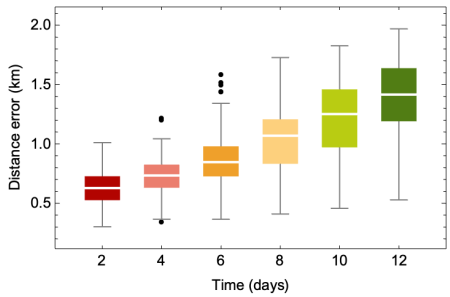

Figure 2: Box-and-whisker plots showing the distance error (km) between AIDA and BestHSGP4 for the sample of 110 TLEs and a time span of 12 days.

Fig. 3 shows the box-and-whisker plots of the distance error between AIDA and SGP4 for the unseen 70 TLEs used for testing the predictive model. The time span considered in this process is also 12 days. In this sample, the maximum distance error of SGP4 is approximately 23.88 km after twelve days, this is about 45 km less than the dataset used to create the predictive model. The outliers from the eight day are due to the dispersion of the time series ε^{θ}.

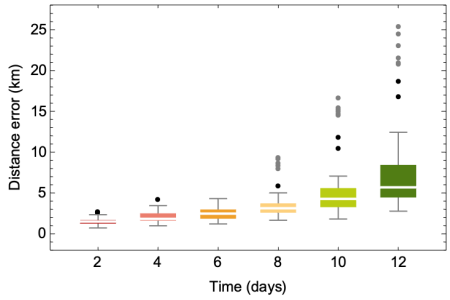

Figure 3: Box-and-whisker plots showing the distance error (km) between AIDA and SGP4 for the sample of 70 TLEs and a time span of 12 days.

Fig. 4 shows the box-and-whisker plots of the distance errors between AIDA and BestHSGP4 for the same 70 TLEs set. The Fig. 2 indicates that the the magnitude of the BestHSGP4 distance error obtained with the 70 TLEs set is similar to the 110 TLE set.

Once the NN model has been trained and included in the hybrid propagation module (HSGP4), we evaluate the performance of the new propagator. First, the HSGP4 is compared with SGP4 so as to assess how well the model fits at 2, 4, 6, 8, 10, and 12 days of propagation for the known 110 TLEs used when the model was fit. Fig. 5 depicts the box-and-whisker plots of the distance errors between AIDA and HSG4.

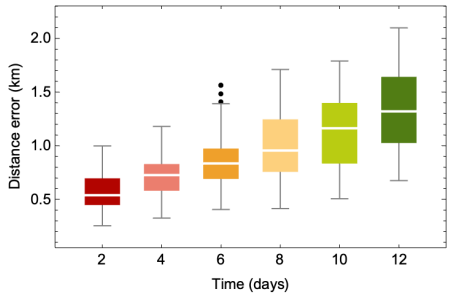

Figure 4: Box-and-whisker plots showing the distance error (km) between AIDA and BestHSGP4 for the sample of 70 TLEs and a time span of 12 days.

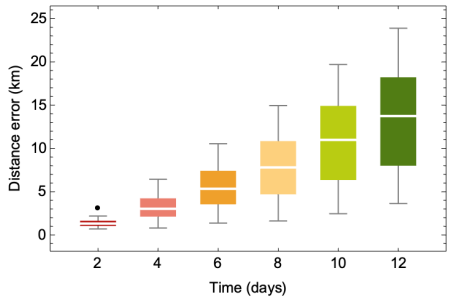

Figure 5: Box-and-whisker plots showing the distance error (km) between AIDA and HSGP4 for the sample of 110 TLEs and a time span of 12 days.

The capacity of generalization on the HSGP4 is evaluated on the remaining unseen 70 time series set. Fig. 6 depicts the box-and-whisker plots of the distance error between AIDA and HSG4.

The Q_3 value of the BestHSGP4 is small during the twelve propagation days and their values similar to the obtained with the 110 TLE set. However, the value of HSGP4 grows as quickly as the previous 110 but remains slight below the SGP4 value, less than 1 km. It is due to the values of the trend of the 70 TLE set is less than the 110 set.

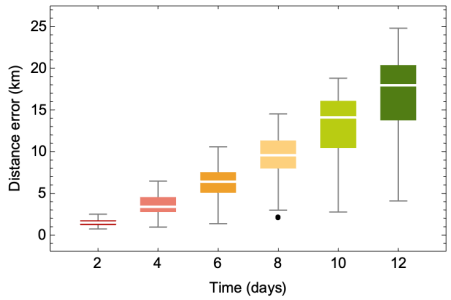

Figure 6: Box-and-whisker plots showing the distance error (km) between AIDA and HSGP4 for the sample of 70 TLEs and a time span of 12 days.

The two TLE datasets used for training and testing the HSGP4 propagator follow the same behaviour, as

can be seen in Fig. 5 and 6.

Fig. 7 and 8 show two of the best predictions of the argument of latitude of the 70 time series set. The forecasting model only needs the first two revolutions to inicializate the calculus process. In both cases, the model initially reproduces the periodic behaviour of the series. However, as time progresses, the neural network model loses its capability to recognize this periodic pattern while maintaining the trend.

Table 1 and 2 show the distance error between HSGP4 and AIDA for the TLEs 9 and 23. As can be seen, the distance error of HSGP4, in both TLEs, is close to the obtained with BestHSGP4 and reduced by approximately 45 km respect to SGP4

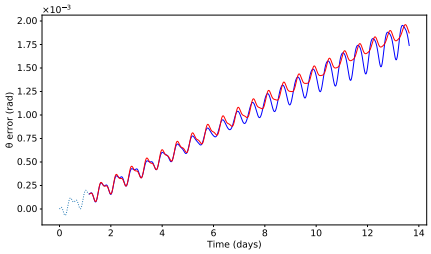

Figure 7: Red represents the predictions of the argument of latitude using the HSGP4 propagator, while in blue the precise data for the test TLE 9.

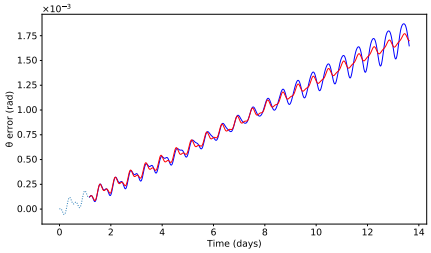

Figure 8: Red represents the predictions of the argument of latitude using the HSGP4 propagator, while in blue the precise data for the test TLE 23.

Table 1: Maximum distance errors in km between HSGP4 and AIDA for the TLE 9 after 2, 4, 6, 8, 10, and 12 propagation days

Error	2	4	6	8	10	12
SGP4	8.36	18.03	25.82	35.07	44.71	52.41
BestHSGP4	0.88	0.94	1.07	1.46	1.74	2.09
HSGP4	0.91	1.15	1.89	3.65	4.90	5.52

Table 2: Maximum distance errors in km between HSGP4 and AIDA for the TLE 23 after 2, 4, 6, 8, 10, and 12 propagation days

Error	2	4	6	8	10	12
SGP4	7.59	15.79	23.25	31.32	41.37	49.12
BestHSGP4	0.80	0.82	0.85	0.92	1.29	1.65
HSGP4	1.07	1.38	1.38	1.99	2.77	4.09

Acknowlegdgements

HC acknowledge to the FPI grant from the University and the Comunidad Autónoma de La Rioja 2019.

References

[1] J. F. San-Juan, M. San-Martín, I. Pérez, and R. López, "Hybrid perturbation methods based on statistical time series models," *Advances in Space Research*, vol. 57, no. 8, pp. 1641–1651, April 2016, Advances in Asteroid and Space Debris Science and Technology - Part 2.

[2] M. San-Martín, I. Pérez, and J. F. San-Juan, "Hybrid methods around the critical inclination," *Advances in the Astronautical Sciences*, vol. 156, pp. 679–693, 2016, paper AAS 15-540.

[3] J. F. San-Juan, I. Pérez, M. San-Martín, and E. P. Vergara, "Hybrid SGP4 orbit propagator," *Acta Astronautica*, vol. 137, pp. 254–260, August 2017.

[4] J. F. San-Juan, M. San-Martín, and I. Pérez, "Application of the hybrid methodology to SGP4," *Advances in the Astronautical Sciences*, vol. 158, pp. 685–696, 2016, paper AAS 16-311.

[5] E. Segura, H. Carrillo, R. López, M. Pérez, I. San-Martín, and J. F. San-Juan, "Deep learning hsgp4: Hyperparameters analysis," in *Proceedings 31st AAS/AIAA Space Flight Mechanics Meeting.* Charlotte, NC, USA: American Institute of Aeronautics and Astronautics, Feb 1-4 2021, paper AAS 21-241.

[6] F. R. Hoots and R. L. Roehrich, "Models for propagation of the NORAD element sets," U.S. Air Force Aerospace Defense Command, Colorado Springs, CO, USA, Spacetrack Report #3, 1980.

[7] D. A. Vallado, P. Crawford, R. Hujsak, and T. S. Kelso, "Revisiting spacetrack report #3," in *Proceedings 2006 AIAA/AAS Astrodynamics Specialist Conference and Exhibit*, vol. 3. Keystone, CO, USA: American Institute of Aeronautics and Astronautics, August 2006, pp. 1984–2071, paper AIAA 2006-6753.

[8] H. Carrillo, E. Segura, R. López, I. Pérez, and J. F. San-Juan, "Hybrid orbit propagator based on neural networks. multivariate time series forecasting approach," in *16th International Conference on Soft Computing Models in Industrial and Environmental Applications (SOCO 2021)*, H. Sanjurjo González, I. Pastor López, P. García Bringas, H. Quintián, and E. Corchado, Eds. Cham: Springer International Publishing, 2022, pp. 695–705.

Apply the hybrid orbit propagators to the association problem in the GEO region

Juan Félix San-Juan*[1], Rosario López†[1], Carlos Yanez‡[2], and Manuel Higueras§[1]

[1]Scientific Computing & Technological Innovation (SCoTIC), University of La Rioja, Logroño, La Rioja, Spain.
[2]Centre National d'Ètudes Spatiales (CNES), 18 Avenue Edouard Belin, 31401 Toulouse, France.

Abstract

Maintaining an accurate and updated catalogue of resident space objects (RSO) is of paramount importance for Space Surveillance and Tracking (SST). The success of catalogue maintenance is mainly driven by the timely availability of observations and the correct association of these observations to the catalogued objects. The latter task can significantly contribute to the computational effort needed in the whole cataloguing chain. The inputs for the association problem are the catalogue of objects at a given time –including extended state vector, associated uncertainty and object characteristics– and a set of observations at a later date. One possibility is to numerically propagate the whole RSO population with the highest accuracy to the observation date to apply the association algorithms (global nearest neighbor, for instance) to the objects that are likely to be within the field-of-view of the sensor. Another possibility, more efficient in time, is to pre-filter a reduced sub-population, applying the previous procedure with an analytical or semi-analytical solution and then using the time-consuming and highly accurate numerical propagator only to that sub-population. The drawback of this alternative is that the accuracy of the analytical or semi-analytical solution can lead to filter out potential candidates and miss the correct global association. Therefore, the use of hybrid propagators, combining the rapidity of analytical or semi-analytical propagators and the accuracy of numerical ones, is a promising alternative.

In many applications, a compromise between accuracy and efficiency must be established, based on a variety of criteria. High-fidelity propagation models usually require step-by-step propagation by using numerical methods, which are computationally intensive because they rely on small step sizes. However, simplified models may admit analytical solutions, which alleviate the computational burden. In either case, the orbit propagation program relies uniquely on the initial conditions, as well as on the propagation model, to make its predictions. On the other hand, the collection of past ephemerides can be used to improve orbit predictions by taking non-modeled effects into account.

Indeed, developing a new hybrid modeling approach to address the problem of accuracy inspired us to apply non-invasive techniques, such as machine learning or statistical time series techniques, to forecasting methods. This approach, proposed by San-Juan et al. [1, 2, 3, 4], asses that the hybrid modelling approach for orbit propagation is feasible and comparable to traditional models, improving their accuracy in most cases. Basically, this methodology investigates the main dynamical effects provided by any orbit propagator and make important contributions modelling its error and emulating other non-modelled dynamics.

The first step to develop a hybrid version of SGP4 is to understand the behavior of this propagator during the considered interval of time. To assess this, data from a space catalogue with 510 TLEs downloaded from Space Track[1] from different GEO orbits have been propagated using the analytical propagator SGP4 and PSIMU[2], a high-accuracy orbital propagator developed by the Centre National d'ÃĽtudes Spatiales (CNES).

PSIMU is implemented in Java and includes the following perturbation forces: geopotential acceleration computed up to an arbitrary degree and order for the harmonics, atmospheric drag, solar radiation pressure, rediffused solar radiation pressure, third body perturbations from Sun and Moon, and ocean and terrestrial tides. PSIMU implements a Dormand-Prince of 8th order with variable step-size and uses PATRIUS (PATrimoine de base siRIUS)[3]. It is the reference low level library used for mathematical and flight dynamics functions, as well as other supplementary libraries. The perturbation model taking into account in PSIMU includes Earth's gravitational field (up to 8×8), solar radiation pressure models with A/m = 1, 0.5, 0.1, 0.05, 0.01, 0.001 m^2/kg, and third

*Email: juanfelix.sanjuan@unirioja.es. Research supported by Centre National d'Ètudes Spatiales.
†Email: rosario.lopez@unirioja.es.
‡Email: carlos.yanez@cnes.fr.
§Email: manuel.higueras@unirioja.es.

[1]https://www.space-track.org
[2]https://logiciels.cnes.fr/en/content/psimu
[3]https://logiciels.cnes.fr/en/content/patrius

body point mass force models.

On the other hand, SGP4 is based on the analytical theories of the artificial satellite of [5] and [6]. Initially, the perturbations modelled by SGP4 consisted of only zonal gravitational terms (up to J4) and drag based on the work of [7]. When Molniya and geostationary orbits became more common, deep space modelling (Simplified Deep-space Perturbation-4, SDP4) was integrated into SGP4 [8, 9]. This included the lunisolar effects, and resonance effects of tesseral harmonics developed by [10].

In this study, for each TLE of our sample and different values of A/m, twenty days of accuracy numerical pseudo observations were generated with PSIMU, using as initial conditions the osculating elements provided by SGP4 at the same epoch t_{TLE} for each previous defined TLE. After that, a new TLE is calculated using a differential corrector method from the arc of t_{TLE} +10 days given by PSIMU. Finally, ten backward and forward propagation days are done using SGP4 from the new TLE. From now, the set of TLE given at the epoch t_{TLE} +10 will be considered as our new TLE sample, one for each value of A/m making a total of 3060 TLEs. It is worth noting that this scenario intends to simulate the same scenario given in the association problem in which during the process a high accuracy propagation can be obtained.

Then, we calculate the time series of the error $\boldsymbol{\varepsilon}_t^{\mathbf{x}} = \mathbf{x}_t^{\mathrm{PSIMU}} - \mathbf{x}_t^{\mathrm{SGP4}}$, where $\mathbf{x}$ represents any set of variables, such as cartesian, Delaunay, polar-nodal, or equinoctial elements, $\mathbf{x}_t^{\mathrm{PSIMU}}$ is the pseudo-observation given by PSIMU at epoch t, and $\mathbf{x}_t^{\mathrm{SGP4}}$ is the data obtained from SGP4 at the same epoch. The six time series $\boldsymbol{\varepsilon}_t^{\mathbf{x}}$ contain the complete information related to SGP4 errors, which are caused by the perturbation forces not taken into account by the SPG4 algorithm and by the integration method used with this analytical propagator.

In order to understand the real influence that each variable, as well as some of their combinations, may have on the accuracy of the SGP4 propagation for GEO orbits, an Exploratory Data Analysis (EDA) is performed for the TLEs considered in this study. The variables and their combinations are ranked in terms of their capability to reduce the distance errors of SGP4 propagations. The main conclusion of this analysis is that the argument of the latitude θ and the argument of the node ν using the polar-nodal set allow reducing the distance error of SGP4 for all considered TLEs by modeling the evolution of their error.

An EDA of the distance error between PSIMU and SGP4, and PSIMU and the optimum hybrid SGP4 propagator (OptHSGP4) for a given predictive horizon t is performed as a second step. The OptHSGP4 propagator is obtained when the time series of the errors are zero, $\varepsilon^{\theta} = \varepsilon^{\nu} = 0$, that is, $\theta^{\mathrm{PSIMU}} = \theta^{\mathrm{SGP4}}$ and $\nu^{\mathrm{PSIMU}} = \nu^{\mathrm{SGP4}}$.

In a third step, a preliminary analysis of the time series of error ε^{θ} and ε^{ν} is done. The analysis examines the approximate entropy (ApEn) during the training period. The training period is given in satellite revolutions and it varies between 3 and 10 revolutions. Approximate entropy was introduced to quantify the amount of regularity and the unpredictability of fluctuations in a time series. A low entropy value indicates that the time series is deterministic; a high value indicates randomness.

The four step applies the seasonal Autoregressive Integrated Moving Average (**A**RIMA) and Exponential Smoothing (**E**) forecasting methods to each time series ε^{θ} and ε^{ν}. The number of points per revolution considered is 12, whereas the trained period varies between 3 and 10 revolutions. In this report, the total number of models ($\mathcal{M}$) evaluated has been 48960 (510 TLEs × 2 time series × 8 trained periods × 6 A/m values). From the combination of the two forecasting methods, four hybrid propagators have been developed: HSGP4(A,A), HSGP4(A,E), HSGP4(E,E) and HSGP4(E,A). In the cases of distance error improvement respect to SGP4, the EDA analysis includes box-and-whisker plots, outliers analysis, the relationship between the TLEs and the magnitude of their errors These models, automatically generated, can be used as a first attempt at classifications in function of the TLE. Finally, from these four hybrid propagators we derive the best hybrid combination (BestHSGP4) and try to identify what conditions allow to select the best combination. In the cases that there is no improvement in the distance error of SGP4, the time series are identified and their shapes characterized.

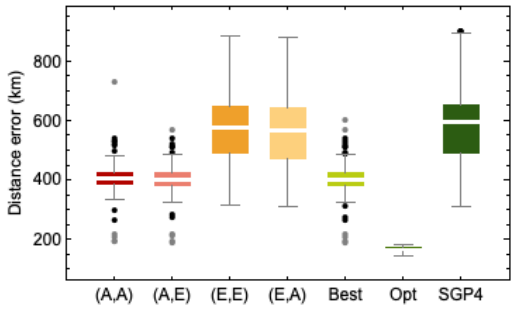

Figure 1: Box-and-whisker plots of the distance error (km) between PSIMU and the four hybrid SGP4, the BestHSGP4 and OptHSGP4 propagatosr for a time span of 10 days and A/m = $1m^2/kg$.

Figure 1 and 2 show the box-and-whisker plots of the distance error (km) between PSIMU and the four hybrid SGP4, the BestHSGP4 and OptHSGP4 propagators for a time span of 10 days and A/m = 1, $0.001m^2/kg$. The forecasting model have been training using 10 satellite revolutions. The distance

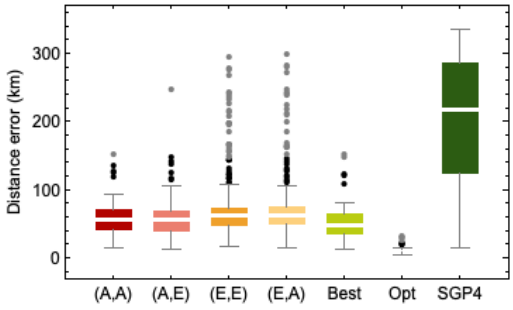

Figure 2: Box-and-whisker plots of the distance error (km) between PSIMU and the four hybrid SGP4, the BestHSGP4 and OptHSGP4 propagators for a time span of 10 days and A/m = $0.001m^2/kg$.

error can be reduced from about 80% in the case of low A/m value to 35% in the case of high A/m value at 10 propagation days for the 75% of the cases.

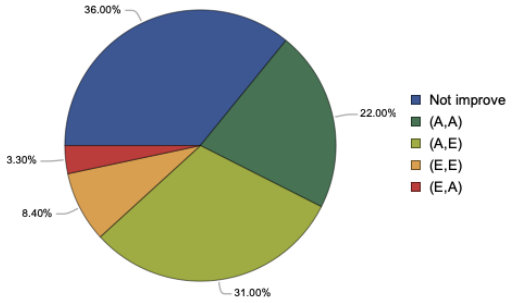

Figure 3: Percentage of forecasting models of the BestHSGP4 propagator for a time span of 10 days and A/m = $1m^2/kg$.

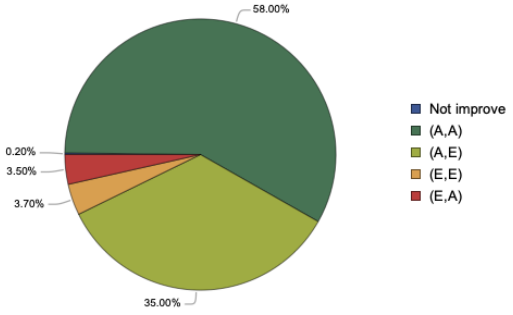

Figure 4: Percentage of forecasting models of the BestHSGP4 propagator for a time span of 10 days and A/m = $0.001m^2/kg$.

Figure 3 and 4 plot the percentage of forecasting models of the BestHSGP4 propagators with the previous assumptions. The BestHSGP4 propagator improves from almost 100% in the best case (A/m = $0.001m^2/kg$) to 65% in the worse case (A/m = $1m^2/kg$).

References

[1] J. F. San-Juan and M. San-Martín, "New families of hybrid orbit propagators based on analytical theories and time series models," *Advances in the Astronautical Sciences*, vol. 136, pp. 547–565, 2010, paper AAS 10-136.

[2] J. F. San-Juan, M. San-Martín, and D. Ortigosa, "Hybrid analytical-statistical models," *Lecture Notes in Computer Science*, vol. 6783, no. 2, pp. 450–462, 2011.

[3] M. San-Martín, "Métodos de propagación híbridos aplicados al problema del satélite artificial. Técnicas de suavizado exponencial," Ph.D. dissertation, University of La Rioja, Spain, 2014.

[4] J. F. San-Juan, M. San-Martín, and I. Pérez, "Application of the hybrid methodology to SGP4," *Advances in the Astronautical Sciences*, vol. 158, pp. 685–696, 2016, paper AAS 16-311.

[5] D. Brouwer, "Solution of the problem of artificial satellite theory without drag," *The Astronomical Journal*, vol. 64, no. 1274, pp. 378–397, November 1959.

[6] Y. Kozai, "Second-order solution of artificial satellite theory without air drag," *The Astronomical Journal*, vol. 67, no. 7, pp. 446–461, September 1962.

[7] M. H. Lane and K. H. Cranford, "An improved analytical drag theory for the artificial satellite problem," in *Proceedings of the AIAA/AAS Astrodynamics Specialist Conference*. Princeton, NJ, USA: American Institute of Aeronautics and Astronautics, August 1969, paper AIAA 69-925.

[8] F. R. Hoots, P. W. Schumacher, Jr., and R. A. Glover, "History of analytical orbit modeling in the U.S. space surveillance system," *Journal of Guidance, Control, and Dynamics*, vol. 27, no. 2, pp. 174–185, March-April 2004.

[9] D. A. Vallado, P. Crawford, R. Hujsak, and T. S. Kelso, "Revisiting spacetrack report #3," in *Proceedings 2006 AIAA/AAS Astrodynamics Specialist Conference and Exhibit*, vol. 3. Keystone, CO, USA: American Institute of Aeronautics and Astronautics, August 2006, pp. 1984–2071, paper AIAA 2006-6753.

[10] R. S. Hujsak, "A restricted four body solution for resonating satellites without drag," U.S. Air Force Aerospace Defense Command, Colorado Springs, CO, USA, Spacetrack Report #1, 1979.

Manoeuvre detection based on S3TSR data

Rafael Vazquez*[1], Jose M. Montilla†[1], Julio C. Sanchez‡[1], Jorge Galan-Vioque§[1], Javier Rey Benayas¶[2], and Jan Siminski‖[3]

[1]Universidad de Sevilla, ETSI, Camino de los Descubrimientos s.n. 41092 Sevilla, Spain.
[2]Indra Sistemas, Crta Loeches 9, 28850 Torrejón de Ardoz, Madrid, Spain.
[3]Space Debris Office, ESA-ESOC, Darmstadt, Germany.

Abstract

This work outlines and assesses several metrics for the detection of manoeuvres from radar data. The surveillance radar provides precise tracking information, i.e. ranging and line-of-sight, for objects in Low-Earth orbit. The main starting assumption is that the object under analysis has an orbit known some time before the manoeuvre takes place, which in turn happens before the radar data is obtained. The orbit may possibly also have been computed with radar data (a filter combining orbit determination and manoeuvre detection was also developed and is briefly commented on at the end of this work). The detection metrics are based on reachability analysis of the state (correlating its prediction set with the next track from the radar) and use of attributables. Two metrics are presented: one based on the Mahalanobis distance, and another on stochastic optimal control theory. They are implemented using the free low-level space dynamics library OREKIT. Results are given based on real data from the Spanish Space Surveillance and Tracking (S3T) surveillance radar (S3TSR), with manoeuvre information and ephemerides obtained from ESA and DLR to assess the results.

1 Introduction

In the field of Space Surveillance and Tracking (SST), accurate orbital determination and manoeuvre detection is of upmost importance to infer objects' orbital information and their future behaviour, as well as to be able to carry out tasks such as prediction of potential conjunctions with operating satellites, taking avoidance orbital corrections, predicting re-entries, identifying fragmentations or updating orbital elements of known satellites, among others.

Satellites performing unknown manoeuvres pose a challenge when trying to associate the new collected observations (obtained by laser, radar, or by any other means from the SST infrastructure) with the previously known reference orbits (which are stored in SST catalogues). Indeed, one of the main motivations of manoeuvre detection is that it can significantly reduce the number of uncorrelated targets detected by the SST sensors infrastructure. Most of these uncorrelated objects are just known satellites, which have performed unpublished manoeuvres (typically while not being observed), in such a way that their new orbits do not match with the predictions.

This work (an extended version of which has already been submitted to a journal, see see [1] for the preprint) presents two metrics for the detection of manoeuvres in Low Earth Orbit (LEO) from radar data. An initial validation of the metrics is provided with real tracks from S3TSR [2], the Spanish surveillance radar developed, installed and validated by Indra with the funding of the Spanish Government under the technical and contractual management of ESA on behalf of Centro de Desarrollo Tecnólogico e Industrial (CDTI). Manoeuvre information and ephemerides are obtained from ESA/ESOC and DLR/GSOC to assess the results, for a number of selected scenarios. The final aim is to have these metrics integrated in the Spanish SST (S3T) Cataloguing system in order to provide routine automatic manoeuvre detection capabilities to the system in the future.

2 Manoeuvre Detection Metrics

This Section introduces the metrics used in the paper as well as one of the main tools on which the metrics are based, namely the concept of attributables.

2.1 Attributables

Radar tracks are composed of a number of plots (typically 5-20 per track). At each plot, the radar provides range (ρ), range-rate ($\dot{\rho}$), elevation (El) and azimuth (Az) observables. In order to compare tracks with different lengths, the information of all plots is combined

*Email: rvazquez1@us.es
†Email: jmontillag.es
‡Email: jsanchezm.es
§Email: jgv@us.es
¶Email:jreyb@indra.es
‖Email:Jan.Siminski@esa.int

into a single value. For that porpuse, the theory of attributables [3, 4] is used; it allows to "compress" several measurements into a single, higher-quality measurement, fitting a batch of measurements into a single polynomial expression.

Fitting the information of the observables independently is one option, but it is possible to improve the uncertainty of the resulting virtual measurement if one incorporates the definition of range-rate into the modelling, so that it shares the parameters with the range (see [1] for details). The method manages to average out noise and reduce the standard deviation of the virtual range and range-rate observables.

2.2 Mahalanobis Distance Metric (MD)

The first metric is based on comparing the range and range-rate attributable obtained from measurements with the ones predicted from the initial orbit, by means of the Mahalanobis distance [4], a measure of the distance between a point P and a distribution.

Assume that at the start time, one knows the initial position and velocity and its associated covariance matrix; and the attributable time t_a, one knows the virtual values of range, range-rate, azimuth and elevation, as well as the associated uncertainty in the form of a covariance matrix. Through a Monte Carlo-type propagation, one propagates a cloud of initial sample points up to time t_a, obtaining a "cloud" of projected measurements, from which one can obtain its mean (which we denote as the *projected* attributable) as well as the associated uncertainty in the form of a covariance matrix.

Then, the real and projected attributable can be compared. If no manoeuvre has been performed, one would expect that their *difference* should be close to zero; and the covariance of the difference can be approximated as the sum of the covariances of the real and projected attributables. Thus, under an assumption of normality, the computed difference should belong to a normal distribution of zero mean with the obtained covariance This can be checked through the Mahalanobis distance (MD), which can give a probability of belonging to the distribution (see [1] for details), since it follows a $\chi^2(\cdot, n)$ distribution with as many degrees of freedom n as the number of considered observables. Considering only range and range rate, the probability would be computed as follows:

$$p_{MD} = \max\{0, 2(\chi^2(MD; 2) - 0.5\} \tag{1}$$

This way, if the MD has a probability of 50% or less of occurring (a selected threshold), it is assumed that there is no manoeuvre, to reduce false positives. If the MD has a probability of more than 50% of happening, then it is scaled; thus, if one gets, e.g., a probability of a certain MD of 80%, the probability of manoeuvre becomes 60%.

2.3 Control Distance Metric (ΔV)

The second metric is based on the use of stochastic optimal control theory. Following previous works [5, 6] one can compute a distribution of the required manoeuvre that connects the uncertain orbit with the (also uncertain) measurement. This distribution can then be used to obtain the likelihood of a manoeuvre having been performed and represents a proper metric of the distance between the orbit and the mesurements. The optimal control problem is posed as follows:

$$\begin{aligned} &\min_u \int_{t_0}^{t_a} u^T(t)u(t)dt \\ \text{s.t.} \quad &x'(t) = f(x(t), u(t), t) \\ &x(t_0) = x_0 \\ &h(x(t_f)) = [\rho \quad \dot{\rho}]^T \end{aligned} \tag{2}$$

In (2), the initial point x_0 is known from the precise orbit whereas the function h at the final point represents the function relating position and velocity with range and range-rate (the most precise measurements) which should take the value obtained with attributables. The function f represents the orbital dynamics, including any modelled perturbations. The problem is solved with CasADi [7], an open-source solver for MATLAB, with a multiple shooting method discretizing the orbital dynamics in N time intervals; for each of these, since impulses are small, the orbital dynamics is replaced with a linearized model obtained from OREKIT (computing the State Transition Matrix), with the discrete ΔVs applied at the beginning. As a first step, the problem has been solved in a deterministic way. Since the solution is fast (seconds or less), to incorporate the stochasticity of the problem (both in initial orbit and measurements), a Monte Carlo algorithm is implemented as a simple, albeit rather time-consuming, solution.

The ΔV distribution is obtained both for the computed and the projected attributable, as in Section 2.2. Then, the distributions are compared to determine which one is "smaller". A novel metric based on the smaller percentiles (initial tails of the distribution) was developed as follows. The percentile 10% is computed for the non-manoeuvred distribution (projected attributable) obtaining ΔV_{10} and now one computes from the potentially manoeuvred distribution (computed attributable) the probability $p = P(\Delta V < \Delta V_{10})$. Then:

$$p_{\Delta V} = \max 0, 0.1(0.1 - p) \tag{3}$$

This way, if p is above 10% the probability becomes zero (the lower tail of the potentially manoeuvred distribution is the left of the non-manoeuvred distribution) and if it is below 10%, the difference is multiplied by 10 (thus, having 0 probability of being below ΔV_{10} would represent a 100% probability of manoeuvre).

3 Real Results

A total of 15 scenarios were selected, using radar data obtained from S3TSR; manoeuvre information and precise ephemerides are obtained from ESA/ESOC and DLR/GSOC. The satellites under consideration were Sentinel-1A, Sentinel-1B, Sentinel-2A, Sentinel-2B, Swarm-C, TerraSAR-X and TanDEM-X. In total, 158 segments (which were defined as the interval after one radar track up to the next and lasted from 12 hours to more than 48 hours in some cases) were considered, 24 of them with manoeuvres and 134 without manoeuvres, to assess not only the capability of the metrics to detect manoeuvres but also to avoid false positives. From the precise ephemerides, an OREKIT propagator was developed to best fit the ephemerides by taking into account gravity harmonics (up to order 40), third-body perturbations (Sun and Moon), solar radiation pressure and drag (with the NRLMSISE-00 atmosphere model).

3.1 MD probability metric results

The metric was able to detect only about 42% of manoeuvres, even with some of them being rather intense. The rate of false positives was quite good on the other hand (3%). Most false positives present less than 10 plots in the track following the manoeuvre. Thus, the main cause of false positives is tracks with a low number of plots. Most false negatives were on segments of length equal to or larger than one day. Thus, the main cause of false negatives is longer propagations accumulating additional propagation error. Sometimes these longer propagation periods are due to missed radar observations right after the manoeuvre. The most challenging scenarios are those with TanDEM-X/TerraSAR-X due to the abundance of manoeuvres (all segments have at least one) and the scarcity of data. This metric performs poorly in those scenarios compared with the other scenarios.

3.2 ΔV probability metric results

The metric detected 54% of manoeuvres, a more positive results than the MD metric, but in need of improvement. The rate of false positives was worse, about 8%. The causes of errors are similar as for the MD metric. However, as opposed to it, this metric performed excellently in TanDEM-X/TerraSAR-X scenarios compared with the other scenarios.

4 Conclusions and Future Work

Two metrics for the detection of manoeuvres in LEO from radar data have been presented. Real data was used to validate the metrics, detecting about half the manoeuvres, with a low rate of false positives. Thus, the metrics can be considered a promising start, but are in need of further improvement. The main identified difficulty was the scarcity of measurements (low number of tracks resulting in long propagation times without information and/or low number of plots). Future expansion of the capabilities of S3TSR may improve the quality of the metrics, as well as considering other sources of data. The aim is to have these metrics integrated in the S3T Cataloguing System in order to provide routine automatic manoeuvre detection capabilities to the system in the future.

An extended version of this work has already been submitted to a journal, see see [1] for the preprint.

References

[1] Montilla, J. M., Sanchez, J. C., Vazquez, R., Galan-Vioque, J., Benayas, J. R., and Siminski, J. Manoeuvre detection in low earth orbit with radar data, (2022). Preprint, `https://arxiv.org/abs/2203.03590`.

[2] Gomez, R., Salmerón, J. M.-V., Besso, P., Alessandrini, M., Pinna, G. M., and Prada, M. A. R. Initial operations of the breakthrough spanish space surveillance and tracking radar (s3tsr) in the european context. In *1st ESA NEO and Debris Detection Conference.*, (2019).

[3] Reihs, B., Vananti, A., Schildknecht, T., Siminski, J. A., and Flohrer, T. Application of attributables to the correlation of surveillance radar measurements. *Acta Astronautica* **182**, 399–415 (2021).

[4] Vananti, A., Schildknecht, T., Siminski, J., Jilete, B., and Flohrer, T. Tracklet-tracklet correlation method for radar and angle observations. In *Proc. 7th European Conference on Space Debris*, 18–21, (2017).

[5] Holzinger, M. J., Scheeres, D. J., and Alfriend, K. T. Object correlation, maneuver detection, and characterization using control distance metrics. *Journal of Guidance, Control, and Dynamics* **35**(4), 1312–1325 (2012).

[6] Singh, N., Horwood, J. T., and Poore, A. B. Space object maneuver detection via a joint optimal control and multiple hypothesis tracking approach. In *Proceedings of the 22nd AAS/AIAA Space Flight Mechanics Meeting*, volume 143, 2012–159, (2012).

[7] Andersson, J. A., Gillis, J., Horn, G., Rawlings, J. B., and Diehl, M. Casadi: a software framework for nonlinear optimization and optimal control. *Mathematical Programming Computation* **11**(1), 1–36 (2019).

Session 5:

COLLISION PROBABILITY COMPUTATION

Analyzing transport phenomena in orbital conjunctions

Raquel Molina*[1], Guillermo Escribano†[1], and Manuel Sanjurjo-Rivo‡[1]

[1]Bioengineering and Aerospace Engineering Department, University Carlos III of Madrid, Spain

Abstract

Given the conjunction geometry between two objects in orbit is inherently defined by the intersection between their respective orbital planes, it is reasonable to study the dynamical evolution of their relative position when one of them is located along such intersection. Methods for determining the probability of collision are either computationally intensive or referred to a specific time of closest approach. Identifying the domain of attraction for a collision, i.e. the region within the initial probability distribution that leads to a minimum distance below a prescribed threshold, can aid in providing accurate estimates for collision probability computations.

1 Introduction

Computationally efficient methods for determining the probability of collision between two objects in orbit are crucial for the continuation of Earth orbital activities. The number of objects in Earth orbit capable of producing a catastrophic collision is currently on the order of 10^5. Continuously monitoring these objects and foreseeing close approaches among them thus requires a huge computational effort. Driven by this requirement, operational methods for determining the probability of collision between two objects typically depend on linear-gaussian and geometric assumptions that have been shown to fail for certain type of approaches, e.g. low velocity encounters. Various works have been proposed to overcome these limitations, but their associated computational cost is still beyond the current industry capabilities.

Within this work, the authors propose to study the transport phenomena in the dynamical system that models a collision in orbit. Through appropriate coordinate transformations, it is possible to efficiently explore the initial probability distribution function of the state of both objects with the aim of determining the domain of attraction of a potential collision. The latter could be extremely useful in the computation of the probability of collision as defined by the integral over all possible state realizations that lead to a minimum distance smaller than certain threshold.

*Email: 100345788@alumnos.uc3m.es.
†Email: guescrib@ing.uc3m.es.
‡Email: msanjurj@ing.uc3m.es.

2 Conjunction Geometry

For a collision to occur between two objects in orbit, both objects need to be located at one of the two orbital plane intersections. The direction of such intersections is commonly referred to as relative line of nodes and is defined by

$$\mathbf{n}_c = \pm \frac{\mathbf{h}_1 \times \mathbf{h}_2}{|\mathbf{h}_1 \times \mathbf{h}_2|}, \tag{1}$$

where $\mathbf{h}_i = \mathbf{r}_i \times \mathbf{v}_i$ is the angular momentum vector of object $_i$. Under the assumption of Keplerian dynamics, i.e. the only forces acting on the subjects are due to a central gravity field modeled as a restricted two-body problem, the necessary conditions for a collision reduce to:

1. The radii of both orbits along the collision direction should be coincident. This is measured by the quantity
$$\Gamma_c = 1 - \frac{r_{2,c}}{r_{1,c}}, \tag{2}$$
being $r_{i,c} = (h_i^2/\mu)/(1 + e_i \cos \nu_{i,c})$ and $\cos \nu_{i,c} = \mathbf{n}_c \cdot \mathbf{e}_i / |\mathbf{e}_i|$. Note that in Keplerian motion this angle remains constant for each relative node.

2. Both objects need to be located at a common orbit intersection point, which can be measured by the angular distance
$$\Delta_c = \nu_2(t_{c,m}) - \nu_{2,c}. \tag{3}$$
This distance corresponds to the phase between the collision anomaly of object two $\nu_{2,c}$, i.e. the angular position of the secondary that complies with the orbital intersection, and the actual angular position of the secondary $\nu_2(t_{c,m})$ when the primary is located at its respective collision anomaly, i.e. $\nu_1(t_{c,m}) = \nu_{1,c}$. Under Keplerian assumptions, the time invested by object 1 to reach the collision direction can be computed from Kepler's equation
$$\sqrt{\frac{\mu}{a_1^3}}(t_{c,0} - t_0) = (E_{1,c} - E_{1,0}) - e_1 (\sin E_{1,c} - \sin E_{1,0}), \tag{4}$$

where $t_{c,m} = t_{c,0} + mT_1$ and T_1 is the orbital period of the primary. In a similar fashion, the corresponding true anomaly of the secondary $\nu_2(t_{c,m})$ can be derived from

$$\sqrt{\frac{\mu}{a_2^3}}(t_{c,m} - t_0) = (E^m_{2,c} - E_{2,0}) - e_2\left(\sin E^m_{2,c} - \sin E_{2,0}\right). \quad (5)$$

Moreover, the change in eccentric anomaly between two consecutive passages of the primary through a relative node can be computed as

$$2\pi\sqrt{\frac{a_1^3}{a_2^3}} = (E^{m+1}_{2,c} - E^m_{2,c}) - e_2\left(\sin E^{m+1}_{2,c} - \sin E^m_{2,c}\right). \quad (6)$$

Appropriate thresholds may then be set for the distance in the conjunction map $\xi = [\Gamma,\ \Delta]^T$. Assuming a combined hard body radius $R_c = 10\ m$, such thresholds would be $\Gamma_{th} \sim 10^{-6}$ and $\Delta_{th} \sim 10^{-6}$ for a typical LEO encounter at an altitude of $1,000\ km$. Similarly, a conjunction in the Geostationary region with the same R_c would require distances in the conjunction map on the order of $\Gamma_{th} \sim 10^{-7}$ and $\Delta_{th} \sim 10^{-7}$.

3 Assessment of the approach

The proposed mapping based on relative orbital geometry has been successfully applied to collision risk analysis, allowing to efficiently determine the Earth's orbital congestion (see [3]). Within this work, we want to explore the capabilities of the method and, in particular, determine the ability to approximate the dynamical evolution of the conjunction geometry in an efficient manner.

In fact, we seek to perform low order approximations to the difference between the predicted mapping at the closest approach $\xi(t_{c,m})_{kep}$ under Keplerian motion, and the reference mapping $\xi(t_{c,m})$ computed using high-fidelity propagation. To validate the approach, a Monte Carlo simulation has been carried out for a representative LEO test case based on the Iridium-Kosmos 2009 collision [1]. The initial state of the objects is assumed to follow a Gaussian distribution with mean states at the initial epoch $t_0 =$ 2009 FEB 03 20:01:28.126 UTC

$$\mathbf{r}_1^{ECI}(t_0) = \begin{bmatrix} 1286.102 \\ -1129.618 \\ -6957.400 \end{bmatrix},\ \mathbf{v}_1^{ECI}(t_0) = \begin{bmatrix} -3.970654 \\ 6.062485 \\ -1.718518 \end{bmatrix}$$

$$\mathbf{r}_2^{ECI}(t_0) = \begin{bmatrix} 6308.427 \\ 3294.617 \\ -916.8711 \end{bmatrix},\ \mathbf{v}_2^{ECI}(t_0) = \begin{bmatrix} -0.158786 \\ 2.243546 \\ 7.103635 \end{bmatrix}$$

expressed in km and km/s. The initial co-variance is assumed equal for both objects and given by

$$\mathbf{P}^{RTN}(t_0) = \mathrm{diag}\begin{bmatrix} 41.42 \\ 2533 \\ 70.98 \\ 5.744 \cdot 10^{-3} \\ 1.049 \cdot 10^{-5} \\ 1.091 \cdot 10^{-6} \end{bmatrix}$$

expressed in m^2 and m^2/s^2. $N = 500$ samples are drawn from a Gaussian distribution combining both objects, and then propagated with a deterministic dynamical model considering drag [4], solar radiation pressure, Earth's non spherical gravity up to degree and order 10 and the Sun and Moon as third bodies. A total propagation time of 7 days is set in order to cover the reference collision epoch $t_c^* =$ 2009 FEB 10 16:55:59.806 UTC.

Figure 1 depicts the distribution of the distance of closest approach with respect to the occurrence epoch. Note there is a color code indicating the Mahalanobis distance of each sample with respect to the initial distribution, defined as

$$d_{M,i} = \sqrt{\begin{bmatrix} \mathbf{x_{1,i}} - \mathbf{x_1} \\ \mathbf{x_{1,i}} - \mathbf{x_1} \end{bmatrix}^T \begin{bmatrix} \mathbf{P} & 0 \\ 0 & \mathbf{P} \end{bmatrix}^{-1} \begin{bmatrix} \mathbf{x_{1,i}} - \mathbf{x_1} \\ \mathbf{x_{1,i}} - \mathbf{x_1} \end{bmatrix}}$$

where both $\mathbf{x}$ and $\mathbf{P}$ are referred to t_0. While most of the particles that lead to minimum distances lower that 1 km correspond to high probability (low d_M) regions, there is an even higher portion of particles that lead to higher distances within the gross of the initial distribution. This suggests that the domain of attraction of a potential collision may not present a smooth behavior in the probability space. In addition, the scatter in the time of closest approach (TCA) suggests that analyses based on a single reference epoch may not be sufficient to determine the set of states that lead to collision, note that relative velocities are of the order of 10 km/s for this particular case.

Fig. 2 shows the conjunction geometry at the first node passage with a colormap indicating the distance of closest approach. Note that at this specific pass (referred to $t_{c,0}$), the two objects are separated by an angular distance of 75^o and there is not a clear region that leads to (future) lower minimum distances. Nonetheless, one can apply the same mapping to a future conjunction (referred to $t_{c,m}$) assuming Keplerian motion, obtaining the distribution shown in Fig. 3. Therein, one can see that the samples are somehow ordered so there is a clear relation between $||\xi_{kep}(t_{c,m})||$ and $||\mathbf{r}_{1,c} - \mathbf{r}_{2,c}||$. Thereafter, the transport of particles that lead to collision cannot be characterized as a two-dimensional transformation $\mathcal{T}' : \mathbb{R}^2 \to \mathbb{R}^2$ but

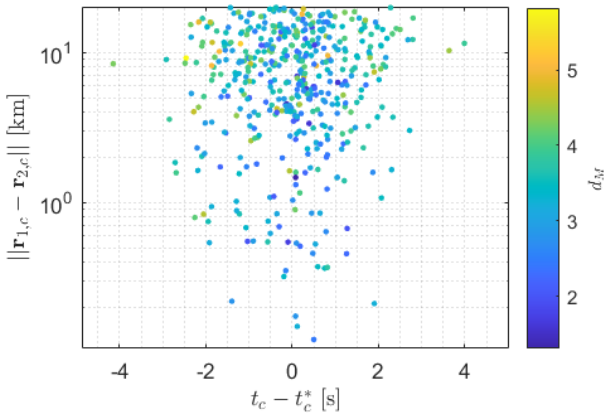

Figure 1: Minimum distance as a function of time. Here t_c^* is the reference collision epoch and d_M is the Mahalanobis distance with respect to the initial sampling distribution.

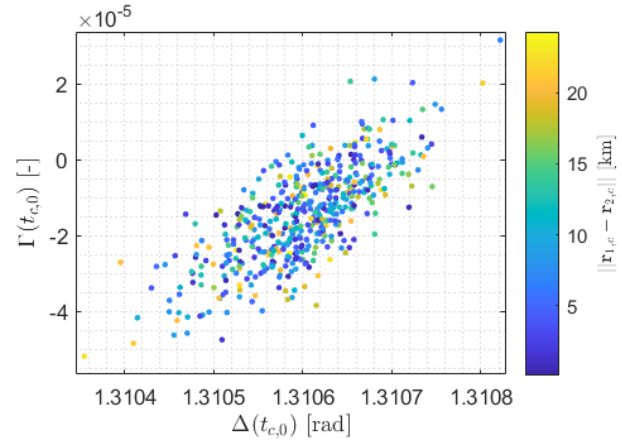

Figure 2: Conjunction geometry at first node passage.

requires analyzing the complete dimensionality of the state, thus the mapping $\mathcal{T} : \mathbb{R}^{12} \rightarrow \mathbb{R}^2$. As a consistency check, if the projection onto the conjunction plane is performed for the particles propagated using the high-fidelity dynamical model, the resulting distribution is very similar to the one predicted by the Keplerian model (see Fig 4).

4 Preliminary conclusions

Statistical numerical integration has shown that there is a class of two-dimensional mappings that naturally captures the dynamical evolution of a conjunction in orbit. Moreover, this mapping is not referred to a specific conjunction geometry but simply the one that leads to the closest approach, thus being free from any temporal or spatial limitation. Based on these preliminary results, it is possible to determine the domain of attraction of a collision, as suggested by the extreme value theory. The authors propose to 1) derive a low-

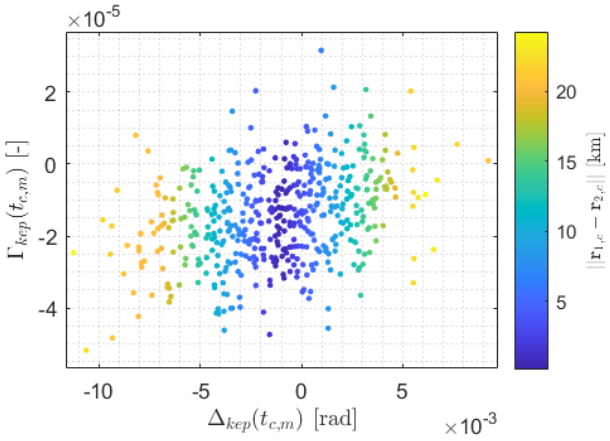

Figure 3: Conjunction geometry at closest approach under Keplerian dynamics.

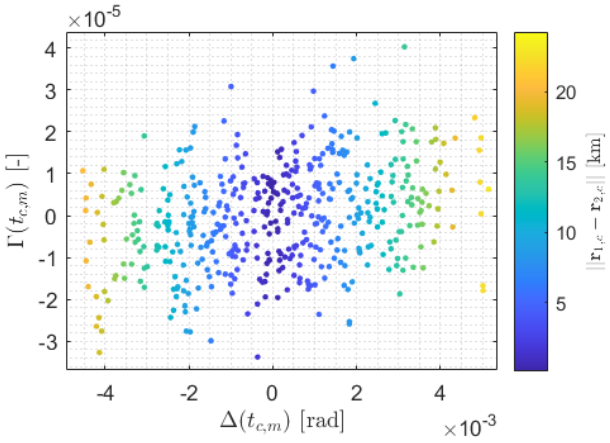

Figure 4: Conjunction geometry at closest approach with high-fidelity propagation.

order expansion of the effect of orbital perturbations in the conjunction geometry or 2) utilize sequential sampling methods to approximate the domain of attraction of the collision in lieu of developing efficient methods for computing the probability of collision.

References

[1] NASA (Oct. 2009). The Collision of Iridium 33 and Cosmos 2251: The Shape of Things to Come. *60th International Astronautical Congress.*

[2] Russell P. Patera (2007). Satellite Collision Probability for Nonlinear Relative Motion. *Journal of Guidance, Control and Dynamics*, Vol. 26, No. 5.

[3] Jorge Martinez, Guillermo Escribano & Manuel Sanjurjo-Rivo (2021). Orbital congestion assessment based on dimensionality reduction.

[4] Bruce Bowman et al. (Aug. 2008). A new empirical thermospheric density model JB2008 using new solar and geomagnetic indices. *AIAA/AAS astrodynamics specialist conference and exhibit (p. 6438).*

Astrodynamical methods for collision avoidance automation

Jan Siminski*[1], Klaus Merz[1], and Volker Schaus[1]

[1]Space Debris Office, ESA/ESOC

1 Introduction

The growth in launch traffic and the emergence of large constellations, the continuing occurrence of fragmentations, and the improved capabilities of surveillance systems increases the number of detected close approaches in space and consequently also the need for automated collision avoidance manoeuvre planning, coordination, and execution. Collision avoidance is already part of routine operations for space missions. It is a labor-intensive task requiring expert knowledge to identify critical events out of hundreds of potential close approaches per satellite every week. The main objectives of the "Collision Risk Estimation and Automated Mitigation" cornerstone in ESA's Space Safety programme are the reduction of operator and analyst efforts by automating the decision process, shortening the time between manoeuvre decision and close approach, and decreasing the number of false alerts.

2 Astrodynamical methods

Various research and development activities have been started in the framework of the programme cornerstone in the past two years to investigate the different aspects of collision avoidance automation. These activities require the development of new supporting astrodynamical theories and methods, e.g.: the robust design of trajectories avoiding multiple encounters; the early identification of events that require mitigation; collision probability computation under large uncertainties; data fusion of multiple catalogues; efficient on-board computations, early identification of manoeuvrable spacecraft where the reachable domain intersects the target orbit. The next two sections discuss two of these aspects: the introduction of new decision metrics into an operational process and the identification of manoeuvrable spacecraft for avoidance coordination.

2.1 Operational process

The collision avoidance process is based on the predicted orbit of the operated spacecraft (target) and conjunction data messages provided by space surveillance systems. For ESA supported missions the process is described in [5]. The data messages contain state and covariance information of catalogued objects (chasers) at the time of closest approach for all events with the miss-distance inside a screening volume around the target. The actionable events from this large set of conjunctions are identified by monitoring the probability of collision, but also other parameters that describe the quality of data, any trends or large variability. The probability of collision is then compared against a predefined reaction threshold, which is often selected to reduce the collision risk over the lifetime of the mission to an acceptable level. This threshold assessment can be performed before the launch and also considers fuel constraints [6]. Collision probabilities are then re-computed and events re-evaluated whenever new data arrives, i.e. when the flight dynamics team updates the predicted trajectory for the target or when new chaser data is received in a conjunction data message. The avoidance decision process therefore requires a time-series analysis, which is considered in the performed machine learning activities using conjunction data [9].

The improved detection performance of new space surveillance systems will increase the number of tracked small debris pieces. The orbital uncertainty for these currently not catalogued objects may be large depending on number of observations used for the orbit determination. Similarly, large manoeuve campaigns e.g. the orbit raising during initial orbit acquisition, lead to larger uncertainties for the target satellite.

These large uncertainties complicate the interpretation of the collision probablity as a criterion due to the so-called dilution of probability [1, 2]. Alternative metrics such as confidence interval intersection have been proposed [2], but operationally they can be difficult to implement as it constraints the amount of safe trajectories during the planning process [5]. The collision probability, however, may underpredict the criticality of the situation and then may suddenly increase once new data arrives. As collision avoidance is a real-time process, the next data update in principle reduces the uncertainty and this information can be used.

*Email: jan.siminski@esa.int

One idea to overcome the limitations of the collision probability is to consider the effect of future data updates already in the planning process. The GNSS-derived orbit determination update for the target will provide a state estimate with a predictable covariance. This future covariance can be used to constrain the expected probability of collision for the next update. This means that an event with a time of close approach after the predicted next update can be classified early as a false alarm or potentially critical. For chaser updates the effect of the next update is not as predictable as for target, but this can be at least approximated with a feasible range from historic data, as e.g. performed in [7]. The next collision probability estimate can then be bounded by maximizing the collision probability within the expected uncertainty range.

2.2 Operator coordination

Before executing any avoidance manoeuvres, the optimised trajectory must be screened against the catalogue and coordinated with other operators to avoid potentially other, new high-risk approaches. Manoeuvre plans as well as orbit predictions are currently directly exchanged between spacecraft operators for each event individually, but the increased number of operational satellites creates the necessity to establish a more efficient exchange mechanism between operators. This concurrent coordination will become an unmanageable task in a future with an increasing launch rate and deployments of smaller satellites and large constellations.

In order to initiate avoidance manoeuvre coordination, manoeuvreable spacecraft in close proximity must be identified. This can be achieved by flagging spacecraft as manoeuvrable on coordination platforms developed in the programme activities. However, in case of unregistered spacecraft such an automated exchange will not be possible and any avoidance action may require additional contact attempts or safety margins. Additionally, uncoordinated manoeuvre plans lead to sudden appearance of conjunction events, which cannot be avoided any more due to limited reaction time.

Several approaches have been developed to identify manoeuvrable spacecraft, e.g. in [4, 3]. These methods detect maneouvre activity in the orbital state time-series from public catalogues. Similarly, historic data can be used to learn manoeuvre patterns and predict future states [8]. The exact estimation is however challenging with no a-priori knowledge on the strategy and optimisation constraints, especially for low-thrust orbit control and initial orbit acquisition. The inferred manoeuvre pattern or identified manoeuvre capabilities of spacecraft can then be used to compute a reachable domain of the post-manoeuvre state and allow early detection of possible close approaches in advance.

3 Summary

The presentation outlines the operational requirements for mathematical methods which are needed to enable future safe operations, summarises first findings from the currently running activities, and presents internal analysis results, i.e. introduction and assessment of alternative collision probability methods, and Delta-V metrics to identify manoeuvrable spacecraft in close proximity that need to be monitored.

References

[1] Balch, M. S., Martin, R., Ferson, S., Satellite conjunction analysis and the false confidence theorem. *Proceedings of the Royal Society* 475 (2019).

[2] Hejduk, M. D., Snow, D. E., Newman, L. K., Satellite conjunction assessment risk analysis for "dilution region" events: Issues and operational approaches, *Space Traffic Management Conference*, Austin, Texas, USA (2019).

[3] Ko, H.C., Scheeres, D.J., Maneuver detection with event representation using thrust fourier coefficients. *Journal of Guidance, Control, and Dynamics*, 39(5) (2016), 1080-1091.

[4] Lemmens, S., Krag, H., Two-line-elements-based maneuver detection methods for satellites in low earth orbit. *Journal of Guidance, Control, and Dynamics*, 37(3) (2014), 860-868.

[5] Merz, K., Siminski, J., Virgili, B.B., Braun, V., Flegel, S., Flohrer, T., Funke, Q., Horstmann, A., Lemmens, S., Letizia, F. and Mclean, F.,ESA's Collision Avoidance Service: current status and special cases, *8th European Conference on Space Debris*, Darmstadt, Germany (2021).

[6] Merz, K., Virgili, B. B., Braun, V., Risk reduction and collision risk thresholds for missions operated at ESA. *27th International Symposium on Space Flight Dynamics*, Melbourne, Australia, (2019).

[7] Metz, S., *Implementation and comparison of data-based methods for collision avoidance in satellite operations*, Thesis (2020).

[8] Siminski, J., Flohrer, T., Schildknecht, T., Assessment of post-maneuver observation correlation using short-arc tracklets. *Journal of the British Interplanetary Society*, 70 (2017),63-68.

[9] Uriot, T., Izzo, D., Simões, L.F., Abay, R., Einecke, N., Rebhan, S., Martinez-Heras, J., Letizia, F., Siminski, J., Merz, K., Spacecraft collision avoidance challenge: design and results of a machine learning competition. *Astrodynamics* (2021), 1-20.

Automation of the collision risk management from conjunction data message reception up to the decision-making

Alexis Petit*[1], Romain Lucken†[1], Sacha Redel‡[2], Florent Deleflie§[2], Vincent Morand¶[3], and François Laporte‖[3]

[1]Share My Space, 14 rue Crespin du Gast, 75011 Paris, France
[2]IMCCE, 77 avenue Denfert Rochereau, 75014 Paris, France
[3]CNES, 18 avenue Edouard Belin 31400 Toulouse, France

Abstract

The automation of the risk management is a major issue for the sustainability of space activities. The number of conjunction alerts is increasing and it will soon overwhelm space traffic management services. In this paper, a bottleneck like conjunction assessment with all catalogued space objects and the detection of past manoeuvres and the prediction of the future ones for secondary objects involved in conjunctions are studied. Solutions are integrated in a simulator of space traffic management challenging our capacity to minimize human interventions.

1 Introduction

Since a couple of years, evolutions of the space traffic management systems are investigated to overcome the new challenges due to the significant increasing number of satellites and space debris but also the diversity of new actors involved (historical operators or new operators of large constellations, universities, startups). A consequence of this change of paradigm is the growing number of conjunction alerts emitted by a conjunction assessment (CA) provider. All do not lead to a collision but a collision risk assessment has to be made and if the risk is above a given threshold, then a collision avoidance manoeuvre can be triggered. The intensification and a complexification of the space traffic has rendered classical approaches unadapted to the current situation.

In the framework of the EUSST, a consortium including Share My Space, the Institut de Mécanique Céleste et de Calcul des Éphémérides (IMCCE) and Quasar Science Resources, was mandated by the Centre National d'Études Spatiales (CNES) to study blocking points for the automation of space traffic management and to propose a simulator of such a system to this end. The study focuses on the following works : The characterisation of the secondary objects involved in a conjunction, The optimisation of the conjunction screening, The simulation of the decision tree of a space traffic management system leading to the final decision to perform or not a manoeuvre. The final purpose is to assess the extent to which the automation can be applied to quantify the cases where human actions are still required.

*Email: alexis.petit@sharemyspace.space.
†Email: romain.lucken@sharemyspace.space.
‡Email: sacha.redel@obspm.fr.
§Email: florent.deleflie@obspm.fr.
¶Email: vincent.morand@cnes.fr.
‖Email: francois.laporte3@cnes.fr.

2 Secondary object classification

Increasingly more satellites are launched each year, whether it be by small or large operators, in LEO, MEO or GEO, using chemical or electrical propulsion. Therefore, their orbital behaviors differ according to their strategies, for example during orbit raising phase or to perform station keeping. Without systemic communication of ephemerides including scheduled manoeuvres by operators, the risk management based only on SP ephemerides computed and provided by the 18th Space Defense Squadron (SDS) can lead to wrong decisions and, in worst cases, to a catastrophic collision event. Thus, the characterisation of secondary behavior i.e. if a satellite is able to maneouvres or not, and the prediction of a future manoeuvre is crucial.

For this purpose, the historical state vectors are a valuable source of data for manoeuvre operations detection. Two types of data are provided by the 18 SPC:

- Two-line element (TLE) sets are public data available through the 18 SDS plaform (`www.space-track.org`), and they contain mean orbital elements of an object in the TEME frame. The TLE are in the public domain and their accuracy is limited. They are provided for about 22,000 objects non-classified by the US Air Force, and refreshed at a variable rate, typically 12 hours.
- SP vectors are generated by 18 SDS using the Special Perturbation theory and contain osculat-

ing elements of an orbiting object. The positions and velocities of the object are given in TEME frame and generated once a day. The state vector epoch can vary from an object to another.

A first method is well suited to historical TLE data [5]. It allows to detect abrupt changes in the orbital parameters such as the semi-major axis for in-plane manoeuvres or inclination for out-of-plane ones. Temporal windows are fitted using polynomials and the filtered differences are computed between each adjacent window. The identification of peaks can then be applied to detect anomalous behavior in the filtered semi-major axis/inclination differences.

A second method is based on the use of SP vectors, which are osculating elements, yielding more precision in manoeuvre detection. Given a pair of SP vectors separated by one day, the algorithm numerically cross-propagates (forward/backward) the trajectories with high-fidelity force models. The relative distance between the two propagated ephemerides can then be computed. The existence of large discrepancies typically indicates that a manoeuvre has been performed between the two observations, therefore the minimum relative distance corresponds to the most likely epoch of the manoeuvre. The delta-V magnitude of the detected manoeuvre can be retrieved at the estimated epoch by interpolating the relative velocity. Besides leading to reliable detection of small chemical manoeuvres (typically at millimeter-per-second accuracy), the main benefit of this method is that it allows to detect low-thrust manoeuvres by applying the cross-propagation iteratively.

3 Screening All versus All

Conjunction assessment is a major issue for collsion risk assessment. It is mainly performed by CA provider like the 18 SDS but screening is required if new data is available, for example if a new satellite ephemeride is generated for collision avoidance manoeuvre. As the number of objects is growing, whether it be due to the annually increasing amount of satellite launches, or to new detected objects, the US catalog will soon reach about 30 000 space objects. A population of N space objects leads to $N(N-1)$ pairs to examine or about 900 millions of pairs for the US catalog expected for the following years.

Fortunately, filters can be applied sequentially to exclude pairs of objects where a close approach is impossible [1] [2]. These are described below:

- Altitude filter: It computes maximum apogees and minimum perigees at the middle epoch of a given interval and compares the values to exlude incompatible orbits.
- Inter-orbit distance filter: It computes the Minimum Orbital Intersection Distance (MOID) using osculating elements at the middle epoch of the time interval. The variation of the inter-orbit distance due to perturbations is taken into account.
- Time filter: The temporal filter determines the interval of time where each object is at the intersection nodes of the orbits. Only both in this place they have a possibility to have a dangerous conjunction.

On each dangerous interval, the Time of Closest Approach (TCA) and the miss distance between two objects are calculated. We implemented a solution using Chebyshev Proxy Polynomials (CPP) [3] [4]. This method proposes to fit the derivative of the relative distance function with CPP and to use an efficient linear algebra library to extract the roots. These roots correspond to the extrema of the relative distance function, and to the TCA and the miss distance in consequence. If the miss distance is lower than a user-defined threshold, typically 5 km for LEO and 10 km for GEO/MEO, a dangerous conjunction is identified.

Moreover, the use of multi-threading with an optimisation of memory management was also implemented to deal with more than 20 000 ephemerides. To this end, ephemerides were converted into binary format to allow faster access and to reduce the memory needed to store all of them. Multi-threading was used on groups of objects, sorted by semi-major axis, to have an efficient process allowing to reach the remarkable performance of less than 2 hours for approximately 21 000 objects.

4 Simulation of a space traffic management system

A simulator was developed to process conjunction alerts as Conjunction Data Messages (CDM) received from the 18th Space Control Squadron (SCS). It includes risk assessment, charaterisation of the secondary objects, and a collision avoidance manoeuvre module providing the final decision to perform a manoeuvre or not. The purpose is the assessment of the number of interactions with other entities (satellite operators/owners, data providers) and the number of cases for which human intervention is required, representing a limit to automation.

Based on the CNES Java libraries, the simulator interacts with a database containing data relative to catalogued objects, space vectors (TLE or SP), satellite operator/owner names and coordinates, historical manoeuvres, pattern-of-life and conjunction events. In Figure 1, the flowchart of the simulator is provided. A configuration file allows to setup the parameters of the CDM processing such as collision probability

threshold or scenarios for collision avoidance manoeuvres. Moreover, it allows to specify the CDM of interest in a large dataset of historical CDM referenced in an indexation table. Then, conjunction events related to missions on specific orbits or a timespan can be selected. The outputs as log files contain all taken actions or interactions with other actors. It outputs as well some interesting metrics on the automation as given by the Figure 2 where the number of CAM design operations, human actions and planned CAM are provided.

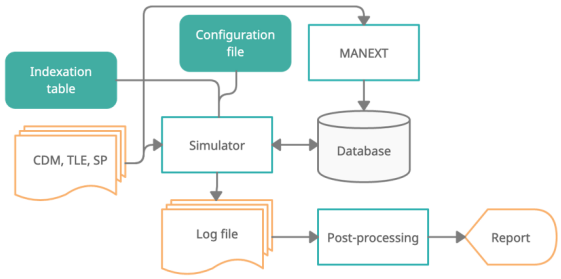

Figure 1: Flowchart of the simulator dealing with CDM to assess conjunction risk and make the decision to perform a manoeuvre or not. The simulator interacts with a database of space objects data in particular a database of historical manoeuvres and pattern-of-life computed with the tool MANEXT.

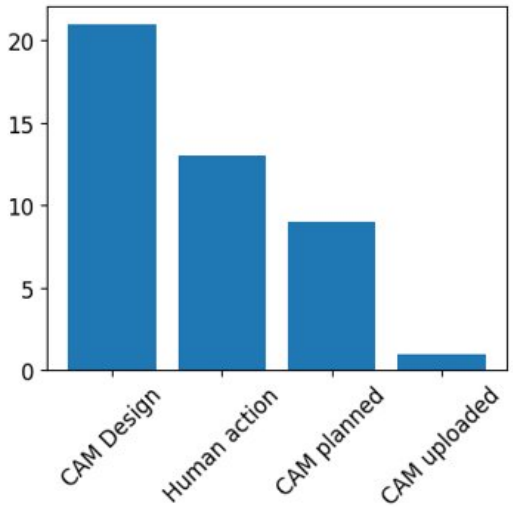

Figure 2: Number of actions related to collision avoidance manoeuvres simulated for a GEO satellite using low-thrust propulsion over a period of one year.

5 Conclusions

The management of the space traffic is very challenging for the years to come. It requires the improvement of the current state-of-the art, in particular to overcome the increasing quantity of data to process. A change of paradigm is arriving with large fleets of several hundreds or thousands of satellites, leading to a tremendous number of conjunction alerts, overwhelming operators.

The automation of the risk assessment and decision-making is becoming a standard. In this context, the simulator developed in this study is a unique tools to test assumptions, new algorithms or rules of the space traffic and giving a feedback of their efficiency. In addition, the improvement of the efficiency of the "all versus all" conjunction screening now achievable, lowering the computation time to a few hours, and the characterization of manoeuvring satellite are two major milestones solving bottlenecks in automation.

Acknowledgements

The EU SST activities have received funding from the European Union programmes, notably from the Horizon 2020 research and innovation programme under grant agreements No 952852, No 785257, No 760459, No 713630 and No 713762, and the Copernicus and Galileo programme under grant agreements No 299/G/GRO/COPE/19/11109, No 237/G/GRO/COPE/16/8935 and No 203/G/GRO/COPE/15/7987.

References

[1] F. R. Hoots, L. L. Crawford, R. L. Roehrich. An analytic method to determine future close approaches between satellites. *Celestial mechanics*, **33(2)** (1984), 143-158.

[2] D. Casanova, C. Tardioli, A. Lemaitre. Space debris collision avoidance using a three-filter sequence. *Monthly Notices of the Royal Astronomical Society*, **442(4)** (2014), 3235-3242.

[3] E. Denenberg, P. Gurfil. Improvements to time of closest approach calculation. Journal of Guidance, Control, and Dynamics, **39(9)** (2016), 1967-1979.

[4] E. Denenberg. Satellite closest approach calculation through Chebyshev Proxy Polynomials. *Acta Astronautica*, **170** (2020), 55-65.

[5] T. Kelecy, D. Hall, K. Hamada, D. Stocker. Satellite maneuver detection using Two-line Element (TLE) data. In Proceedings of the Advanced Maui Optical and Space Surveillance Technologies Conference. Maui, HA: Maui Economic Development Board (MEDB), (2007, September).

Covariance determination for uncertainty realism in collision probability estimates

Alejandro Cano*[1,2], Alejandro Pastor[1], Eduardo Arias[1], Daniel Sáez[1], Joaquín Míguez[2], Manuel Sanjurjo-Rivo[2], and Diego Escobar[1]

[1]GMV, 11 Isaac Newton, 28760 Tres Cantos, Madrid, Spain
[2]University Carlos III of Madrid, Av. de la Universidad 30, 28911 Leganés, Madrid, Spain

1 Introduction

Due to the ever-increasing population of Earth-orbiting objects, either operational or debris, the quality of Space Situational Awareness (SSA) services becomes crucial for the safety and sustainability of space operations. Reliable conjunction detection and collision risk assessment activities are required, especially for over-crowded regions such as Low Earth Orbits (LEO) or Geostationary Orbits (GEO) where most of the space activity occurs. The main objective of collision risk analysis is to provide a Probability of Collision (PoC), one of the main metrics used by the satellite operators to design possible Collision Avoidance Manoeuvres (CAM). Therefore, more reliable estimates of the PoC can improve the decision-making process of the conjunction events, reducing the amount of unnecessary collision avoidance manoeuvres and thus, increasing the mission lifespan and decreasing operator efforts.

Most PoC computation algorithms rely on the state uncertainty, generally represented by a covariance matrix as obtained from typical Orbit Determination (OD) processes. Many existing OD processes are based on batch least-squares estimator, which provide the orbit estimate (state and covariance) as nominal output, assuming that measurements are sufficient and available. Along this process, the dynamical model is usually deterministic, and the only source of uncertainty considered is the measurement noise [1]. The resulting covariance matrix is known as the noise-only covariance [2]. However, one of the main sources of uncertainty during OD and subsequent propagation are the errors in the underlying dynamical models, which are typically disregarded [3, 2]. Neglecting the dynamical models uncertainty leads to overly-optimistic covariance matrices which are not representative of the actual uncertainty of the estimate (i.e. not realistic) [4]. The loss of the covariance realism, regardless of undersized or oversized estimations, has a significant impact on the PoC reliability [5, 6].

In operational scenarios, simple techniques are required to improve covariance realism. A widely applied technique is the covariance scaling, this is, inflating the covariance with a certain scalar factor. Some authors propose the computation of such scaling based on increasing the initial position uncertainty to match the velocity error [7]. Others explore the use of the Mahalanobis distance of the orbital differences to find the scale factor for both the primary and secondary object, based on the analysis of historical information of the conjunction event [8]. These methods lead to the so-called Scaled PoC. One of the main drawbacks of covariance scaling techniques is that a single factor is applied to the complete covariance matrix, similar to a safety factor, losing the physical sense of the covariance inflation. For instance, the uncertainty related to the atmospheric density in LEO accumulates mostly in the direction of the velocity, which cannot be characterised by a single scaling factor for the entire covariance matrix.

A different method for covariance realism improvement is presented in this work, introduced in previous studies [9] and more recently in [10, 11]. The methodology, detailed in Section 2, is based on the *consider parameter* theory and the χ^2 distribution, using the orbital differences between estimated and predicted orbits to infer the variance of the considered parameters introduced in the dynamical model. One of the benefits of the presented approach is that a clear traceability of the uncertainty sources is kept, maintaining the physical interpretation of the covariance correction and improving the covariance realism by targeting specific uncertainty sources.

In this work, we present the main concepts behind this covariance determination methodology, highlighting the main ideas and covariance realism improvement results. Once introduced the methodology to improve the realism of the estimated covariance, we want to analyse its impact in the computation of the PoC. The objective is to compare the PoC impact of this consider parameter correction of the covariance with the performance of other scaling factor methods that are widely used for PoC, such as the Scaled PoC method of Kp-Ks. For this purpose, different simu-

*Email: alcano@gmv.com

lated scenarios will be designed, in this case focusing on High Interest Events with different collision geometry (head-on and lateral), and also in a well known collision event such as the Cosmos-Iridium. The simulation process is not limited to the conjunction event itself, but also the population of estimated and predicted orbits required for the proper functioning of the covariance determination methodology must be simulated accordingly, introducing realistic uncertainty in the dynamical models.

2 Methodology

A very brief description of the covariance determination methodology is provided next, based on previous works [10, 11, 9]. The proposed covariance determination method improves the realism of the covariance by characterising the dynamic and measurement models' uncertainty using the *consider parameter* theory. A set of uncertain parameters are included in the underlying dynamical models, in such a way that the model uncertainty is represented by the variance of these parameters. These parameters are assumed to follow a zero-mean Gaussian distribution, and an unknown variance a-priori ($c_i \sim \mathrm{N}\left(0, \sigma_i^2\right), i = 1, \cdots, n$) The estimated covariance is affected by the variance of the introduced parameters as [1]

$$\mathbf{P}_c = \mathbf{P}_n + \mathbf{KCK}^T \in \mathbb{R}^{n_y \times n_y} \tag{1}$$

$$\mathbf{K} = \mathbf{P}_n \left(\mathbf{H}_y^T \mathbf{W} \mathbf{H}_c\right) \in \mathbb{R}^{n_y \times n_c} \tag{2}$$

where n_y is the dimension of the state, $\mathbf{H_y}$ corresponds to the Jacobian of the observations with respect to the estimated state, $\mathbf{W}$ is the weighting matrix containing the expected noise of each measurement and the possible correlation among the measurements and $\mathbf{C}$ is a diagonal matrix containing the variance of the consider parameters, of size n_c. Therefore, the consider covariance is obtained as the sum of the noise-only covariance and a covariance correction, which depends linearly on the consider parameter variances.

The main drawback of the consider parameter theory is that realistic variances of the consider parameters are not known a-priori. The covariance determination process that is applied in this work infers the variance of the consider parameters based on the observed distribution of the Mahalanobis distance of the differences between predicted and estimated orbits. By comparing orbit estimations (backed-up by observations) with orbits propagated using the same dynamical model, the error present in the models are expected to be observable within the orbital differences, and they shall follow a χ^2 distribution under Gaussian assumption provided that the covariance is realistic.

The Mahalanobis distance (d_M) is a well-known statistical metric that describes how far a state $\mathbf{y}(t)$ is from a certain reference $\mathbf{y}_{ref}(t)$, projected into the covariance space [12]:

$$d_M^2 = \left(\mathbf{y} - \mathbf{y}_{ref}\right)^T \left(\mathbf{P} + \mathbf{P}_{ref}\right)^{-1} \left(\mathbf{y} - \mathbf{y}_{ref}\right) \tag{3}$$

where $\mathbf{P}$ and $\mathbf{P}_{ref}$ are the covariance matrices of the state and the reference, respectively. Combining Equations 1 and 3, we obtain

$$d_M^2(t) = \frac{\Delta\mathbf{y}(t)^T \Delta\mathbf{y}(t)}{\mathbf{\Psi}\left(t, t_0\right)\left(\mathbf{P}_n + \mathbf{KCK}^T\right)\mathbf{\Psi}\left(t, t_0\right)^T + \mathbf{P}_{ref}} \tag{4}$$

where $\Delta\mathbf{y}(t) = \mathbf{y}_{ext}(t) - \mathbf{y}_{ref}(t)$. $\mathbf{\Psi}$ represents the extended State Transition Matrix (including both state and sensitivity matrices) [2], applied to propagate linearly the covariance to the desired comparison epoch. The reference orbit $\mathbf{y_{ref}}(t)$ that is required for the Mahalanobis distance can correspond to a precise ephemeris information of a known object, but it is also showed in [9, 10, 11] that estimated orbits can be used as reference as well, not requiring external sources of ephemeris. Equation (4) allows to compute the Mahalanobis distance at any epoch along the propagation arc as a function of the consider parameter variances contained in matrix $\mathbf{C}$, assuming that a batch least-squares parameter estimation process has been performed, followed by a propagation step.

Therefore, the proposed covariance determination methodology consists in, given a population of orbits from a certain object, finding the variance of the consider parameters (included in matrix $\mathbf{C}$) so that the observed d_M^2 distribution resembles the theoretical χ^2 distribution. This is achieved in a muti-variable minimisation process, where Empirical Distribution Function (EDF) statistics are used as cost function, such as Cramer-von-Mises or Kolmogorov-Smirnov statistics [13].

3 Covariance determination results

The proposed methodology has been validated in a realistic simulated scenario in [9] and more recently in [10, 11]. It has been applied as well to real data of Sentinel 3A [9], also showing a significant improvement in the realism of the covariance. Here we present some examples of the covariance realism enhancement achievable with the proposed covariance determination methodology. Figure 1 below shows the final distribution of the d_M^2 population after the minimisation process, in this case using 3 degrees of freedom (position covariance), for a LEO object. Three different consider parameters were included in this analysis, representing the uncertainty in the drag force (drag coefficient, area, mass and atmospheric density), the

uncertainty in the prediction of the space weather proxies and the uncertainty in the range bias. The resulting variance of the consider parameter is very similar to the input uncertainty in the system, and the final distribution matches properly the theoretical χ^2 one, confirming that the selected dynamic model is satisfactory. Additionally, the Cumulative Distribution Function (CDF) of the distribution without applying any consider parameter correction is depicted in black, showing that in the presence of model errors, the noise-only covariance is not realistic.

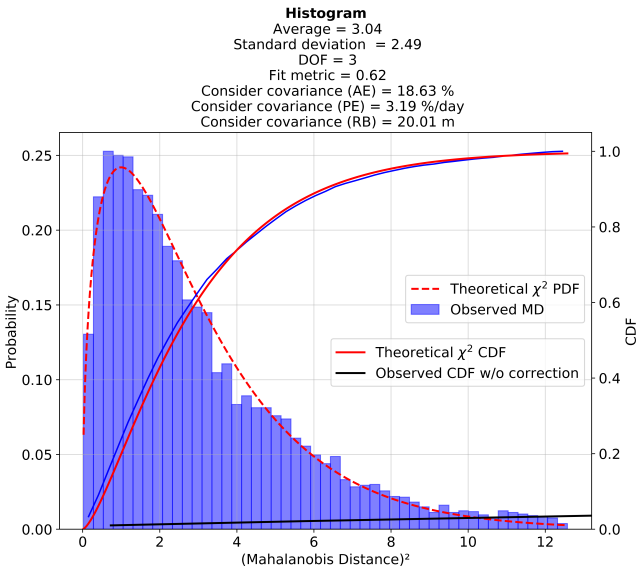

Figure 1: d_M^2 distribution with optimum consider covariance results. Input test uncertainty were: $\sigma_{AE} = 20\%$; $\sigma_{RB} = 20$m; $\sigma_{PE} = 3$ %/day. From [10].

To assess the covariance realism, covariance containment tests can be applied [7, 14] to assess the amount of samples of the population that lay inside the covariance ellipsoid, comparing it against the theoretical expectations of a multivariate Gaussian distribution. Table 1 shows containment results with the proposed covariance determination methodology, at several propagation days for different covariance ellipsoids. The average containment obtained with this methodology is similar to the theoretical expectations, which is one indicator of covariance realism. The average containment obtained when no consider parameter correction is applied has been included as baseline. Additionally, the realism of the noise-only covariance does not hold when model uncertainty is present in the system.

Table 1: Consider covariance containment, from [10]

Containment [%]	1σ	2σ	3σ	4σ
Average [noise-only]	0.25	1.23	2.58	3.99
Average	21.39	71.73	94.96	99.66
Theoretical (3DOF)	19.90	73.90	97.10	99.87

References

[1] B. D. Tapley, B. E. Schutz, and G. H. Born, *Statistical Orbit Determination*. San Diego, California: Elsevier Academic Press, 2004.

[2] O. Montenbruck and E. Gill, *Satellite Orbits: Models, Methods and Applications*. Berlin: Springer-Verlag Berlin Heidelberg, 2000.

[3] K. Alfriend and M. Wilkins, "Covariance as an estimator of orbit prediction error growth in the presence of unknown sensor biases," *American Astronomical Society*, vol. 103, pp. 99–422, 01 2000.

[4] D. A. Vallado, *Fundamentals of Astrodynamics and Applications*. Space Technology Library, Hawthorne, CA: Springer and Microcosm Press, forth ed., 1997.

[5] S. Alfano and D. Oltrogge, "Probability of collision: Valuation, variability, visualization, and validity," *Acta Astronautica*, vol. 148, pp. 301–316, 2018.

[6] M. D. Hejduk, "Satellite conjunction assessment risk analysis for "dilution region" events: Issues and operational approaches," in *Space Traffic Management Conference*, no. 28, 2019.

[7] Z. Folcik, A. Lue, and J. Vatsky, "Reconciling covariances with reliable orbital uncertainty," in *Advanced Maui Optical and Space Surveillance Technologies Conference*, p. E34, Sept. 2011.

[8] S. Laurens, P. Seimandi, J. Couetdic, and J. Dolado, "Covariance matrix uncertainty analysis and correction," in *68th International Astronautical Congress*, 2017. id: IAC-17,A6,7,2,x37415.

[9] A. Cano, A. Pastor, and D. Escobar, "Covariance determination for improving uncertainty realism," in *8th European Conference on Space Debris*, ESA Space Debris Office, 2021.

[10] A. Cano, A. Pastor, D. Escobar, J. Míguez, and M. Sanjurjo-Rivo, "Covariance determination for improving uncertainty realism in orbitdetermination and propagation," *Advances in Space Research*, 2022, (Accepted for publication, AISR-D-22-00023).

[11] A. Cano, A. Pastor, S. Fernández, J. Míguez, M. Sanjurjo-Rivo, and D. Escobar, "Improving orbital uncertainty realismthrough covariance determination in geo," *Journal of the Astronautical Sciences*, 2022, (accepted for publication, JASS-D-22-00019).

[12] P. Mahalanobis, "On the generalised distance in statistics," in *Proceedings of the National Institute of Sciences of India*, vol. 2, pp. 49–55, 1936.

[13] R. B. D'Agostino and M. A. Stephens, *Goodness-of-fit techniques*, vol. 68 of *STATISTICS: Texbooks and Monographs*. New York: MARCEL DEKKER, INC, 1986.

[14] W. Wiesel, *Modern Orbit Determination*. Beavercreek, OH: Aphelion Press, 2003.

Deep learning for all-vs-all conjunction detection

Emma Stevenson*[1], Victor Rodriguez-Fernandez†[1], Hodei Urrutxua‡[2], and David Camacho§[1]

[1]School of Computer Systems Engineering, Universidad Politécnica de Madrid, Calle de Alan Turing, 28038 Madrid, Spain

[2]European Institute for Aviation Training and Accreditation, Universidad Rey Juan Carlos, Camino del Molino 5, 28942 Fuenlabrada, Spain

Abstract

This paper explores the use of different deep learning techniques for detecting conjunction events in an efficient and accurate way for improved space situational awareness. Framing the problem as a machine learning classification task, we present the performance of different data representations and model architectures on a realistic all-vs-all dataset generated using the CNES BAS3E space surveillance simulation framework, and compare the approaches to operationally used classical filters in screening performance and computational efficiency. Finally, we also investigate a novel methodology for improving the performance and generalisation ability of the models using a pre-trained orbit model, ORBERT, based on self-supervised learning techniques.

1 Introduction

Ensuring the safety and sustainability of space operations in the New Space era is an ever-increasing challenge for Space Traffic Management (STM), in which one of the most important activities is the detection and prevention of on-orbit collisions. Although many conjunction events involving active satellites may be safely evaded through collision avoidance manoeuvres, albeit with significant effort, conjunctions between two non-manoeuvrable space debris objects are far more frequent, and threaten both the safety of current day space assets as well as the long-term usability of the space environment [1]. The so-called *all-vs-all* problem, for which conjunctions are screened for over all possible sets of catalogued objects, is therefore crucial to space situational awareness (SSA), but is a computational challenge owing to the vast and growing number of possible conjunction pairs. To address the challenges posed by the scale and complexity of these activities, one emerging approach is the exploitation of recent advancements in the fields of machine learning (ML) and, in particular, deep learning (DL) [2, 3], a subfield of machine learning that uses neural networks with multiple hidden layers, enabling its models to outperform classical machine learning algorithms in both accuracy and scalability.

In this work, we propose to apply these techniques to the problem of efficient large-scale conjunction detection, and investigate whether they can be used to accurately identify high risk conjunction cases whilst simultaneously reducing computational expense. In our approach, we therefore do not propose to replace the entire conjunction assessment pipeline with an end-to-end black box artificial intelligence (AI) system, but rather use it as an efficient first filter or initial screening to complement existing systems, as illustrated in Figure 1. This enables a significantly reduced set of high risk candidates to be passed to pre-existing operationally used, and trusted, numerical or analytical methods for performing further refinement and collision risk evaluation. Here, we employ a realistic dataset of conjunction pairs in Low Earth Orbit (LEO) over a typical 7-day screening period, and present an analysis of different deep learning techniques which can be used to address and aid in this problem.

2 Conjunction dataset

We base our data-driven approach on a conjunction dataset that was generated using the CNES BAS3E (**B**anc d'**A**nalyse et de **S**imulation d'un **S**ysteme de **S**urveillance de l'**E**space – Simulation and Analysis Bench for Space Surveillance System) space surveillance simulation framework [4] for all catalogued object pairs in LEO over a 7-day screening period. For this, we considered the two-line element set (TLE) LEO population on the 1st of June 2020, as retrieved from space track, which comprised 18415 objects, and consequently 170 million possible conjunction pairs. These objects were propagated over a 7-day period using a full force model, accounting for atmospheric drag and Sun and Moon third body perturbations,

*Email: emma.stevenson@upm.es. Research supported by the EU H2020 MSCA ITN Stardust-R, grant agreement 813644.
†Email: victor.rfernandez@upm.es
‡Email: hodei.urrutxua@urjc.es
§Email: david.camacho@upm.es

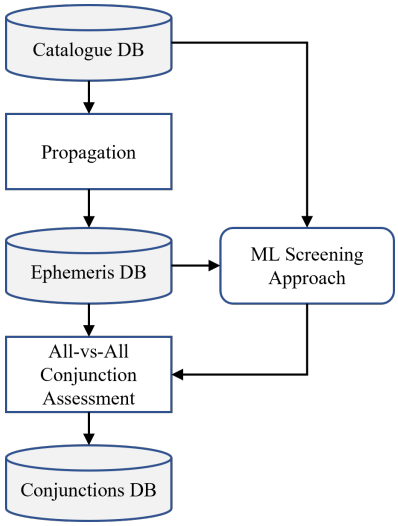

Figure 1: Illustration of machine learning screening concept to aid and complement existing operational all-vs-all conjunction assessment.

and checked pairwise for conjunctions using a distance based threshold of 20 km (spherical shape of the safety volume). 1.5 million close conjunction cases were found as a result, forming less than 1% of the total number of object pairs, and thus the dataset can be seen to be both of a large-scale and highly imbalanced nature. Owing to the large number of object pairs, this process was extremely computationally expensive, taking approximately 4 days of computation time on the CNES High Performance Computing (HPC) service, which demonstrates the interest of investigating ML screening techniques for current and future space object populations.

3 Training a conjunction detection model

Based on this dataset, we phrase the concept of conjunction detection as a machine learning classification task. In this way, a machine learning model learns to predict a binary class as to whether a given object pair will have a conjunction over the next 7 days, based on orbital data as input, and class labels (conjunction or no conjunction) provided by BAS3E [2]. The trained model can then be used to predict and subsequently filter or discard non-conjunction pairs based on their orbital data, thus reducing the computational burden on the full operational all-vs-all conjunction assessment procedure.

In this work, we explored the use of different data representations and architectures for this task, focusing on two main families of models, tabular models based only on initial states, and more complex time series models based on full ephemerides. Comparing these approaches to classical filtering techniques such as the apogee-perigee and path geometric filters [5], as well as the ephemeris based "smart sieve" [6], we found that these models can offer improvements both in filtering performance and computational expense. There is, however, a trade-off between the additional accuracy gained by using more complex models, that can better capture the effects of perturbations towards the end of the screening period, and the additional computation expense required for both training and inference of such models. A second trade-off is present between the overall accuracy of the model, and the number of False Negatives (FNs) generated by the model, conjunction cases which are misdiagnosed as non-conjunction cases and thus wrongly, and potentially critically, discarded by the screening process. Several methods were developed for forcing the importance of these cases including weighted loss functions, and the tuning of the class probability threshold to ensure that only cases for which the model has high confidence are rejected, which we translate into an operator constraint.

Although this approach was found to be promising and competitive on in-distribution data, over the same epochs and altitude regime as the training data, some weaknesses were identified in the ability of the models to generalise out of distribution. To account for this, we are investigating the use of pre-trained orbit models to better inform the conjunction detection models on orbit behaviour in different perturbation regimes.

4 Pre-training an orbit model

Pre-training a model is the first important step in *transfer learning*, in which the weights of a model trained on a "pretext task" can be updated (or "fine-tuned") on a final task, commonly known as the downstream task, to improve downstream performance and efficiency. This pre-text task may be different to the downstream task, allowing the pre-trained model to capture fundamental representations from a large unlabelled dataset that may aid in the final task. For example, in the field of Natural Language Processing (NLP), pre-training a language model to predict missing words or phrases from a large corpus of unlabelled text enables the model to learn meaningful language representations, which can then be used for downstream tasks such as sentiment analysis, to predict whether a given phrase is positive or negative. This approach makes use of a novel technique called self-supervised learning, so-called because the labels used for training are embedded in the data itself.

Taking inspiration from these techniques, we instead construct a pre-trained orbit model that is able to leverage large quantities of readily available orbital data to learn meaningful orbit representations, which can in turn be used to improve the performance of downstream SSA tasks such as conjunction detec-

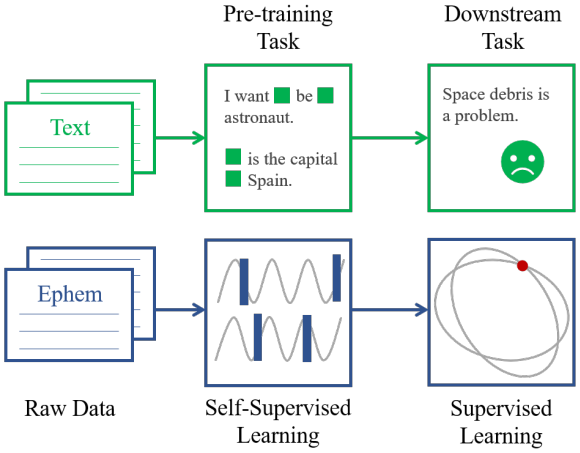

Figure 2: Analogy of the proposed pre-trained orbit modelling approach with that used in the domain of Natural Language Processing (NLP).

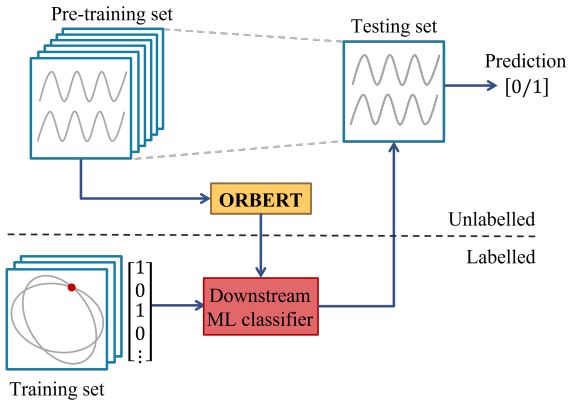

Figure 3: Illustration of the pre-training concept which leverages available orbit data to improve the performance of downstream supervised tasks such as conjunction detection.

tion [3] (see Figure 2). Our orbit model, ORBERT (named after Google's breakthrough BERT language model [7]), is trained using a self-supervised approach for time series [8], where, instead of masking words or phrases, sections of orbit ephemeris are masked, and the model tasked with their reconstruction. This enables it to learn meaningful orbit representations which can be passed to orbit-related tasks, as illustrated in Figure 3. To promote generalisation, we can include ephemerides from a variety of different epochs and altitude regimes in the pre-training set to cover different perturbation regimes to train ORBERT. These learnt weights may then be used to initialise the training of our downstream conjunction detection classifier, passing on an underlying understanding of the perturbing forces affecting space objects, to provide better conjunction predictions on the final testing set.

Acknowledgements

This research is supported by the EU H2020 MSCA ITN Stardust-R, grant agreement 813644. The authors would like to thank Vincent Morand for his help and technical support in providing the BAS3E dataset. The authors would also like to acknowledge the Spanish State Research Agency and the European Regional Development Fund for their support through the research grant PID2020-112576GB-C22 (AEI/ERDF, UE).

References

[1] Bonnal, C., McKnight, D., Phipps, C., Dupont, C., Missonnier, S., Lequette, L., Merle, M., and Rommelaere, S. Just in time collision avoidance – A review. *Acta Astronautica* **170**, 637–651 May (2020).

[2] Stevenson, E., Rodriguez-Fernandez, V., Urrutxua, H., Morand, V., and Camacho, D. Artificial intelligence for all vs. all conjunction screening. In *Proceedings of the 8th European Conference on Space Debris*, April (2021).

[3] Stevenson, E., Rodriguez-Fernandez, V., Urrutxua, H., Morand, V., and Camacho, D. Self-supervised machine learning based approach to orbit modelling applied to space traffic management. In *Proceedings of the 11th International Association for the Advancement of Space Safety Conference*, October (2021).

[4] Morand, V., Yanez, C., Perez, J. C. D., Fernandez, C., Roussel, S., Pucel, X., and Vidal, V. BAS3E: A framework to conceive, design, and validate present and future SST architectures. In *Proceedings of the 1st NASA International Orbital Debris Conference*, December (2019).

[5] Hoots, F. R., Crawford, L. L., and Roehrich, R. L. An analytic method to determine future close approaches between satellites. *Celestial mechanics* **33**(2), 143–158 June (1984).

[6] Alarcón Rodríguez, J. R., Martínez Fadrique, F., and Klinkrad, H. Collision risk assessment with a 'smart sieve' method. In *Proceedings of Joint ESA-NASA Space-Flight Safety Conference*, volume 486, 159–164, (2002).

[7] Devlin, J., Chang, M.-W., Lee, K., and Toutanova, K. BERT: Pre-training of deep bidirectional transformers for language understanding. In *Proceedings of the 2019 Conference of the North American Chapter of the Association for Computational Linguistics*, 4171–4186, June (2019).

[8] Zerveas, G., Jayaraman, S., Patel, D., Bhamidipaty, A., and Eickhoff, C. A transformer-based framework for multivariate time series representation learning. *arXiv* **abs/2010.02803** (2020).

Fast Orbit Propagation for Conjunction Screening

Ana S. Rivero*[1], Claudio Bombardelli†[2], and Rafael Vazquez‡[1]

[1]Escuela Técnica Superior de Ingeniería, Universidad de Sevilla, Spain.
[2]Grupo de Dinámica Espacial, Universidad Politécnica de Madrid, Spain.

Abstract

Predicting the risk of a collision in space has become a increasingly challenging task, given the steady increase of number of objects in space. In this prediction, the first step that needs to be performed is on-orbit conjunction assessment (CA) or conjunction screening (CS), a process that iteratively identifies close approaches between resident space objects (RSOs) in a time horizon of a few days (typically 5-10 days). The United States 18th Space Control Squadron (18 SPCS) performs CS of the whole 18 SPCS catalogue of roughly 25,000 objects using restricted high accuracy catalogue data (HAC) as well as ephemeris data provided by different spacecraft owner/operators (O/O). A CS operation can also be performed by an O/O starting from the operational orbit file of a specific satellite to identify close approaches between the covered satellite mission (the "target object") and an accessible space catalogue of "chaser objects". The screening frequency is normally once every 24 hours but can be increased to once every 8 hours for conjunctions belonging to a concern list. The task of detecting all close approaches for a large population of RSOs is highly demanding from the computational time point of view and the use of conjunction filters (or other filters) as well as extremely fast propagation methods is paramount. Here, we propose the use of advanced orbital motion formulations coupled to simple fixed-step numerical integrators to reduce the computation time to a minimum while retaining sufficient conjunction detection accuracy. The tradeoff between computation time and accuracy while considering covariance limitations of available ephemeris data is discussed in detail.

1 Introduction

Predicting the risk of a collision in space has become a increasingly complex and challenging task for control centers in charge of space monitoring, given the steady increase of number of objects in space. Indeed, in recent years, several companies have started the deployment of large constellations of small to medium-sized satellites, which will considerably increase the complexity of space operations. Two dozen companies, when taken together, have proposed placing well over 20,000 satellites in orbit in the next 10 years [1]; to put this number into perspective, one must take into consideration that only around 8000 objects were placed in Earth orbit since the beginning of the space age. In addition, one must take into account the population of space debris; in fact, the number of small orbital debris in near-Earth space is several orders of magnitude greater than the number of large, cataloged space objects and is growing progressively [2].

Thus, the risk of losing a satellite during a collision is not negligible [3] and such an event would not only result in the destruction of the two objects, but also in the creation of a large amount of debris, which can in turn produce more collisions; thus it is in everyone's best interest to avoid collisions from happening. A primary example took place on 10 February 2009, when two intact satellites, Cosmos 2251 and Iridum 33 collided at an altitude of 789 km above Siberia [4], generating thousands of debris. Cosmos 2251 was a Strela-2 Russian spacecraft used for military communications, which had been decommissioned more than ten years earlier. Iridium 33 was an operational spacecraft of the homonymous private constellation satellite phone services. The event boosted the catalogued population in Low Earth Orbit by more than 40%. The effect of this event extended beyond orbits close to the originating objects. For instance, the ISS had to perform collision-avoidance manoeuvres in 2014 due to fragments generated in the Cosmos-Iridium event [5], five years later than the event happened.

To manage the risk of collision, operators use the available space surveillance data, which allows them to predict close encounters (a few days in advance), assess the threat level by computing the probability of collision, and then, if deemed necessary, carry out a collision avoidance maneuver, which slightly alters the satellite's trajectory so it passes a safe distance away from the dangerous object. The first step in the process is to find close approaches between objects of interests and other objects. This is accomplished by conjunction screenings, in which the pre-

*Email: asanchez8@us.es
†Email:claudio.bombardelli@upm.es
‡Email: rvazquez1@us.es

dicted positions of the primary object and all other space objects that survive a previous filtering process are compared [6]. The filtering process is performed in order to reduce the computational load as there are pair of objects that can never lead to a collision, to cite a very basic example, objects in LEO vs. objects in GEO.

While conjunction analysis methods are functional at the present, the tremendous increase in the space object population that is expected in the next few years will require screening processes to be adapted to deal with larger volumes of data [7]. This works aims to reduce the computational load, without loss of accuracy, for the processes of conjunction screening, including the use of conjunction filters, both of which are defined next in more detail in Sections 2 and 3, respectively. We then introduce our ideas to close approach detection in Section 4, to be presented at the workshop, and finish with some concluding remarks in Section 5.

2 Conjunction Screening

On-orbit conjunction assessment (CA) or conjunction screening (CS) is a process that iteratively identifies close approaches between resident space objects (RSOs) in a time horizon of a few days (typically 5-10 days). The United States 18th Space Control Squadron (18 SPCS) performs CS of the whole 18 SPCS catalogue of roughly 25,000 objects using restricted high accuracy catalogue data (HAC) as well as ephemeris data provided by different spacecraft owner/operators (O/O). The screening frequency is normally once every 24 hours but can be increased to once every 8 hours for conjunctions belonging to a Concern List [8].

In particular, a CS operation can be performed by an O/O starting from the operational orbit file of a specific satellite to identify close approaches between the covered satellite mission (the target object) and an accessible space catalogue of chaser objects. Often, publicly available 18 SPCS TLEs are the only source of information fully accessible by the O/O. Privileged access data are sometimes available; for instance, CNES satellite operators can access data from the French GRAVES radar-based space surveillance.

Typically, a CS process can be performed based on a miss-distance criterion (which is equivalent to a spherical screening volume), a more accurate ellipsoidal screening volume accounting for the typically larger along-track uncertainty of an RSO, or a collision probability computation. In the last case, scaled covariances can be adopted to account for the expected shrinking of the uncertainty region following new observations before the TCA [9].

One crucial aspect of the CS process is the need to make it automated in order to reduce the process risk. The conjunction screening process can be computationally intensive and is usually performed following an iterative process that starts with a set of filters (typically apogee-perigee filter, orbit path filter, time filter, see [10]) before more accurate computations can be carried out.

3 Conjunction Filters

The calculation of collision probabilities between RSOs is highly computationally intensive and therefore, it is imperative to remove the RSO pairs that have practically no chance of collision from the search space. The classical preliminary conjunction screening methods proposed in the literature (e.g. the work of Alfano and Finkleman [10]) could be in principle extended to the low-thrust problem but this would likely result in a considerable loss of efficiency/effectiveness. Already for the unperturbed problem, for instance, Alfanos classical filters (apogee/perigee, orbital path and time filter) require some padding or buffering to account for the difference between the mean and real orbit due to short-periodic effects and uncertainties, and the tuning of the padding is a delicate (and risky) operation.

Recent ideas on the concept of "space occupancy" [11] can allow to improve the efficiency of these filters. Space occupancy is defined as the domain occupied by an individual satellite as it moves along its nominal orbit under the effects of environmental perturbations throughout a given interval of time. Considering the domain occupied by an RSO throughout a given timespan (in this case the typical 1-week screening window) and using analytical relations derived from frozen orbit theory (see [11]), it is possible to establish whether or not two RSOs can have overlapping SOVs. A non-overlap condition will lead to discard a pair of objects from further analysis.

4 Close Approaches Detection

The close approach detection, with a typical 1-week search horizon, will be addressed using a combination of fixed-step propagation and recursive interpolation using, for both tasks, the GEqOEs formulation (see [12] for more details). Crucially, the use of GEqOEs will allow much wider integration and interpolation steps compared to state-of-the-art propagators . We envision the possibility of selecting an adequate step size depending on the class of orbit (e.g., GEO, GTO, LEO, etc) for maximum computational performance.

We will present some initial results of our work; in particular, a preliminary study of the conjunction screening process and propose the use of advanced orbital motion formulations based on GEqOEs coupled to simple fixed-step numerical integrators to reduce

the computation time to a minimum while retaining sufficient conjunction detection accuracy. The trade-off between computation time and accuracy while considering covariance limitations of available ephemeris data will be discussed in detail.

5 Concluding remarks

Predicting risks of collisions in space is becoming a complex and daunting task, given the steady increase of number of objects in space due to the deployment of large constellations and the already large population of space debris. The first step to be performed is on-orbit conjunction screening, a process that iteratively identifies close approaches between resident space objects. The task of detecting all close approaches for a large population of objects is highly demanding from the computational time point of view and the use of conjunction filters (or other filters) as well as extremely fast propagation methods is paramount. We will present our initial findings aiming to reduce the computational load of these processes, without significant loss of accuracy.

Acknowledgements

Claudio Bombardelli acknowledges funding by MINECO/AEI and FEDER/EU under Project PID2020-112576GB-C21. Ana S. Rivero and Rafael Vazquez acknowledge support from grant PGC2018-100680-B-C21 funded by MCIN/AEI/10.13039/501100011033. Ana S. Rivero was also funded by a FPU grant from the Spanish Ministerio de Universidades.

References

[1] Muelhaupt, T. J., Sorge, M. E., Morin, J., and Wilson, R. S. Space traffic management in the New Space era. *Journal of Space Safety Engineering* **6**(2), 80–87 (2019).

[2] Adushkin, V., Aksenov, O. Y., Veniaminov, S., Kozlov, S., and Tyurenkova, V. The small orbital debris population and its impact on space activities and ecological safety. *Acta Astronautica* **176**, 591–597 (2020).

[3] Sgobba, T. and Allahdadi, F. A. *Safety Design for Space Operations: Chapter 8. Orbital Operations Safety*. Elsevier, (2013).

[4] Pardini, C. and Anselmo, L. Review of past on-orbit collisions among cataloged objects and examination of the catastrophic fragmentation concept. *Acta Astronautica* **100**, 30–39 (2014).

[5] Hudoba de Badyn, M. and Tahir, A. Orbital electromagnetic field generators as a method for removing small and untrackable space debris. In *AIAA SPACE 2015 Conference and Exposition*, 4660, (2015).

[6] Krage, F. J. Nasa spacecraft conjunction assessment and collision avoidance best practices handbook. Technical report, NASA, (2020).

[7] Kerr, E. and Ortiz, N. S. State of the art and future needs in conjunction analysis methods, processes and software. In *Proc. 8th European Conference on Space Debris*, (2021).

[8] 18th Space Control Squadron. Spaceflight safety handbook for satellite operators. `https://www.space-track.org/documents/Spaceflight_Safety_Handbook_for_Operators.pdf`.

[9] Laporte, F. JAC software, solving conjunction assessment issues. In *Advanced Maui Optical and Space Surveillance Technologies Conference*, E4, (2014).

[10] Alfano, S. and Finkleman, D. On selecting satellite conjunction filter parameters. *Acta Astronautica* **99**, 193–200 (2014).

[11] Bombardelli, C., Falco, G., Amato, D., and Rosengren, A. J. Space occupancy in Low-Earth Orbit. *Journal of Guidance, Control, and Dynamics* **44**(4), 684–700 (2021).

[12] Baù, G., Hernando-Ayuso, J., and Bombardelli, C. A generalization of the equinoctial orbital elements. *Celestial Mechanics and Dynamical Astronomy* **133**(11), 1–29 (2021).

Session 6:

UNCERTAINTY QUANTIFICATION AND PROPAGATION

A convex optimisation-based approach to detect and estimate manoeuvres

Laura Pirovano *[1] and Roberto Armellin †[1]

[1]Te Pūnaha Ātea – Space Institute, University of Auckland, New Zealand

1 Introduction

Since the advent of the space era, the number of resident space objects (RSOs) has grown and with it the problem of accurately determining their state. This is fundamental to maintain a collision-free environment in space, predict space events and perform activities. One of the many tasks pertaining to space situational awareness (SSA) is thus to build and maintain a catalogue of RSOs. While building the catalogue, it is important to associate multiple observations to the same object to perform orbit determination (OD) and improve the orbit's knowledge [1, 2]. To maintain the catalogue, RSOs need to be timely re-observed and the new observations need to be statistically compatible with the known object. Most association routines assume natural motion of the body in between observations, with association metrics deciding whether observations belong to the same RSO. However, active RSOs may perform manoeuvres which are not included in the dynamical model used for association. This mismodelling deteriorates the association routine, creating a mismatch where on the one hand an unknown RSO is detected - the new observation - and on the other hand a known object stops being updated - the spacecraft before the manoeuvring event. This paper outlines a new step to be added to the catalogue maintenance where a manoeuvre profile is estimated to connect two otherwise uncorrelated orbits and recover the association.

2 Problem formulation

In order to make the description clearer, refer to fig. 1 for the following paragraph. Suppose two states - the outcome of an OD - are available at two epochs t_0 and t_1, simplified with a black dot and a shaded ellipse, $(\mathbf{X}_{0,0}, \Sigma_{0,0})$, $(\mathbf{X}_{1,1}, \Sigma_{1,1})$. The state at the earliest epoch is propagated forward to the second one, determining a reference trajectory, the white line with black squares, $(\mathbf{X}_{0,1}, \Sigma_{0,1})$. The propagated and determined states will not correlate with typical data association techniques [3, 4, 1], but correlation may be recovered assuming a manoeuvre has happened. The proposed methodology considers the implementation of an impulsive maneuver $\Delta\mathbf{v}_i$ at every node in which the reference trajectory is discretised $i \in [0, N]$, the black squares, where $i = 0$ coincides with t_0 and $i = N$ with t_1.

State transition matrices (STMs) $\left(M_i \in \mathbb{R}^{6x3}\right)$ are used to map these maneuvers' effects forward in time, as shown by the red and green dashes. For example, a manoeuvre performed at node i will be mapped at node $j > i$ with

$$\Delta\mathbf{X}_{j,\delta\mathbf{v}_i} = \left[\prod_{k=i}^{j} M_{k,i}\right] \Delta\mathbf{v}_i. \tag{1}$$

The final deviation due to the cumulative effect of all manoeuvres until t_1 is then:

$$\Delta\mathbf{X}_{1,\delta\mathbf{v}} = \sum_{i=0}^{N} \left[\prod_{k=i}^{N} M_{k,i}\right] \Delta\mathbf{v}_i. \tag{2}$$

STMs $\left(R_i \in \mathbb{R}^{6x6}\right)$ are also used to map a deviation $\Delta\mathbf{X}_0$ in the initial state forward in time (blue dashes):

$$\Delta\mathbf{X}_{1,\delta X_0} = \prod_{k=0}^{N} \left(R_k\right) \Delta\mathbf{X}_0. \tag{3}$$

The cumulative effect of all manoeuvres and initial deviation allows the state at t_1 to reach the desired location.

The goal is to find the trajectory with the least amount of propellant used:

$$\min \sum_{i=0}^{N} \|\delta\mathbf{v}_i\|, \tag{4}$$

having the $\delta\mathbf{v}$ components at each node, the state at each node $\mathbf{X}$, and the initial and final deviations $\delta\mathbf{X}_0, \delta\mathbf{X}_1$ as optimisation variables ($9N + 12$ variables), meeting the following constraints:

- maximum Δv at each node (which defines the impulsive or low-thrust nature of the maneuver)

$$\|\delta\mathbf{v}_i\| \leq \Delta v_M \quad \forall i \in \{1, \ldots, N\} \tag{5}$$

*Email: laura.pirovano@auckland.ac.nz
†Email: roberto.armellin@auckland.ac.nz

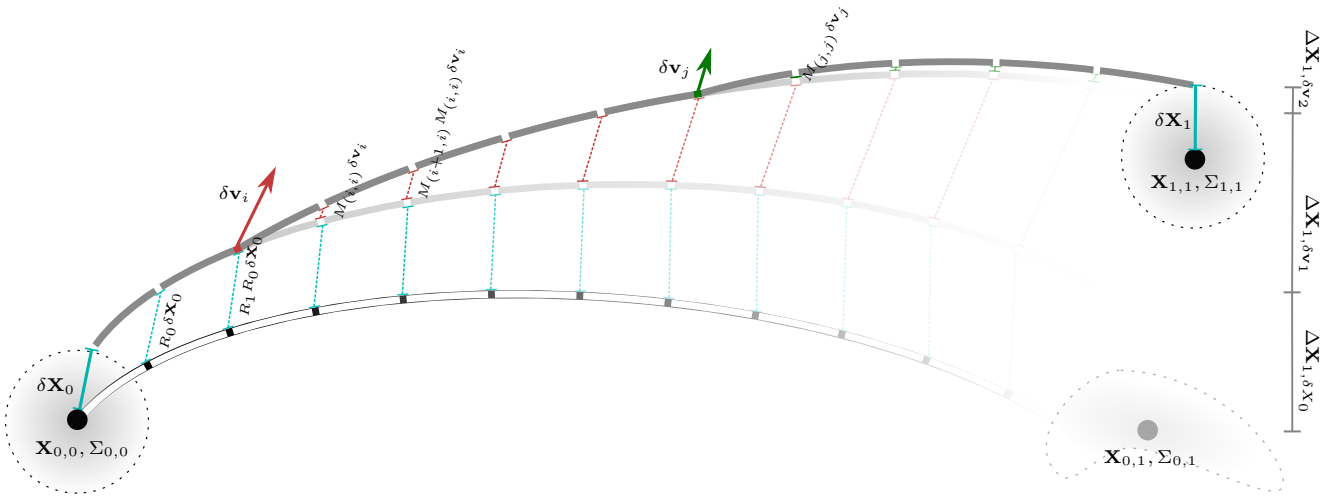

Figure 1: Initial trajectory and linear influence of initial deviation and mid-course manoeuvres to match final deviation.

- maximum variation on initial and final states to account for the OD uncertainty, in the form the Mahalanobis distance, through a chi-square quantile with confidence level α:

$$\frac{1}{2}\delta\mathbf{X}_j^T\Sigma_{(j,j)}\delta\mathbf{X}_j \leq q_{\chi^2}(\alpha,6) = \mathcal{M} \quad j=0,1 \quad (6)$$

- continuity of the trajectory, where $\tilde{\mathbf{X}}_i$ is the initially propagated state at node i while $\mathbf{X}_i$ is the state optimisation variable at node i:

$$\mathbf{X}_{i+1} - [R_i|M_i]\begin{bmatrix}\mathbf{X}_i\\ \delta\mathbf{v}_i\end{bmatrix} = \tilde{\mathbf{X}}_{i+1} - [R_i|M_i]\begin{bmatrix}\tilde{\mathbf{X}}_i\\ \mathbf{0}\end{bmatrix} \quad (7)$$

- matching of the propagated maneuvered state with the final state:

$$\mathbf{X}_{0,1} + \Delta\mathbf{X}_{1,\delta X_0} + \Delta\mathbf{X}_{1,\delta\mathbf{v}} = \mathbf{X}_{1,1} + \delta\mathbf{X}_1. \quad (8)$$

The problem is purposely handled with linear and quadratic constraints to obtain a convex optimisation formulation, for which convergence and a global minimum are ensured. Slack variables for the δvs magnitude and Mahalanobis distance are introduced to transform the objective function into a linear one and enforce bounds on the Δv and $\delta\mathbf{X}$ magnitude with second-order cone constraints, to finalise the convexification of the problem. Indeed, a quadratic constraint can become a second-order cone with the following variable transformation:

$$\begin{aligned}&\tfrac{1}{2}\mathbf{x}^T A\mathbf{x} + \mathbf{a}^T\mathbf{x} \leq b \iff (w,z,\mathbf{y}) \in \mathcal{Q}_r,\\ &\text{where } \begin{cases}\mathbf{y} = F\mathbf{x}, & Q = FF^T,\\ z = 1, & w = b - \mathbf{a}^T\mathbf{x}\end{cases}\end{aligned} \quad (9)$$

Hence:

$$eq.\ (5) \iff (2v_M, 1, \delta\mathbf{v}_i), \quad (10)$$

and

$$eq.\ (6) \iff \left(2\mathcal{M}, 1, \sqrt{\Lambda^{-1}}Q\delta\mathbf{X}_j\right), \quad (11)$$

where $\Sigma_{(j,j)} = Q\Lambda Q^T$. Once the optimization is completed, the reference trajectory is updated with the optimal maneuver. The accuracy of the final orbit is checked by accurate forward propagation. If constraints are not met to a prescribed accuracy, the procedure is repeated following a standard successive convex optimisation approach, hence modifying eq. (7) introducing an iteration counter k:

$$\mathbf{X}_{i+1}^k - [R_i|M_i]\begin{bmatrix}\mathbf{X}_i^k\\ \delta\mathbf{v}_i^k\end{bmatrix} = \tilde{\mathbf{X}}_{i+1} - [R_i|M_i]\begin{bmatrix}\mathbf{X}_i^{k-1}\\ \delta\mathbf{v}_i^{k-1}\end{bmatrix}. \quad (12)$$

An infeasible flag from the optimization process means that there can't be a maneuver specified by the constraints that can correlate the two objects, and non-correlation is concluded.

Reference trajectories and state transition matrices are developed in C++ using the library Differential Algebra Computing Engine (DACE) [1] and the accurate numerical propagator Accurate Integrator for Debris Analysis (AIDA) [5]. The Matlab interface of the optimizer MOSEK[2] is used to solve the problem with the primal-dual interior-point method for conic quadratic optimization. In principle, any type of coordinates can be chosen for the state representation. However, modified equinoctial elements were chosen because of the easiness to set bounds on the nodes variation and lack of singularities.

3 Keeping a statistical approach

The optimisation finds a deterministic path for this two-boundary value problem. However, the initial and final deviations hold a statistical meaning: the further from the mean states the final solution is, the

[1] https://github.com/dacelib/dace
[2] http://docs.mosek.com/9.0/toolbox/index.html

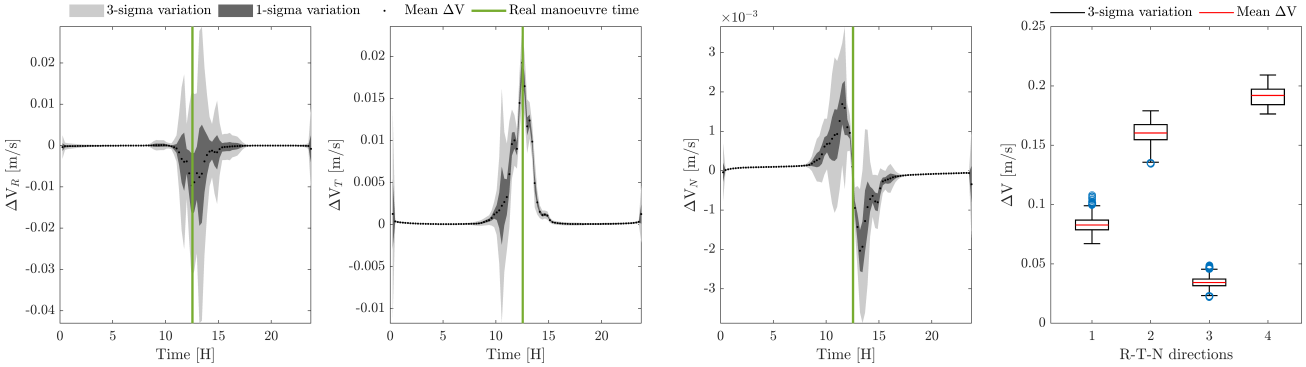

Figure 2: Manoeuvre estimation for two states retrieved one week apart for METEOSAT-8. An East-West station keeping (EWSK) manoeuvre is estimated and statistical properties are retrieved with the conjugate unscented transform (CUT)-4.

less probable the path found is to happen. By simply constraining the initial and final deviations to be less than a value as in eq. (6), the optimiser will see the deviations as "free propellant" hence taking full advantage of them, but actually creating the least probable path. For this reason, ΔX_0 and ΔX_1 cannot be determined within the optimisation but need to be determined beforehand. The fourth order CUT [6] was chosen to do so: by running the optimisation N^2+2N+1 times, where $N=12$ is the dimension of the problem, it is possible to reconstruct a-posteriori the first four momenta of the final distribution, thus making it possible to analyse the effect of uncertainty in the states on the overall maneuver existence and estimation. Sigma points drawn from the initial and final covariance bound the initial and final deviations, so that the constraint in eq. (6) is substituted by:

$$\begin{bmatrix}\delta\mathbf{X}_{0,0}\\ \delta\mathbf{X}_{1,1}\end{bmatrix}_i = \Delta\mathbf{X}^{12x1}_{CUT4,i} \quad i\in\left\{1,\dots,N^2+2N+1\right\}. \tag{13}$$

4 Example: METEOSAT EWSK manoeuvre

To test the optimisation and statistical handling of the uncertainty, a manoeuvre is here reconstructed following the availability of two states with covariances from EUMETSAT weekly newsletter. The data pot also includes the type of manoeuvre and manoeuvre time, but not the profile. Given the long window of time between the two available states, a filter is initially applied to only consider one day where to look for a manoeuvre. To do so, the two states are forward and backward propagated to find the instant in time where they were the closest, and a symmetric 1-day window is considered around that point. Figure 2 shows the manoeuvre time-profile in R, T, and N and the boxplot of the manoeuvres magnitude per components (1-2-3) and overall (4) in the right plot. A clear manoeuvre is visible in the tangential direction, where the 3σ uncertainty is well above zero. Preliminary results are encouraging, but further testing is necessary to make sure that all regimes and manoeuvre types can be handled with successive convexification.

5 Acknowledgments

The work presented is supported by AOARD under Grant FA2386-21-1-4115.

References

[1] L. Pirovano, D. Santeramo, R. Armellin, P. Di Lizia, and A. Wittig, "Probabilistic data association: the orbit set." *Celestial Mechanics and Dynamical Astronomy*, vol. 132, no. 2, p. 15, 2020.

[2] L. Pirovano, R. Armellin, J. Siminski, and T. Flohrer, "Differential algebra enabled multi-target tracking for too-short arcs," *Acta Astronautica*, vol. 182, pp. 310–324, 2021. [Online]. Available: https://www.sciencedirect.com/science/article/pii/S0094576521000977

[3] K. Hill, K. Alfriend, and C. Sabol, "Covariance-based uncorrelated track association," in *AIAA/AAS Astrodynamics Specialist Conference and Exhibit*, 2008, p. 7211.

[4] J. A. Siminski, O. Montenbruck, H. Fiedler, and T. Schildknecht, "Short-arc tracklet association for geostationary objects," *Advances in Space Research*, vol. 53, pp. 1184–1194, Apr. 2014.

[5] A. Morselli, R. Armellin, P. Di Lizia, F. Bernelli-Zazzera, E. Salerno, G. Bianchi, S. Montebugnoli, A. Magro, and K. Z. Adami, "Orbit Determination of Space Debris Using a Bi-Static Radar Configuration with a Multiple-Beam Receiver," *Proceedings of the International Astronautical Congress, IAC*, pp. 1–11, 2014.

[6] "Conjugate unscented transformation: Applications to estimation and control," *Journal of Dynamic Systems, Measurement and Control, Transactions of the ASME*, vol. 140, no. 3, Mar. 2018.

Assessment of uncertainty propagation techniques for the network embedding of the space resident population

Matteo Romano*[1], Timoteo Carletti†[1], Anne Lemaitre‡[1], and Jérôme Daquin§[1]

[1]Department of Mathematics and naXys (Namur Institute for Complex Systems), University of Namur, Namur, Belgium

1 Introduction

Currently, more than 23,000 objects orbiting around the Earth are catalogued and tracked. However, only 6% represent actually active satellites, while the rest is composed by defunct spacecraft, rocket stages, and mission-related and fragmentation debris. The number of new satellites is consistently rising due to a higher importance of space in economic and geo-political matters, with megaconstellations representing the new frontier of space exploitation. Currently, in low-Earth orbit alone, hundreds of close approaches between catalogued space residents are notified to satellite operators per week, in possible collision scenarios, and several fragmentations occur every year adding new debris to the population.

The WALSAT (WALlonia Space Awareness Technology) project proposes a novel method to study the topology of the space resident population from a complex system perspective using network theory. The population is embedded into a network: each node represents a space object, and links between them represent a conjunction event between any two objects occurring within a given time period. A weight can be assigned to each link depending on the characteristics of the collision, such as distance, collision probability, etc. The obtained network is analysed using metrics such as degree, centrality, and clustering coefficient. This complex system approach allows to rank and classify sensitive objects or groups of objects contributing the most to the overall collision risk.

A first approach to use networks to study the evolution of collisional risk was made by Lewis et al. [1], who used simulated future launches and fragmentations to study the evolution of the space population, which was embedded building multi-relational networks. The resulting network was used to identify candidates for Active Debris Removal missions with the goal of reducing the overall collision risk and debris production rate.

In this work, we present a network embedding which weights the links considering the probability of impact during a conjunction. The probability is estimated from the state uncertainty distributions of the two objects involved at the moment of the conjunctions, which is in turn estimated by propagating an initial covariance matrix associated to each orbital state. Various uncertainty propagation techniques will be presented to show their effects on the network topology and the resulting ranking of objects based on the network properties and the collisional risk, considering both the numerical accuracy and the computational cost in the assessment.

2 Methodologies

2.1 Dataset

In this work, the space population is described by data obtained from a reference database in the form of Two-Line Elements (TLEs) [2]. The database is the `NORAD` catalogue accessible online via the Space-Track portal (`https://www.space-track.org/#recent`), which is updated daily with the TLEs of most trackable space resident objects.

2.2 Orbital propagation

The orbital states represented by the TLEs are propagated forward in time for a given time period to obtain ephemeris tables for each object. The propagation is performed using different propagators to exploit the characteristics of each:

- `SGP4` (Simplified General Perturbations No. 4), as known, is an analytical propagator which allows fast evaluations of orbital states starting from TLEs, with an accuracy limited to timescales of a few days due to the approximations of the analytical model and the quality of the information provided by TLEs [3, 4];

*Email: matteo.romano@unamur.be, BEWARE2 fellow
†Email: timoteo.carletti@unamur.be
‡Email: anne.lemaitre@unamur.be
§Email: jerome.daquin@unamur.be, F.R.S.-FNRS fellow

- `NIMASTEP`, initially developed at the University of Namur, is a numerical propagator able to integrate osculating motion in Cartesian coordinates over longer time scales using a high-fidelity dynamic model including several perturbations [5, 6, 7]
- `NEPTUNE` (NPI Ephemeris Propagation Tool with Uncertainty Extrapolation, `https://github.com/Space-Systems/neptune`), developed at the European Space Agency, is also a high-fidelity numerical propagator integrating the osculating state in Cartesian coordinates, with the addition of covariance matrix propagation using variational equations to integrate the state error transition matrix [8, 9].

2.3 Network embedding

The network is built by detecting close conjunctions between each pair of objects using a three-filter sequence to prune the population and reduce the computational load [10]. The resulting network is composed by the objects experiencing a conjunction between them below a given threshold distance.

2.4 Uncertainty propagation methods

The initial state uncertainty is defined as a 6x6 covariance matrix in Cartesian coordinates. The propagation of the initial covariance matrix is performed in different methods [11]:

- Monte Carlo (MC) simulation, which consists of the propagation of a large number of initial conditions obtained by "perturbing" the reference initial state according to the uncertainty distribution;
- the Extended Kalman Filter (EKF), already implemented in `NEPTUNE`, which consists in a local linearisation of the dynamics allowing to propagate the initial covariance by integrating the State Transition Matrix alongside the orbital state;
- the Unscented Transformation (UT), which consists in the propagation of a subset of points which are representative of the initial uncertainty distribution using the fully non-linear dynamics;
- the integration of the Fokker-Plank equation, which is a partial differential equation describing the evolution in time of an uncertainty distribution subjected to the dynamics of the system.

3 Preliminary results

Figures 1, 2, and 3 show two clusters of a network obtained by embedding the space objects in the daily NORAD catalogue during the month of February.

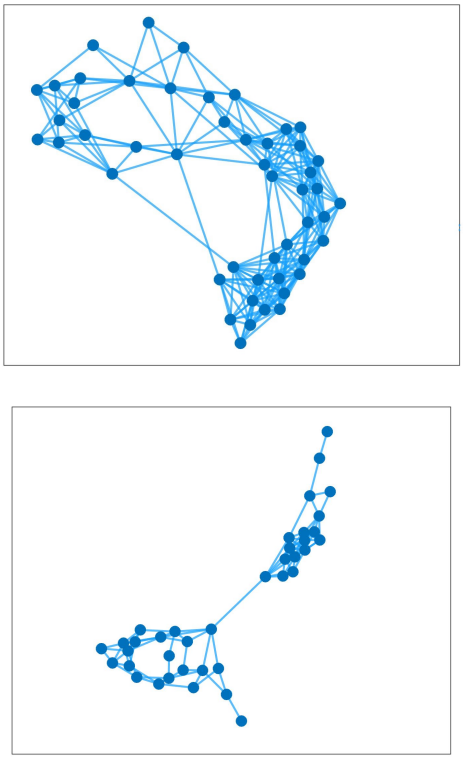

Figure 1: Two isolated components of the network.

The database was accessed every day, and each TLE was propagated forward over a period of 5 days, recoding all conjunctions with other objects within a distance of 5 km. These results do not consider the collision probability, only the occurrence of conjunctions.

Figure 1 generically represents the two isolated clusters, while Figures 2 and 3 highlight different properties of the networks: respectively, degree and betweenness. The degree of a node is defined as the number of links it is connected to, representing the number of other objects encountered by any given one. Betweenness is instead defined as the number of shortest paths between any two nodes pass through a given node, as a measure of how central each node is within the network: here it highlights which nodes act as "bridges" between different groups.

By analysing the networks using various properties, the differences in their topologies become more evident, as each node has a different weight on the overall collisional risk.

4 Conclusions

This work will present a comparison of different uncertainty propagation methods to assess their accuracy and computational costs in the embedding of the network. Considerations will be made depending on the feasibility of their use for the network embedding and

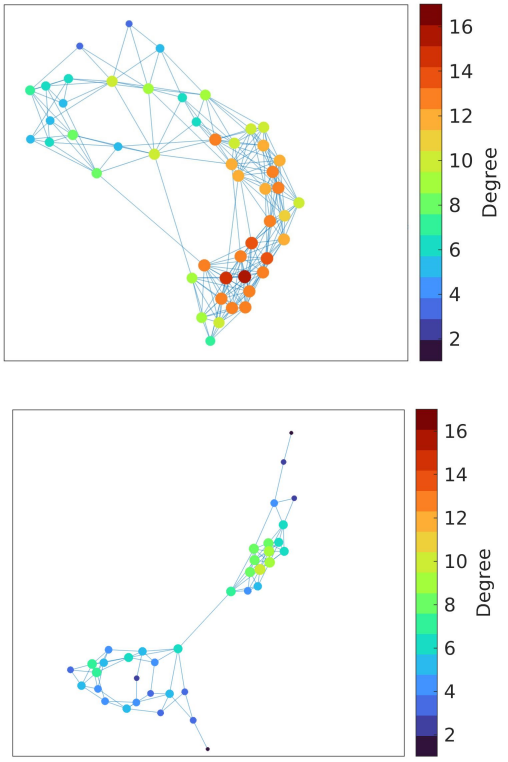

Figure 2: Highlighting the degree of the nodes in the network.

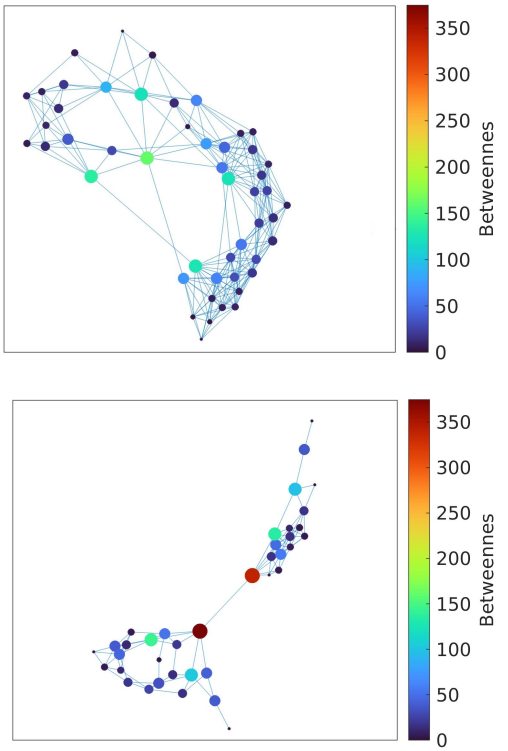

Figure 3: Highlighting the betweenness of the nodes in the network.

on the effect on the topology of the network itself, to measure the robustness of the embedding with respect of the uncertainty treatment.

Acknowledgements

This work is funded via the BEWARE programme by the government of the Wallonia region and by the European Commission (Marie Skłodowska Curie Actions grant agreement 847587) as part of the Horizon 2020 research and innovation programme, with a partnership between the naXys (Namur Institute for Complex Systems) institute at the University of Namur and the industrial partner Aerospacelab.

References

[1] Lewis H. G., Newland R. J., Swinerd G. G., and Saunders A., A new analysis of debris mitigation and removal using networks, *Acta Astronautica* **66.1-2** (2010), 257–268, https://doi.org/10.1016/j.actaastro.2009.05.010.

[2] CelesTrak. Norad two-line element set format. `https://www.celestrak.com/NORAD/documentation/tle-fmt.php`.

[3] Hoots F. R., and Roehrich R. L., Spacetrack Report #3: Models for Propagation of the NORAD Element Sets, *U.S. Air Force Aerospace Defense Command, Colorado Springs, CO* (1980).

[4] Vallado D. A., Crawford P., Hujsak R., and Kelso T. S., Revisiting Spacetrack Report #3, presented at the *AIAA/AAS Astrodynamics Specialist Conference, Keystone, CO, 2006 August 21–24* (2006).

[5] Delsate N., and Compere A., NIMASTEP: a software to modelize, study, and analyze the dynamics of various small objects orbiting specific bodies, *Astronomy & Astrophysics* **540** (2012), A120.

[6] Hubaux C., Lemaitre A., Delsate N., and Carletti T., Symplectic integration of space debris motion considering several Earth's shadowing models, *Advances in Space Research* **49.10** (2012), 1472-1486.

[7] Petit A., and Lemaitre A., The impact of the atmospheric model and of the space weather data on the dynamics of clouds of space debris, *Advances in Space Research* **57.11** (2016), 2245-2258.

[8] Braun V., and Horstmann A, Networking/Partnering Initiative TU-BS/ESOC (2011 - 2015). Technical report, Institute of Space Systems (2015).

[9] Braun V., Providing orbit information with predetermined bounded accuracy, Thesis for: Dr.-Ing. Technische Universität Braunschweig (2016), 10.5281/zenodo.228164.

[10] Casanova D., Tardioli C., and Lemaitre A., Space debris collision avoidance using a three-filter sequence, *Monthly Notices of the Royal Astronomical Society* **442.4** (2014), 3235-3242.

[11] Luo, Y-z., and Zhen Y., A review of uncertainty propagation in orbital mechanics, *Progress in Aerospace Sciences* **89** (2017), 23-39.

Cislunar Space Domain Awareness: Improved characterization and uncertainty quantification

Pablo Machuca*[1] and Aaron J. Rosengren†[1]

[1]Department of Mechanical and Aerospace Engineering, University of California San Diego, USA

1 Introduction

Cislunar space is expected to be increasingly populated in the coming decades. The dynamical complexity of the environment and wide range of available orbits pose a significant new challenge for Space Domain Awareness (SDA); namely, the catalog maintenance of xGEO (beyond GEO) objects. The intrinsic stability/instability of orbits, increasingly complex trajectory designs, plethora of station-keeping strategies, and limited visibility windows necessitates a better understanding of this non-traditional orbital environment. Accordingly, we aim to provide: (1) a robust characterization of the cislunar multi-body dynamical environment geared towards typical scenarios of interest; (2) an intuitive, familiar parametrization to describe the motion of xGEO objects; and (3) an uncertainty quantification analysis of the orbit determination (OD) process, with the overall goal of understanding how uncertainties affect viewing geometries and observation campaigns for catalog maintenance.

Specifically, we reproduce and characterize relevant mission profiles in the Circular Restricted Three-body Problem (CR3BP) and in an ephemeris model, including: (a) transfers between quasi-periodic halo orbits (including that baselined for the Lunar Gateway); (b) transfers into distant retrograde orbits (DROs), which have been proposed as parking orbits for interplanetary missions; and (c) lunar mean-motion resonance orbits (MMRs), like those used by the IBEX and TESS spacecraft. We then propose a parameterization approach to describe such trajectories based on piecewise orbital elements (geocentric or selenocentric, as the physical picture dictates). We show that, despite the non-Keplerianity of such orbits, the classical elements are still well defined and can provide an intuitive and useful representation of characteristic xGEO trajectories. Finally, we model and propagate uncertainties involved in the OD process to better understand the inherent sensitivities that plague cislunar space, and we highlight their implications to viewing geometries, required revisit rates, and surveillance volumes for improved catalogue maintenance.

Some preliminary results are summarized herein, with a focus on the family of halo orbits around the second Earth-Moon Lagrange point (L2).

2 Sample mission scenario

The multi-body dynamics of cislunar space offer a wide range of orbits that permit more complex trajectory designs and mission profiles. We begin our analysis by reproducing cislunar trajectories that may be of interest to future missions. As a sample scenario, we consider the family of Southern L2 halo orbits and transfers between such orbits. Halo orbits around L2 have been proposed for payloads supporting lunar exploration and communication [1, 2, 3], including the Lunar Gateway [4, 5], and also as parking orbits for the efficient insertion of satellites into low-Earth orbit [6]. A variety of halo orbits may be employed in the future, from those originating in the vicinity of the Lagrange point, up to near-rectilinear halo orbits (NRHOs) with closer lunar passages.

In this scenario, we consider a spacecraft that is initially stationed along a Southern 9:2 resonant orbit around L2, such as that baselined for the Lunar Gateway, which then transfers to a smaller halo orbit in the vicinity of L2 through a total of 12 intermediate orbits (Fig. 1). This scenario may be representative of a spacecraft leaving the Lunar Gateway with the intent of departing the Earth-Moon system through lower-energy halo orbits [4]. It also allows us to consider a range of halo orbits along the Southern L2 family, including the natural motion along such orbits and transfer maneuvers from/to these orbits.

Periodic orbits are initially computed in the CR3BP and then transitioned into quasi-periodic orbits in the ephemeris model. This approach allows us to assess the utility of the CR3BP for the identification and characterization of features and general trends, and to identify differences in the orbital-element representation. Furthermore, transfer arcs between halo orbits leverage unstable and stable manifold trajectories associated to the departure and arrival halo orbits: an approach that may become standard in cislu-

*Email: pmachucavarela@ucsd.edu. Research supported by the Air Force Office of Scientific Research, under grant agreement FA9550-21-1-0191.

†Email: ajrosengren@ucsd.edu.

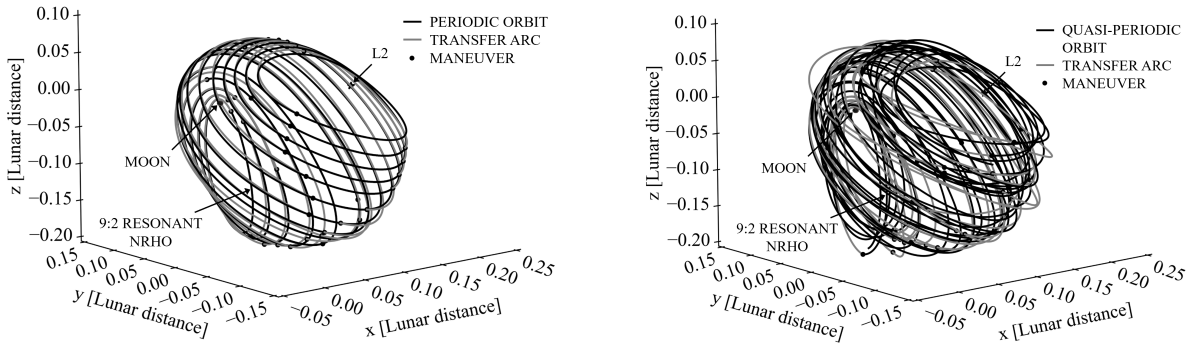

(a) CR3BP model.

(b) Ephemeris model.

Figure 1: Transfer from L2 Southern 9:2 resonant NRHO to a smaller halo orbit through a chain of 12 intermediate orbits.

nar space. Note, however, that the resulting transfer arcs—departure/arrival trajectories that actually intersect each other in position—are generally close to but may not necessarily remain on the invariant manifolds of the departure/arrival orbits.

It is worth highlighting here that the design of transfer trajectories assumes impulsive maneuvers in both models, but the design process is done separately for the CR3BP and for the ephemeris model. In both models, we leverage invariant manifold dynamics to generate initial guesses for the departure/arrival transfer arcs, but the time of flight along halo orbits and the location of maneuvers, magnitudes, and transfer times may differ between both models. As a result, the whole CR3BP transfer takes a total of 343 days and 631 m/s, and the ephemeris-model transfer takes 557 days and 1140 m/s instead.

Lastly, no claim is made on the optimality of the transfers, and, indeed, it is likely that lower Δv transfers may be found (although of the same order of magnitude). This scenario, nevertheless, allows us to consider a range of maneuver locations—at perilune, apolune, and intermediate points—and magnitudes (between 7 m/s and 35 m/s in the CR3BP, and between 2 m/s and 97 m/s in the ephemeris model).

3 Orbital-element parametrization

In search of an intuitive parametrization approach to describe the potentially complex motion of xGEO objects, we considered a piecewise representation based on orbital elements: selenocentric if within the Moon's Hill sphere, or geocentric if outside of it. We found that the instantaneously-inertial Earth-Moon synodic reference frame provides the most insightful representation for (quasi-) periodic orbits. It is observed that, in such a frame, the orbital elements describing the shape and size of halo orbits (semi-major axis and eccentricity), and also the elements describing the orbit orientation (inclination, argument of periapsis, and longitude of the ascending node), all display repetitive, nearly-cyclical patterns. Such patterns are perfectly periodic along halo orbits in the CR3BP, and a similar trend, but not periodic, is observed in the ephemeris model. As an example, Fig. 2 illustrates the behavior of the semi-major axis along the CR3BP and ephemeris-model transfers.

The geocentric semi-major axis is illustrated in black in Fig. 2, and the selenocentric semi-major axis is illustrated in grey. It is observed that a continuous representation of trajectories can be provided by this piecewise orbital-element parametrization. In particular, long segments along the halo orbits remain outside the Moon's Hill sphere, and the switch to selenocentric elements occurs only at perilune passages.

It is further observed that the oscillation in orbital elements is smaller for orbits closer to the Moon (left-most orbits in Fig. 2), which effectively resemble highly-elliptical circumlunar orbits. For those orbits that are closer to the Lagrange point (right-most orbits), third-body dynamics are more prominent and result in larger orbital-element oscillations. Furthermore, the oscillations along transfer arcs generally remain within the bounds defined by the departure and arrival orbits. This holds true for nearly fuel-optimal transfer arcs that remain close to the manifolds. Transfers that employ larger Δv maneuvers, however, such as those providing shorter-duration transfer arcs, may result in orbital-element oscillations beyond the range imposed by the departure and arrival orbits.

Additionally, maneuvers, which are modeled here as instantaneous changes in velocity, are observed to result in sudden changes in orbital elements too, and so discontinuities in orbital parameters may be leveraged to identify orbital transfers. As a general trend, it is observed that larger Δv maneuvers may lead to larger changes in orbital elements, but the magnitude of these changes also depends on factors like the direction and location of these impulsive maneuvers.

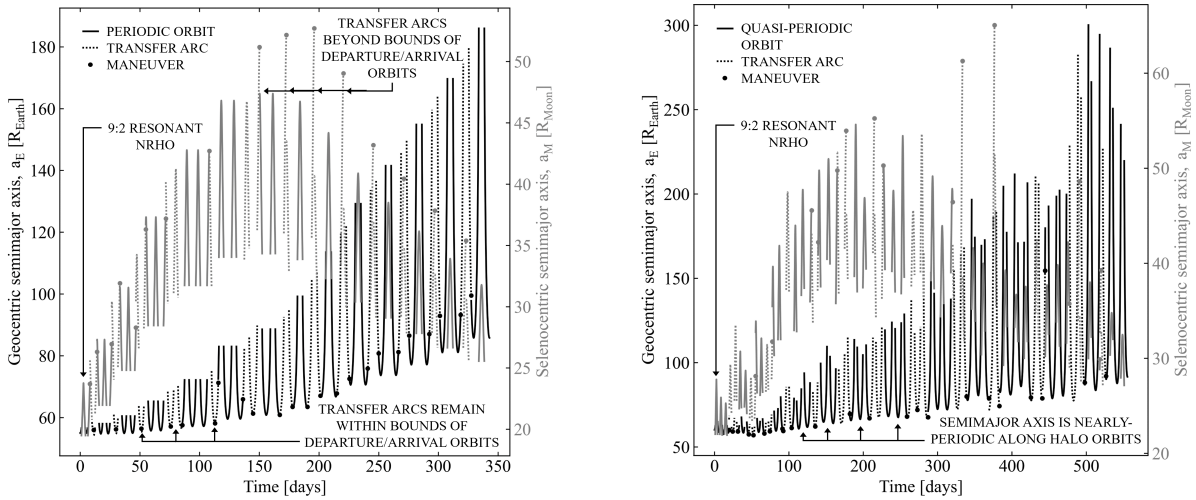

(a) CR3BP model.

(b) Ephemeris model.

Figure 2: Evolution of geocentric (*left*) and selenocentric (*right*) semi-major axis along chain of halo orbits.

4 Next steps

Preliminary results show that, despite the non-Keplerianity of cislunar trajectories, geocentric and selenocentric orbital elements are still well defined and can provide an insightful, familiar representation of scenarios of interest. Such an approach is also applied to DROs and to MMRs, and the usefulness of such a representation will be discussed further.

In support of SDA efforts, we also model the OD process and characterize the accuracies to be expected along such scenarios, through a Monte Carlo analysis. See Fig. 3 for a transfer from a 9:2 NRHO to a 13.8-day DRO.

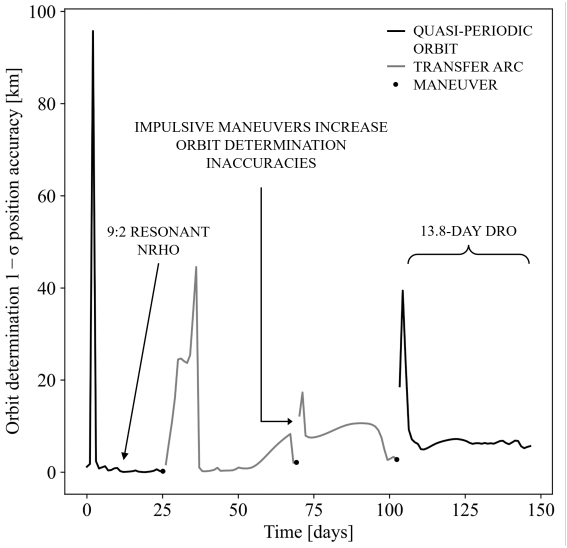

Figure 3: Evolution of OD accuracy along transfer from L2 Southern 9:2 resonant NRHO to 13.8-day DRO.

Clouds of uncertainty are forward propagated to assess the sensitivity of cislunar trajectories, and the evolution of these uncertainties is ultimately linked back to viewing geometries, required revisit rates, and surveillance volumes for proper detection, identification, tracking, and cataloguing of the soon-to-be-populated cislunar space.

References

[1] D. Chongrui, M. K. Fain, and O. L. Starinova, "Analysis and design of halo orbits in cislunar space," *IOP Conference Series: Materials Science and Engineering* **984** (2020), 1–11.

[2] S. Trofimov, M. Shirobokov, A. Tselousova, and M. Ovchinnikov, "Transfers from near-rectilinear halo orbits to low-perilune orbits and the Moon's surface," *Acta Astronautica* **167** (2020), 260–270.

[3] M. Bolliger, M. R. Thompson, et al., "Ground-based navigation trades for operations in Gateway's near-rectilinear halo orbit," *Proceedings of the AAS/AIAA Space Flight Mechanics Conference*, Paper AAS 21-450 (2021), 1–16.

[4] R. E. Pritchett, E. Zimovan, K. Howell, "Impulsive and low-thrust transfer design between stable and nearly-stable periodic orbits in the restricted problem," *Proceedings of the 2018 Space Flight Mechanics Meeting*, Paper AIAA 2018-1690 (2018), 1–23.

[5] S. Yun, K. Tuggle, R. Zanetti, and C. D'Souza, "Sensor configuration trade study for navigation in near-rectilinear halo orbits," *The Journal of the Astronautical Sciences* **67** (2020), 1755–1774.

[6] N. H. Crisp, K. Smith, and P. Hollingsworth, "Launch and deployment of distributed small satellite systems," *Acta Astronautica* **114** (2015), 65–78.

Combining Taylor polynomials and multifidelity dynamics for the efficient propagation of uncertainties in orbital mechanics

Alberto Fossà*[1], Roberto Armellin[2], Emmanuel Delande[3], Matteo Losacco[1], and Francesco Sanfedino[1]

[1]Institut Supérieur de l'Aéronautique et de l'Espace, Toulouse, 31055, France
[2]The University of Auckland, Auckland, 1010, New Zealand
[3]Centre National d'Études Spatiales, Toulouse, 31401, France

1 Introduction

Accurate propagation of uncertainties is central in Space Surveillance and Tracking (SST) applications. Since an analytical solution to the Uncertainty Propagation (UP) problem does not exist in the nonlinear orbital dynamics, several methods have been proposed to approximate the transformed state Probability Density Function (PDF) [1]. A novel multifidelity (MF) method to tackle the nonlinear orbit UP problem is presented in this work. This approach focuses on computational efficiency while guaranteeing an high accuracy for the final estimate. The state PDF is approximated as a Gaussian Mixture Model (GMM) whose number of components is adapted online to match the specified accuracy [2]. Each Gaussian kernel is propagated in the Differential Algebra (DA) framework [3] as a second-order Taylor polynomial and a Nonlinearity Index (NLI) is defined to detect any departure from linearity within its domain of definition. When the NLI crosses the imposed threshold, the propagation is halted, the polynomial is split according to a preselected splitting library and the propagation is resumed on the newly generated kernels. The hypothesis of quasi-linearity of the transformation is thus locally satisfied. This splitting technique is named LOADS (Low-Order Automatic Domain Splitting) [4] in agreement to the ADS algorithm originally proposed by Wittig et al. [5] for higher-order Taylor expansions. To further improve the computational efficiency, multifidelity techniques [6] are employed to perform most of the computations in low-fidelity (LF) dynamics while propagating the kernels means in high-fidelity (HF) to preserve the accuracy of the final estimate. The impact of different orbit state parametrizations on the final number of GMM components is also analyzed, demonstrating that a proper selection of coordinates preserves Gaussianity for longer time spans.

*Email: alberto.fossa@isae-supaero.fr

2 Multifidelity Uncertainty Propagation

The multifidelity approach comprises four main steps detailed in Sections 2.1 to 2.4

1. run the LOADS algorithm in LF dynamics
2. propagate the kernel means in HF dynamics
3. correct the LF solution with the HF samples
4. estimate the final PDF from the MF solution

Uncertainties on the input state $\boldsymbol{x}$ are assumed Gaussian with known mean $\boldsymbol{\mu_X}$ and covariance $\boldsymbol{P_X}$. The DA vector input to step 1 is computed as

$$[\boldsymbol{x}] = \boldsymbol{\mu_X} + \boldsymbol{V} \cdot \left\{ c\sqrt{\boldsymbol{\lambda}} \cdot \delta\boldsymbol{x} \right\} \tag{1}$$

with c confidence interval, $\boldsymbol{\lambda}, \boldsymbol{V}$ eigenvalues and eigenvectors of $\boldsymbol{P_X}$ such that $\boldsymbol{P_X} = \boldsymbol{V}\boldsymbol{\Lambda}\boldsymbol{V}^T$ with $\boldsymbol{\Lambda} = \text{diag}(\boldsymbol{\lambda})$ and $\delta\boldsymbol{x}$ first-order deviations around $\boldsymbol{\mu_X}$. $[\boldsymbol{x}]$ is then associated to a single Gaussian kernel with weight $\alpha = 1$, mean $\boldsymbol{\mu_X}$ and covariance $\boldsymbol{P_X}$.

2.1 LOADS-GMM algorithm

Consider the nonlinear transformation $\boldsymbol{f} : \mathbb{R}^n \to \mathbb{R}^m$ defined as $\boldsymbol{y} = \boldsymbol{f}(\boldsymbol{x})$. The LOADS-GMM algorithm maps the input $[\boldsymbol{x}]$ through $\boldsymbol{f}$ and computes the NLI on the output $[\boldsymbol{y}]$. If it exceeds the imposed threshold, the polynomial $[\boldsymbol{x}]$ and associated kernel $(\alpha, \boldsymbol{\mu_X}, \boldsymbol{P_X})$ are split into three new polynomials and components, and mapped again through $\boldsymbol{f}$. They are otherwise stored together with the output $[\boldsymbol{y}]$. The result is a recursive algorithm which terminates after the NLIs of each component satisfy the imposed threshold. To perform the split, a univariate splitting library is used. These libraries are obtained by minimizing the L_2 distance between the standard Gaussian distribution and a univariate GMM with $L = 3$ components [2, 7].

2.2 High-fidelity samples

Outputs of the previous step comprise the initial and final polynomials $[\boldsymbol{x}^{(p)}], [\boldsymbol{y}_{LF}^{(p)}]$ and Gaussian kernels $(\alpha^{(p)}, \boldsymbol{\mu_X}^{(p)}, \boldsymbol{P_X}^{(p)})$ for all P components obtained eval-

is now evaluated point-wise on each kernel mean $\boldsymbol{\mu}_{\boldsymbol{X}}^{(p)}$ (equal to the constant part of $[\boldsymbol{x}^{(p)}]$) to obtain an accurate reference $\overline{\boldsymbol{y}}_{HF}$ for the subsequent correction.

2.3 Multifidelity correction

The LF solution is corrected by re-centering the previously computed Taylor expansions $[\boldsymbol{y}_{LF}^{(p)}]$ on the newly obtained references $\overline{\boldsymbol{y}}_{HF}^{(p)}$ $\forall p = 1, \ldots, P$ such that

$$[\boldsymbol{y}_{MF}^{(p)}] = \overline{\boldsymbol{y}}_{HF}^{(p)} + \left\{ [\boldsymbol{y}_{LF}^{(p)}] - \overline{\boldsymbol{y}}_{LF}^{(p)} \right\} \tag{2}$$

2.4 Final PDF estimate

The output PDF $p_{\boldsymbol{Y}}$ is approximated as a GMM whose components means and covariances are computed from the MF solution obtained in Eq. (2). For each component, Unscented Transform [8] sigma points $\{\boldsymbol{x}_s\}_{s=1,\ldots,N_s}$ are drawn from the initial distribution $\mathcal{N}(\boldsymbol{\mu}_{\boldsymbol{X}}^{(p)}, \boldsymbol{P}_{\boldsymbol{X}}^{(p)})$. The polynomial $[\boldsymbol{y}_{MF}^{(p)}]$ is then evaluated in $\boldsymbol{x}_s^{(p)}$ $\forall s$ and the propagated mean and covariance obtained from the output samples $\boldsymbol{y}_s^{(p)}$ as

$$\begin{aligned} \boldsymbol{\mu}_{\boldsymbol{Y}}^{(p)} &= \sum_{s=1}^{N_s} w_s \boldsymbol{y}_s^{(p)} \\ \boldsymbol{P}_{\boldsymbol{Y}}^{(p)} &= \sum_{s=1}^{N_s} w_s \left(\boldsymbol{y}_s^{(p)} - \boldsymbol{y}_{\boldsymbol{Y}}^{(p)} \right) \left(\boldsymbol{y}_s^{(p)} - \boldsymbol{y}_{\boldsymbol{Y}}^{(p)} \right)^T \end{aligned} \tag{3}$$

with w_s sigma points weights. The transformed PDF is finally given by

$$p_{\boldsymbol{Y}}(\boldsymbol{y}) \simeq \sum_{p=1}^{P} \alpha^{(p)} p_{\mathcal{N}} \left(\boldsymbol{y}; \boldsymbol{\mu}_{\boldsymbol{Y}}^{(p)}, \boldsymbol{P}_{\boldsymbol{Y}}^{(p)} \right) \tag{4}$$

3 Numerical Applications

The algorithm described in Section 2 is now applied to the problem of nonlinear orbit UP and its performances assessed against reference MC simulations. Three test cases are analyzed: High Earth Orbit (HEO), Low Earth Orbit (LEO) and Medium Earth Orbit (MEO) regimes. Nominal initial conditions (ICs) are given in Table 1.

Regime	a, km	e	i, deg
HEO	35 000.0	0.2	0.0
LEO	6678.0	0.01	0.0
MEO	29 600.135	0.0	56.0

Table 1: Nominal initial conditions

The initial covariances are expressed in cartesian parameters with diagonal elements set to $\sigma_x^2 = \sigma_y^2 = 1.0\,\mathrm{km}^2, \sigma_{vx}^2 = \sigma_{vy}^2 = 1.0\,\mathrm{m}^2\,\mathrm{s}^{-2}$ in HEO, $\sigma_x^2 = 1.69\,\mathrm{km}^2, \sigma_y^2 = 0.25\,\mathrm{km}^2, \sigma_{vx}^2 = 6.25\,\mathrm{m}^2\,\mathrm{s}^{-2}, \sigma_{vy}^2 = 25.0\,\mathrm{m}^2\,\mathrm{s}^{-2}$ in LEO and $\sigma_x^2 = 0.25\,\mathrm{km}^2, \sigma_y^2 = \sigma_z^2 = 1.0\,\mathrm{km}^2, \sigma_{vx}^2 = \sigma_{vy}^2 = \sigma_{vz}^2 = 0.25\,\mathrm{m}^2\,\mathrm{s}^{-2}$ in MEO. Omitted parameters are set to zero.

The LF dynamical model used with the LOADS-GMM algorithm of Section 2.1 is the analytical SGP4 theory with deep space corrections for the HEO and MEO test cases. The HF samples are then propagated numerically in the perturbed Keplerian dynamics. The following forces are included: 8×8 Earth non-uniform gravity field, Sun and Moon third-body attraction, Solar Radiation Pressure (SRP) with umbra and penumbra transitions, atmospheric drag for the LEO regime. ICs are propagated for two revolutions of the corresponding nominal orbits.

Agreement to the reference MC simulations is demonstrated plotting the isoprobability contours of the final state PDF on top of the propagated MC samples. Projections onto the $x - y$ plane of the position uncertainties for the HEO and LEO cases are shown in Figs. 1 and 2 respectively. These plots show that the strongly non-Gaussian PDF is correctly captured by its GMM approximation.

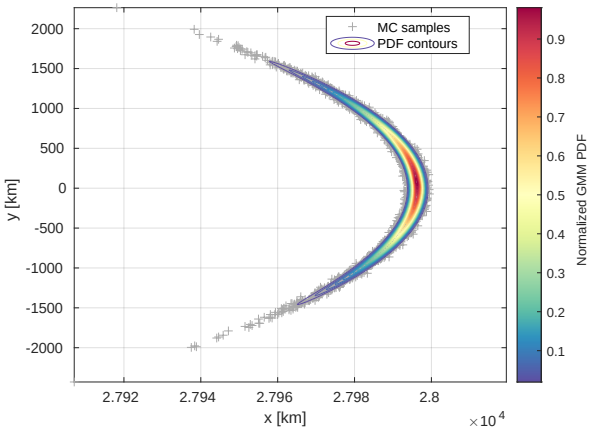

Figure 1: Isoprobability contour for HEO case

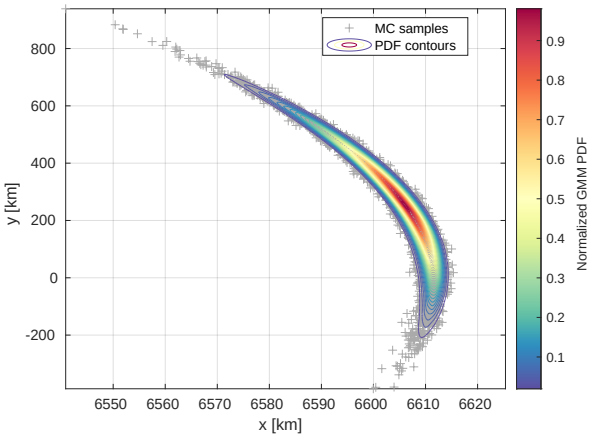

Figure 2: Isoprobability contour for LEO case

The accuracy of the solution is assessed computing the Root Mean Square Error (RMSE) between expected samples, obtained with point-wise propagations in HF, and actual ones, obtained by evaluating the Taylor polynomials $[\boldsymbol{y}_{MF}^{(p)}]$. The RMSE never exceeds 10.0 m in position and 10.0 mm s^{-1} in velocity for all scenarios.

To analyze the impact of the state parametrization on the number of GMM components, simulations are carried out in cartesian parameters, equinoctial elements, Modified Equinoctial Elements (MEEs) and alternate equinoctial elements [9]. Both true and mean longitudes L, λ are used as fast variable where applicable. Results are summarized in Table 2. Cartesian parameters are clearly the most nonlinear since they lead to the largest number of kernels required to describe the transformed PDF. On the opposite side, the use of alternate elements with λ as sixth coordinate results in a quasi-linear transformation which is correctly captured by a single polynomial. Equinoctial elements and MEEs stand in between.

	HEO		LEO		MEO	
Parameters	L	λ	L	λ	L	λ
Cartesian	6561	-	2187	-	729	-
Equinoctial	3115	3	277	3	9	1
MEEs	2187	729	2221	83	243	3
Alternate	729	1	93	1	1	1

Table 2: Number of GMM components

The computational load of the multifidelity method is then compared to that of its fully high-fidelity counterpart. For the second, the LOADS-GMM is run directly with the HF dynamics and no correction step is performed. A 15 to 20 times speedup is observed in favor of the MF approach for which most of the time is spent in step 2. This fact is more marked in LEO where low altitude and inclusion of atmospheric drag force further slow down the numerical integration.

4 Conclusions

A novel multifidelity approach to the problem of nonlinear Uncertainty Propagation (UP) is presented. This method approximates the transformed Probability Density Function as a Gaussian Mixture Model whose number of components is adapted online for maximum efficiency. Differential Algebra (DA) techniques are used to propagate the Gaussian kernels using second-order Taylor polynomials. A DA-based measure of nonlinearity is introduced to detect departure from linearity within the domain of each expansion and trigger automatic splits if needed. The proposed method is applied to the problem of orbit UP and three test cases are analyzed. Agreement to reference MC samples is demonstrated both visually and computing the Root Mean Square Error between expected and actual samples. The multifidelity method guarantees a 15 to 20 times speedup with respect to its fully high-fidelity counterpart.

Acknowledgments

This work is co-funded by the CNES through A. Fossà's PhD program, and made use of the CNES orbital propagation tools, including the PACE library.

References

[1] Y. Luo and Z. Yang. "A review of uncertainty propagation in orbital mechanics". In: *Progress in Aerospace Sciences* 89 (2017), pp. 23–39. DOI: 10.1016/j.paerosci.2016.12.002.

[2] K. J. DeMars, R. H. Bishop, and M. K. Jah. "Entropy-based approach for uncertainty propagation of nonlinear dynamical systems". In: *Journal of Guidance, Control, and Dynamics* 36.4 (2013), pp. 1047–1057. DOI: 10.2514/1.58987.

[3] M. Valli et al. "Nonlinear mapping of uncertainties in celestial mechanics". In: *Journal of Guidance, Control, and Dynamics* 36.1 (2013), pp. 48–63. ISSN: 0731-5090. DOI: 10.2514/1.58068.

[4] A. Fossà et al. "Multifidelity orbit uncertainty propagation using Taylor polynomials". In: *AIAA SCITECH 2022 Forum*. San Diego, California, Jan. 2022, pp. 1–16. DOI: 10.2514/6.2022-0859.

[5] A. Wittig et al. "Propagation of large uncertainty sets in orbital dynamics by automatic domain splitting". In: *Celestial Mechanics and Dynamical Astronomy* 122.3 (2015), pp. 239–261. DOI: 10.1007/s10569-015-9618-3.

[6] B. A. Jones and R. Weisman. "Multi-fidelity orbit uncertainty propagation". In: *Acta Astronautica* 155 (2019), pp. 406–417. DOI: 10.1016/j.actaastro.2018.10.023.

[7] *HSL. A collection of Fortran codes for large scale scientific computation.* 2013. URL: http://www.hsl.rl.ac.uk/.

[8] S. J. Julier and J. K. Uhlmann. "Unscented filtering and nonlinear estimation". In: *Proceedings of the IEEE* 92.3 (2004), pp. 401–422. DOI: 10.1109/JPROC.2003.823141.

[9] J. T. Horwood, N. D. Aragon, and A. B. Poore. "Gaussian sum filters for space surveillance: theory and simulations". In: *Journal of Guidance, Control, and Dynamics* 34.6 (2011), pp. 1839–1851. DOI: 10.2514/1.53793.

Non-linear set propagation with generalised equinoctial orbital elements

Max I. Hallgarten La Casta*[1], Luis Sánchez Fernandez-Mellado†[2], Davide Amato‡[1], and Massimiliano Vasile§[2]

[1]Imperial College London, United Kingdom
[2]University of Strathclyde, United Kingdom

1 Introduction

Due to the non-linearity of orbital motion, the propagation of uncertainty on the state of a spacecraft is a challenging and computationally intensive task. Most of the uncertainty quantification methods in orbital mechanics represent uncertainty through Probability Density Functions (PDFs) in Cartesian coordinates. This approach is relatively simple and physically intuitive; however, the uncertainty realism is rapidly lost due to the non-linearity of the system even in the unperturbed (Keplerian) case. Therefore, the representation of the uncertainty of a spacecraft in a state space in which non-linearities evolve slowly is particularly attractive.

2 Generalised Equinoctial Orbital Elements (GEqOEs)

Equinoctial Orbital Elements (EqOEs) are a set of orbital elements which are similar to traditional Keplerian orbital elements, albeit with several improvements, most notably the removal of singularities experienced for orbits approaching either zero eccentricity or inclination.

A recently introduced version of EqOEs, known as GEqOEs, embeds the perturbing potential in the definition of the elements, further improving their performance over classical EqOEs in the presence of perturbations [1]. This formulation provides more linear propagation of states, and is therefore better suited for uncertainty propagation, as shown previously by other authors using linear methods such as State Transition Matrices (STMs) [2].

In this work, we use GEqOEs for uncertainty quantification through non-linear techniques. These methods are currently being integrated in the Robust State Estimation (RSE) module of CASSANDRA, a suite of tools for automated Space Environment Management (SEM) under development at the University of Strathclyde [3]. Uncertainty in orbital states is propagated in CASSANDRA by propagating sets of states and deriving the PDF through sampling, as opposed to directly propagating the PDF itself. This operation can be conducted in two separate ways: with non-intrusive methods, or with intrusive methods; each designed to propagate large sets of states at a lower overall computational cost.

3 Non-intrusive Methods

Non-intrusive methods assume that the orbital propagator is a "black box", where its internal operations are unknown by CASSANDRA. The advantage of this method is that little work is required to integrate new propagators into the RSE module, other than a wrapper for Input/Output (I/O).

The non-intrusive method reduces the computational cost of propagating large sets of states by propagating a smaller subset of states [4]. This subset is obtained by using stochastic collocation, more specifically with Smolyak sparse grids [5] in this case, which builds a grid of points from the initial set of states. Once the points in the grid are propagated using the corresponding orbital propagator, a surrogate model that maps the initial states with all the possible propagated states is built. In this work, the surrogate uses Chebyshev polynomials as basis functions. The propagated state of the remaining points in initial set is then obtained by evaluating the surrogate model.

Evaluation of the surrogate model is inexpensive relative to the computational cost of propagating the entire initial set; therefore, significant performance gains can be realised. Significant improvements in capturing the propagation of the set, as a whole, were made by generating the surrogate model in GEqOE space, as opposed to Cartesian space, as shown in Figures 1 and 2. The accuracy of the methods was measured using the Root-Mean-Square Error (RMSE) relative to a Monte Carlo analysis. For any given degree, the accuracy of the surrogate created in GEqOE space outperforms the equivalent Cartesian surrogate. The inclusion of execution time (Table 1) highlights that for a similar execution time, GEqOE-based surrogates provide significant improvements in accuracy.

*Email: m.hallgarten-la-casta21@imperial.ac.uk
†Email: luis.sanchez-fdez-mellado@strath.ac.uk
‡Email: d.amato@imperial.ac.uk
§Email: massimiliano.vasile@strath.ac.uk

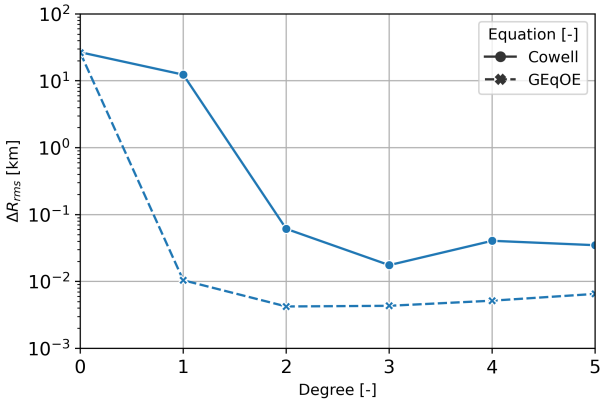

Figure 1: Final position errors of the non-intrusive methods, with respect to a Monte Carlo simulation, as a function of the degree of the sparse grid.

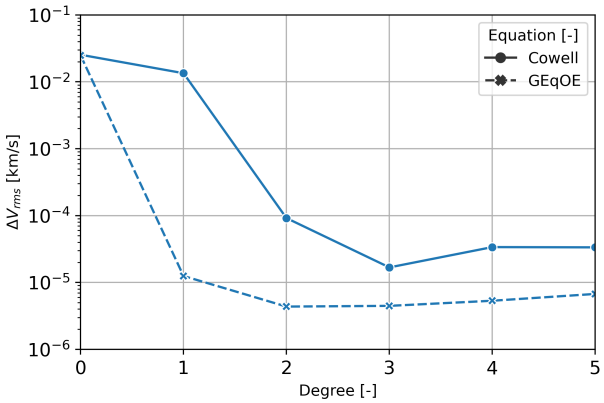

Figure 2: Final velocity errors of the non-intrusive methods, with respect to a Monte Carlo simulation, as a function of the degree of the sparse grid.

Table 1: Execution time using the non-intrusive method with 10^4 samples. The execution time of a reference Monte Carlo simulation was 118.75 s.

Polynomial Degree [-]	Number of points [-]	Execution time [s]	
		Cartesian	GEqOE
0	1	0.05683	0.0954
1	13	0.2331	0.2575
2	97	1.3588	1.7226
3	545	7.0568	8.6102
4	2561	31.8146	39.4057
5	10625	131.758	161.298

4 Intrusive Methods

Intrusive methods remove the assumption that the orbital propagator is a "black box", and remove the use of a surrogate model. Instead, the polynomials are propagated directly using Polynomial Algebra (PA). This is a technique where values in the set of real numbers are replaced with polynomials, forming an algebra with the inclusion of the necessary mathematical operations, such as addition, subtraction, multiplication, and division. Entire continuous sets of states can be propagated via this method, removing the requirement for a surrogate model as all the samples can be propagated in one execution of the propagator.

Implementing the PA-based methods revealed several key restrictions which, although not preventing the use of the methods, must be considered for their effective implementation. These were found to affect both the PA-based methods in general, independently of the space used for propagation; and the GEqOE implementation specifically.

The J_2-term perturbation revealed that numerical issues can arise from the truncations that occur within PA when multiplying or dividing. This perturbation is particularly sensitive to polynomial truncation error due to the high order inverse of the radial distance required to calculate both the perturbing acceleration ($\propto r^{-5}$), and the perturbing potential ($\propto r^{-3}$). This numerical issue can be bypassed by propagating in non-dimensional form, in this case using the initial semi-major axis, and the gravitational parameter as scaling factors.

The implementation of GEqOEs with PA highlighted one of the limitations of PA-based methods: their inability to handle discontinuities without special considerations. The initial conversion into GEqOEs, as described in [1], uses traditional Keplerian elements, however these are subject to a number of discontinuities, particularly for orbits with very low eccentricities and/or inclinations. The initial conversions for two of the six GEqOEs were redefined purely in terms of the angular momentum vector, hence bypassing the discontinues, and enabling the propagation of these elements with PA.

PA-based set propagations in GEqOEs were found to outperform the equivalent in Cartesian by approximately 2.5 times for a given accuracy (using RMSE) in the final set of states of a Low Earth Orbit (LEO) test case, as illustrated in Figures 3 and 4. The relative performance of Cowell's method and GEqOEs is highlighted by using Pareto fronts. This method, typically used in the field of multi-objective optimisation, shows the most optimal solutions relative to multiple metrics, in this case for minimising both the solution error and the execution time.

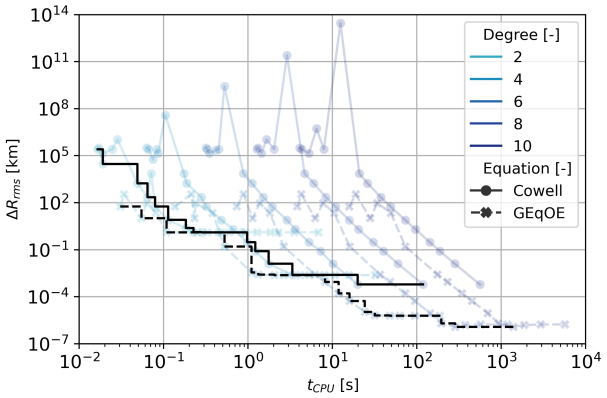

Figure 3: Final position errors of the intrusive methods, with respect to a Monte Carlo simulation, as a function of execution time.

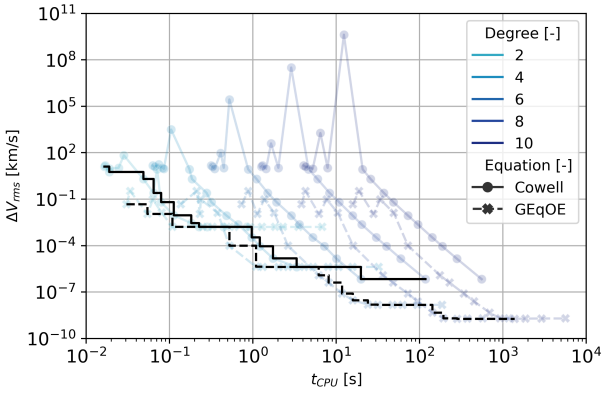

Figure 4: Final velocity errors of the intrusive methods, with respect to a Monte Carlo simulation, as a function of execution time.

5 Conclusions

In this presentation, non-intrusive and intrusive set propagation methods using GEqOEs are presented, discussing their implementation into CASSANDRA, an automated SEM tool under development at the University of Strathclyde.

For non-intrusive methods, surrogate models built in GEqOE space are shown to provide significantly improved results over models built in Cartesian space; and for intrusive methods, GEqOEs are shown to obtain a significant reduction in execution time of up to 2.5 times for a given solution accuracy, compared to traditional Cowell's method.

The challenges which were faced during the integration, both for non-intrusive and intrusive methods, for propagating uncertainty in orbital states will be highlighted; centring on the restrictions that must be considered when using PA-based methods for orbit propagation, and the analytical and numerical techniques available to mitigate any potential issues.

Acknowledgements

This work was carried out under the UKSA NSTP/SST grant titled "Artificial Intelligence for Space Surveillance and Tracking (AI4SST)", grant reference UKSAG21_0066.

References

[1] G. Baù, J. Hernando-Ayuso, and C. Bombardelli, A generalization of the equinoctial orbital elements, *Celestial Mechanics and Dynamical Astronomy* **133** (2021).

[2] J. Hernando-Ayuso, et al., Near-Linear Orbit Uncertainty Propagation in Low-Earth Orbit, in: *31st JAXA Workshop on Astrodynamics and Flight Mechanics*, Sagamihara, Japan, 26-27 July 2021.

[3] L. Sánchez, and M. Vasile, CASSANDRA: Computational Agent for Space Situational Awareness aNd Debris Remediation Automation, in: *Stardust-R - Second Global Virtual Workshop*, 13-17 September 2021.

[4] C. Greco, C. Campagnola, and M. Vasile, Robust Space Trajectory Design using Belief Optimal Control, *Journal of Guidance, Control, and Dynamics* (2022), pp. 1-18.

[5] J. Bäck, et al., Stochastic spectral Galerkin and collocation methods for PDEs with random coefficients: a numerical comparison, in: *Spectral and High Order Methods for Partial Differential Equations*, Lecture Notes in Computational Science and Engineering, Springer Berlin Heidelberg, Berlin, Heidelberg, 2011, pp. 43–62.

Session 7:

MISSION DESING

Disposal Options below the GEO protected region

Despoina K. Skoulidou*[1] and Stijn Lemmens†[1]

[1]Space Debris Office, ESOC, ESA, Darmstadt, Germany

1 Introduction

The Geosynchronous Orbital region (GEO) is the second most populated region after the Low Earth Orbital region. Since the late 90's, the IADC guideline [1] related to the disposal of a spacecraft placed in GEO suggest the usage of near-circular "graveyard" orbits above the GEO protected region (super-GEO) and provide a formula to target a minimum perigee altitude to minimise long term interference. Numerous studies have been performed for the stability of the disposal orbits in this region, and in recent years these have been extended with dynamical studies for highly-inclined GEO orbits ([4]-[9]).

Most of the GEO satellites have been launched into their operational orbits via a Geostationary Transfer Orbit (GTO), but in recent years the opportunities for direct-to-GEO missions have been increasing. For example, the new Ariane 6 launch and older Atlas V vehicles offers such a service. The IADC guidelines, for direct injection of payloads into near GEO, suggest to insert the upper stage and payload directly into a disposal orbit above or below the GEO protected region and to have the payload then perform a manoeuvre to place itself into GEO.

International space debris mitigation implementation strategies derived from the IADC guidelines or related standards have given indications on apogee limits below the GEO protected region (e.g. lower than 550 km) that avoid long-term interference[2]. However, those limits are not as well studied as those for the disposal of spacecraft above the GEO region. On the other hand, there were 127 rocket bodies found crossing the GEO protected region in 2020, where a significant number of them were placed in altitudes lower that the GEO region (sub-GEO)[3]. Hence, a detailed study on the dynamics of the objects in the near GEO region, with focus on the sub-GEO region is relevant to define guidance on where to dispose space objects without risking long term interference.

The main goal is to investigate if an apogee formula, similar to the IADC perigee formula, can be applicable for the sub-GEO region for long periods of orbital motion. For convenience, a given form is sought:

$$\Delta Q = (r_{GEO} - Q) = \Delta Q_o + b_r \cdot C_r \cdot \frac{A}{m}, \quad (1)$$

where $\Delta Q = (r_{GEO} - Q)$ is defined as the apogee difference limit, with r_{GEO} the geosynchronous semi-major axis[1], Q the maximum compliant apogee limit for every initial condition, ΔQ_o (constant term) is the apogee difference limit due to lunisolar and gravitational perturbations (i.e., no SRP), A/m is the area-to-mass ratio, C_r is the reflectivity coefficient, and b_r term is multiplied with the effective area-to-mass-ratio of the space object. Note that ΔQ is increasing as Q is decreasing. As a consequence ΔQ is increasing as a is decreasing given a fixed e.

2 Results

For this purpose, a propagator suitable for satellite motion is used to numerically construct the limit cases. The dynamical model taken into account in the propagator is the geopotential up to 2 degree and order (J_{22}), lunisolar perturbations, and SRP (cannonball model). For finding the formula, several thousand of fictitious orbits are propagated for a time span of 100 years, starting from epoch 2027/12/22 00:00:00 UTC and lunisolar configurations that maximize the effect of the perturbations that could lead to drifting in the GEO protected region. For direct-to-GEO missions, a limitation in $e \leq 0.003$, $i \leq 18°$, $\frac{A}{m} \leq 0.02 \frac{m^2}{kg}$, $C_r \in [1, 2]$ is considered.

ΔQ_o is found to be increasing linearly as function of i by analysing the simulations without the SRP effect. The maximum complaint ΔQ_o values correspond to the highest examined e values. Figure 1 shows the maximum compliant ΔQ_o as function of i, for various e values (distinguished by various colours). The green line corresponds to the final form for ΔQ_o, $\Delta Q_{ou}(i) = (235 + 2 \cdot i)$km.

From the simulations that include the SRP effect, the b_r term, which is the ratio of increasing of the compliant ΔQ w.r.t. $C_r \cdot A/m$ term, is increasing as function of i. The maximum b_r values are found for the lowest examined e values. Figure 2 shows the maximum b_r, as function of i, for various e values

*Email: despoina.skoulidou@esa.int
†Email: stijn.lemmens@esa.int

[1] $r_{GEO} \simeq 42165$km

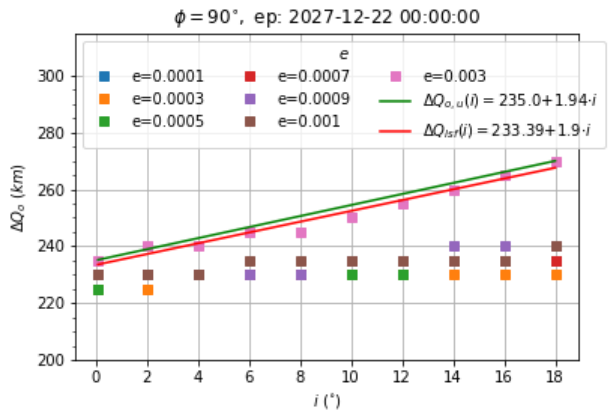

Figure 1: Maximum compliant ΔQ_o as function of i, for various e values (colour). The green line corresponds to the final form for ΔQ_o, $\Delta Q_{ou}(i) = 235 + 2 \cdot i\,(km)$.

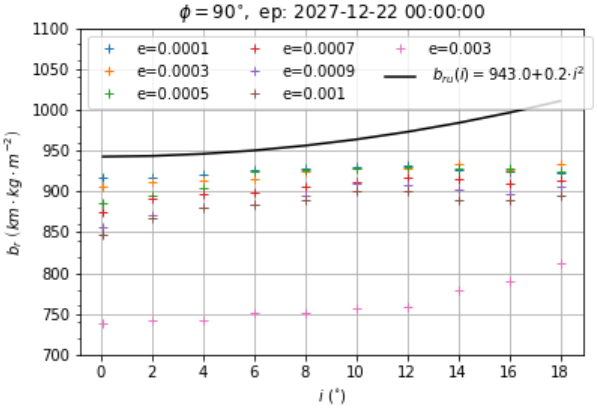

Figure 2: Maximum b_r term, as function of i, for various e values (colour). The black line corresponds to final form for the b_r term, $b_{ru}(i) = 943 + 0.2 \cdot i^2$ (km·kg·m^{-2}).

(distinguished by various colours). The black line corresponds to the final form for the b_r term, $b_{ru}(i) = 943 + 0.2 \cdot i^2$ (km·kg·m^{-2}). It is assumed that it should be always above of the br values used for the computation.

Hence, the final apogee formula has the form (in km):

$$\Delta Q_u\left(i, C_r, \frac{A}{m}\right) = \Delta Q_{ou}(i) + b_r(i) \cdot C_r \cdot \frac{A}{m}$$

$$\Delta Q_u\left(i, C_r, \frac{A}{m}\right) = 235 + 2 \cdot i + \left(943 + 0.2 \cdot i^2\right) \cdot C_r \cdot \frac{A}{m} \quad (2)$$

The formula is applicable for $e \leq 0.003$, $i \leq 18°$, $\frac{A}{m} \leq 0.02 \frac{m^2}{kg}$, $C_r \in [1, 2]$, is expressed in osculating elements terms, and is achieved using results from runs with starting epoch 2027/12/22 00:00:00 UT. Figure

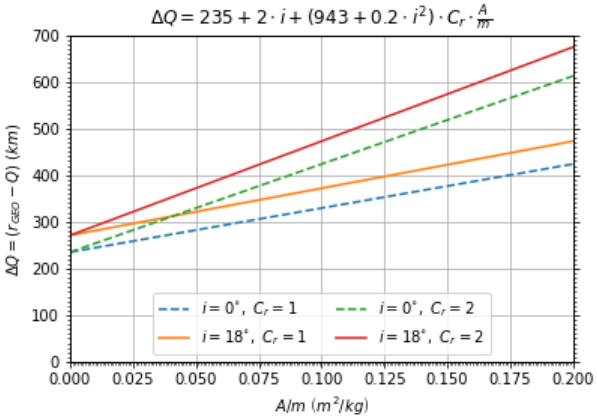

Figure 3: Maximum compliant ΔQ_u as function of A/m, and for the minimum and maximum examined values of i and C_r.

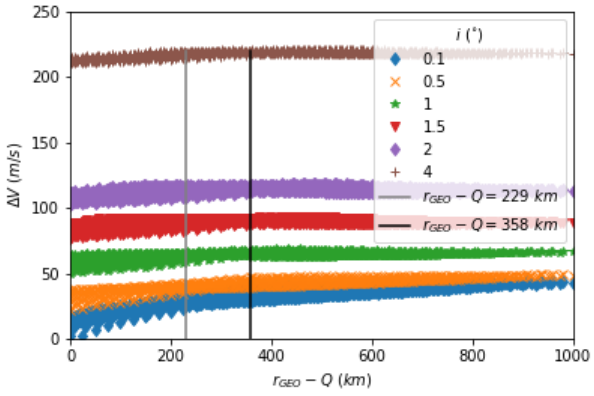

Figure 4: ΔV required to reach a geostationary orbit from sub-GEO region with respect to the apogee difference ΔQ. The colour denotes the inclination of the starting orbit

3 shows ΔQ_u as function of A/m, and for the minimum and maximum examined values of i and C_r. For $i = 0$ and $i = 18°$, maximum compliant ΔQ is found between $235 - 610$km and $270 - 680$km, respectively.

Finally, the cost in ΔV terms to reach a geostationary orbit from the sub-GEO region is computed [10]. Figure 4 shows that $\Delta V \leq 50$m/s feasible for starting and target orbits with difference in inclination $\Delta i \leq 0.5°$ and $\Delta Q = r_{GEO} - Q < 400$km for the starting orbit.

References

[1] IADC (2011). IADC space debris mitigation guidelines,`http://www.iadc-online.org/`, last accessed 2022/04/01

[2] ESA (2015). ESA space debris mitigation compliance verifications guidelines, ESSB-HB-U-002

[3] ESA Space Debris Office (2021). Classification of geosynchronous objects. issue 23, GEN-DB-LOG-00290-OPS-SD, ESA/ESOC, Darmstadt, Germany.

[4] Anselmo A., Pardini C., Space debris mitigation in geosynchronous orbit, *Advance in Space Research* **41** (2008), 1091–1099.

[5] Anselmo A., Pardini C., On the end-of-life disposal of spacecraft and orbital stages operating in inclined geosynchronous orbits, in: *Proceedings of the 9th IAASS International Space Safety Conference, Toulouse (France), 18-20 October 2017*, International Association for the Advancement of Space Safety (IAASS), ISBN: 978-90-828378-0-3, 2017, 87–94

[6] Chao C.-C., Campbell, S., Long-Term Perigee Height Variations of Geo Disposal Orbits a Revisit, in: *4th European Conference on Space Debris, Darmstadt, Germany, 18-20 April 2005*, 2005

[7] Delong N., Fremeaux C., Eccentricity management for Geostationary satellites during end of life operations, in: *4th European Conference on Space Debris, Darmstadt, Germany, 18-20 April 2005*, 2005

[8] Gkolias, I., Colombo, C., Towards a sustainable exploitation of the geosynchronous orbital region, *Celestial Mechanics and Dynamical Astronomy* **131** (2019), 19

[9] Lewis H.G., Swinerd G.G., Martin C.E., Campbell W.S., The stability of the disposal orbits at super-synchronous altitudes, *Acta Astronautica* **55** (2004), 299—310.

[10] Skoulidou D.K, and Lemmens S., The Geosynchronous orbital region and reaching it from lower apogee altitudes, in: *8th European Conference on Space Debris, Darmstadt, Germany, 20-23 April 2021*, 2021

Preliminary analysis of an active debris removal mission for large constellations: A Constraint Programming methodology

Adrian Barea*[1], Juan Luis Gonzalo†[2], Camilla Colombo‡[2], and Hodei Urrutxua§[1]

[1]Aerospace Systems and Transport Research Group, Universidad Rey Juan Carlos, Fuenlabrada, Spain
[2]Department of Aerospace Science and Technology, Politecnico di Milano, Milan, Italy

1 Introduction

The formation of high-density clusters of spaceborne objects poses a significant risk for the sustainability of future space operations. This is particularly critical for regions of special operational interest, such as Low Earth Orbit (LEO) or Geostationary Orbit, because it could render them unusable for their future exploitation. Currently, several initiatives to deploy large constellations in the LEO region are being carried out. It is expected that the operation of such constellations will include the end-of-life deorbiting of their defunct satellites. Nevertheless, the failure of said disposal processes poses a threat, not only for the space environment, but also for the constellation performance. This has motivated the assessment of the feasibility of constellation-servicing debris removal missions. In particular, the Sunrise project, funded by the European Space Agency (ESA), intends to identify affordable active debris removal strategies for large constellations in LEO. Moreover, this project plans to develop the necessary technologies to perform these missions so as to, eventually, provide a competitive service in the international market. Under this project, a consortium comprising D-Orbit SpA and Politecnico di Milano has completed the phase A design for this service [1, 2, 3].

As the objects to be removed in constellation-servicing debris removal missions are not known beforehand, the preliminary design of such missions requires an exhaustive analysis of complex mission configurations, especially when dealing with the coordination of several servicing satellites. Constraint Programming is a classical artificial intelligence paradigm characterised by its flexibility for the modelling of complex problems. In the field of space operations, this approach has been successfully used for mission planning and scheduling [4]. This work proposes a framework that leverages the strengths of Constraint Programming for the preliminary analysis of space missions. Specifically, it uses constraint propagation and search techniques to thoroughly explore the configuration space of a mission in an efficient manner. Consequently, it is able to quantify the performance of precomputed mission choices with respect to the mission requirements, as well as generate new ones that optimise such performance.

The proposed methodology has been particularised for an application case involving an active debris removal mission for large constellations in LEO. This case comprises servicing satellites that install deorbiting kits in each of the failed satellites associated to them, except for the one removed in the last place. This way, the servicing satellite will only transport this object, while the deorbiting kits will carry out the disposal of the rest of them. A preliminary mission analysis developed under ESA's Sunrise project has been evaluated [1]. New values for the semimajor axes of the phasing orbits and the inclinations of the injection and drifting orbits have been computed. Thus, significantly reducing the mission time, while complying with a predefined ΔV budget.

2 Problem description

The problem at hand involves a LEO constellation comprising several orbital planes with failed satellites, which will be cleared by a set of servicing satellites. Each servicing satellite is assigned a subset of the constellation planes and will install deorbiting kits to each of its corresponding targets, save for the last of them, which will be directly removed by the servicing satellite. This way, each of the deorbiting kits, as well as the servicing satellite, will transport a target to its corresponding disposal orbit.

In particular, all the servicing satellites will be injected into the same orbit, where they will coast until they achieve the Right Ascension of Ascending Node (RAAN) of their first associated constellation plane. This RAAN variation is exclusively produced by the nodal drift resulting from the J_2 perturbation. Then, each servicing satellite will rendezvous with each of the targets within that plane to deploy the deorbiting kits. After that, they will transfer to a drifting

*Email: adrian.barea@urjc.es.
†Email: juanluis.gonzalo@polimi.it.
‡Email: camilla.colombo@polimi.it.
§Email: hodei.urrutxua@urjc.es.

orbit so that they can achieve the RAAN of the next constellation plane to be cleared. This process is repeated until every servicing satellite has cleared its associated planes and is located in a disposal orbit, along with the last target.

3 Methodology

The resolution of a Constraint Programming problem involves the interaction of two different processes, namely constraint propagation and search. The purpose of the constraint propagation process is twofold. On the one hand, it checks the feasibility of a given constraint for the considered variable domains (i.e., if there is at least one possible value assignment, from the domains of the considered variables, that fulfills such constraint). On the other hand, it prunes values from the variable domains that cannot appear in a feasible solution.

In general, the use of constraint propagation alone does not guarantee the determination of a feasible solution (or infeasibility) of the problem. However, this can be achieved with the inclusion of an additional search process. This process follows a divide-and-conquer approach to split the variable domains of the original problem, thus partitioning it into several subproblems. The purpose of this technique is to obtain subproblems simple enough so that the constraint propagation process is able to determine their feasibility.

Consequently, the usual workflow of Constraint Programming alternates the constraint propagation and search processes until a feasible solution of one of the subproblems is found or the infeasibility of all the subproblems is demonstrated. However, in the particular case addressed in this work, the whole set of feasible solutions of the problem has to be determined. Therefore, every single one of the subproblems has to be demonstrated to be feasible or infeasible.

The general resolution process of Constraint Programming problems has been tailored to solve the mission analysis problem at hand. This particular process (Figure 1) involves the partitioning of the search space of the concerning problems into problem instances. The feasibility of each of those problem instances with respect to a series of constraints (i.e., the mission requirements) is evaluated. If the feasibility (or infeasibility) of a problem instance is unambiguously determined, a domain pruning process will evaluate the implications of its feasibility for the rest of the problem instances. In turn, if the feasibility of a problem instance is inconclusive, it is partitioned into simpler instances, which will be later evaluated in a similar fashion.

The feasibility of an instance depends on a set of controlled and uncontrolled variables, and it is determined by means of bounding the range of constraint

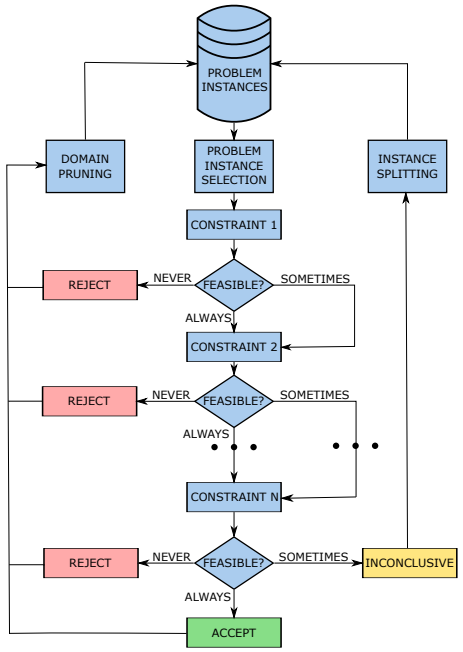

Figure 1: Problem resolution process.

values that would be obtained for that set of variables. As such bounds are not unique, two possibilities have been considered. On the one hand, the feasibility bounds are obtained when using both the controlled and uncontrolled variables to minimise (or maximise) the constraint value. On the other hand, the optimality upper bound is obtained when using the controlled variables to minimise the constraint value, while the uncontrolled variables try to maximise it. Consequently, the optimality bounds provide a tighter interval, but are more computationally expensive.

4 Results

The considered application case involves a constellation comprising twelve orbital planes. Its associated performance baseline involves two different scenarios. On the one hand, *Scenario 1* considers nine objects to remove within each of the constellation planes, such that each of those planes has associated its own servicing satellite. On the other hand, *Scenario 2* also involves removing nine objects with each satellite. However, in this case, those objects are distributed among two adjacent constellation planes. Moreover, the mission requirements impose a maximum mission time and a ΔV budget.

The problem instances that partition the search space of the problem can be defined with (N, P) tuples, where N is the number of objects to be removed

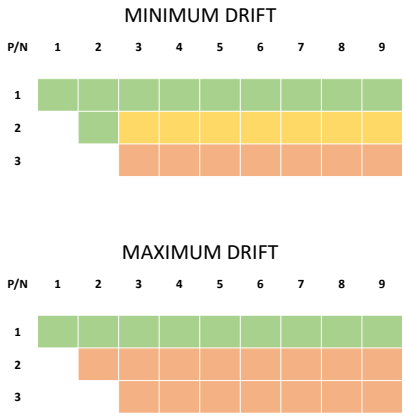

Figure 2: Problem instance feasibility diagram.

and P is the number of constellation planes in which they are distributed. Figure 2 shows the results of computing the feasibility bounds for the (N, P) problem instances of up to nine objects, where the green instances are feasible in any case, the red ones are always infeasible and the yellow ones are inconclusive. In particular, this figure depicts the problem instance diagrams for the servicing satellites that serve the planes closer to and farther from the injection orbit, respectively labeled as minimum and maximum drift cases. It has to be noted that the feasibility of both mission time and ΔV requirements is considered in such diagrams, i.e., if one of those constraints is infeasible for an instance, such instance is deemed infeasible. In turn, for an instance to be feasible, both requirements have to be feasible for the whole variable domain.

It can be seen that *Scenario 1* is feasible in any case. In turn, for *Scenario 2*, the fulfilment of the mission requirements is not guaranteed, even for the servicing satellite with minimum drift. So as to improve the mission performance for *Scenario 2*, the semimajor axes of the phasing orbits and the inclinations of the injection and drifting orbits have been considered as controlled variables. A dual based method has been used to optimise such controlled variables [5], thus obtaining the optimality bounds associated to their new values. Figure 3 compares the feasibility and optimality bounds of the mission time, for each of the servicing satellites considered in *Scenario 2*. It has to be noted that the ΔV budget requirement is fulfilled by every servicing satellite for both the feasibility and optimality bounds. It can be observed that the optimised mission parameters significantly reduce the mission time. In fact, this new mission configuration is able to fulfill both of the mission requirements for every problem instance of *Scenario 2*.

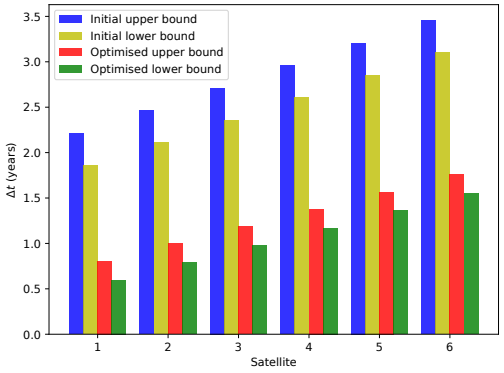

Figure 3: Mission time bounds.

Acknowledgments

A. Barea and H. Urrutxua were supported by the Spanish State Research Agency and the European Regional Development Fund through the research grant PID2020-112576GB-C22 (AEI/ERDF, UE). A. Barea also wishes to acknowledge funding from grant PREDOC20-003 of "Universidad Rey Juan Carlos". J.L. Gonzalo and C. Colombo were supported by the COMPASS project funded by the European Research Council (ERC) under the European Union's Horizon 2020 research and innovation program (grant agreement No 679086 - COMPASS).

References

[1] S Huang, C Colombo, JL Gonzalo, A Masserini, M Nugnes, L Vallini, and M Petit. Preliminary mission analysis of active debris removal service for large constellations. In *71st International Astronautical Congress (IAC 2020)*, pages 1–6, 2020.

[2] Camilla Colombo, Simeng Huang, Giacomo Borelli, Francesco Cavenago, Marco Nugnes, JL Gonzalo, Gabriella Gaias, Mauro Massari, Lorenzo Vallini, Mathieu Petit, et al. Mission analysis and design for an active debris removal service for large constellations. In *8th European Conference on Space Debris, ESA/ESOC*, pages 1–11. ESA, 2021.

[3] Giacomo Borelli, G Gaias, C Colombo, and L Vallini. Rendezvous and proximity operations design of an active debris removal service to a large constellation fleet. In *72nd International Astronautical Congress (IAC 2021)*, pages 1–13, 2021.

[4] Joseph C Pemberton and Flavius Galiber. A constraint-based approach to satellite scheduling. *DIMACS Series in Discrete Mathematics and Theoretical Computer Science*, 57:101–114, 2001.

[5] Adrian Barea, Hodei Urrutxua, and Luis Cadarso. Dual-based method for global optimization of impulsive orbital maneuvers. Submitted for publication.

GPU-assisted search for low-cost transfers between whiskered tori, with applications to resonance transfers in a restricted 4-body model

Bhanu Kumar*[1], Rodney L. Anderson†[2], and Rafael de la Llave‡[1]

[1]School of Mathematics, Georgia Institute of Technology
[2]Jet Propulsion Laboratory, California Institute of Technology

Abstract

When the planar circular restricted 3-body problem is periodically perturbed, most unstable periodic orbits become invariant tori. However, 2D Poincaré sections no longer work to find their manifolds' intersections; new methods are needed. In this study, we first present a method of restricting the intersection search to only certain manifold subsets. We then implement this search using Julia and OpenCL, representing the manifolds as discrete meshes and using methods inspired by computer graphics collision detection algorithms with GPUs to find approximate intersections of the manifolds. After some demonstrations using the comparatively simpler Jupiter-Europa planar elliptic RTBP model, we apply the tools to the problem of finding low-cost transfers from Jupiter-Ganymede to Jupiter-Europa resonances in a Jupiter-Europa-Ganymede planar restricted 4-body model.

1 Introduction

In the planar circular restricted 3-body problem (PCRTBP), at each mean motion resonance, families of stable and unstable periodic orbits exist over a range of energy levels. Of these, the unstable resonant orbits possess attached stable and unstable invariant manifolds. Owing to the Chirikov resonance-overlap criterion, it is the intersection of manifolds from different resonances that generates global chaos and enables large-scale natural transport across the system phase space. This instability in turn can be profitably leveraged for the purposes of low-energy space mission trajectory design. Indeed, prior studies have used the stable and unstable manifolds of resonant periodic orbits for mission design in the Jupiter-Europa [1] and Saturn-Titan [6] PCRTBP systems.

In the PCRTBP, due to the presence of the conserved energy integral of motion, it is possible to find heteroclinic and homoclinic connections relatively easily. As the phase space is 4-dimensional, fixing an energy level restricts the dynamics to a 3D submanifold, and the Poincaré section further reduces the dimensionality of the system to 2D. Since the manifolds of the periodic orbits are 2D cylinders in the full phase space, taking the Poincaré section reduces the manifolds to 1D curves in the section, so the problem of finding connections between periodic orbits reduces to finding the intersection of two 1D manifold curves in a 2D plane; this is done in many studies e.g. [2, 4].

When the PCRTBP is subjected to a time-periodic Hamiltonian forcing, however, two things occur. First of all, there is no longer a constant energy integral of motion. Second of all, the unstable periodic orbits from the PCRTBP persist not as periodic orbits, but as mostly quasi-periodic orbits in the new system [5]. By considering stroboscopic maps instead of the continuous-time flow, we can take these quasi-periodic orbits to be invariant 1D tori (circles) in the 4D map phase space, with 2D cylindrical stable and unstable manifolds. Even though the map-invariant manifold dimension is the same as the PCRTBP, in the absence of the energy integral, the usual method of using a 2D Poincaré section to find intersections of the manifolds for heteroclinic connections will not work. Also, manifold intersections in the perturbed system will occur at isolated points, rather than along continuous trajectory curves. Hence, a different method of searching for and computing homoclinic and heteroclinic connections in the full 4D phase space is required.

One reason that periodically-forced PCRTBP systems are important is that the effect of a third large body on the spacecraft motion can be modeled as such a system. A common feature of the previously mentioned research into mean motion resonances has been that the search for connections was done between different resonant orbits, but for all orbits resonant with the same moon. However, when designing multi-moon tours of planetary systems, it is necessary to transition from orbits resonant with one moon to those resonant with a different moon. And in the region where this transition must occur, the gravitational influence of both moons plays an important role, motivating the

*Email: bkumar30@gatech.edu. Research supported by NASA Space Technology Research Fellowship, grant 80NSSC18K1143
†Email: Rodney.L.Anderson@jpl.nasa.gov.
‡Email: rafael.delallave@math.gatech.edu.

use of restricted 4-body models to study the dynamics and possible trajectories for the spacecraft.

In this study, we develop tools to very quickly search for near-intersections of stable and unstable manifolds of whiskered tori in such periodically-forced PCRTBP models. These near-intersections in turn can serve as initial candidates for a two-point boundary value problem solver when trying to compute a true intersection. Furthermore, even when one is unable to correct a near-intersection into a true intersection, these near-intersections may still be useful as low-Δv maneuver opportunities. Indeed, we investigate transfer options between Jupiter-Ganymede and Jupiter-Europa resonances in a planar concentric circular restricted 4-body model; although thus far we are still searching for true heterocliinc connections, the approximate intersections found still are of use.

2 GPU-assisted manifold mesh intersection search

As was mentioned earlier, using stroboscopic maps instead of the periodically-forced continuous-time flow reduces the dimensionality of the objects and phase space considered, so defining $F : \mathbb{R}^4 \to \mathbb{R}^4$ as the stroboscopic map, we henceforth consider F-invariant objects rather than the flow-invariant ones.

In earlier work [5], we developed methods for efficient computation of F-invariant tori as well as Fourier-Taylor parameterizations of their local stable/unstable manifolds in periodically-forced PCRTBP models. By numerically integrating points found using these stable/unstable local manifold parameterizations, we were also able to to find discrete quadrilateral (quad) mesh representations of the globalized stable/unstable torus manifolds. The first part of this study presents very fast computational methods for finding intersections of these 2D manifold meshes, which in turn give near-intersections of the true continuous manifolds.

Before working directly with manifold meshes, we are able to partition the global manifolds into subsets we call layers; for the unstable manifold W^u, the layers are denoted $U_n, n \in \mathbb{Z}$ and for the stable manifold W^s, the layers are denoted $S_n, n \in \mathbb{Z}$. Each manifold is the disjoint union of all its layers, whose key property is that $F(U_n) = U_{n+1}$ and $F(S_n) = S_{n-1}$. When searching for heteroclinic connections, this property allows us to restrict the search for manifold intersections to only pairs of layers of form $(U_{\tilde{n}}, S_{\tilde{n}})$ and $(U_{\tilde{n}}, S_{\tilde{n}-1})$ for $\tilde{n} \in \mathbb{Z}$ without loss of generality.

After identifying the pairs of manifold layers which need to be checked for intersection, we take the mesh subsets corresponding to those layers, and develop a method which very quickly identifies the quad pairs (one unstable quad, one stable quad) which intersect, as well as computing the intersections. For this, checking each unstable quad with each stable quad for an exact intersection can be prohibitively expensive; thus, we use a two-phase approach inspired by 3D computer graphics collision detection algorithms. The first phase of our method is the broad phase, where a potentially (but not certainly) intersecting set of quad pairs is identified using very simple and computationally inexpensive computations. This eliminates the very vast majority of the quad pairs from further consideration. After this, the narrow phase entails applying the exact quad-quad intersection test (which is itself comprised of 4 triangle-triangle intersection tests) to only the potentially intersecting quad pairs.

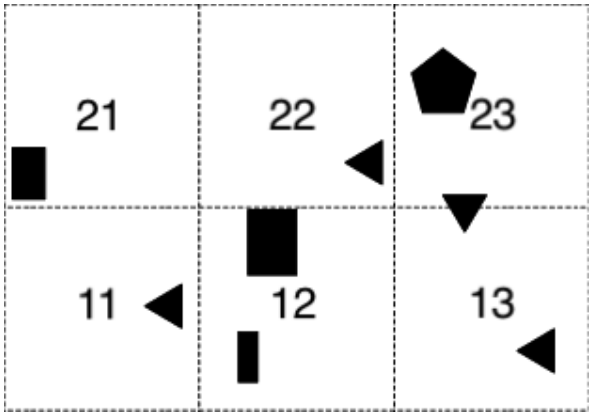

Figure 1: Uniform grid spatial partitioning.

The broad phase is comprised of 3 steps; the first step, done on the CPU, is a uniform grid spatial partitioning, where we sort the quads into boxes such that only two quads overlapping the same box may intersect, as schematically illustrated in Figure 1. Note that this is linear in the number of quads, not quad pairs. The next step, done on the GPU, is to carry out a bounding box test in parallel on all the pairs of quads identified by the spatial partitioning; this is illustrated in Figure 2. The last broad test, also done on the GPU, checks whether one quad of a pair is on the same side of the planes formed by the vertices of the other quad; if so, they cannot intersect. Finally, the narrow phase is a CPU linear-algebra based test for the triangle pairs which were not eliminated by the rough test. The algorithm is programmed using Julia along with the OpenCL.jl library for the bounding-box test, which allows for the code to work with both Nvidia and AMD GPUs, as well as multicore CPUs in case no GPU is available.

We used a Jupiter-Europa planar elliptic RTBP model for computational benchmarking of these tools, finding near-intersections of unstable manifolds of a 3:4 resonant orbit with the stable manifolds of a 5:6 resonant orbit, both globalized out to 14 layers. The near-intersection search took only approximately 11-12 seconds on a 2019-era consumer laptop as well as a desktop with a 2011-era CPU and 2016-era consumer-

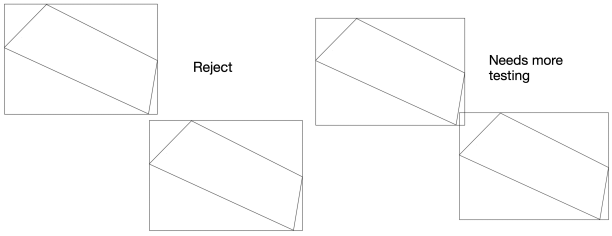

Figure 2: Illustration of bounding box test in 2D

grade GPU to process all of these layers, demonstrating the effectiveness of the tools developed here.

3 Search for low-cost Jupiter-Ganymede to Jupiter-Europa resonance transfers

With algorithms for finding manifold near-intersections developed, we next apply them to the previously mentioned problem of transitioning from resonant flybys of one moon to a resonance with a different moon. Obviously, this problem cannot be addressed in the PCRTBP which does not contain both moons (unless one patches together two PCRTBP models). Thus, to study the Jupiter-Ganymede to Jupiter-Europa resonance problem, we use a planar concentric circular restricted 4-body model (CCR4BP) to model the spacecraft motion, assuming that Europa and Ganymede revolve in coplanar, concentric circles around Jupiter.

After applying the tools of our previous paper [5] to compute the tori and manifolds at Jupiter-Europa and Jupiter-Ganymede resonances, we use the algorithm of the previous section to search for near-intersections. Doing this, we found near-intersections of unstable manifolds of both 7:5 and 3:2 Jupiter-Ganymede resonant tori with stable manifolds of 3:4 Jupiter-Europa resonant tori. Indeed, the 3:2 Jupiter-Ganymede to 3:4 Jupiter-Europa near-intersection case is not altogether unexpected, given the 2:1 Laplace resonance between Europa and Ganymede's orbits around Jupiter.

4 Conclusion

We presented an overview of our methodology for using GPUs, combined with the concept of manifold layers, for rapidly finding near-intersections of torus manifolds. These algorithms improve upon our previous work [3], and should also be possible to generalize to higher dimensional manifolds in higher-dimensional phase space, by replacing quads (which can be divided into triangles) with prisms comprised of higher-dimensional simplices. Using our tools, we demonstrated a variety of low-cost transfer options from various Jupiter-Ganymede resonances to the 3:4 Jupiter-Europa resonance. Further work is ongoing to search for true heteroclinic connections between Jupiter-Ganymede and Jupiter-Europa resonances.

References

[1] Rodney Anderson and Martin Lo. Flyby design using heteroclinic and homoclinic connections of unstable resonant orbits. In *Advances in the Astronautical Sciences*, volume 140, Feb 2011.

[2] Wang Sang Koon, Martin W Lo, Jerrold E Marsden, and Shane D Ross. *Dynamical systems, the three-body problem and space mission design*. Marsden Books, 2011.

[3] B. Kumar, R. L. Anderson, and R. de la Llave. Using GPUs and the parameterization method for rapid search and refinement of connections between tori in periodically perturbed planar circular restricted 3-body problems. In *AAS/AIAA Space Flight Mechanics Meeting*, number AAS 21-349, February 2021.

[4] Bhanu Kumar, Rodney L. Anderson, and Rafael de la Llave. High-order resonant orbit manifold expansions for mission design in the planar circular restricted 3-body problem. *Communications in Nonlinear Science and Numerical Simulation*, 97:105691, 2021.

[5] Bhanu Kumar, Rodney L. Anderson, and Rafael de la Llave. Rapid and accurate methods for computing whiskered tori and their manifolds in periodically perturbed planar circular restricted 3-body problems. *Celestial Mechanics and Dynamical Astronomy*, 134(1):3, 2022.

[6] Mar Vaquero Escribano. *Spacecraft Transfer Trajectory Design Exploiting Resonant Orbits In Multi-Body Environments*. PhD thesis, Purdue University, 2013.

Shape-based low-thrust trajectory optimization enhanced via orthogonal functions, collocation and regularization

Sergio Cuevas del Valle*[1], Hodei Urrutxua†[2], and Pablo Solano-López‡[2]

[1]Universidad Rey Juan Carlos, Camino del Molino 5, 28942, Fuenlabrada, Spain
[2]Aerospace Systems and Transport Research Group, Universidad Rey Juan Carlos, Camino del Molino 5, 28942, Fuenlabrada, Spain

Abstract

This work investigates novel aspects and approaches to previously-developed shape-based methods for optimal control and navigation problems in astrodynamics. The main contributions of our research refer to the introduction of new functional descriptions of the orbital motion, along with sampling point locations compliant with collocation theory, and hybridized with classical regularization techniques, in order to enhance the numerical performance of the proposed algorithms.

1 Introduction

Shape-based methods have gained increasing attention within the astronautical community in recent times, with extensive applications within optimization problems. The rationale behind such methodologies lies in exploiting particular functions to represent the orbital motion of the system, typically a spacecraft. Such analytical expressions, usually given by direct application of the boundary conditions of the problem, enable a quick and fast generation of preliminary mission design trajectories or initial guesses, which may undergo further refinement within more complex optimization solvers. Clearly, the function in-use is a key element of the methodology, whose fundamental features define the radius of convergence of the algorithm together with the intrinsic capabilities of the method to represent complex dynamics and associated solutions.

Shape-based methods for trajectory design were first introduced by Petropoulos and Longuski [1], by selecting an exponential sinusoid function to describe the trajectory of a low-thrust accelerated spacecraft. Thereafter, sinusoids have been a traditional choice to represent spacecraft dynamics for other applications [3]. Wall and Conway [6] presented inverse polynomials to match the spacecraft boundary conditions and its intrinsic dynamics. More recently, Xie et al. [7] suggested a rapid shaping method based on the radial coordinate form of the initial and target orbits, and Roa et al. [4] introduced the concept of generalized logarithmic spirals in a series of works.

Orthogonal polynomial bases, as well as general spirals, have been used massively in direct transcription optimal control solvers and numerical approximation across a wide range of fields, from Fluid Mechanics to Astrodynamics. However, they are not often selected to construct shape-based methods for orbital mechanics applications. More recently, Taheri [5] introduced a shape-based formulation to describe spacecraft trajectories based on a finite Fourier series. Based on these latter results, Hou et al. [8, 2] presented a shape-based method to design the 3D trajectories of electric solar wind sails, relying on a Bézier curves approximation, which builds upon the family of Bernstein polynomials. Despite their successful application to this low-thrust trajectory design optimization, their mathematical formulation has not been completely explored yet to its full potential, nor their numerical and computational advantages have been exploited. In addition, despite some recent work on optimal control [9], general shape-based methods have not been employed as a core optimization engines, but as a low-cost, fast technique to generate dynamically-compliant trajectories to be refined afterwards in more detail design phases.

This work presents a novel approach to tackle optimization problems in astrodynamics using enhanced shape-based methods, together with a real assessment of the viability of these algorithms as general optimization solvers. Two specific problems are mainly studied: the design of orbital transfers for active debris removal missions and orbit determination for propelled spacecraft. In particular, we introduce new functional representations of the system's time evolution by means of an orthogonal version of the Bernstein polynomials family, in order to enhance the algorithm's numerical behaviour and improve on it con-

*Email: s.cuevas.2017@alumnos.urjc.es. Research supported by PID2020-112576GB-C22 (AEI/ERDF, UE).

†Email: hodei.urrtuxua@urjc.es. Research supported by PID2020-112576GB-C22 (AEI/ERDF, UE).

‡Email: pablo.solano@urjc.es Research supported by PID2020-112576GB-C22 (AEI/ERDF, UE).

vergence properties. Additionally, a direct performance comparison is performed and presented against classical orthogonal bases, which have still not been employed in this methodology. The optimization-associated collocation problem is then reformulated, initially on the natural nodes of the selected functional bases and then in regularized coordinates, to explore the solution's intrinsic features and dynamics. Research on the effect of the collocation mesh on the final optimal solution is also conducted and presented. Finally, several benchmark missions are introduced and solved by the proposed techniques for demonstration purposes.

2 Shape-based methods

A great variety of methods have been developed for numerically solving optimal control problems. Due to their numerical performance and ease of pose, direct transcription methods, despite not being the most accurate, are among the most extensively used. Direct transcription methods project the state evolution and the control input onto given functional bases and pose a discretized Non Linear Programming (NLP) Problem to solve the given general Bolza problem of interest [10].

Shape-based methods, which show different formulations, are closely related to direct transcription solvers, as they also project the state of the system onto given selected functional bases. However, when compared against each other, all shape-based methods impose boundary conditions into the solution by quasi-analytically selecting appropriate constants or weights in the state functional expansion. This allows for a quick generation of boundary-compliant initial guesses for optimization solvers (notably, for direct transcription ones) as long as the selected functional base is able to capture the problem's intrinsic dynamical features.

In our particular case, additionally to imposing boundary conditions as already explained, when used as a general NLP optimization core, shape-based methods minimize the problem's cost function by selecting the optimal weights for each of the function of the base used in the state expansion. Such cost function shall be expressed as a residual of the state functional series and the problem's dynamics, therefore intrinsically imposing dynamic and path constraints at prescribed, discrete sampling points on the independent variable in the equations of motion.

3 Orthogonal functional bases

Shape-based methods are primarily constructed upon the selection of an appropriate functional basis on which to decompose the orbital motion evolution. Such selection may be accomplished by balancing different criteria, from the computational cost and complexity of evaluating the function to its analytical expression and suitableness to express the problem dynamics. Despite the existence of a vast number of options, previous work have focused on a really narrow range of bases, whose mathematical and approximation properties are still to be objectively explored. In particular, in spite of showing clear advantages within general optimization algorithms, to the best of our knowledge, orthogonal polynomials have not been introduced into the topic, so their behavior and actual performance is still to be unveiled.

Firstly, this work presents a novel approach to the application of Bézier curves to these optimization problems using an alternative functional basis; in particular, an orthogonal version of their generating Bernstein polynomials are proposed, to enhance their numerical behaviour and improve on their convergence. Secondly, the use of additional orthogonal bases is investigated, such as that of Chebyshev or Legendre, due to the intrinsic benefits they may bring when constructing shape-based methods upon them. Finally and as further discussed, direct comparison is performed between the different functional bases considered, together with exploring the intrinsic applications and characteristics of each of them.

4 Nodal and regularized discretization grid

One of the main drivers of the performance of the algorithm is the trajectory sampling grid, given by the discretization of the independent variable of the problem. This work introduces two major novelties from which the overall performance of the algorithm may benefit.

Up to now, previous work has focused on functional discretization and interpolation by means of non-optimal node selection techniques. Specifically, shape-based method have relied on classical collocation nodes, such as those of Legendre-Gauss-Radau or Legendre-Gauss-Lobatto [2], to define the trajectory sampling points, i.e. the time instants at which both, the control and dynamic constraints are evaluated. While this may show advantages when the optimal solution is then used as an initial guess in an spectral optimization solver, based on such classical nodes, it does not exploit the intrinsic approximation capabilities of the selected functional bases, nor they minimize the approximation error as compared to using their natural collocation nodes [11]. By exploiting the natural formulation of these polynomials, the numerical performance of these curves, as used in shape-based methods, is increased: their interpolation accuracy is not only ensured but the problems-at-hands dimensionality is also reduced, with clear advantages within standard optimization NLP solving techniques.

However, the definition of this discretization grid by means of a time-like variable may not be the optimal choice, due to the intrinsic dynamics of the Keplerian gravitational problem. Although applied to perturbed trajectories, orbital regularization techniques may also provide a particularly interesting approach to express the problem's dynamic constraints. They enable the definition of linearly-spaced grid points in a fictitious time scale, while ensuring to capture the natural features of the optimal solution trajectory and associated orbital motion evolution.

5 Applications and benchmark missions

The proposed algorithms and techniques are demonstrated and validated within several end-to-end low-thrust mission design cases, as shown in Figure 1. Specifically: 1) low-thrust transfers within low Earth orbit are solved using low-order, orthogonal functions to illustrate the performance of the proposed enhancements in orbit raising problems and active debris removal missions for towing defunct satellites; and 2) preliminary orbit determination for low-thrust propelled spacecraft is achieved by re-purposing the proposed shape-based techniques, thus demonstrating their suitability to perform orbit determination with the presence of thrusting trajectory arcs. The computational benefits of this novel formulation are shown by confronting them in the aforementioned missions against other traditional approaches: the use of other mentioned orthogonal polynomial bases, and the already described Bézier functions. The effect of several regularization techniques and the resulting regularized sampling points is also studied, together with their benefits and possible added drawbacks.

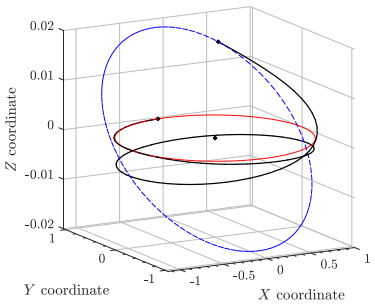

Figure 1: LEO low-thrust orbit transfer in normalized coordinates.

6 Conclusions

This work presents an extended formulations of shape-based methods for general astrodynamics optimization problems, with particular applications within low-thrust trajectory optimization. Such methodology enables a low-cost NLP optimization to replace classical direct transcription optimal control problems. New functional bases on which to express the system's motion are presented together with their performance comparison against classical orthogonal polynomials. Additionally, time regularization is employed to construct a sampling grid that exploits the natural features of orbital motion, thus enhancing the performance of shape-based methods. Several benchmark missions are presented and solved using the aforementioned techniques to demonstrate their capabilities in real mission scenarios. Finally, new ideas, extensions and follow-up work for the presented optimization techniques are introduced and discussed.

References

[1] A. E. Petropoulos and J.M. Longuski, shape-Based algorithm for automated design of low-thrust, gravity-assist trajectories, *Journal of Spacecraft and Rockets* **41** (2004), 787–796.

[2] Z. Fan, M. Huo , N. Qi, C. Zhao, Z. Yu and T. Lin, Initial design of low-thrust trajectories based on the Bézier curve-based shaping approach, *Journal of Aerospace Engineering* **234** (2020).

[3] D. Izzo, Lambert's problem for exponential sinusoids, *Journal of Guidance, Control, and Dynamics* **29** (2006), 1242—1245.

[4] J. Roa, J. Peláez and J. Senent, New analytic solution with continuous thrust: generalized logarithmic spirals, *Journal of Guidance, Control, and Dynamics* **36** (2016), 2336—2351.

[5] O. Abdelkhalik and E. Taheri, Approximate on-off low-thrust space trajectories using Fourier series, *Journal of Spacecraft and Rockets* **49** (2012), 962—965.

[6] B. Wall and B. Conway, Shape-based approach to low-thrust rendezvous trajectory design, *Journal of Guidance, Control, and Dynamics* **32** (2009), 95—102.

[7] C. Xie, G. Zhang and Y. Zhang, Shaping approximation for low-thrust trajectories with large out-of-plane motion, *Journal of Guidance, Control, and Dynamics* **39** (2016), 2776—2786.

[8] M. Huo, G. Mengali, A. Quarta et al, Electric sail trajectory design with Bezier curve-based shaping, *Aerospace Science and Technology* **88** (2019), 126—135.

[9] D. Morante, M. Sanjurjo and M. Soler, Multi-objective low-thrust interplanetary trajectory optimization based on generalized logarithmic spirals, *Journal of Guidance, Control, and Dynamics* **42** (2018), 1—15.

[10] B. Conway, A survey of method available for the numerical optimization of continuous dynamic systems, *Journal of Optimization Theory and Applications* **152** (2012), 271—306.

[11] L. Trefethen, *Approximation Theory and Approximation Practice*, 2013.

Orbit Transfer using Theory of Functional Connections via change of variables

Allan K. de Almeida Jr*[1], Antonio F. B. A. Prado†[1], and Daniele Mortari‡[2]

[1]INPE - National Institute for Space Research, São José dos Campos, SP, Brazil
[2]Aerospace Engineering, Texas A&M University, College Station TX, 77843

1 Introduction

The Theory of Functional Connections (TFC) is a new important and recent mathematical framework [1, 2] providing efficient solving methods to constrained optimization problems. This mathematical tool allows to transform constrained optimization problems, such as Boundary Value Problems (BVP), into unconstrained ones. This is done by deriving *constrained expressions*, which are functionals with embedded constraints. These functionals reduce the whole function space (where to search the solution) to just the function subspace that fully satisfying the problem constraints. This way the constrained problem is transformed into an unconstrained problem that can be solved using more simple, robust, accurate, fast and reliable methods. As an example, a BVP on a linear ODE is directly solved by linear least-squares.

The TFC framework is fully developed for linear constraints. Therefore, its technique to solve ODE is straightforward in the case where the constraints of the problem are linear on its variables [3, 4]. On the other side, it may be harder to be used in the case the constraints are nonlinear in the variables, where the *constrained expression* mathematical form obtained from the solution of the functional coefficients may not be unique. Furthermore, the TFC technique may be hard to be used for multidimensional problems subject to constraints in which the variables are coupled, i.e. in the case where one dependent variable depends on the value of another dependent variable. For instance, a kind of constraint where x(t) depends on the values of y(t) at a specified time.

In this work, we show that a class of astrodynamics problems - whose constraints are given by the mission - can be solved using the mathematical framework provided by the TFC [5, 6] after a proper change of coordinates. In these problems, the constraints are initially written in non-linear and coupled mathematical forms when classical rectangular coordinates are used. A new system of coordinates is used to transform the non-linear constraints into linear ones. Furthermore, the change of the coordinates is also used to decouple the variables of the constraints. Therefore, the TFC technique can be used to solve the ordinary differential equations under the constraints of the mission.

An application is done for an orbit transfer of a spacecraft around the Earth under the perturbation of the Moon. A proper change of coordinates is done by taking the advantage of symmetries of the system. After that, the TFC technique is applied to find numerical solutions for the One Tangent Burn transfer method.

2 The Theory of Functional Connections

In this section, the univariate TFC technique to solve the BVP is briefly summarized, with the required conditions to be applied. Essentially, the TFC technique reduces the space of all possible functions to its subspace in which the functions must satisfy the constraints of the problem. The TFC involves a functional interpolation in which the constraints of the problem are analytically embedded in an expression called the *constrained expression*. The general equation to derive the *constrained expression* comes from

$$x(t, g(t)) = g(t) + \sum_{k=1}^{n} \eta_k(t, g(t))\, s_k(t) \qquad (1)$$

where n is the number of constraints, $g(t)$ is the free function, the $s_k(t)$ constitute a set of n support functions, which must be linearly independent, and $\eta_k(t, g(t))$ are unknown functional coefficients. The unknown functional coefficients are determined using Eq. (1) subject to the constraints of the problem under consideration. After that, they are substituted in Eq. (1) to form the *constrained expression*, in which all the constraints of the astrodynamic (physical) problem are mathematically embedded.

After substituting the *constrained expression* into the differential equation, a new differential equation arises written in terms of $g(t)$, instead of $x(t)$. Note

*Email: allan.junior@inpe.br Reseach supported by FAPESP - São Paulo Research Foundation through grants 2018/07377-6 and 2016/24561-0.
†Email: antonio.prado@inpe.br
‡Email: mortari@tamu.edu

that this new differential equation is subject to no constraints. The free function $g(t)$ is then expressed as a linear combination of a set of basis function given by orthogonal polynomials:

$$g(t) = \sum_{j=0}^{m} \xi_j \, h_j(t) \tag{2}$$

where m is the number of basis functions, ξ_j (for $j = 0, 1, \cdots, m$) are unknown coefficients, and h_j (for $j = 0, 1, \cdots, m$) are orthogonal polynomials. The Chebyshev polynomials - which are used in this research - are defined only in the range $t \in [-1, 1]$, hence an appropriate change of units of time must be done accordingly. In order to solve the problem, it is enough to find the unknown coefficients ξ_j (for $j = 0, 1, \cdots, m$). Hence, the new differential equation is discretized for a set of N values of time t. The best points of t to be chosen is to use Chebychev-Gauss-Lobato nodes [7], which can be evaluated as

$$t_i = -\cos\left(\frac{i\pi}{N}\right) \qquad \text{for } i = 0, 1, \cdots, N \tag{3}$$

The system of N equations with m unknowns is then solved for the ξ_j (for $j = 0, 1, \cdots, N$) coefficients using the nonlinear least-squares numerical method. The iterative process is written in Python language, and it uses an automatic differentiation and just-in-time (JIT) compiler [8, 9, 10]. More details of the TFC technique to solve ODE can be found in [1, 4, 11, 12].

3 Results

The Hohmann transfer is a particular case of the one-tangent burn transfer method [13] in the case where the time T of the transfer (without perturbation) is $T_h = (\pi/2)\sqrt{(r_0 + r_f)^3/\mu}$. This kind of transfer can be seen in Fig. 1 from an initial circular orbit of radius r_0 to another circular final orbit of radius r_f. In this figure, the red dots represent the trajectory for the Hohmann transfer, the blue dots represent the trajectory when the tie of transfer is lower than the time of the Hohmann transfer, and the green dots represent the trajectory when the time of transfer is higher the the Hohmann transfer. The three constraints of the one-tangent burn transfer are:

1. The radius of the initial orbit is r_0
2. The radius of the final orbit is r_f
3. The velocity is tangent to the path when $t = 0$

Using the TFC framework combined with an appropriate change of variables, the solution to the transfer satisfying the three constraints shown above can be obtained for a satellite under perturbations.

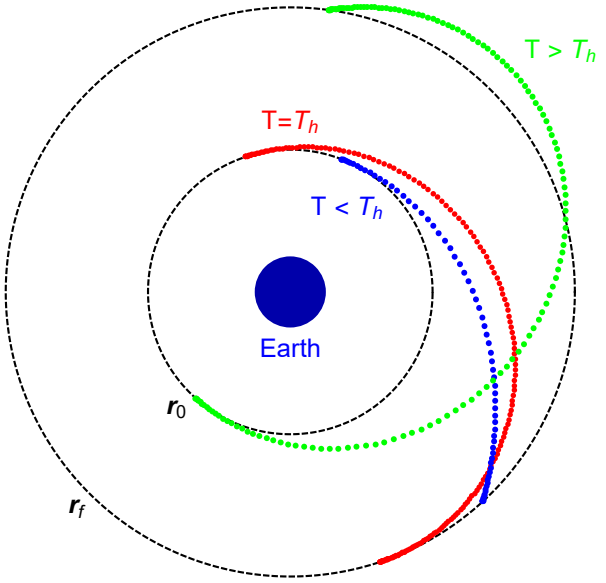

Figure 1: The one-tangent burn transfer trajectories from r_0 to r_f for different values of time of flight. The trajectory in red is coincident with the Hohmann transfer.

References

[1] Daniele Mortari. The Theory of Connections: Connecting Points. *Mathematics*, 5(4):57/1–15, 2017. https://www.mdpi.com/2227-7390/5/4/57.

[2] Daniele Mortari and Carl Leake. The Multivariate Theory of Connections. *Mathematics*, 7(3):296/1–22, 2019. https://www.mdpi.com/2227-7390/7/3/296.

[3] Daniele Mortari. Least-Squares Solution of Linear Differential Equations. *Mathematics*, 5(4), 2017. https://www.mdpi.com/2227-7390/5/4/48.

[4] Daniele Mortari, Hunter Johnston, and Lidia Smith. High Accuracy Least-squares Solutions of Nonlinear Differential Equations. *Journal of Computational and Applied Mathematics*, 352:293 – 307, 2019. http://www.sciencedirect.com/science/article/pii/S0377042718307325.

[5] Allan Kardec de Almeida Junior, Hunter Johnston, Carl Leake, and Daniele Mortari. Fast 2-Impulse Non-Keplerian Orbit Transfer using the Theory of Functional Connections. *The European Physical Journal Plus*, 136:223, 2021. https://link.springer.com/article/10.1140/epjp/s13360-021-01151-2.

[6] Allan Kardec de Almeida Junior and Antonio Fernando Bertachini de Almeida Prado. Compar-

isons between the circular restricted three-body and bi-circular four body problems for transfers between the two smaller primaries. *Scientific Reports*, 12(4148):1–19, 2022. https://doi.org/10.1038/s41598-022-08046-x.

[7] C. Lanczos. *Applied Analysis*, page 504. Dover Publications, Inc., New York, 1957.

[8] James Bradbury, Roy Frostig, Peter Hawkins, Matthew James Johnson, Chris Leary, Dougal Maclaurin, and Skye Wanderman-Milne. JAX: composable transformations of Python+NumPy programs, 2018.

[9] Roy Frostig, Matthew Johnson, and Chris Leary. Compiling machine learning programs via high-level tracing. In *SysML Conference*, 2018.

[10] Carl Leake and Hunter Johnston. TFC: A Functional Interpolation Framework, 2021. https://github.com/leakec/tfc.

[11] Mario De Florio, Enrico Schiassi, Andrea D'Ambrosio, Daniele Mortari, and Roberto Furfaro. Theory of functional connections applied to linear odes subject to integral constraints and linear ordinary integro-differential equations. *Mathematical and Computational Applications*, 26(3), 2021. https://www.mdpi.com/2297-8747/26/3/65.

[12] Carl Leake, Hunter Johnston, and Daniele Mortari. The multivariate theory of functional connections: Theory, proofs, and application in partial differential equations. *Mathematics*, 8(8):1303, Aug 2020. http://dx.doi.org/10.3390/math8081303.

[13] D. A. Vallado. *Fundamentals of Astrodynamics and Applications*. Springer, 3 edition, 2007.

On optimal trajectories of solar sails

Alesia Herasimenka*[1], Lamberto Dell'Elce[2], Jean-Baptiste Caillau[1], and Jean-Baptiste Pomet[2]

[1]Université Côte d'Azur, CNRS, Inria, LJAD, Nice, France
[2]Inria, Sophia Antipolis, France

Abstract

Trajectory design and maintenance of solar sails in orbit about a celestial body can be formulated as control problems with positivity constraints. We propose a methodology to find the optimal control action aimed at enforcing and maximizing the displacement of the sail toward an arbitrary direction. A thorough analysis of the switching function is carried out to deduce an upper bound on the number of bangs between controlled and coasting arcs. The solution of the optimal control problem is achieved by first leveraging on convex programming to obtain an excellent initial guess of the co-state variables, followed by a multiple shooting scheme. Hence, the entire methodology does not need any initial guess.

1 Introduction

A large body of literature on solar sailing focuses on the mathematical formulation and numerical solution of optimal interplanetary transfers [1]. Our goal is to propose an optimal feedback algorithm which relies on solution of an optimal control problem to move the sail toward a desired direction of the phase space after one orbital period. By maximizing the rate of change of an arbitrary function of orbital elements, available contributions on local optimal feedback strategies develop laws that maximize the projection of the displacement toward the gradient of the aforementioned function. Conversely, our formulation enforces the exact direction of the displacement while maximizing its magnitude. This is of use to size the sail to compensate a given orbital perturbation or to develop a simple feedback control strategy for a rectilinear transfer in the orbital elements space. After detailing necessary conditions for optimality of the optimal control problems (OCP), inspection of the switching function reveals that the number of bangs between controlled and coasting arcs is smaller than 6. This result entails clear consequences on the complexity of the control structure. Numerical solution is then achieved by means of shooting techniques in two step: first, a convex optimization problem is solved to get an excellent initial guess of the adjoint variables. This solution is associated to a feasible but sub-optimal control action. Then, multiple shooting method is implemented to obtain the optimal solution. Hence, no initial guess is required by the overall methodology.

*Email: alesia.herasimenka@univ-cotedazur.fr.
Research supported by European Space Agency

2 Parametrization of the control set and equations of motion

Controlling sail's attitude, *i.e.*, the normal vector $\hat{\boldsymbol{n}}$, allows to change the direction and magnitude of the resulting solar radiation pressure (SRP). A reliable inference of optical coefficient is indeed mandatory to accurately estimate the mapping between $\hat{\boldsymbol{n}}$ and $\boldsymbol{f}_{SRP}$.

Solar sail dynamics is conveniently modeled as a nonlinear control-affine system, where the control variable is homogeneous to the force vector, namely $\boldsymbol{u} := \dfrac{\boldsymbol{f}_{SRP}}{\varepsilon(r_\odot)}$. Control

set $\mathcal{U} \subset \mathbb{R}^3$ is then given by:

$$\mathcal{U} = \left\{ \frac{\boldsymbol{f}_{SRP}(\hat{\boldsymbol{n}})}{\varepsilon(r_\odot)}, \quad \hat{\boldsymbol{n}} \in \mathbb{R}^3, \ \|\hat{\boldsymbol{n}}\| = 1 \right\}.$$

Figure 1 shows the projection of $\mathcal{U}$ on the plane generated by $\hat{\boldsymbol{n}}$ and $\hat{\boldsymbol{s}}$ for various optical properties. The set is a surface of revolution with axis $\hat{\boldsymbol{s}}$, and it is non-convex unless reflectivity coefficient $\rho = 1$. Note that the interior of the surface is not part of $\mathcal{U}$. Although sails are designed to be as ideal as possible, partial absorption of the energy is unavoidable in real-life applications and optical properties exhibit degradation with time.

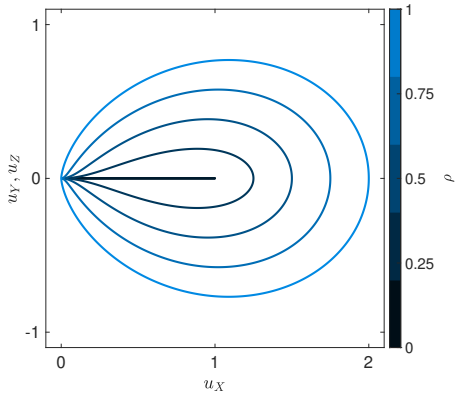

Figure 1: Control sets for different reflectivity coefficients. Here, u_X is the projection of $\boldsymbol{u}$ toward $\hat{\boldsymbol{s}}$, while u_Y and u_Z are orthogonal components.

Solar sail in orbit around a celestial body is considered in this study. Equations of motion are written in a set of Keplerian-like orbital elements, which leverages on the axial symmetry of the problem with respect to the Sun's direction. Motion of slow elements, I, is governed by

$$\frac{\mathrm{d}\, I}{\mathrm{d}\, t} = \varepsilon F(I, f)\, \boldsymbol{u}$$

where f is the true anomaly.

3 Optimal control over one orbital period

An optimal control law allowing to realize the desired maneuver for a sail orbiting around a planet or an asteroid might have multiple applications. First, it can impose physical properties of the sail for feasibility of an observation mission: for example, how large might be the sail in order to be able to stay on the same orbit and compensate an orbital perturbation. Another direct application is control law used in the context of a deorbiting mission using solar sail.

Because of its control-affine character, the Hamiltonian associated to the slow-state variables is given by:

$$H_I = H_0 + u\, H_1 = H_0 + \varepsilon\, u\, p_{\delta I} F(I, f) \quad (1)$$

with H_0 part of Hamiltonian independent on the control u, $p_{\delta I} \in \mathcal{M}_{1,5}(\mathbb{R}), \|p_{\delta I}\| = 1$, the adjoint vector and $F(I, \varphi)$ the matrix associated to Gauss variational equations (GVE). An important simplification occurs by assuming that the slow state I can be considered as fixed for one orbital period. Thus, with $I = \bar{I}$, $p_{\delta I} = \bar{p}_I$, $F(I, \varphi) = \bar{F}(\bar{I}, \varphi)$ and Pontryagin maximum principle (PMP) is reduced to choose the control such that

$$u^* = \arg \max_{u \in U} \ u\, H_1 \max_{u \in U} u\, \bar{p}_I \bar{F}(\bar{I}, \varphi).$$

Given that $\bar{I}$ and $\bar{p}_I$ are fixed and variations of $\bar{F}(\bar{I}, \varphi)$ are only due to the fast variable φ, one can geometrically distinguish two different cases of PMP. Consider a convex cone K_α tangent to the control set U. For illustration only, let us project the dynamics $\bar{p}_I \bar{F}(\bar{I}, \varphi)$ of the system in the two-dimensional coordinates system (u_1, u_2). According to PMP, the control should be chosen as to maximize the scalar product $u \bar{p}_I \bar{F}(\bar{I}, \varphi)$. Therefore, two different cases should be considered depending on relative position of $\bar{p}_I \bar{F}(\bar{I}, \varphi)$ and the polar cone K_α^o, as shown in Fig. 2.

The optimal control problem that we formulate, as mentioned afore, consists in moving the system exactly in the desired direction of slow variables d_I. Therefore, we need first

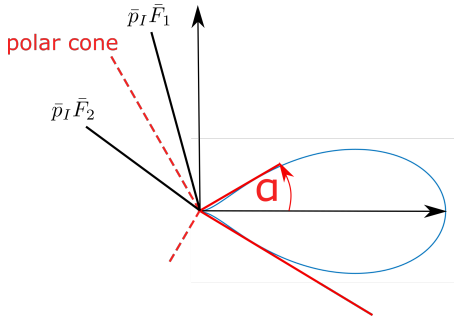

Figure 2: Geometrical illustration of PMP: if $\bar{p}_I\bar{F}_2(\bar{I},\varphi) \in K^o_\alpha$, $u = 0$; if $\bar{p}_I\bar{F}_1(\bar{I},\varphi) \notin K^o_\alpha$, u is such that $\max_{u\in U} u\,\bar{p}_I\bar{F}(\bar{I},\varphi)$.

to impose the constraint of parallelity given by $\delta I(2\pi) \parallel d_I$. Transversality conditions give a constraint on the adjoint vector: $p_{\bar{I}} \cdot d_I = 0$.

The optimality of the solution is measured with Mayer cost that corresponds to maximization of the displacement ζ while respecting the constraint of moving the system exactly and only according to d_I. Finally, the OCP is:

$$
\begin{aligned}
\max \quad & \delta I(\varphi_f) \cdot d_I = \zeta \quad \text{subject to} \\
& \delta I'(\varphi) = \varepsilon \sum_i u_i \bar{F}_i(\bar{I},\varphi), \qquad u \in U \\
& \delta I(\varphi_f) = \int_{\varphi_0}^{\varphi_f} \delta I' \,\mathrm{d}\varphi = \zeta d_I \\
& \delta I(\varphi_0) = 0, \quad \delta I(\varphi_f) \parallel d_I \\
& p_{\bar{I}} \cdot d_I = 0 \\
& \varphi_0 = 0, \quad \varphi_f = 2\pi,
\end{aligned}
$$

where δI is the displacement.

In order to use indirect shooting methods, we need first a reliable initial guess. The initial conditions can be obtained by solving a convex optimization problem by approximating the original control set by a convex bounded cone. A delicate choice of cone approximation allows to find the admissible non-optimal controls. For this reason, the convex cone is bound at the points of tangency, as shown in Fig. 3.

Once we have the initial guess, different strategies might be adopted to solve the initial problem with a real control set, such as multiple shooting or continuous differentiation.

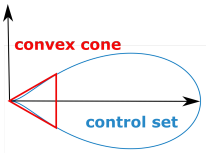

Figure 3: Approximation of the control set by a cone bounded at the points of tangency.

An important observation made after solving the initial problem using multiple shooting method is a possible change of structure between the solutions obtained for a bounded convex cone and the real control set. Indeed, by replacing the bounded cone with a real set, we "inflate" the set on the right side. The optimal solutions will be either situated on the "inflated" part of the control set or the zero. Therefore, the solution has a bang-bang structure (since the control set doesn't inclulde its interior). Moments of switches can be predicted using a switch function based on geometrical representation of the PMP. In fact, by transorming classical GVE to make them exact trigonometric polynomials in f, the H_1 given by Eq. (1) is an exact trigonometric polynomial. Therefore, one can find the switch function as well as its zeros. Finally, a multiple shooting method with automatic detection of structure is used to find the solutions.

References

[1] C. R. McInnes, *Solar Sailing*, Springer London, 1999.

Session 8:

PERTURBATION MODELING AND INTEGRATION

Dynamical geometry associated with the collision manifold in the circular restricted three-body problem

Joshua Fitzgerald*[1] and Shane Ross†[2]

[1]Engineering Mechanics Program, Virginia Tech, USA
[2]Aerospace and Ocean Engineering, Virginia Tech, USA

Abstract

In the circular restricted three-body problem, the linearized phase space structure about the Lagrange points controls dynamical transit at low energies because the geometry of the zero-velocity curve forces the particle to pass through neighborhoods surrounding the equilibria. At high energies, the zero-velocity curve disappears, so the Lagrange points no longer dominate the dynamics. Recent numerical research has revealed the existence of "arches of chaos" which dramatically affect the courses of high-energy solar system trajectories. We demonstrate through numerical and analytical techniques that the arches of chaos coincide with the finite-time stable and unstable manifolds to the singularities at the primaries. Under Levi-Civita regularization, the singularities can be viewed as collision manifolds and the finite-time stable and unstable manifolds can be viewed as approaching the collision manifolds asymptotically, which enables the use of linearization techniques. These linearization techniques, as well as numerical experiments, yield insight into the local geometry.

1 Introduction

Investigating the topological structures that underlie particle dynamics in higher-fidelity models such as the circular restricted three body problem (CR3BP) is a critical area of research in astrodynamics. Some of these structures and their implications for spacecraft transport are well-understood—one example is the manifold geometry emanating from the CR3BP Lagrange points that controls transit throughout the CR3BP at low energies [1]—whereas the identification and analysis of others is a topic of active study. For example, a recent study by Todorović et al., which applied the finite Lyapunov indicator (FLI) to solar system dynamics, has revealed the existence of "Arches of Chaos" stretching throughout phase space [2]. Initial conditions on either side of these structures diverge dramatically under the flow. In this work, we demonstrate that the arches of chaos may be identified with the stable and unstable manifolds to the singularities in the CR3BP.

*Email: joshfitz@vt.edu.
†Email: sdross@vt.edu.

2 The Levi-Civita Regularization

The CR3BP Hamiltonian in the planar case is as follows [1]:

$$H_{\text{CR3BP}} = \frac{1}{2}\left(p_x^2 + p_y^2\right) - xp_y + yp_x - \frac{1-\mu}{r_1} - \frac{\mu}{r_2} \quad (1)$$

r_i is the distance between the particle and the ith primary, $i \in 1, 2$, and μ is the mass parameter. The Hamiltonian diverges as $r_i \to 0$, and so singularities are present at the locations of the primaries, creating challenges for numerical and analytical investigation in arbitrarily small neighborhoods about the two masses.

To resolve these difficulties, we utilize the Levi-Civita regularization, which reformulates the CR3BP in order to remove one of the singularities from the system. We assume that the singularity to be regularized is the singularity about m_2. Then, the Levi-Civita regularization recasts the phase space variables into the following form [3]:

$$\begin{aligned} x - 1 + \mu &= u_1^2 - u_2^2, \\ y &= 2u_1u_2, \\ p_x &= \frac{U_1u_1 - U_2u_2}{2\left|u\right|^2}, \\ p_y - 1 + \mu &= \frac{U_1u_2 + U_2u_1}{2\left|u\right|^2} \end{aligned} \quad (2)$$

with $\left|u\right|^2 = u_1^2 + u_2^2$. In addition, the standard time t is rescaled into the Levi-Civita time τ according to the conversion equation

$$dt = \left|u\right|^2 d\tau. \quad (3)$$

Regularization recasts the singularity as a *collision manifold* [4] which is included within the Levi-Civita phase space. Regularization, in addition to its analytical value, also facilitates numerical investigation:

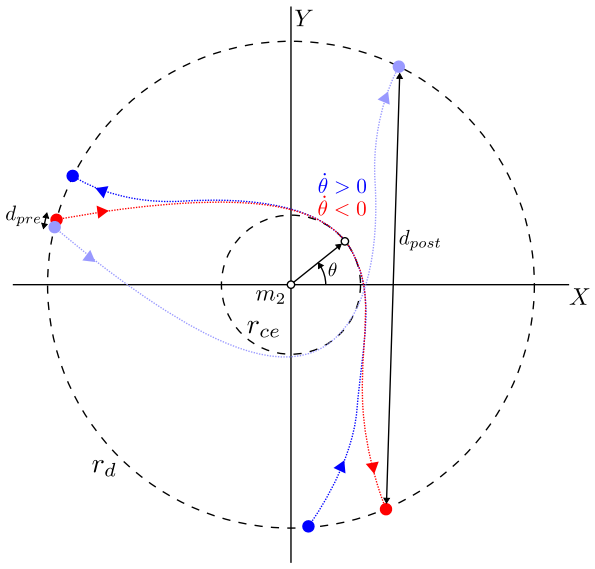

Figure 1: A schematic of the numerical experiment for examining how trajectories on either side of the stable manifold to the singularity move throughout phase space. The red and dark blue trajectories are generated at an initial radius r_{ce} but have $\dot{\theta} < 0$ and $\dot{\theta} > 0$, respectively. They reflect one choice of θ, but a whole family of trajectories for different values of θ must be generated in order to match + and - pairs along the detection radius r_d. We integrate forwards and backwards and then match those + and - trajectories whose final position in backwards time was nearest to each other; in the schematic, the red - trajectory has been matched with a light blue + trajectory, generated in the same way as the dark blue trajectory for a different value of θ. We then compare the pre-encounter, four-dimensional phase space distance d_{pre} with the post-encounter distance d_{post} for each matched pair.

attempting to integrate the standard CR3BP equations of motion in the vicinity of the singularity often causes the algorithm to fail as the step size becomes too small. Performing the procedure in the Levi-Civita equations of motion and then converting to and from standard form as required is a very efficient workaround.

3 Linearization of the Collision Manifold

The Hamiltonian for the system becomes

$$H_{\text{LCR}} = \frac{\left(U_1 + 2|u|^2 u_2\right)^2}{8} + \frac{\left(U_2 - 2|u|^2 u_1\right)^2}{8} - \frac{|u|^6}{2} - \mu - |u|^2\left(E + \frac{(1-\mu)^2}{2}\right) - (1-\mu)|u|^2\left(\frac{1}{\sqrt{1+2(u_1^2-u_2^2)+|u|^4}} + u_1^2 - u_2^2\right)$$

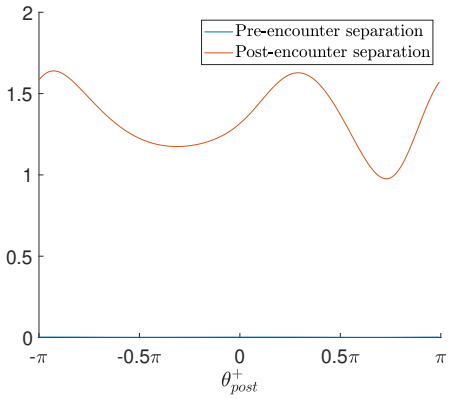

Figure 2: The + and - trajectories have an essentially constant, very small initial separation pre-encounter, but post-encounter their separation varies significantly depending on the angle along the detection circle (in this case, we use θ^+_{post}, the post-encounter angle of each + trajectory, as the angle for identifying and sorting matched pairs of + and - trajectories).

where E is the H_{CR3BP} energy of the trajectory under consideration. H_{LCR} is defined at the collision manifold; although E diverges, $|u|^2 = 0$, and so the Hamiltonian overall does not diverge. Furthermore, the right-hand side of the equations of motion associated with this Hamiltonian is equal to zero at the collision manifold, and so the singularity becomes an equilibrium point under Levi-Civita regularization.

We demonstrate that linearizing this singularity reveals it to be a saddle × saddle point in Levi-Civita space. Although the point itself is excised from the phase space when converted back to the standard CR3BP, *the local geometry about the point is preserved*, and so linearizing the collision manifold is key to understanding the dynamical geometry in standard form.

4 Sample Numerical Results

4.1 Quantifying divergence due to the manifolds

We investigate the collision manifold and its stable and unstable manifolds using numerical experiments in order to develop intuition regarding the nature of the system.

For example, consider only the stable manifolds for simplicity. In m_2-centered polar coordinates $\begin{bmatrix} r & \theta & \dot{r} & \dot{\theta} \end{bmatrix}^T$, initial conditions sufficiently close to the singularity along the stable manifolds have the form $\begin{bmatrix} r & 0 & \dot{r} & 0 \end{bmatrix}^T$ for $0 < r \ll 1$ and $\dot{r} \gg 1$. One can consequently construct initial conditions on either side of the stable manifold that narrowly miss the singularity and whose local closest encounter distance to the singularity is given by r_{ce}. These initial conditions

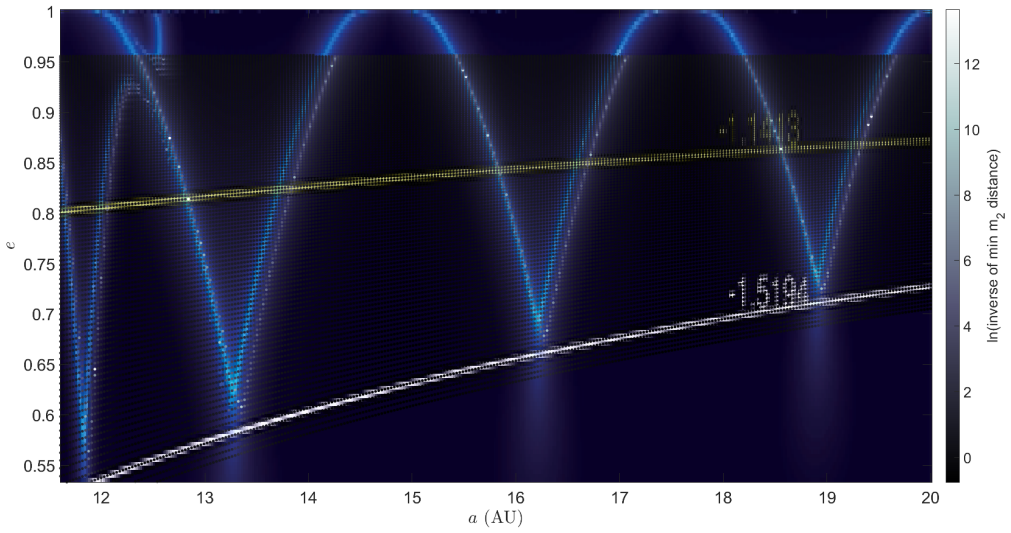

Figure 3: A portion of the semi-major axis/eccentricity plot of the Arches of Chaos given in [2], overlaid with the closest encounter distances of trajectories integrated within the basic CR3BP. The structures correspond almost exactly.

are given by $\begin{bmatrix} r_{ce} & \theta & 0 & \pm\dot{\theta} \end{bmatrix}^T$ where $\theta \in [-\pi, \pi)$, $\dot{\theta}$ is chosen to target a desired energy, and the choice of $\pm$ determines the side to which these initial conditions belong. For convenience, we call trajectories with positive $\dot{\theta}$ "+ trajectories" and trajectories with negative $\dot{\theta}$ "- trajectories."

We integrate + and - trajectories forwards and backwards until they intercept a detection radius $r_d \gg r_{ce}$ around m_2 in both directions. + and - trajectories are matched into pairs based on which trajectories in each set had the closest pre-encounter angles along the detection radius with respect to each other. We then compare the pre-encounter distance d_{pre} and post-encounter distance d_{post} for each matched pair of + and - trajectories (see Figure 1). We discover that different intercept angles along the detection circle yield noticeably different post-encounter distances between + and - trajectories even though they start with the same extremely small pre-encounter distances (see Figure 2).

4.2 Replication of the arches

One very straightforward numerical experiment that demonstrates the connection between the stable and unstable manifolds to the singularities and the Arches of Chaos is to integrate grids of initial conditions and then to determine the minimum encounter distance of each trajectory to the singularity. By definition, trajectories with closer encounters to the singularity are closer to lying on the stable and unstable manifolds. By generating and plotting initial conditions in the same manner as in [2], the resultant structures can be compared (see Fig. 3).

References

[1] W. S. Koon, M. W. Lo, J. E. Marsden, S. D. Ross, *Dynamical Systems, the Three-Body Problem, and Space Mission Design*, Marsden Books, 2011.

[2] N. Todorović, D. Wu, A. J. Rosengren, The arches of chaos in the solar system, *Science Advances* **6** (2020), eabd1313.

[3] R. I. Paez, M. Guzzo, A study of temporary captures and collisions in the Circular Restricted Three-Body Problem with normalizations of the Levi-Civita Hamiltonian, *International Journal of Non-Linear Mechanics* **120** (2020), 103417.

[4] J. Llibre, On the restricted three-body problem when the mass parameter is small, *Celestial mechanics* **28** (1982), 83-195.

Canonical Modeling of The Solar Radiation Pressure Perturbation

Nir Vegh*[1] and Vladimir Martinusi†[2]

[1]Department of Aerospace Engineering, Technion – Israel Institute of Technology
[2]Department of Aerospace Engineering & Asher Space Research Institute,
Technion – Israel Institute of Technology

Abstract

The Solar Radiation Pressure (SRP) represents a relevant perturbing factor for a spacecraft with a large cross-sectional area to mass ratio exposed to the Sun. The paper presents a fist-order fully analytic solution to the orbital motion of such spacecraft, providing closed-form expressions for the variations of the orbital elements due to the SRP. The model shows that the effect of the SRP reduces significantly the interplanetary orbit insertion impulsive velocity.

1 Introduction

The solar radiation pressure (SRP) is a relatively weak perturbation that needs to be taken into account when very high-accuracy orbit prediction is required. For *interplanetary missions*, on the other hand, the SRP becomes the main perturbing force influencing the spacecraft's orbit. Consequently, the question of incorporating this force into the analytical modeling and prediction of the orbit becomes relevant.

The most efficient perturbation models in Astrodynamics are developed by making full use of the tools of *symplectic geometry*. In such models, the system is modeled by using the framework of Hamiltonian mechanics, and the small perturbations are approached by using the classical perturbation theory. Two fundamental perturbation methods exist, the Poincaré-von Zeipel method [1, 2] and the Lie-Hori-Deprit method [3, 4, 5]. These methods are based on the same concept: the original dynamical system, usually highly non-integrable, is transformed through specialized mathematical tools, into a simplified version that satisfies the integrability requirement. In many cases, for such integrable system an analytic solution can be found.

The apparent drawback of the aforementioned methods is that these very efficient (and globally valid) approaches are *applicable only for conservative systems*, namely for the particular situation when the force is derived from a potential scalar function [6].

*Email: nir.vegh@campus.technion.ac.il
†Email: vmartinusi@technion.ac.il

Two relevant perturbations in Astrodynamics do not exhibit this conservative feature (and they allow the system to exchange energy with the environment): the *atmospheric drag* (acting upon satellites orbiting Earth at altitudes smaller than 800 kilometers) and the *solar radiation pressure* (acting upon any object that receives an influx of photons from a nearby source).

The present work offers an analytic solution to the heliocentric orbital motion perturbed by the solar radiation pressure. By using the method of doubling the variables [7] (dubbed *Hamiltonization* by some authors [8]), the non-integrable, non-canonical dynamical system is first transformed into a conservative one, and the new system is treated with the tools of the classical aforementioned canonical perturbation methods. In the end, an analytical model is offered, the equations of motion being expressed in a closed form. The given solution involves only purely algebraic methods and has the same numerical complexity as the solution of the unperturbed Kepler problem itself.

2 Method of Solution

2.1 Canonical Extension of Dynamical Systems

Consider a $n \geq 1$ DOF dynamic system expressed as a set of $2n$ first-order differential equations:

$$\begin{cases} \dot{q}_k = f_k\left(q_1, ...q_n, p_1, ...p_n\right) \\ \dot{p}_k = F_k\left(q_1, ...q_n, p_1, ...p_n\right) \end{cases}, \; k \in \{1, ...n\} \qquad (1)$$

If the dynamic system is non-conservative, it is impossible to bring Equations (1) to a canonical form. To overcome this issue, the following procedure (similar but not identical to the one suggested by Birkhoff [7]) is introduced. Denote:

$$\mathbf{q} = [q_1, ...q_n]^T; \quad \mathbf{p} = [p_1, ...p_n]^T$$
$$\mathbf{f} = [f_1, ...f_n]^T \quad \mathbf{F} = [F_1, ...F_n]^T$$

Define the *mirror variables:*

$$\mathbf{Q} = [Q_1, ...Q_n]^T; \; \mathbf{P} = [P_1, ...P_n]^T$$

such that:

$$\begin{cases} \dot{Q}_l = \sum_{k=1}^{n} \left(P_k \frac{\partial f_k}{\partial q_l} - Q_k \frac{\partial F_k}{\partial q_l} \right) \\ \dot{P}_l = \sum_{k=1}^{n} \left(-P_k \frac{\partial f_k}{\partial p_l} + Q_k \frac{\partial F_k}{\partial p_l} \right) \end{cases}, \; l \in \{1, ...n\}$$

and define the functional $\mathcal{K} : (\mathbb{R}^n)^{\times 4} \to \mathbb{R}$:

$$\mathcal{K}(\mathbf{q}, \mathbf{Q}, \mathbf{P}, \mathbf{p}) = \mathbf{P}^T \mathbf{f} - \mathbf{Q}^T \mathbf{F} \tag{2}$$

Then in the extended $4n$ dimensional space, the variables

$$\Theta = \left[\mathbf{q}^T, \mathbf{Q}^T\right]^T ; \; \mathbf{\Pi} = \left[\mathbf{P}^T, \mathbf{p}^T\right]^T$$

are canonical, since they satisfy Hamilton's canonical equations

$$\dot{\Theta}_k = \frac{\partial \mathcal{K}}{\partial \Pi_k}; \; \dot{\Pi}_k = -\frac{\partial \mathcal{K}}{\partial \Theta_k}; \; k \in \{1, ...2n\} \tag{3}$$

The original dynamic system *has been embedded into a canonical one*, described by Equations (3). The Hamiltonian flow is defined by the vector-valued function:

$$\mathbf{X} = \left[\mathbf{q}^T, \mathbf{Q}^T, \mathbf{P}^T, \mathbf{p}^T\right]^T$$
$$\dot{\mathbf{X}} = \mathbb{J}_{4n} \left[\frac{\partial \mathcal{K}}{\partial \mathbf{X}}\right]^T \tag{4}$$

where

$$\mathbb{J}_{2m} = \begin{bmatrix} \mathbb{O}_m & \mathbb{I}_m \\ -\mathbb{I}_m & \mathbb{O}_m \end{bmatrix}, \; m \geq 1$$

When the original system (1) is subject to a perturbation depending on a small parameter, canonical perturbation methods *may now be applied to the extended system* (3). Note that the *mirror variables* $\mathbf{Q}$ and $\mathbf{P}$ do not interfere in the variation of the original $\mathbf{q}, \mathbf{p}$ (the new variables have no effect on the dynamics of the original system whatsoever). These variables are used only as a tool for embedding the non-conservative system into a conservative (Hamiltonian) one. Equations (1) can be recovered from the first and the last n equations in Equation (3):

$$\begin{aligned} \dot{q}_k &= \frac{\partial \mathcal{K}}{\partial P_k} = f_k(q_1, ...q_n, p_1, ...p_n) \\ \dot{p}_k &= -\frac{\partial \mathcal{K}}{\partial Q_k} = F_k(q_1, ...q_n, p_1, ...p_n) \end{aligned} \tag{5}$$

2.2 The Hamiltonized System

The motion under the influence of the SRP dynamical system that is not conservative. A *Hamiltonization* procedure is used as follows. First, define the set of *mirror variables* $\mathbf{Q} = [Q_a, Q_e, Q_i]^T, \mathbf{P} = [P_M, P_\omega, P_\Omega]^T$ and determine the Hamiltonian describing the motion in a 12-dimensional phase space (by using Equation (2)).

$$\begin{aligned} \mathbf{X} &= [M, \omega, \Omega, Q_a, Q_e, Q_i, P_M, P_\omega, P_\Omega, a, e, i]^T \\ \mathcal{K}(\mathbf{X}) &= \dot{M} P_M + \dot{\omega} P_\omega + \dot{\Omega} P_\Omega - \dot{a} Q_a - \dot{e} Q_e - \dot{i} Q_i \end{aligned}$$

In this way, a canonical system has been obtained. From this point, any canonical perturbation method is at reach.

Practically, in the discussed case, the extended system has the Hamiltonian $\mathcal{K} = \mathcal{K}(\mathbf{X})$:

$$\begin{aligned} \mathcal{K}(\mathbf{X}) &= nP_M \\ &+ \frac{\beta}{Gr} \frac{\eta}{e^2} \left[\left(\kappa - e^2 - \sigma^2\right) d_r \right. \\ &\left. - (2 + \kappa) \sigma d_\theta \right] P_M \\ &+ \frac{\beta}{Gr} \left[-\frac{\kappa(1+\kappa)}{e^2} d_r + \frac{(2+\kappa)\sigma}{e^2} d_\theta \right. \\ &\left. - \frac{c \sin\theta}{s} d_h \right] P_\omega \\ &+ \frac{\beta}{Gr} \frac{\sin\theta}{s} d_h P_\Omega \\ &- \frac{\beta}{Gr} \frac{2a(1+\kappa)}{\eta^2} \left[\sigma d_r + (1+\kappa) d_\theta\right] Q_a \\ &- \frac{\beta}{Gr} \left[\frac{\sigma(1+\kappa)}{e} d_r \right. \\ &\left. + \frac{\left(\kappa^2 + 2\kappa + e^2\right)}{e} d_\theta \right] Q_e \\ &- \frac{\beta}{Gr} \cos\theta d_h Q_i \end{aligned} \tag{6}$$

2.3 The Reduced (Averaged) System

After formulating the osculating system in its Hamiltonian form, the averaged system's Hamiltonian is:

$$\begin{aligned} \mathcal{M}(\mathbf{Y}) &= nP_{\overline{M}} - 2n \frac{\beta}{\mu} d_r P_{\overline{M}} \\ &- \frac{2\beta}{\eta G} d_\theta Q_{\overline{a}} - \frac{\beta e \eta}{aG(1+\eta)} d_\theta Q_{\overline{e}} \end{aligned} \tag{7}$$

and its solution is expressed with respect to the independent variable τ as:

$$\begin{cases} M(\tau) = M_0 + (1 - 2A)\tau \\ \omega(\tau) = \omega_0 \\ \Omega(\tau) = \Omega_0 \\ i(\tau) = i_0 \end{cases}$$

The full set of 6 analytical equations that describe the variation of the orbital elements are:

$$\begin{cases} \tau = \frac{1}{B} \left[\eta - \eta_0 + \ln\left(\frac{1-\eta}{1-\eta_0}\right) \right] \\ a = a_0 \left(\frac{(1-\eta)\eta_0}{(1-\eta_0)\eta} \right)^2 \\ M = M_0 + \frac{1-2A}{B} \left[\eta - \eta_0 + \ln\left(\frac{1-\eta}{1-\eta_0}\right) \right] \\ i = i_0 \\ \omega = \omega_0 \\ \Omega = \Omega_0 \end{cases} \tag{8}$$

with:

$$\eta = \sqrt{1-e^2}; \quad \eta_0 = \sqrt{1-e_0^2}$$

2.4 The Contact Transformation

In order to complete the full approximated solution to the original system, the *infinitesimal contact transformation* that stems from the perturbation method needs to be determined. Once this is done, the orbit propagation paradigm is completed. The orbit propagation algorithm takes an initial condition in the original, 3-DOF (six dimensional phase space) system, and Hamiltonizes it to create a new Hamiltonian osculating system within a 12 dimensional phase space. The Hamiltonized problem is projected onto the averaged system using the *inverse* contact transformation to obtain the initial conditions of the averaged system, $\mathbf{Y}_0 = \mathbf{Y}_{(t_0)} = CT^{-1}(\mathbf{X}_0)$. Given those mean initial conditions, the system is *analytically propagated* to find the future mean state for any $Y_{(t)}$ *such that* $t > t_0$. Having calculated the mean state in the desired future time, the *contact transformation* is used once again to approximate the future osculating state at time t being $\widetilde{\mathbf{X}}_{(t)} = CT\left(\mathbf{Y}_{(t)}\right) = \mathbf{X}_{(t)} + O\left(\varepsilon^j\right)$, where j is the order of approximation. In this case: $j = 1$, $\varepsilon = \beta\mu^{-1}$. After having approximated the future state of the osculating system, the original system's state is retrieved.
The homological equation yields successively [5]:

$$\begin{aligned} \left\langle \widetilde{\mathcal{K}}_{\beta=0} | W_{XY} \right\rangle &= \widetilde{\mathcal{M}} - \widetilde{\mathcal{K}} \\ \langle n_0 P_M | W_{XY} \rangle &= \widetilde{\mathcal{M}} - \widetilde{\mathcal{K}} \\ -\frac{\partial W_{XY}}{\partial M} &= \frac{1}{n_0}\left(\widetilde{\mathcal{M}} - \widetilde{\mathcal{K}}\right) \end{aligned} \tag{9}$$

Equation (9) is solved via a simple quadrature, and the analytical expression of the infinitesimal contact transformation is:

$$\begin{aligned} \Delta M &= \epsilon\eta e^{-1}\left\{\left(\frac{2e^2}{1+\kappa} - 1\right)\sigma d_r \right. \\ &\quad \left. - \left[\kappa + \ln(1+\kappa)\right] d_\theta\right] \end{aligned} \tag{10}$$

$$\begin{aligned} \Delta\omega &= \epsilon\left\{\sigma e^{-1} d_r + e^{-1}\left[\kappa + \ln(1+\kappa)\right] d_\theta \right. \\ &\quad \left. - c\xi d_h\right\} \end{aligned} \tag{11}$$

$$\Delta\Omega = \epsilon\xi d_h \tag{12}$$

$$\begin{aligned} \Delta a &= 2\epsilon a\eta^{-2}\left[\kappa d_r \right. \\ &\quad \left. - \left(f - E + \frac{1+\kappa+\sigma}{1+\kappa}\sigma\right) d_\theta\right] \end{aligned} \tag{13}$$

$$\begin{aligned} \Delta e &= \epsilon\left[\kappa d_r \right. \\ &\quad \left. - \left(f - E + \frac{\eta - \eta^2 + 1 + \kappa}{1+\kappa}\sigma\right) d_\theta\right] \end{aligned} \tag{14}$$

$$\begin{aligned} \Delta i &= -\epsilon\left[\left(f - \frac{E}{\eta}\right)\cos\omega \right. \\ &\quad \left. + \ln(1+\kappa)\sin\omega d_h\right] \end{aligned} \tag{15}$$

where f is the true anomaly, E is the eccentric anomaly and:

$$\begin{aligned} \xi &= \frac{\eta\ln(1+\kappa)\cos\omega - (\eta f - E)\sin\omega}{\eta s} \\ \epsilon &= \beta n_0 (\mu n e)^{-1} \end{aligned}$$

3 Conclusions

Describing a physical system using an analytical model is extremely beneficial for both computational and qualitative reasons. On the computational part, we have managed to introduce explicit algebraic equations that allow an instantaneous approximated propagation of a spacecraft's state to any future time, given a set of initial conditions. Numerical simulations have shown the order of magnitude of the errors involved in such a first-order approximation. On the qualitative part, the equations that were obtained exposed new insights regarding the long term effect of the SRP on a satellite. The separation between the mean SRP effect and its periodic parts allowed a deeper and more intuitive understanding of the dynamics of the system.

References

[1] H. Poincaré, *Les methodes nouvelles de la mecanique celeste*. Paris, Gauthier-Villars et fils, 1892.

[2] H. Zeipel, *Recherches sur le mouvement des petites planètes*. Almqvist & Wiksells Boklvyekevi-AB, 1921.

[3] S. Lie and G. Scheffers, *Geometrie Der Berührungstransformationen*. Leipzig B.G. Teubner, 1896.

[4] G. Hori, "Theory of General Perturbation with Unspecified Canonical Variable," *Publications of the Astronomical Society of Japan*, vol. 18, pp. 287–296, Jan. 1966.

[5] A. Deprit, "Canonical transformations depending on a small parameter," *Celestial Mechanics*, vol. 1, pp. 12–30, Mar. 1969.

[6] H. Goldstein, *Classical Mechanics*. Addison-Wesley, 1980.

[7] G. Birkhoff, *Dynamical Systems*. American Mathematical Society, 1927.

[8] A. A. Kamel, "Lie Transforms and the Hamiltonization of Non-Hamiltonian Systems," *Celestial Mechanics*, vol. 4, pp. 397–405, Dec. 1971.

CUDA implementation of the first derivative of the gravity potential

Carlos Rubio*[1], Jesús Gonzalo†[1], Jan Siminski‡[2], and Alberto Escapa§[1,3]

[1]Dept. of Aerospace Engineering, University of León, León, Spain
[2]European Space Agency – European Space Operations Centre (ESA/ESOC). Darmstadt, Germany
[3]Dept. of Applied Mathematics, University of Alicante, Alicante, Spain

1 Introduction

The demand for more efficient and faster orbital propagation algorithms is increasing with the advent of large satellite constellations and the ever growing number of space debris [1]. These algorithms are needed to propagate all satellites in a catalogue, e.g. to determine close approaches or to correlate new observations, playing the Low Earth Orbit (LEO) regime a special role. This task is computationally expensive. One way to optimize it is parallelizing algorithms, models, or to perform the whole propagations using Graphics Processor Units (GPUs).

We present the preliminary results for a highly optimized Compute Unified Device Architecture (CUDA) version [2] of the geopotential spherical harmonic expansion based on the Cunningham method [3] and its gradient (first-order). The proposal includes several variants with different tradeoffs between speed and accuracy. Its performance was evaluated against GMAT [4], GODOT [5], and Orekit [6] astrodynamics packages.

We also explored the suitability of variants with mixed (single and double) precision arithmetic. The mixed precision version performs all the internal computations in single precision arithmetic with the exception of some input data and the final summations that are computed in double precision arithmetic.

2 Results

The precision of the CUDA double variant, represented in Figure 1, is comparable to the other astrodynamics frameworks. The relative error is that of the first-order gradient (acceleration) of the geopotential, degree 100, with respect to the colatitude for the considered CUDA case. As a reference solution for computing such error, we took the same acceleration, but evaluated in quadruple precision arithmetic. The errors for the mixed precision version, Figure 2, run from $10^{-7.7}$ to $10^{-6.5}$.

*Email: carlos.rubio@unileon.es
†Email: jesus.gonzalo@unileon.es
‡Email: Jan.Siminski@esa.int
§Email: alberto.escapa@unileon.es

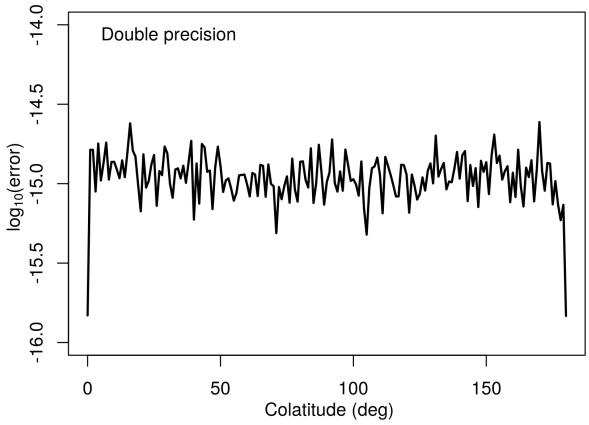

Figure 1: Maximum relative errors of the acceleration components of the geopotential (degree 100) as a function of the colatitude for the double precision CUDA version.

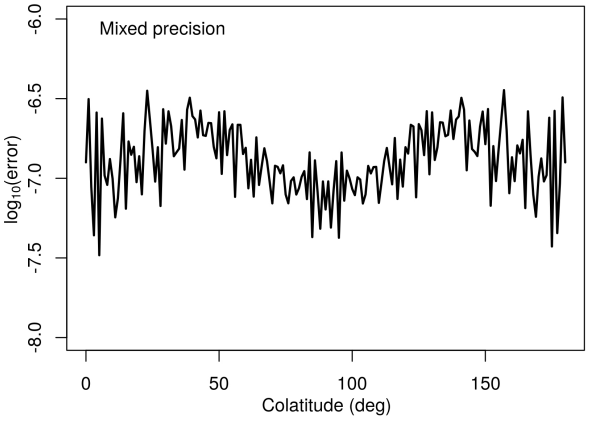

Figure 2: Maximum relative errors of the acceleration components of the geopotential (degree 100) as a function of the colatitude for the mixed precision CUDA version.

We checked the usability of that mixed precision version for LEO by means of a satellite propagation, comparing its induced distance error with that of the others perturbations. The selected satellite was the IceSat (NORAD ID 27642), propagated from the TLE

at epoch Feb 19, 2003. The satellite follows a near-circular orbit at the height of 598.7 km. The impact in the distance error after four days of propagation for the different perturbations is represented in Fig. 3. The induced error level due to using mixed precision was of the same order of magnitude as the spherical harmonic contributions of degrees higher than 100 and much smaller than the other considered perturbations (relativity, ocean tides, SRP, albedo, solid tides, third body, and drag).

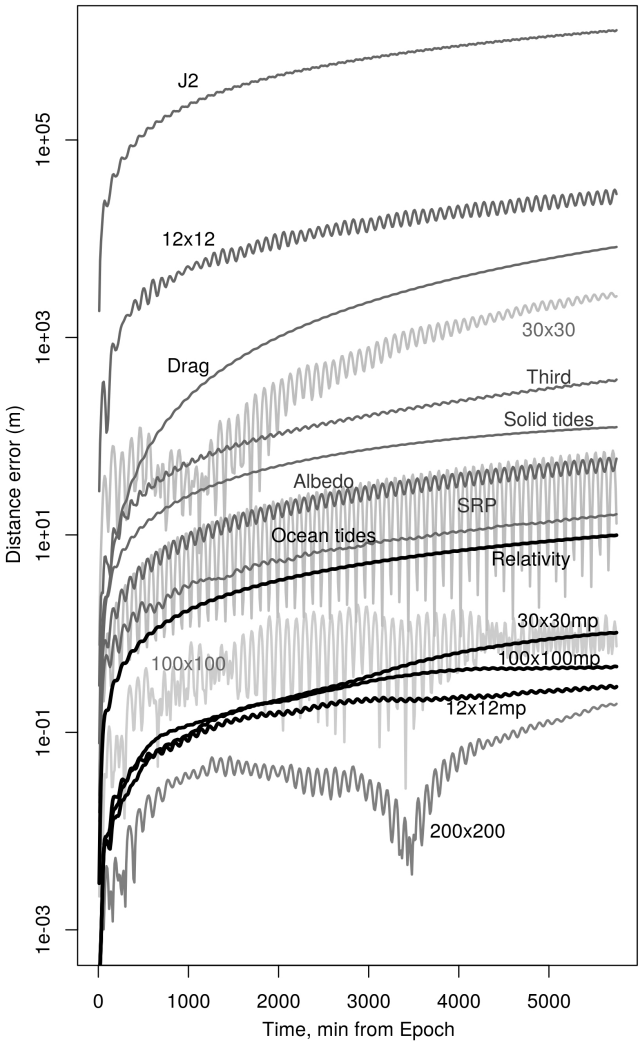

Figure 3: Distance errors caused by the different perturbations to an IceSat satellite numeric propagation. The 12×12 mp, 30×30 mp, and 100×100 mp lines represent the error caused by the mixed precision with respect to the double precision CUDA versions of the same degree.

In terms of execution speed, Figure 4, the GPU version is not competitive with respect to the most efficient Central Processing Unit (CPU) implementations for low degree-order and one single computation. For high degree-order (greater than 150 degree), the CUDA variants are faster than CPU implementations as expected due to the reduction of the algorithmic complexity from $\mathcal{O}(n^2)$ to $\mathcal{O}(n)$.

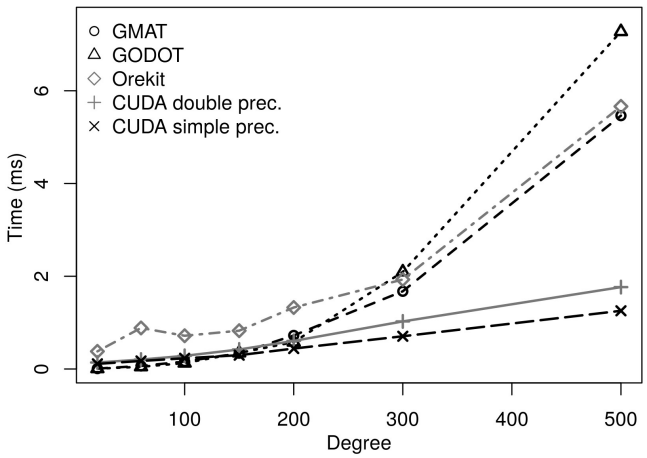

Figure 4: Single geopotential gradient computation times. Measured as the mean value of ten computations after a warm-up of another ten. The CUDA versions were executed in a NVIDIA GeForce GTX 1050i.

In the case of multiple simultaneous computations, they can reach very high speed-up ratios for both the mixed and double precision versions, as can be observed in Figure 5. Given that the errors introduced by the mixed precision formulation are of the same order as of a spherical harmonic expansion truncated at degree 100, we consider the CUDA mixed precision variant the best solution to perform massive LEO propagations.

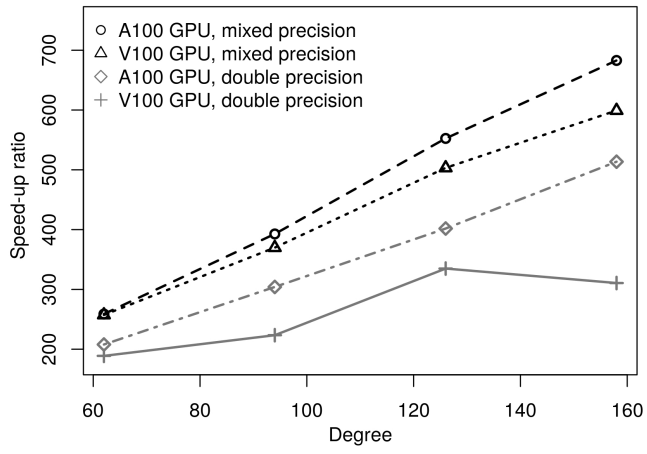

Figure 5: Speed-up ratios with respect to single-core CPU for 2000 simultaneous gradient computations in GPU. The CUDA versions were executed in Tesla V100-SXM2 (V100 in legend) and NVIDIA A100-SXM4 (A100 in legend) GPUs.

Acknowledgements

This work is a part of the PhD Thesis by C. Rubio under the supervision of A. Escapa at the University of León (Spain).

References

[1] Adushkin, V., Aksenov, O. Y., Veniaminov, S. et al. The small orbital debris population and its impact on space activities and ecological safety. *Acta Astronautica*, 176 (2020), 591597. https://linkinghub.elsevier.com/retrieve/pii/S0094576520300175. doi:10.1016/j.actaastro.2020.01.015.

[2] NVIDIA-Corporation. About CUDA. Retrieved April 17, 2022 (https://developer.nvidia.com/about-cuda).

[3] Cunningham, L. E. On the computation of the spherical harmonic terms needed during the numerical integration of the orbital motion of an artificial satellite. *Celestial Mechanics*, 2(2) (1970), 207216. http://link.springer.com/10.1007/BF01229495. doi:10.1007/BF01229495.

[4] NASA. GMAT. SourceForge. Retrieved April 17, 2022 (https://sourceforge.net/projects/gmat/).

[5] ESA. GODOT Documentation. Retrieved April 17, 2022 (https://godot.io.esa.int/docs/0.7.0).

[6] CS-Group. About Orekit. Retrieved April 17, 2022 (https://www.orekit.org/).

CUDAjectory: a GPU-based software for massive parallel orbit propagation

Adriano Filippo Inno*[1], Camilla Colombo†[1], Alessandro Masat‡[1], Lorenzo Bucci§[2], and Florian Renk¶[3]

[1]Politecnico di Milano
[2]DEIMOS Space for ESA - European Space Agency
[3]ESA - European Space Agency

1 Introduction

Graphics Processing Units (GPU)s provide much higher instruction throughput and memory bandwidth than a Central Processing Unit (CPU) within a similar price range [1]. High-efficiency GPU software can exploit this benefit and grant a huge computational time speed-up with respect to classical CPU programs, up to two order of magnitude. Recently, the employment of GPUs for space mission design-related programs is increasing. Orbit propagation software are suited to be accelerated by graphic cards, allowing to propagate tens of thousands bodies in parallel. However, the difficulties related to implementing efficient GPU algorithms for orbital interference and event detection during the propagation make the usage of graphic-cards less appealing. Moreover, GPU programming can be hard, and it is not the focus of space engineers. GPU software are particularly powerful in large-scale analyses, such as Monte-Carlo methods or grid search optimisations. However, handling the consequent huge sets of output arrays complicates the development of the software itself.

The aim of the work is to tackle the described problems suggesting some event detections algorithms that exploit logical arithmetic to efficiently run in a GPU based application, as well as efficient techniques to handle the outputs.

The work presents the development of the event detection algorithms in CUDAjectory, an open source orbit propagation GPU software available under European Space Agency (ESA) Community License, recently developed by the mission analysis team of ESA. The developments focus on the implementation of four algorithms: close-approach, Low Earth Orbit (LEO) protected region, Geostationary Earth Orbit (GEO) protected region, and massless bodies collision. A significant part of the work is also devoted to lower the computational effort of the output handling, which is a significant bottleneck of GPU/CPU interaction. The ultimate goal for the software is to enrich its interference and detection capabilities in order to increase both the amount of analyses perform-able and the user pool, particularly focusing on large-scale simulation for planetary protection applications.

*Email: adriano ilippo.inno@mail.polimi.it
†Email: camilla.colombo@polimi.it
‡Email: alessandro.masat@polimi.it
§Email: Lorenzo.Bucci@ext.esa.int
¶Email: Florian.Renk@esa.int

2 Brief overview of CUDAjectory

CUDAjectory is written in C++, CUDA and Python. It is optimised to propagate millions of bodies, called *samples*, on GPUs. The output consists in the final states of the samples and the events detected during the propagation. The user can exploit multiple gravity models and orbital perturbations to tune the accuracy of the simulation to their needs.

The propagation of each sample is carried on with the patched conic approach [2]. An event algorithm detects the change of Sphere Of Influence (SOI) and updates the integration centre of each sample. Another algorithm detects the collisions between the samples and the celestial bodies. The third event detection algorithm available is the *close-approach*, which outputs the points of closest approach to each celestial body. The goal and the development of the algorithm is presented in Section 3.

The position and velocity vector of celestial bodies is retrieved at running time by exploiting planetary ephemerides. The ephemerides data are an input of the simulation and must be passed using the NAIF-JPL Satellite and Planet Kernels (SPK) format. Many SPK types exist, and CUDAjectory is currently compatible with respect to SPK types 2 and 3 only. These two file formats are optimised to evaluate planetary motions [6].

In CUDA, the main functions executed on GPUs are called *kernels*, and are issued by the CPU. The samples are propagated in parallel by the computational units of the GPUs. In CUDAjectory, the simulation is divided in multiple sequential kernels, each one performing N consecutive integrational steps, where the amount of consecutive steps can be tuned by the user. This simulation layout comes from a

previous optimisation of the ephemerides evaluation described in details in [3, 4]. After the execution of each kernel, the partial output containing the eventual events detected and the intermediate states of the samples is post-processed and the useful data are saved.

3 Close-approach algorithm

The goal of the close-approach algorithm is to detect the nearest point of each sample with respect to its closest celestial body during the propagation. The outcomes of the algorithm can be utilised by the users for multiple purposes, for example to check and identify potentials fly-by happened during the propagation. The algorithm exploits a bisection-like procedure to converge at the event condition. The iterations are performed imposing the next time step according to the *range rate* (rr), which is the radial component of the relative velocity between a sample and its closest celestial body:

$$rr = \frac{\boldsymbol{r}_k^{rel} \cdot \boldsymbol{v}_k^{rel}}{||\boldsymbol{r}_k^{rel}||} \tag{1}$$

where the subscript k indicates the closest celestial body. When the range rate is equal to zero, the sample is in its close-approach. The iterations start when the algorithm detects a change of sign of the range rate; the event is contained in the time interval between that epoch (t_b) and the epoch at previous integration step (t_a). Fig. 1 shows the timeline during the propagation of a sample, together with its sign of the range rate function, supposing that the integration is carried on for 100 steps.

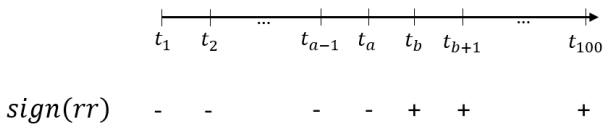

Figure 1: Timeline of the close-approach event during the propagation of a sample.

The rationale of the loop is to half the time interval at every iteration taking the part in which the event is contained, until a tolerance is met, like in a bisection. The algorithm imposes the integration step accordingly. Logical arithmetic is used to keep the number of if-else statements as low as possible, in order reduce the warp divergence (i.e. a typical GPU performance issue in which threads are stalled because of branch-dependant instructions) [1].

4 Earth protected regions algorithms

The goal of the LEO and GEO protected region algorithms is to detect the conditions at which the samples cross one of the boundaries of the two regions. This implementation aims to extend the simulation capabilities to Earth planetary protection and space debris analyses. Fig. 2 shows the conventions adopted to define the protected regions, according to the Inter-Agency space Debris coordination Committee (IADC) space debris mitigation guidelines [5].

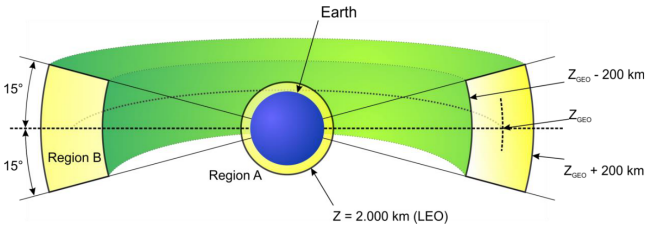

Figure 2: Earth protected regions - IADC conventions [5]

The work presents the reasons why a bisection-like method is not a robust choice for these two algorithms. Instead, an adaptive step refinement procedure is used to update the next time step according to a prediction of the altitude and the latitude (for the GEO algorithm only). Calling the altitude z, the latitude l, and the time step interval h, the predictions are:

$$\begin{aligned} z_{n+1} &\approx z_n + \dot{z}_n h_{n+1} \\ l_{n+1} &\approx l_n + \dot{l}_n h_{n+1} \end{aligned} \tag{2}$$

where indicates n the current time step. Eq. (2) are based on a linear extrapolation of the first order derivatives. The derivative of the altitude is given by the radial velocity of the sample, while the derivative of the latitude is approximated with the backwards finite difference of the latitude between two time steps. The predictions in Eq. (2) depend on the next time step interval (h_{n+1}) which is not known in advance. However, the work proposes a robust way to predict its worst possible value related to the integrator scheme used in the software. The predictions are used to identify potential crossings over the LEO or GEO boundaries at running time. If this happens, the step is adjusted in order to converge at the predicted crossed boundary.

5 Massless bodies collision algorithm

The Massless bodies collision algorithm is aimed at finding the collisions between the samples and a set of user-defined bodies. The radius of the collision sphere around each body is defined by the user. The massless bodies are modeled as orbiting points without a

proper mass. Consequently, the gravity acceleration acting on the samples is not perturbed by this set of bodies and the integrational step-size is not intrinsically refined by the integrator. The massless bodies are not propagated by CUDAjectory. The goal is to utilise a user-prompted ephemerides file to evaluate the position and velocity of the requested massless bodies.

As presented in Section 2, the current compatibility of CUDAjectory with respect to SPK types limits the possibility to provide data for non-planetary bodies. For this reason, the work focused on the analytical implementation of the Libration points motion, in order to be utilised as massless bodies. Libration points are equilibrium points under the influence of a primary and a secondary mass [2].

The proposed algorithm exploits an adaptive step refinement procedure based on the prediction of the distance (d) between each sample and a massless body, to converge at the detection. The prediction is computed as:

$$d_{n+1} \approx d_n + \dot{d}_n h_{n+1}$$

The derivative ($\dot{d}_n$) is given by the range rate, computed as in Eq. (1).

Since the Libration points are modelled as massless points, the time steps are not automatically refined in the proximity of the points themselves during the integration. As a consequence, the linear first order extrapolation is not robust enough. In order to improve the robustness of the prediction, the algorithm also uses the magnitude of the sample velocity instead of the range rate, which represents an upper boundary of the range rate itself.

6 Software optimisation

In its early implementation, the output handling of CUDAjectory took more than the 99% of the total computational time in most of the simulations, representing a huge execution bottleneck. This part of the work was aimed at optimising the computational time of the output handling, in order to make the software much faster than orbit propagation packages on CPUs. The implementation is based on the usage of a common data-type structure to contain the kernel output of every event detection algorithms, improving the final results retrieval efficiency. Since the detections are mutually exclusive, a single common data structure is allocated for each time step and for each sample. The size of the whole allocation can be in the order of tens of GigaBytes (GB). As a consequence, simulations are often limited by the memory capacity of the computer and the user must decrease the number of samples to be propagated. For this reason, the work focuses on the minimisation process of the common data structure size, performed to reduce the total memory required.

Nowadays, operating systems deal with the so called *virtual memory* to store the applications data. The required memory is divided in small chunks of few KiloBytes (KB), called *pages*. When the required memory is higher than the physical memory available, the operating system relocates some pages from the physical memory into additional virtual pages. The additional pages are temporarily stored in the computer storage, causing a huge performance bottleneck in many applications. The optimised output handler ensures that the physical memory is enough to store all the required data, without using additional virtual pages and consequently avoiding potential bottlenecks.

CPU memory allocations are *pageable* by default, which means that can be moved into the storage if needed. It is possible to request physical, non-pageable memory, which is called *pinned* or *page-locked* memory. The optimised output handler exploits the mapped pinned memory, which is a specific-type of pinned memory, to allocate the kernel output and to further improve the performance.

7 Final remarks

The paper will present the development of the CUDAjectory software and its powerful application possibility to massive orbit propagation problems, such as planetary protection studies. The improvement with respect to previous versions of the software will be shown, emphasizing the additional features developed throughout this work, in order to give a clear understanding of the rationale for the chosen solutions, and showing where additional margin for improvement is available, paving the way for future works on the software.

References

[1] Nvidia, *CUDA C++ Programming Guide*, 2021, v11.4.

[2] H. Curtis, Orbital Mechanics for Engineering Students, Elsevier, The Boulevard, Langford Lane, Kidlington, Oxford, 2010.

[3] M. Geda, *Massive parallelisation of trajectory propagaitions using GPUs*, Delft University of Technology, 2019.

[4] F. Schrammel, *Alternative Ephemeris Representations for Astrodynamical Simulations on Accelerators*, Technisch Univeritat Darmstadt, 2019.

[5] IADC, *Space Debris Mitigation Guidelines*, 2021.

[6] NAIF-JPL, *SPK Required Reading*, 1999.

Time integrator for second order in time problems

Blanca Bujanda*[1] and Alejandro Duque†[2]

[1]Dpto. de Estadística, Informática y Matemáticas and INAMAT2, Universidad Pública de Navarra.
[2]Universidad Pública de Navarra.

Abstract

We present a new method in order to realize an efficient temporal integration of Initial Boundary Value Problems of second order in time. Such method can be used to approximate the solution of these problems combined with an adequate spatial discretization. The goal of this time integration technique is, among others, the decrease in the number of time steps that must be carried out, adjusting the size of such steps to the behavior of the solution.

1 Introduction

It is well known that the partial differential equations of second time order together with adequate initial and boundary conditions allow the modeling of a large number of physical situations, for example, in strength of materials. Let $u(\mathbf{x},t)$ be the solution of such problem which admits a general formulation as

$$\begin{cases} \dfrac{\partial^2 u}{\partial t^2}(\mathbf{x},t) + A(\mathbf{x},t)u(\mathbf{x},t) = f(\mathbf{x},t), \\ \qquad\qquad \text{with } (\mathbf{x},t)\in\Omega\times[t_0,T], \\ u(\mathbf{x},t_0) = u_0(\mathbf{x}), \quad \text{with } \mathbf{x}\in\Omega, \\ \dfrac{\partial u}{\partial t}(\mathbf{x},t_0) = u_0^1(\mathbf{x}), \quad \text{with } \mathbf{x}\in\Omega \\ Bu(\mathbf{x},t) = g_\partial(\mathbf{x},t), \quad \text{with } (\mathbf{x},t)\in\partial\Omega\times[t_0,T], \end{cases} \tag{1}$$

being $\mathbf{x}=(x_1,\cdots,x_n)^T\in\Omega\subset\mathbb{R}^n$ the spatial variables, $f(\mathbf{x},t)$ is the source term, B is the boundary operator, $u_0(\mathbf{x})$, $u_0^1(\mathbf{x})$ and $g_\partial(\mathbf{x},t)$ are initial and boundary data. We will also assume enough smoothness and compatibility conditions on the data. $A(\mathbf{x},t)$ is a linear differenctial operator of order $d\in\mathbb{N}$ which contains the spatial derivatives. In the wave equation

$$A(\mathbf{x},t)=\sum_{i=1}^{n}\triangle_{x_i}$$

and in the Euler-Bernoulli equation

$$A(\mathbf{x},t)=\sum_{i=1}^{n}\triangle_{x_i}^2.$$

Last equation is also called the beam equation for $n=1$, the membrane equation if $n=2$ and the generalized membrane equation for $n\geq 3$.

A common way to solve (1) is the method of lines, this technique combine a spatial discretization (Finite Differences, Finite Element, Spectral methods,...) with a time discretization (Runge-Kutta (RK), Runge-Kutta-Nyström (RKN), ...). Both discretizations can be made in any order, we can discretize firstly in space or in time. The final result will be the same, but the theoretical study of the process will be lightly different. If the spatial discretization is firstly made, a family of Stiff Initial Value Problems is obtained:

$$\begin{cases} U''(\mathbf{x},t) + A_h(\mathbf{x},t)U(\mathbf{x},t) = f_h(\mathbf{x},t), \\ \qquad\qquad \text{with } (\mathbf{x},t)\in\Omega_h\times[t_0,T], \\ U(\mathbf{x},t_0) = U_0(\mathbf{x}), \text{ with } \mathbf{x}\in\Omega_h, \\ U'(\mathbf{x},t_0) = U_0^1(\mathbf{x}), \text{ with } \mathbf{x}\in\Omega_h, \end{cases} \tag{2}$$

here h is the size of the mesh Ω_h, $A_h(\mathbf{x},t)$ is discretization of the operator $A_h(\mathbf{x},t)$ by including the boundary conditions.

The numerical integration of (2) can be made by using both explicit or implicit RK classical methods, nevertheless to use this methods we have to double the dimension of the problem which implies increasing (sometimes in a very important way) the computational cost. To avoid this problem have been designed methods like RKN methods (see [4]). In both cases, the explicit methods have the disadvantage of requiring some restrictions between the spatial and temporal step, which can entail a high computational cost; the implicit methods have the drawback of high computational costs per time step, due to the high dimension and complexity of the systems involved

The Alternating Direction Implicit (ADI) methods were designed to avoid this type of disadvantages for some concrete problems. The same design idea in a more general context permit us to integrate PVI of

*Email: blanca.bujanda@unavarra.es. Research supported by PRO-UPNA (6158), RTI2018-095499-B-C31, Ministerio de Ciencia, Innovación y Universidades. Proyectos Retos Investigación.

†Email: duque.129483@e.unavarra.es.

first order (by using FSRK methods) and second order by means FSRKN methods (see [1]). The main additional advantage of such schemes is their unconditional convergence and low cost per time step. The only requirement is realize a suitable splitting of the space differential operator $A_h(\mathbf{x}, t)$ as a sum of simpler operators in a certain sense.

Classically another improvement that has been searched is the change of the temporal step by adapting it to the behaviour of the solution (see [2],[3],[5]). The use of embedded pairs permits us to study adequately the local error estimation and in this way to adapt adequately the time step obtaining a better solution with lower computational cost.

2 The method

An FSRKN method of s stages and m levels applied to solve problem (2) is a numerical algorithm given by:

$$\begin{aligned} K_{n,i} &= U_n + c_i\tau V_n + \\ &+ \tau^2 \sum_{l=1}^{m}\sum_{j=1}^{i} a_{l,ij}\left(-A_{hl}(t_{n,j})K_{n,j} + f_{hl}(t_{n,j})\right), \\ &\qquad i = 1,\dots,s, \\ V_{n+1} &= V_n + \qquad (3) \\ &+ \tau \sum_{l=1}^{m}\sum_{j=1}^{s} b_{l,j}\left(-A_{hl}(t_{n,j})K_{n,j} + f_{hl}(t_{n,j})\right), \\ U_{n+1} &= U_n + \tau V_n + \\ &+ \tau^2 \sum_{l=1}^{m}\sum_{j=1}^{s} \beta_{l,j}\left(-A_{hl}(t_{n,j})\,K_{n,j} + f_{hl}(t_{n,j})\right). \end{aligned}$$

Here the spatial operator and the source term has been decompose as

$$A_h = \sum_{l=1}^{m} A_{hl}, \qquad \text{and } f_h(t) = \sum_{l=1}^{m} f_{hl}(t)$$

respectively. The operators A_{hl} must be verify some properties such as being self-adjoint and negative semi-definite among other. Similarly to RK or RKN methods $K_{n,i}$ are the intermediate stages, $i = 1,\dots,s$, and $(U_n, V_n)^T$ is the numerical approximation to the exact solution $(U_h(t_n), U_h'(t_n))^T$.

In order to apply adequately (3) it is necessary to impose the following restrictions among their coefficients, if

$$a_{\bar{l},ij} \neq 0, \beta_{\bar{l},j} \neq 0 \text{ or } b_{\bar{l},j} \neq 0$$

then

$$a_{l,ij} = 0, \beta_{l,j} = 0, b_{l,j} = 0, \quad \forall\, l \neq \bar{l} \text{ and } \forall\, i,$$

where $t_{n,j} = t_n + c_j\tau$ and $t_n = n\tau$, $n = 1,\dots,N$, the time step is $\tau = T/N$ and N the number of steps. A tableau, which is similar to Butcher's tableau for RK methods, can be used to express these coefficients

$$\begin{array}{c|c|c|c} c & \mathcal{A}_1 & \dots & \mathcal{A}_m \\ & \beta_1^T & \dots & \beta_m^T \\ & b_1^T & \dots & b_m^T \end{array}$$

$$= \begin{array}{c|c|ccc|c|ccc} c_1 & a_{1,11} & & & & & a_{m,11} & & \\ \vdots & \vdots & \ddots & & & & \vdots & \ddots & \\ c_s & a_{1,s1} & \cdots & a_{1,ss} & \dots & a_{m,s1} & \cdots & a_{m,ss} \\ \hline & \beta_{1,1} & \cdots & \beta_{1,s} & \dots & \beta_{m,1} & \cdots & \beta_{m,s} \\ & b_{1,1} & \cdots & b_{1,s} & \dots & b_{m,1} & \cdots & b_{m,s} \end{array}.$$

The solution of an IVP can exhibit a very different behaviour depending on the region due to the variation in the magnitude of the derivatives of the function. In such cases the adaptation of the time step (by decreasing it when the slope increase or decrease quickly and by increasing it when the slope remains stable) has been showed as an important tool. To avoid this inconvenience embedded pairs are used. The idea is to construct two FSRKN methods of different order in such a way that the lower order method is embedded inside the higher order method. This way, at each step we calculate two methods with just one set of stages and an estimate of the local error can be found. Selecting a tolerance for the local error and a criteria for the next step size one obtains an adaptive step size method.

We will present the first embedded pair FSRKN designed, which is a pair 2(1) of four stages a two levels. It is a very simple method, but it opens the way to the building of another methods of higher order.

References

[1] B. Bujanda, J. C. Jorge, M.J. Moreta Numerical resolution of linear evolution multidimensional problems of second order in time, Numer. Methods Partial Differential Equations 28 (2012), no. 2, 597–620.

[2] J.R. Dormand, Numerical Methods for Differential Equations. A computational Approach. *CRC Press*, 1996.

[3] J.R. Dormand, M.E.A. El-Mikkawy, P.J. Prince, Families of Runge-Kutta Nystrom Formula, IMA Journal of Numerical Analysis, 7: 235-250. (1987).

[4] E. Hairer, G. Wammer, Solving Ordinary Differential Equations II, *Springer*, 1996.

[5] F. Ismail, M. Suleman Embedded singly diagonally implicit Runge-Kutta methods (4,5) in (5,6) for the integration of stiff systems of odes, International Journal of Computer Mathematics, 66 (3-4) (1998) 325-341.

Session 9:

RELATIVE DYNAMICS

A curvilinear generalization of the Yamanaka-Ankersen state transition matrix

Alicia Martínez-Cacho*[1] and Claudio Bombardelli†[1]

[1]Grupo de Dinámica Espacial, Universidad Politécnica de Madrid, Spain

1 Introduction

The work of Yamanaka and Ankersen (hereafter YA) in [1] represents a breakthrough in the modelling of relative motion along close Keplerian orbits. In that paper, the authors were able to obtain a fully analytical state transition matrix (STM) starting from the linearized equations of relative motion with respect to a Keplerian elliptical orbit, also known as Tschauner-Hampel (TH) equations. Since that proposed STM works for an arbitrary value of the nominal orbit eccentricity it is considered a milestone result in astrodynamics and is widely employed in the literature. A fundamental, often overlooked, step in the derivation of the YA STM, is the use of a "pulsating" reference length unit very similar to the one employed in the Nechvile curvilinear coordinates for the study of the restricted three-body problem.

In this work, we rewrite the relative motion equations in pulsating cylindrical coordinates, then linearize them obtaining a curvilinear analogue of the TH equations, and finally obtain a curvilinear analogue of the YA STM. The advantage of working with curvilinear coordinates instead of Cartesian ones has already been analyzed, for example in [2][3] for a circular case with a cylindrical system, and in [4] for an elliptical orbit with a spherical one. Here, we apply the cylindrical coordinates STM to the propagation of orbit uncertainties showing an improvement in uncertainty realism compared to the Cartesian case in the great majority of relevant space situational awareness applications.

2 Curvilinear system definition

Let us use the distance from the target to the central body in each instant of time, $R = {}^{p}/_{\gamma(\nu)}$, as a pulsating unit of distance, where $\gamma(\nu) = 1 + e\cos\nu$ and $p = a(1-e^2)$, being a, e and ν the semi-major axis, eccentricity and true anomaly of the target's orbit, respectively. Using this, we define the in-plane curvilinear coordinates, that appear on Figure 1, as:[1]

$$\rho = \sqrt{(1+x)^2 + (y)^2} - 1, \tag{1}$$

$$\theta = atan2^*(y, 1+x), \tag{2}$$

where the position of the chaser relative to the target in the local-horizontal (LVLH) frame, with the orthonormal basis $\{\mathbf{i}, \mathbf{j}, \mathbf{k}\}$ (Figure 1)[2], is:

$$\mathbf{d} = x\mathbf{i} + y\mathbf{j} + z\mathbf{k}. \tag{3}$$

The out-of-plane curvilinear coordinate coincides with the Cartesian one, that is, the mentioned z.

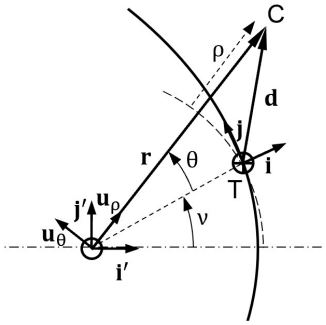

Figure 1: Relative motion geometry using the instant radious of the target as the unit of distance.

3 State transition matrix in curvilinear coordinates

First of all, we need the equations of motion in the curvilinear coordinates. These are:

$$\begin{cases} \rho'' - 2\theta' - \dfrac{3}{\gamma}\rho = a_{i\rho} + \dfrac{1}{\gamma}a_{g\rho} \\ \theta'' + 2\rho' = a_{i\theta} \\ z'' + z = \dfrac{1}{\gamma}a_{gz}, \end{cases} \tag{4}$$

*Email: alicia.martinez.cacho@upm.es. Research supported by a PhD grant under UPM "Programa Propio".

†Email: claudio.bombardelli@upm.es. Research supported by MINECO/AEI and FEDER/EU under Project PID2020-112576GB-C21. The authors thank the MINECO/AEI of Spain for their financial support.

[1]The function $atan2^*$ is $\mod(atan2(x,y) + 2\pi, 2\pi)$.

[2]Notice that the basis $\{\mathbf{i}', \mathbf{j}', \mathbf{k}'\}$ corresponds to the perifocal coordinate system.

where the right side contains the non-linear terms:

$$\begin{aligned} a_{i\rho} &= \theta'^2(1+\rho) + 2\theta'\rho, \\ a_{g\rho} &= -2\rho + 1 - \frac{(1+\rho)}{\left[(1+\rho)^2+z^2\right]^{3/2}}, \\ a_{i\theta} &= \frac{2\rho'(\rho-\theta')}{1+\rho}, \\ a_{gz} &= z - \frac{z}{\left[(1+\rho)^2+z^2\right]^{3/2}}. \end{aligned} \tag{5}$$

These equations are obtained following a procedure similar to the one used in [2], but with an elliptical orbit for the target instead of a circular one. The true anomaly of the target is used as the independent variable (whose derivatives are indicated with primes).

The linearized version of these equations has the same structure as the TH equations:

$$\begin{cases} \rho'' - 2\theta' - \dfrac{3}{\gamma}\rho = 0 \\ \theta'' + 2\rho' = 0 \\ z'' + z = 0. \end{cases} \tag{6}$$

This similarity allows us to obtain a STM similar to the YA one by following the same mathematical development followed in [1]. Hence, the problem has to be subdivided in the out-of-plane and in-plane motions.

3.1 Out-of-plane

In the out-of-plane motion, curvilinear and Cartesian coordinates coincide. [3] Therefore, the STM coincides too, being:

$$\begin{bmatrix} z \\ z' \end{bmatrix} = \frac{1}{\gamma_{\nu-\nu_0}} \begin{bmatrix} c & s \\ -s & c \end{bmatrix}_{\nu-\nu_0} \begin{bmatrix} z_0 \\ z_0' \end{bmatrix}, \tag{7}$$

where $c = \gamma\cos\nu$ and $s = \gamma\sin\nu$.

3.2 In-plane

In this motion, cylindrical and Cartesian coordinates differ. However, as the equations have a similar structure, the curvilinear STM can be obtained following the same procedure depicted in [1]. The result is:

$$\begin{bmatrix} \rho \\ \theta \\ \rho' \\ \theta' \end{bmatrix} = \begin{bmatrix} 0 & s & c & (2-3esJ) \\ -1 & c\,(1+1/\gamma) & -s\,(1+1/\gamma) & -3\gamma^2 J \\ 0 & s' & c' & -3e\left(s'J + s/\gamma^2\right) \\ 0 & -2s & -2c+e & -3\,(1-2esJ) \end{bmatrix}_{\nu} \begin{bmatrix} K_1 \\ K_2 \\ K_3 \\ K_4 \end{bmatrix} \tag{8}$$

$$\begin{bmatrix} K_1 \\ K_2 \\ K_3 \\ K_4 \end{bmatrix} = \frac{1}{e^2-1} \begin{bmatrix} 3e(s/\gamma)(1+1/\gamma) & e^2-1 & 2-ec & es(1+1/\gamma) \\ -3(s/\gamma)(1+e^2/\gamma) & 0 & c-2e & -s(1+1/\gamma) \\ -3(c/\gamma+e) & 0 & -s & -c(1+1/\gamma)-e \\ 3\gamma+e^2-1 & 0 & es & \gamma^2 \end{bmatrix}_{\nu_0} \begin{bmatrix} \rho_0 \\ \theta_0 \\ \rho_0' \\ \theta_0' \end{bmatrix}, \tag{9}$$

[3] Notice that in [1] the coordinate y is oriented following the direction of $-\mathbf{h}$ (being $\mathbf{h}$ the angular momentum vector of the target) while in our system z is oriented towards $\mathbf{h}$.

where $J(\nu) = \int_{\nu_0}^{\nu} \dfrac{d\nu}{\gamma^2(\nu)} = \dfrac{\mu^2}{h^3}(t-t_0)$, being μ the gravitational parameter of the central body and h the angular momentum of the target.

4 Uncertainty Realism

One important application of the STM is the uncertainty propagation. Hence, it is of high interest the evaluation of the performance in uncertainty propagation of the new curvilinear STM by comparing it with the YA STM performance. This is carried out by means of the Uncertainty Realism which is evaluated using the Cramer-von Mises (CvM) test of the Mahalanobis distance distribution. The details of this test can be found in [5].

Considering an initial Gaussian Probability Density Function (PDF) and its corresponding set of orbital states sampled, the CvM test evaluates if the Mahalanobis distance of the samples follows a chi-squared distribution for each epoch. When this is achieved the PDF remains Gaussian, thus the uncertainty is realistic. The Mahalanobis distance is defined as:

$$\mathcal{M}_i(\mathbf{x}_i; \boldsymbol{\mu}, \mathbf{P}) = (\mathbf{x}_i - \boldsymbol{\mu})^T \mathbf{P}^{-1} (\mathbf{x}_i - \boldsymbol{\mu}), \tag{10}$$

where, at each time instance, $\mathbf{x}_i$ is the ith sample state propagated with a full nonlinear orbital dynamics model, $\boldsymbol{\mu}$ is the mean of the set of samples and $\mathbf{P}$ is the linearly[4] propagated covariance matrix. The covariance matrix propagation is done by:

$$\mathbf{P}(t) = \boldsymbol{\Phi}(t, t_0)\mathbf{P}(t_0)\boldsymbol{\Phi}^T(t, t_0), \tag{11}$$

where $\boldsymbol{\Phi}(t, t_0)$ is the STM in the corresponding space.

4.1 Test conditions

In this work, the CvM test is performed in Cartesian coordinates using YA STM and in curvilinear coordinates with the STM obtained in section 3. In both cases the set of samples has a size of $N = 10000$ and the test is performed with a 99.9% confidence level. This pair of confidence level and N implies that the covariance is realistic while the value of the CvM test statistics remains lower than 1.16204 [6]. The set of samples is propagated using Matlab's ode45 and a Keplerian dynamic model.

5 Results

There are two different orbits to be studied whose initial orbital elements are shown in Table 1 and whose initial covariance matrices written in the LVLH frame

[4] Notice that the CvM test can be used with nonlinear covariance propagation methods. However, as our interest lies on the study of a STM, only the linear propagation has been considered

are shown in Table 2. When performing the test for the curvilinear STM, the covariance matrix is transformed by the full nonlinear elements conversion.

Type	r_p (km)	e	i (°)	Ω (°)	ω (°)	M (°)
GEO	42164.1	0	0	0	0	0
LEO	7000	Variable	25	120	0	180

Table 1: Initial orbital elements

Case	σ_x (m)	σ_y (m)	σ_z (m)	$\sigma_{\dot{x}}$ (m/s)	$\sigma_{\dot{y}}$ (m/s)	$\sigma_{\dot{z}}$ (m/s)
GEO	1000	3000	5000	0.3	0.1	0.4
LEO	100	300	500	0.03	0.01	0.04

Table 2: Initial Covariance in LVLH frame

The first case of study is a GEO with a TLE-like covariance matrix. The values of the covariance matrix have been obtained after analyzing the position and velocity uncertainty for different satellites in GEO, whose data were obtained as two-line elements (TLEs) from the webpage `https://www.space-track.org/`. As for the second case, it corresponds to a LEO that is studied for different eccentricities: from the circular case to $e = 0.8$ in intervals of 0.1. For this case, the covariance matrix selected is the the GEO TLE-like covariance reduced by a factor of 10.

The Cramer-von Mises (CvM) test statistics for the circular cases, that is, the GEO and the circular LEO is shown in Figure 2. In both cases, the CvM test fails before 1 orbital period with the Cartesian YA STM whereas with the curvilinear STM the realism is maintained for more than 10 orbits for GEO and more than 16 orbits for the circular LEO. Therefore, in these cases curvilinear coordinates provides a huge improvement in realism with respect to Cartesian ones.

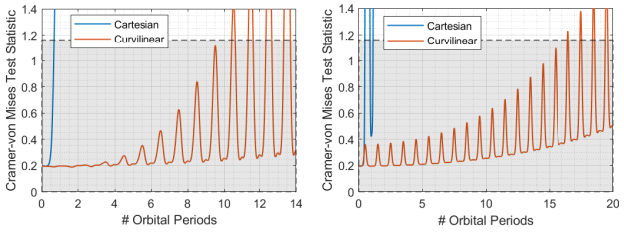

Figure 2: CvM test statistics for: left, GEO; right, circular LEO

Figure 3 shows the results for two of the eccentricities studied for the eccentric LEO: the smallest, $e = 0.1$, and the highest, $e = 0.8$. For $e = 0.1$, the realism is maintained for half an orbit for YA STM and around 4 orbits for curvilinear STM. This result entails a better performance with the curvilinear STM again. Regarding the case of $e = 0.8$, both YA and the curvilinear STM provide the same results. As we can see in the right graphics of figure 3, the test fails before 1 orbital period, which is a poor result.

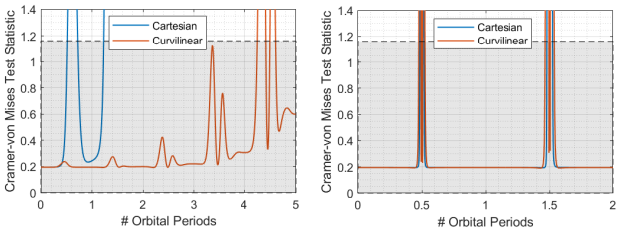

Figure 3: CvM test statistics for the LEO case with: left, $e = 0.1$; right, $e = 0.8$

	Eccentricity								
STM	0	0.1	0.2	0.3	0.4	0.5	0.6	0.7	0.8
Cart	0.47	0.52	1.32	1.38	1.42	1.45	1.46	0.49	0.48
Curv	16.48	4.25	2.37	2.35	2.37	2.4	2.42	1.47	0.48

Table 3: Number of orbital periods for the CvM test before failure for LEO

The results obtained for the rest of the eccentricities are summarized in table 3. As for the Cartesian YA STM, the realism breaks down after only half an orbit or one orbit and a half for all the cases considered. On the other hand, the curvilinear STM maintains covariance realism for a considerably higher number of orbits as long as the eccentricity is not too high. This advantage decreases as the eccentricity grows, disappearing for eccentricities higher than 0.7 where both Cartesian and curvilinear coordinates perform poorly.

References

[1] K. Yamanaka, F. Ankersen, New state transition matrix for relative motion on an arbitrary elliptical orbit, *Journal of Guidance, Control and Dynamics* **25** (2002), 60-66.

[2] C. Bombardelli, J. L. Gonzalo, J. Roa, Approximate solutions of non-linear circular orbit relative motion in curvilinear coordinates, *Celestial Mechanics and Dynamical Astronomy* **127** (2017), 49-66.

[3] D.K: Geller, T.A. Lovell, Angles-Only Initial Relative Orbit Determination Performance Analysis using Cylindrical Coordinates, *J of Astronaut Sci* **64** (2017), 72–96.

[4] C. Han et. al., A linear model for relative motion in an elliptical orbit based on a spherical coordinate system, *Acta Astronautica* **157** (2019), 465-476

[5] J. M. Aristoff, J. T. Horwood, K. T. Alfriend, On a set of J_2 equinoctial orbital elements and their use for uncertainty propagation, *Celestial Mechanics and Dynamical Astronomy* **133** (2021), 1-19.

[6] J. T. Horwood et. al., Beyond covariance realism. A new metric for uncertainty realism, *Signal and Data Processing of Small Targets* **9092** (2014).

Influence of Apophis' spin axis variations on a spacecraft during the 2029 close approach with Earth.

Aljbaae S.*[1], Antonio F. B. A. P[1], Souchay J[2], and Valerio Carruba[3]

[1]Division of Space Mechanics and Control, INPE, C.P. 515, 12227-310 São José dos Campos, SP, Brazil
[2]SYRTE, Observatoire de Paris, PSL Research University. 61 avenue de l'Observatoire, 75014 Paris, France
[3]UNESP, School of Natural Sciences and Engineering, Guaratinguetá, SP, 12516-410, Brazil

1 Introduction

Tumbling asteroids belong to a group of objects, whose angular velocity vector is unaligned with any of its principal axes of inertia. This leads to challenging efforts to model the trajectory of any spacecraft designed to orbit these bodies. The PHA asteroid (99942) Apophis (2004 MN4) is one of the largest tumbling asteroids to have a very close approach to Earth at a distance of ∼38 000 km from the Earth's center, on April 13th.,2029, where dramatic changes in its orbit will be observed.(J. et al., 2005; Souchay et al., 2018) modeled the important changes in the rotational parameters of the axis of rotation. In this work, a preliminary analysis of the orbital dynamics of a spacecraft in orbit close to Apophis is provided. The gravitational field of the target is represented by a cloud of point-masses system distributed inside its polyhedral shape. The impact of the close approach with our planet on the spacecraft is analyzed considering the gravitational perturbations of the planets on the Solar System, the Solar radiation pressure (SRP), and also the effects of the changes of spin state due to the terrestrial torques. A 60-days integration is carried out ranging 43 days before and 16 days after the encounter. In a very large majority of cases, the spacecraft undergoes a collision or escape due to the perturbation caused by the close encounter. A time-series prediction with Neural Networks in Python with Keras is used to classify orbits based on a relationship between the difficulty in the prediction and the stability. This method can isolate the most regular orbits in the system. A good correlation was found between the Time-Series prediction approach and MEGNO or the Perturbation Map. A sliding mode control theory is applied to solve the stabilization problem for the system. With a total ΔV of 0.495 m/s, we successfully stabilized an orbit with an initial semimajor axis of 0.5 km.

2 Dynamical model

The equations of motion used here are referred to an inertial reference frame with origin on the centre of mass of the asteroid. We considered the gravitational influence of the planet-size bodies of our Solar System.

$$\ddot{\mathrm{r}} = U_{\mathrm{r}} + \sum_{i=1}^{14} \mathcal{G} m_i \left(\frac{\mathrm{r}_i - \mathrm{r}}{|\mathrm{r}_i - \mathrm{r}|^3} - \frac{\mathrm{r}_i}{|\mathrm{r}_i|^3} \right) + \nu \mathrm{P}_{\mathrm{R}} \quad (1)$$

where, $\nu \mathrm{P}_{\mathrm{R}}$ represents the acceleration due to the SRP considering the shadowing phenomenon (Aljbaae et al., 2021a), applied for an OSIRIS-REx-like spacecraft with a reflectance of 0.4 and a mass-to-area ratio of 60 kg.m^{-2}. U_{r} is the gradient of the gravitational potential of the asteroid, calculated from a sum of 3996 points after rotating the polyhedral shape about the origin, in terms of longitude, obliquity, and precession (Aljbaae et al., 2021b).

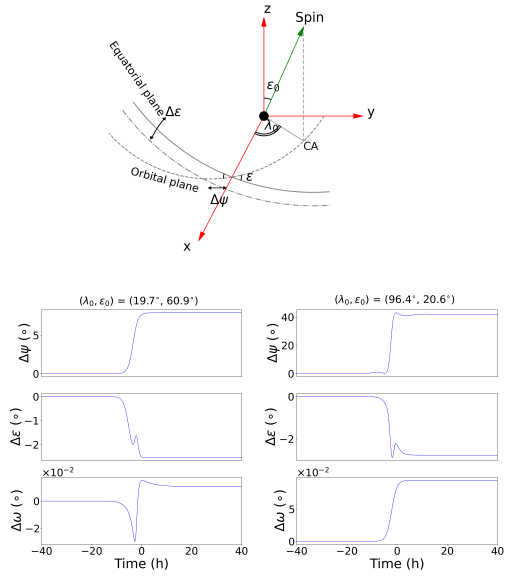

Figure 1: Minimum and Maximum variations of the orientation of Apophis spin axis.

*Email: safwan.aljbaae@gmail.com

3 Results

In Fig. 2, we show the final states of the orbits integrated for 40-days and 60-days. We notice that the large majority of the orbits ($\sim 95\%$) collide or escape from the system just after the close encounter with our planet, whereas the totality of orbits are bounded before. We also remark that the initial Apophis spin orientation slightly affects the distribution of the colliding and escaping orbits.

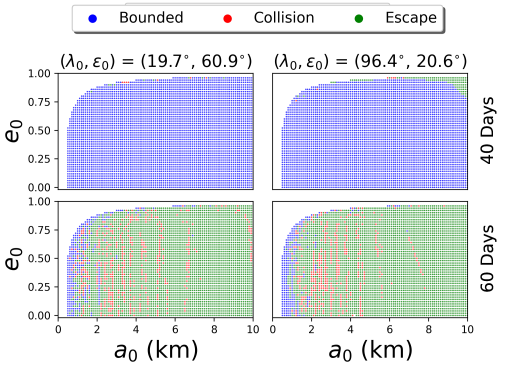

Figure 2: Characterization of the orbits around Apophis for 40 days and 60 days time span starting from March 1, 2029.

3.1 MEGNO algorithm (Mestre et al., 2011)

A global dynamics insight is obtained by calculating the average of the relative divergence of the orbit.

$$\text{MEGNO} = \frac{2}{T}\sum_{k=1}^{T} k \ln\left(\frac{\delta(k)}{\delta(k-1)}\right) \tag{2}$$

where, $\delta(k)$ represents the deviation vector in the phase space, and T is the time of integration. The larger MEGNO values correspond to a higher degree of chaos and a higher chance of instability.

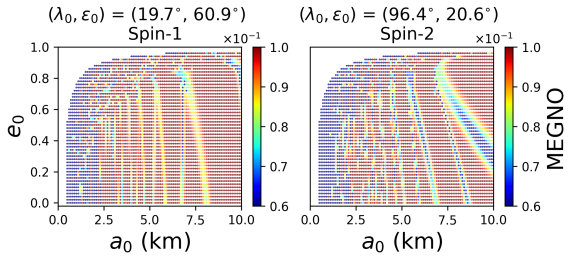

Figure 3: MEGNO dynamical maps for the spacecraft orbits around the Apophis system.

3.2 Perturbation Map of type II (Sanchez and Prado, 2019)

In this method, we calculate the perturbations of energy undergone by the spacecraft.

$$\text{PI}_{ii} = \frac{1}{T}\int_0^T \langle \boldsymbol{a}, \frac{\boldsymbol{v}}{|\boldsymbol{v}|}\rangle dt, \tag{3}$$

where, $\boldsymbol{a}$ is the acceleration due to the whole perturbations of the orbital motion, $\boldsymbol{v}$ is the velocity of the spacecraft, T is the final time of the integration. This approach gives a good indication of the variation of energy caused by the perturbations.

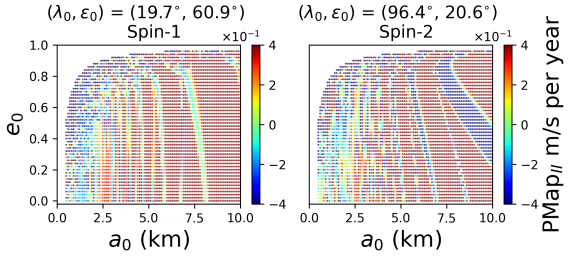

Figure 4: Perturbation maps of type II (PMap) for a spacecraft orbiting around Apophis.

3.3 Time-Series prediction

This method consists in using a sequence of random variables to create a model fitted to historical data and to apply it to predict the future. The dataset for each orbit consists of 6 features (positions and velocity), recorded every 30 seconds. The first 90% of the points in each orbit (54 days) are used to train the model and predict the position of the spacecraft during the last 6 days of the orbit. The area between the predicted and real data ($\mathcal{A}$) is used to classify the orbits. The smaller the area, the more predictable the orbit, which makes the spacecraft mission much easier to be mapped and planned out.

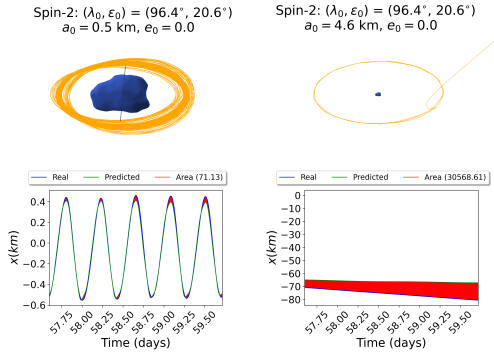

Figure 5: Example of a regular and an irregular orbit for a spacecraft orbiting around Apophis.

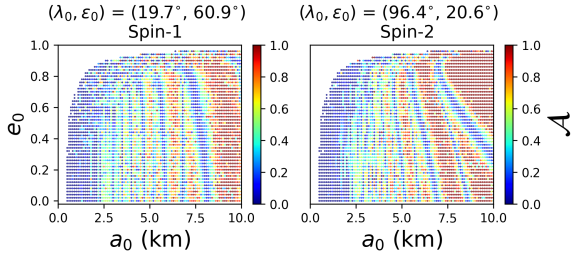

Figure 6: Forecasting maps using the Time-Series prediction for orbits around Apophis.

The coherence between the three methods presented above, using the Pearson correlation coefficient is presented in Fig. 7.

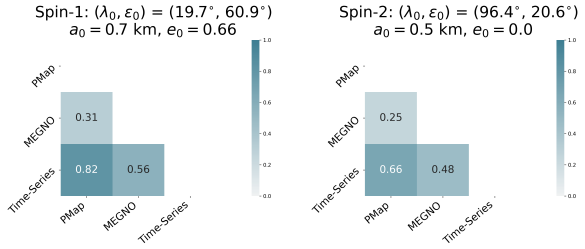

Figure 7: Correlation matrix for the three methods used to investigate the phase space structure associated to Apophis.

3.4 Orbital control around (99942) Apophis

In order to solve the stabilization problem for the system around Apophis, we applied the sliding mode control theory, controlling only the geometry of the orbit, trying to keep the orbital elements nearby the desired values Negri and Prado (2020a,b). In Fig. 9 and 8 we present an example of orbit successfully stabilized using a total ΔV of 0.495 m/s for 60 days of operation.

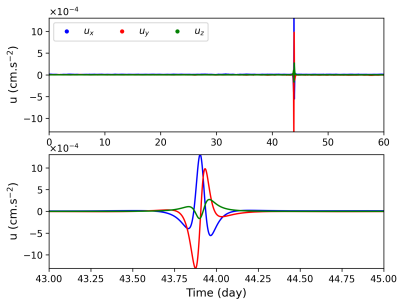

Figure 8: The control components of the orbit shown in Fig. 9

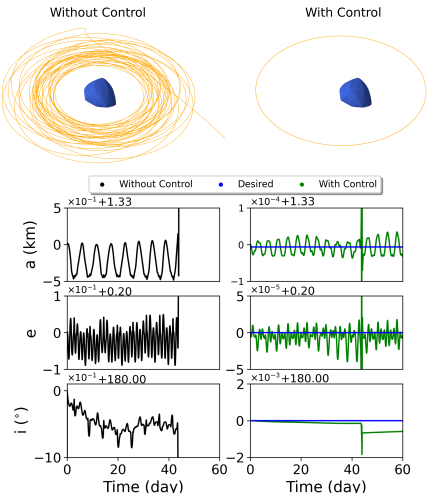

Figure 9: Controlled orbit close to (99942) Apophis, in the inertial frame. a_0 = 0.5 km, e_0 = 0.2, i_0 = 180°, and other orbital parameters are fixed to 0.

References

Aljbaae S, Sanchez DM, Prado AFBA, Souchay J, Terra MO, Negri RB, Marchi LO (2021a) First approximation for spacecraft motion relative to (99942) Apophis. Romanian Astronomical Journal 31(3):241–264

Aljbaae S, Souchay J, Carruba V, Sanchez DM, Prado AFBA (2021b) Influence of Apophis' spin axis variations on a spacecraft during the 2029 close approach with Earth. Romanian Astronomical Journal 31(3):317–337

J SD, M BLA, J OS, A R, F M, P W (2005) Abrupt alteration of Asteroid 2004 MN4's spin state during its 2029 Earth flyby. Icarus 178(1):281 – 283

Mestre MF, Cincotta PM, Giordano CM (2011) Analytical relation between two chaos indicators: FLI and MEGNO. MNRAS414(1):L100–L103

Negri RB, Prado AFBA (2020a) A Novel Robust 3-D Path Following Control for Keplerian Orbits. Submitted to Automatica

Negri RB, Prado AFBA (2020b) Autonomous and Robust Orbit Keeping for Small Body Missions. Submited to Journal of Guidance, Control, and Dynamics

Sanchez DM, Prado AFBA (2019) Searching for Less-Disturbed Orbital Regions Around the Near-Earth Asteroid 2001 SN263. Journal of Spacecraft and Rockets 56(6):1775–1785

Souchay J, Lhotka C, Heron G, Hervé Y, Puente V, Folgueira Lopez M (2018) Changes of spin axis and rate of the asteroid (99942) Apophis during the 2029 close encounter with Earth: A constrained model. A&A617:A74

Formation design selection based on time and cost of reset

Davide Menzio*[1], Ahmed Mahfouz†[1], Florio Dalla Vedova‡[2], and Holger Voos§[1]

[1]University of Luxembourg, Luxembourg
[2]LuxSpace, Luxembourg

1 Introduction

Formation flying is a distributed satellite architecture that foresees two or more spacecraft orbiting in a predefined configuration and synchronizing their operations. Combining their instruments results in an improved spacial and temporal sensing ability that could not be achieved with a single satellite. Several applications benefit of this architecture: in particular, elevation [15] and cloud [21] profiles mapping, geolocalization [11], high resolution imagery, gravimetry [22], and magnetometry [9], but also, technology demonstrations preparing for active debris removal [10] and on-orbit servicing [24].

These complex missions could have not been conceived without the efforts of great astrodynamicists. Several models were developed from the Clohessy-Wiltshare [8] to account for different perturbations, induced by an elliptic orbit of the chief satellite [23] or/and the oblateness of the main body [20, 1, 25]. For Earth-like bodies, the J2 effect induces short-, long-period and secular variations that affect the configuration of the satellites [7]. Schaub and Alfriend noticed that, in first order approximation, the conjugate momenta of the mean elements remains constant while the mean angles grow linearly. With a thoughtful selection of semi-major axis, eccentricity and inclination difference, it is possible to nullify these rates and to bound the motion of the deputy satellites to the chief for few periods [18]. An equivalent reduction of the longitude of the ascending node and the mean argument of the latitude rates can be obtained constraining the along-tracks drift and negating either the differential nodal precession or the differential perigee rotation [2]. Gurfil derived an analytical expression for the inter-satellite distance [12] that was used by Nie to determine conditions for the fifferential nodal precession (DNPN), the differential periapsis drift (DPRN) and minimum acceleration (MAC) [17]. Nie showed that by minimizing the initial drift rate, it is possible to determine solutions in mean elements difference that remain within a 5% margin of the mean inter-satelite distance for about a year.

A different approach is the one of Koon et al. [14], that proposed to initialize the satellite orbits on the center manifold of the periodic orbit that appears in the Routh-reduced system perturbed by zonal harmonics [6]. Nevetheless, upon conversion in osculating elements, the configuration does not survive for more than few days under the effect of the natural drifts. Xu et al. obtained yearly bounded formations by matching the nodal periods and the RAAN drift rates of the psuedo-circular and pseudo-elliptical orbits [26]. Baresi and Scheeres explicitly computed the quasi-periodic invariant tori within the center manifolds of the periodic orbit via a stroboscopic approach and used it to determine trajectories that remain bounded around Earth [5, 4] and asteroids [3].

A notable mention is the integrable intermediary of Lara that captures not only secular variations but also short and long period ones [16]. Based on the observation that the analytical solution of the approximation are 1:1 resonant orbit at the critical inclination, Gurfil showed that initializing the chief satellite on a frozen orbit can reduce the inter-satellite distance growth rate [13].

In this work, we rely on the analytical conditions derived by Nie and Gurfil [17] to initialize orbit of the chief and the deputy satellites. We evaluate different sets of mean elements of the chief and deputy in term of maximum and minimum inter-satellite distance variation, the time within the bounds and the cost of resetting the orbit to the initial conditions.

2 Methodology

When the conjugate momenta of chief and deputy differ, the relative distance between the two is subjected to a secular growth. This can be prevented by negating the along-track drift:

$$\delta\dot{M} + \delta\dot{\omega} + \delta\dot{\Omega}\cos i_0 = 0,$$

and either the differential nodal precession $\delta\dot{\Omega} = 0$ or the differential perigee drift $\delta\dot{\omega} = 0$, resulting in the DNPN and DPRN conditions for the semi-major axis and eccentricity differences, respectively:

*Email: davide.menzio@uni.lu
†Email: ahmed.mahfouz@uni.lu
‡Email: dallavedova@luxspace.lu
§Email: holger.voos@uni.lu

$$DNPN: \begin{cases} \delta a_0 = -\frac{(3\eta_0+4)J_2R_e^2(5\sin 2i_0+2\tan i_0)}{16a\eta_0^4}\delta i_0 \\ \delta e_0 = \frac{\eta_0^2\tan i_0}{4\sqrt{1-\eta_0^2}}\delta i_0 \end{cases},$$

$$DPRN: \begin{cases} \delta a_0 = -\frac{(3\eta_0+4)J_2R_e^2(14\sin 2i_0+5\sin 4i_0)}{16a\eta_0^4(5\cos 2i_0+3)}\delta i_0 \\ \delta e_0 = \frac{5\eta_0^2\sin 2i_0}{2\sqrt{1-\eta_0^2(5\cos 2i_0+3)}}\delta i_0 \end{cases}$$

where a, e, i, Ω, ω and M are the semi-major axis, eccentricity, inclination, longitude of the right ascension, argument of the periapsis and mean anomaly of the chief, *delta* consists in the mean elements difference between the chief and the deputy, and the subscript 0 is associated to the initial condition from which the propagation is started. Moreover, η_0 is defined as,

$$\eta_0 = \sqrt{1-e_0^2}.$$

This result can be further improved by minimising the distance drift rate, assuming that there the semi-major axis and eccentricity differences are proportional to the inclination difference:

$$MAC: \left\{ \ \delta a_0 = k_1^*\delta i_0 \quad \delta e_0 = k_2^*\delta i_0 \quad \right. ,$$

where the expression for k_1^* and k_2^* can be retrieved from [17].

Nie and Gurfil also proposed two constraints that should help in reducing the distance drift:

1. a negative initial drift rate for DNPN, DPRN and MAC conditions;

2. a minimum initial drift rate for the MAC condition, given an initial distance and inclination difference.

If the first condition offers a set of inequality constraints that help choosing the mean angles difference of the deputy satellite, the latter provides their exact solutions [17].

In this paper, we evaluate the role of the initial semi-major axis of the chief satellite, ranging from 400 to 800 km in altitude, the initial inclination difference of the deputy and the initial inter-satellite distance, so that the latter varies between 10 and 1000 km. The other orbital elements of the chief are fixed to 0.05 value of eccentricity, 48 or 88 degrees of inclination as per [18, 17], 0 degrees of right ascension, 90 degrees of argument of the periaspsis and 0 degrees of mean anomaly. The initial semi-major axis, eccentricity, right ascension, argument of the periapsis and mean anomaly differences are determined for the given set of initial inclination difference and initial inter-satellite distance obtained from the MAC condition with minimum initial drift rate.

Different combinations of initial semi-major axis of the chief, initial inclination difference of the deputy and initial inter-satellite distance are evaluated in term of the time and cost of reset. The time of reset is obtained halting the propagation once the maximum osculating distance exceeds twice the initial value while the cost of reset accounts for the delta-v needed to restore the orbit of the deputy to its initial values.

To do so, a Lyapunov-based nonlinear controller is employed. The asymptotic stability of the controller is proven in [19], where the ideal control action is modeled as a continuous acceleration in the LVLH frame of the chief spacecraft. The control acceleration vector is generated according to the following control law:

$$\mathbf{u} = -P\left(\mathbf{B}^\intercal\mathbf{B}\right)^{-1}\mathbf{B}^\intercal\mathbf{e}_{\text{err}}, \tag{1}$$

where P is a scalar control gain, $\mathbf{e}$ being the vector of the mean Keplerian elements, $\mathbf{e}_{\text{err}} = \mathbf{e}_d - \mathbf{e}_{req}$ is the error signal fed to the controller, with $\mathbf{e}_{req}$ and $\mathbf{e}_d$ being the required and the actual mean Keplerian elements of the deputy spacecraft, and

$$\mathbf{B} \coloneqq \frac{\partial\dot{\mathbf{e}}_d}{\partial\mathbf{u}}$$

is the Jacobian matrix of the deputy's mean elements with respect to the control acceleration, derived from the Gauss variational equations. The full expression can be found in [19].

Representing the contour levels associated time and cost of reset superimposed, we hope to shed some light on which are the best combination of initial inclination difference of the deputy and inter-satellite distance for a different initial semi-major axis of the chief satellite.

This work will support LuxSpace in deploying a two satellite formation performing performing bistatic sar imagery at 450 km altitude relyin on inter-satellite link and low-trhust propulsion.

3 Acknowlegment

This work is supported by the Luxembourg National Research Fund (FNR) – AuFoSat project, BRIDGES/19/MS/14302465.

References

[1] K. Alfriend. Nonlinear considerations in satellite formation flying. In *AIAA/AAS Astrodynamics Specialist Conference and Exhibit*, page 4741, 2002.

[2] K. T. Alfriend, S. R. Vadali, P. Gurfil, J. P. How, and L. Breger. *Spacecraft formation flying: Dynamics, control and navigation*, volume 2. Elsevier, 2009.

[3] N. Baresi and D. J. Scheeres. Bounded relative motion under zonal harmonics perturbations. *Celestial Mechanics and Dynamical Astronomy*, 127(4):527–548, 2017.

[4] N. Baresi and D. J. Scheeres. Design of bounded relative trajectories in the earth zonal problem. *Journal of Guidance, Control, and Dynamics*, 40(12):3075–3087, 2017.

[5] N. Baresi, D. J. Scheeres, and H. Schaub. Bounded relative orbits about asteroids for formation flying and applications. *Acta Astronautica*, 123:364–375, 2016.

[6] R. Broucke. Numerical integration of periodic orbits in the main problem of artificial satellite theory. *Celestial Mechanics and Dynamical Astronomy*, 58(2):99–123, 1994.

[7] D. Brouwer. Solution of the problem of artificial satellite theory without drag. *The Astronomical Journal*, 64:378, nov 1959.

[8] W. Clohessy and R. Wiltshire. Terminal guidance system for satellite rendezvous. *Journal of the Aerospace Sciences*, 27(9):653–658, 1960.

[9] E. Friis-Christensen, H. Lühr, and G. Hulot. Swarm: A constellation to study the earth's magnetic field. *Earth, planets and space*, 58(4):351–358, 2006.

[10] E. Gill, S. D'Amico, and O. Montenbruck. Autonomous formation flying for the prisma mission. *Journal of Spacecraft and Rockets*, 44(3):671–681, 2007.

[11] P. Gurfil, J. Herscovitz, and M. Pariente. The samson project–cluster flight and geolocation with three autonomous nano-satellites. 2012.

[12] P. Gurfil and K. V. Kholshevnikov. Manifolds and metrics in the relative spacecraft motion problem. *Journal of guidance, control, and dynamics*, 29(4):1004–1010, 2006.

[13] P. Gurfil and M. Lara. Motion near frozen orbits as a means for mitigating satellite relative drift. *Celestial Mechanics and Dynamical Astronomy*, 116(3):213–227, 2013.

[14] W. Koon, J. Marsden, R. Murray, and J. Masdemont. J2 dynamics and formation flight. In *AIAA Guidance, Navigation, and Control Conference and Exhibit*, page 4090.

[15] R. Kroes, O. Montenbruck, W. Bertiger, and P. Visser. Precise grace baseline determination using gps. *Gps Solutions*, 9(1):21–31, 2005.

[16] M. Lara and P. Gurfil. Integrable approximation of j 2-perturbed relative orbits. *Celestial Mechanics and Dynamical Astronomy*, 114(3):229–254, 2012.

[17] T. Nie, P. Gurfil, and S. Zhang. Analytical conditions for bounded mean inter-satellite distances in the j 2 problem. *Journal of Guidance, Control, and Dynamics*, 41(10):2144–2162, 2018.

[18] H. Schaub and K. T. Alfriend. J2 invariant relative orbits for spacecraft formations. *Celestial Mechanics and Dynamical Astronomy*, 79(2):77–95, 2001.

[19] H. Schaub, S. R. Vadali, J. L. Junkins, and K. T. Alfriend. Spacecraft formation flying control using mean orbit elements. *The Journal of the Astronautical Sciences*, 48(1):69–87, 2000.

[20] S. A. Schweighart and R. J. Sedwick. High-fidelity linearized j model for satellite formation flight. *Journal of Guidance, Control, and Dynamics*, 25(6):1073–1080, 2002.

[21] G. L. Stephens, D. G. Vane, R. J. Boain, G. G. Mace, K. Sassen, Z. Wang, A. J. Illingworth, E. J. O'connor, W. B. Rossow, S. L. Durden, et al. The cloudsat mission and the a-train: A new dimension of space-based observations of clouds and precipitation. *Bulletin of the American Meteorological Society*, 83(12):1771–1790, 2002.

[22] B. D. Tapley, S. Bettadpur, M. Watkins, and C. Reigber. The gravity recovery and climate experiment: Mission overview and early results. *Geophysical research letters*, 31(9), 2004.

[23] J. Tschauner and P. Hempel. Rendezvous zu einem in elliptischer bahn umlaufenden ziel. *Astronautica Acta*, 11(2):104–+, 1965.

[24] D. A. Whelan, E. A. Adler, S. B. Wilson III, and G. M. Roesler Jr. Darpa orbital express program: Effecting a revolution in space-based systems. In *Small Payloads in Space*, volume 4136, pages 48–56. SPIE, 2000.

[25] G. Xu and D. Wang. Nonlinear dynamic equations of satellite relative motion around an oblate earth. *Journal of Guidance, Control, and Dynamics*, 31(5):1521–1524, 2008.

[26] M. Xu, Y. Wang, and S. Xu. On the existence of j 2 invariant relative orbits from the dynamical system point of view. *Celestial Mechanics and Dynamical Astronomy*, 112(4):427–444, 2012.

A Closer Look at Two-Line Elements Data

Andrea Ciccarelli*[1] and Claudio Bombardelli†[2]

[1]Department of Industrial Engineering., University of Naples Federico II, Italy.
[2]Grupo de Dinámica Espacial, Universidad Politécnica de Madrid, Spain.

Keywords: Error analysis, SPG4 accuracy, Space Situational Awareness, Two-Line Elements, Orbital Dynamics

1 Introduction

Two-Line Elements (TLEs) data are a key source of information to understand the evolution of the cirmcumterrestrial space environment. The Two-Line Elements (TLEs) that result from Simplified General Perturbation 4 (SGP4) orbit determination allow rapid, modestly accurate propagation of the entire trackable population of now roughly 20,000 resident space objects. Excluding military restricted assets, TLE data are the only openly available, comprehensive catalogue of space objects and this database supports many technical analyses[1]: the Space Debris Office at ESA predicts conjunction events based on Two-Line Element (TLE) data obtained from the US Space Surveillance Network[2]. In [3] TLE data are a source to estimate satellite lifetime. In addition, collision risk assessment and avoidance has become critical and has attracted significant research attention. However, frequent maneuvering affects spacecraft operational life, and reduces space mission continuity[4]. It would be an asset if each active space object in orbit would be capable of constructing its SSA and compute at least a rough probability of collision using publicly available data, such as the TLE. This would primarily lower the ground workload[5], releasing it from the screening task for detecting collisions. Second, the owner of a constellation could optimize collision avoidance maneuvers taking into account collision probability with other bodies[6]. Due to data errors and forecast errors, the intersection relationships errors inevitably exist. The lack of uncertainty information of TLEs has initiated numerous studies into the accuracy of TLEs, methods for estimating their covariance, and improvements to their accuracy[7]. There is a wide range of methods that allow the uncertainty information to be estimated. These approaches differ greatly in complexity, accuracy and applicability[8].

*Email: andreacicca7@gmail.com
†Email: claudio.bombardelli@upm.es

Much has been said about the accuracy of TLEs compared to true data. For instance, the typical at-epoch position accuracy from TLEs for a large Low-Earth orbit object is an easily memori able figure of m m m in the along-trac radial cross-trac directions. owever, little has been said about the accuracy limitations of propagated TLEs and the impact of the update fre uency, especially when it comes to employ TLEs data to monitor conjunctions.

The aim of this work is to provide a deeper analysis of TLEs accuracy of both LEO and GEO objects considering the frequency of updated TLE data. The analysis is performed exploiting high-accuracy data from DORIS integrated radio-positioning (for LEO) and Wide Area Augmentation System (WAAS) satellites in GEO, as well as a high-fidelity in-house propagator. A comparison with available covariance data from conjunction data messages (CDMs) is also performed. Finally, the implications for conjunction screening (CS) and collision avoidance maneuvering (CAM) are discussed.

2 TLE frequency

In order to develop a complete analysis of the accuracy of TLEs, it is very important to focus the attention on the epoch at which TLE are collected and then released. TLEs are not a real time epoch measurement. This is because the TLE is moved to the last ascending node before release for distribution for LEO satellites. Thus, the time interval between consecutive data is integer multiple of the orbital period of the satellite, that is about 100 minutes, with a tolerance of 0.1 orbits (10 minutes). The frequency of TLE data can vary from 2 orbits up to 15 orbits as shown in Fig. 1 obtained for Jason 3 satellite in 9 months of observation. This has a consequence in the practical applications of TLEs. Unless the event

that has to be study is exactly at the passage of the ascending node, it is necessary to perform a numerical propagation of TLE data to study the phenomenon at the epoch of interest.

Fig. 1 TLE frquency for JASON 3 satellite (LEO)

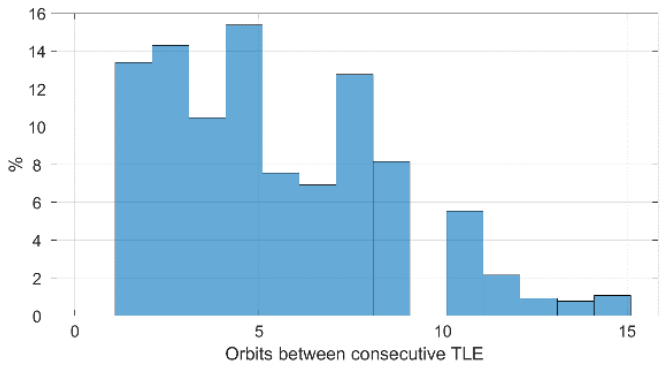

This assumption is not valid for EO satellites, otherwise it will be available, in the best case, only one TLE per day. Fre uency for a EO satellite (AN F -R) are reported in Fig. 2. Note that on x-axis are reported the hours, not the orbits as in the previous plot.

Fig. 2 TLE frequency for ANIK F1-R satellite (GEO)

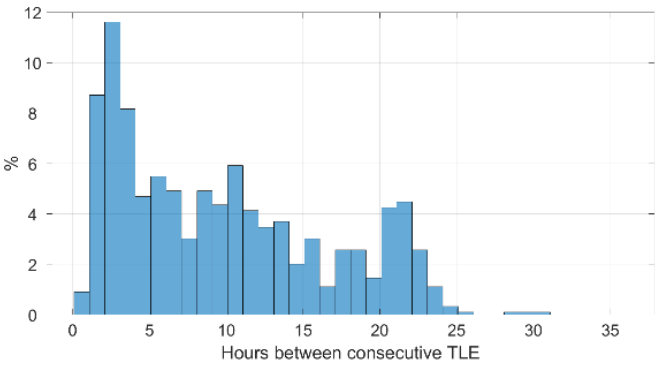

Consequently, to perform an accurate TLE analysis, two main steps have to be conducted:

- At-epoch accuracy: analysis of TLE accuracy as they are released from US Space Surveillance Network;
- Propagated-state accuracy: in this case TLEs are the input of a numerical propagation the aim of which is to obtain the state of the satellite at an epoch between consecutive TLE.

3 At-epoch accuracy

The accuracy of the at-epoch TLE state has been calculated for LEO and GEO satellite comparing the TLE data with two high-accuracy databases, which are respectively DORIS data for LEO satellites and WAAS catalogue for GEO satellite.

Each TLE has been propagated until the closest DOR S (or AAS for EO) data available with a high-accuracy orbital propagator. onsidering that DOR S data have a fre uency of seconds and AAS data are collected each seconds, the time span of the propagation is relatively short. This step is fundamental to have a clear idea of initial error of TLE considering that they will be propagated in the ne t step, which is the main goal of this wor . Results show that, as already nown, position error is smaller than m for LEO satellite and below m for EO satellite. Analysis have been repeated for different LEO satellite e uipped with a DOR S receiver and different EO satellite for which AAS data were available.

4 Propagated state Accuracy

The greatest contribution of this paper is the analysis of the TLE when they are propagated with a high-accuracy numerical propagator in. According to the goals, different LEO satellites have been selected to perform a forward propagation until the Medium Julian Date (JDM) between consecutive TLE. Note that JDM epoch is not a random choice, but it has been considered that for epoch after JDM it is possible to perform a backward propagation from the successive TLE in order to reduce the time of the propagation. Also in this case, JDM state has been compared to the closest DORIS data; for this reason, a second short (less than 30 seconds) propagation is necessary. Magnitude of error is increased after the propagation as shown for JASON 3 satellite in Fig. 3. Errors are projected along normal/tangential/out-of-plane local reference frame.

Fig. 3 Position error at JDM for Jason 3 satellite

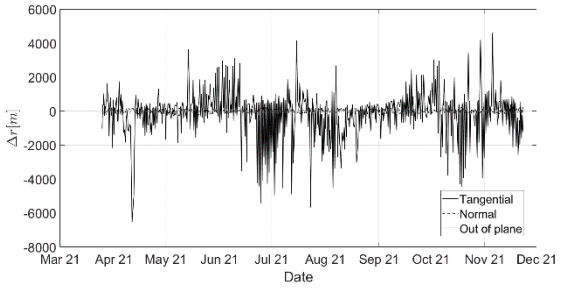

Results show that tangential position error is still the dominant component of error and that due to the propagation the error goes up to 6 km. At this point, the results have been reworked considering that each TLE has been propagated until JDM, and t his means

that the duration of the propagation is directly related to the TLE frequency. Therefore, considering that the along track component of error increases with the interval of the propagation, a possible approach to better understand the results to divide TLE into classes of frequency. Four different classes of frequency have been individuated and named "group" as shown:

- Group 1: frequency smaller than 2 orbits;
- Group 2: frequency between 3 and 4 orbits;
- Group 3: frequency between 5 and 8 orbits;
- Group 4: frequency higher than 9 orbits.

Filtering the error of propagated state in these 4 groups show that the accuracy of the position along the tangential axes is strongly influenced by the classes of frequency selected: it is smaller that 1 km for group 1 and 2, goes to 2 km for group 3 and reaches an error of 4 km only for the 3% of the TLE grouped. Mean and standard deviation for different number of revolutions are also reported in Table 1, which shows how the accuracy is influenced by the frequency of TLE and, consequently, the duration of the propagation.

Table 1 Mean and standard deviation of position magnitude and tangential position error for different number of revolutions

	Position magnitude [m]		*Position error along u_t [m]*	
Number of revs	Mean μ	Std σ	Mean μ	Std σ
2	447,65	306,71	-99,72	494,28
6	963,96	908,75	-285,6	1289,47
11	1683,58	1557,45	-458,24	2258,54
14	1798,76	2299,34	-1362,96	2644,25

5 Conclusions

Two-Line Elements (TLE) data represent a fundamental tool in orbital dynamics and Space Situational Awareness sector. owever, TLEs does contain non-negligible inaccuracies and it is necessary to ta e them into account when performing a collision prediction, an orbit reconstruction or whatever. For LEO and GEO satellite it is possible to state from previous analysis that the position error is respectively 1 km and 40 km. In most of the applications it is not possible to find a TLE and the epoch of interest, so a propagated state has to be obtained. In applying this process, it is firstly necessary to use a high-accuracy orbital propagator. Anyway, the error can strongly increase with the propagation, and it is influenced by the duration of the propagation and the frequency of TLE.

Acknowledgements

This work was supported by MINECO/AEI and FEDER/EU under Project PID2020-112576GB-C21. The authors thank the MINECO/AEI of Spain for their financial support.

References

[1] Dumont J.P., Rosmorduc V., et al., *Jason-3 Products Handbook*, (2015)

[2] Flohrer F., Holger K., Klinkrad H., *Assessment and Categorization of TLE Orbit Errors for the US SSN Catalogue*, (2008)

[3] Xu, Xiao-li, and Yong-qing Xiong., *Orbit error characteristic and distribution of TLE using CHAMP orbit data*, Astrophysics and Space Science 363.2 (2018)

[4] Muelhaupt T.J., Sorge M.E., Morin J., Wilson R.S., *Space traffic management in the new space era*, J. Space Saf. Eng., (2019)

[5] Curzi G., Modenini D., Tortora P., *Two-line-element propagation improvement and uncertainty estimation using recurrent neural networks*, CEAS Space Journal, (2022)

[6] Águeda, A., Aivar, L., Tirado, J., & Dolado, J. C., *In-orbit lifetime prediction for LEO and HEO based on orbit determination from TLE data,* 6th European Conference on Space Debris (Vol. 723, p. 61), (2013)

[7] Vallado, D.A., Cefola, P.J., *Two-Line Element Sets – Practice and Use,* International Astronautical Congress, (2012)

[8] Geul, Jacco, Erwin Mooij, and Ron Noomen, *TLE uncertainty estimation using robust weighted differencing*, Advances in Space Research 59.10, (2017)

Organizers and Sponsors: